IMPACT OF MESOSTRUCTURE ON FUNCTIONAL PROPERTIES OF GRANULAR DIAMOND COMPOSITES

by

David Phillip Harding

A dissertation submitted to the faculty of
The University of Utah
in partial fulfillment of the requirements for the degree of

Doctor of Philosophy

Department of Metallurgical Engineering

The University of Utah

May 2013

The University of Utah Graduate School

STATEMENT OF DISSERTATION APPROVAL

The dissertation of **David Phillip Harding**

has been approved by the following supervisory committee members:

Zhigang Zak Fang, Chair **12 Feb 2013**
Date Approved

Ravi Chandran, Member **12 Feb 2013**
Date Approved

Chen-Luh Lin, Member **12 Feb 2013**
Date Approved

Reaz A Chaudhuri, Member **20 Mar 2013**
Date Approved

Dan Belnap, Member **15 Mar 2013**
Date Approved

and by **Jan Miller**, Chair of

the Department of **Metallurgical Engineering**

and by Donna M. White, Interim Dean of The Graduate School.

ABSTRACT

Granular diamond composites are particulate reinforced composites, where the particulate phase is a grade of high-hardness polycrystalline diamond, embedded in a tougher, hard-material matrix. Granular diamond composites are hierarchically-structured materials. In addition to the macrostructure and microstructure, granular diamond composites have a mesostructure that encompasses the morphology of the matrix and granules and is characterized by parameters such as component volume fraction, granular sphericity, and matrix uniformity. The mesostructure is functionally designed to improve the performance of the composite in petroleum well-drilling applications by increasing the fracture resistance while maintaining the wear resistance. The impact of the mesostructure on the flexural strength, wear resistance, impact resistance, and in-field performance was measured. Physical testing showed that volume fraction of the tougher, matrix phase can be increased significantly before the wear resistance of the composite decreases appreciably. But the testing also showed that the method developed to produce the composites resulted in component materials with inferior properties. The flexural strength of a polycrystalline-diamond/tungsten-carbide material system was explored using several modeling techniques, including analytic, two-dimensional numeric, and three-dimensional numeric models. Residual stresses, arising from the change in conditions after the material is formed in a high-temperature, high-pressure sintering process, have a significant impact on the calculated strength of the composite. Dilatational residual stresses have never been treated in a rigorous manner in the literature and are often neglected completely. In this study, the thermal and dilatational residual stresses were modeled. Stresses from externally applied loads preferentially concentrate in the stiffer diamond phase. Thermal residual stresses strengthen the stiffer and weaker diamond phase through residual compression and weaken the carbide phase through residual tension. The dilatational residual stresses partially counteract the thermal residual stresses. Without thermal residual stresses the composite would have lower strength due to premature failure in the diamond phase. Without dilatational residual stresses the composite would have lower strength due to premature failure in the carbide phase. The strengths predicted by the enhanced models match the measured strengths quite well, despite significant uncertainty in the material properties and process parameters.

To my wife Julia, and our children, Hannah, Jonas, Enoch, and Eve. Make a difference.

TABLE OF CONTENTS

Chapter

LIST OF TABLES

Table

LIST OF SYMBOLS

Symbol	Meaning
σ	normal stress
τ	shear stress
ϵ	normal strain
γ	shear strain
S	compliance tensor
E	Young's modulus
ν	Poisson's ratio
α	coefficient of thermal expansion
Δ	change in
D	dilatational
T	thermal/temperature
P	pressure
r	residual
f	reinforcement (fiber) phase
m	matrix phase
c	component (either phase)
x	axial component/direction
y	transverse component/direction
z	thickness component/direction
u	critical (ultimate)
a	external applied

ACKNOWLEDGMENTS

I would like to express my gratitude for my advisor, Z. Zak Fang, for his guidance and patience over the years. With his help, I was able to complete this journey. I thank my committee members, Ravi Chandran, Chen-Luh Lin, Reaz Chaudhuri, and Dan Belnap for their feedback. I benefited from their diverse experience and suggestions.

Financial and technical support of this research was provided by Smith Megadiamond. I particularly appreciate the guidance and assistance of Dr. Belnap.

I, along with all who read this dissertation, owe a debt of gratitude toward my personal editor, Phillip Harding, a.k.a. Dad, for his invaluable assistance in smoothing over the manuscript and making it much less painful to read.

I'm grateful to the University of Utah community as a whole, the professors, fellow students, support staff, and administration. My education and this dissertation has been impacted by each one of you. I took my first class at the U twenty years ago, and I have thoroughly enjoyed my time of discovery and growth at this institution of learning.

I will always be indebted to my wife, Julia, for her patience and support, and to my employer, Dimicron, for the flexibility and encouragement to complete this work.

Finally, I would like to thank my God for the blessing of all of the aforementioned people in my life, and for the opportunities given that have led me to this point.

CHAPTER 1

SCOPE AND RESEARCH OBJECTIVES

Polycrystalline diamond compact (PDC) bits were developed three decades ago for the drilling of geothermal wells. The technology was adopted by the oil and gas drilling industry and has had a major impact on it, with almost two-thirds of the world's oil currently being extracted through wells drilled with PDC bits.[1] The oil and gas industry is the dominant consumer of polycrystalline diamond (PCD). Considering the number of oil and gas wells being drilled and the role of oil and gas in our global economy and industry, polycrystalline diamond is an important material to mankind.

Previous to the adoption of PCD, cobalt-cemented tungsten carbide (WC-Co) was the material of choice for drilling oil and gas, as well as geothermal, wells. WC-Co is still the default substrate material in PDCs, providing a base for the PCD. In most rock formations PDC bits significantly outperform WC-Co bits. The service life of PDC bits is limited by a different mechanism than WC-Co bits. In general, the limiting functional property in WC-Co bits is the wear resistance of WC-Co. Typically the limiting functional property of PDC bits is the brittleness of the PCD.

The performance of PDC bits could greatly be improved if the toughness of the material could be increased without significantly reducing the wear resistance of the material.

The performance of PDC bits is impacted by numerous factors, not the least of which are the functional properties of the PCD layers and the WC-Co substrate. Because both of these materials are themselves composites, their functional properties are also dependent on a number of other factors. Each material has its own set of microstructural parameters that can be manipulated.

In this research, a novel material arrangement is investigated which, hypothetically, could increase the toughness of the drill bit with a smaller decrease in the material wear resistance than usual. This material is referred to as granular diamond composite (GDC). The composite material is novel, not because of its components, but rather in the arrangement of the material on a mesostructural level. In this investigation, mesostructure is defined as the structure of the material that falls in scale between macrostructure, or the geometry of the part, and the microstructure of the diamond, carbide, and sintering alloy, as well as the fine composite structure of the PCD and WC-Co.

GDC materials have round granules of high-wear PCD, roughly a quarter millimeter in size, embedded in a matrix of higher toughness, as shown in Figure 1.1. In the electron micrograph, the diamond phase is dark and the carbide phase is light.

The stated goal of this research is to determine the effect of mesostructural design on the functional properties of GDC materials.

Functional properties are not intrinsic material properties, but have a close relationship with the performance of a material in an industrial use. The industrial

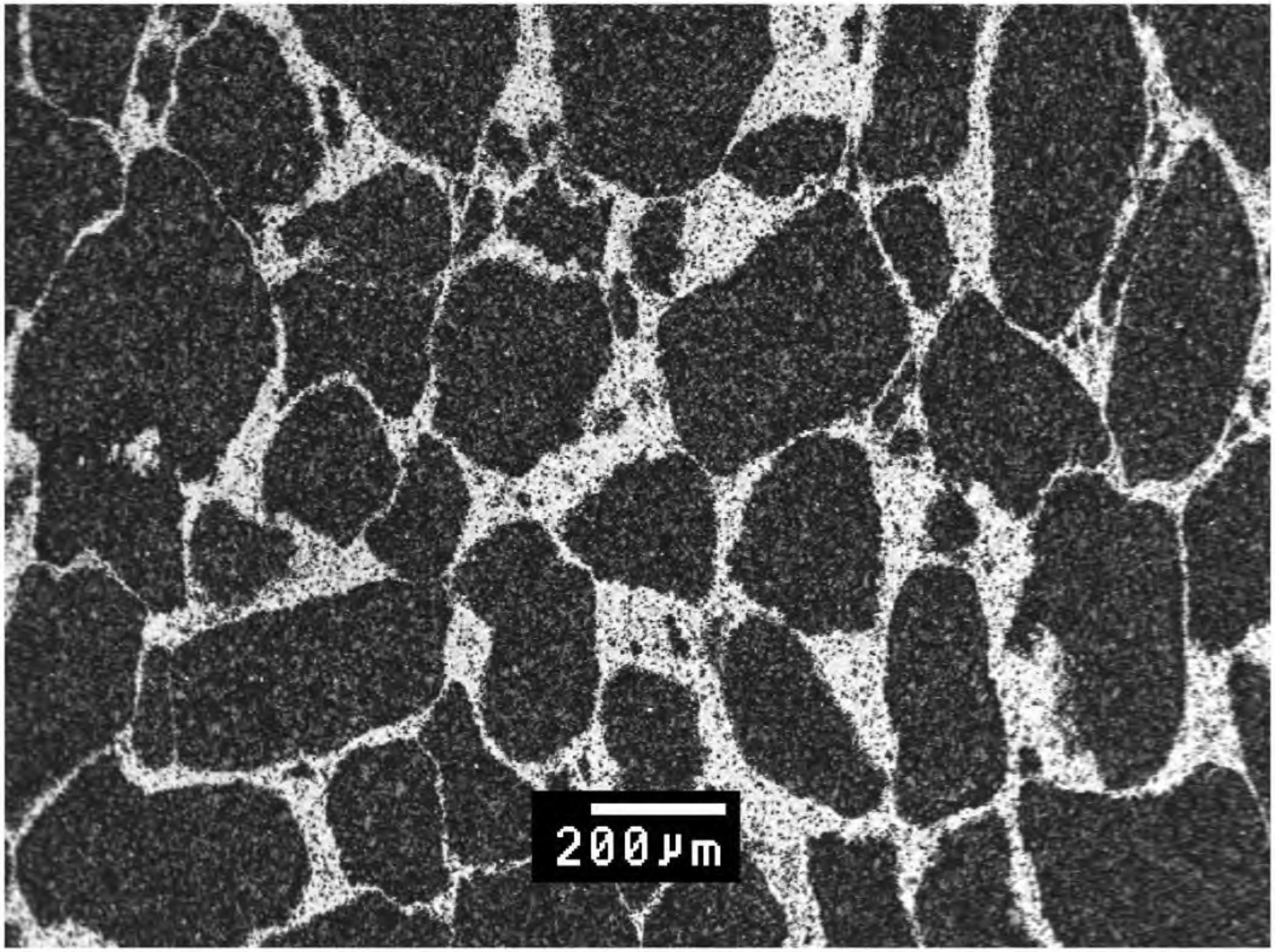

Figure 1.1. A backscatter electron SEM micrograph of the granular diamond composite mesostructure. The diamond phase is dark and the carbide phase is bright.

application selected for this research is down-hole petroleum well drilling. The functional properties selected for this application are transverse rupture strength, wear resistance, and impact resistance. Transverse rupture strength was most extensively used because it is a good indicator of industrial performance and it is more readily measurable compared to the other properties.

The mesostructural design parameters studied include component material, volume fraction, granule shape, and matrix thickness (mean free path) uniformity.

Models were developed to try to describe the effect of the mesostructure on the functional properties. Having a model that well describes the dependence of the functional properties on the mesostructure, sheds light onto the relationship between them and the mechanisms at play at the mesostructural level. It also allows for the optimization of the functional properties with less cost in terms of time, effort, and money required for edisonian experimentation.

During the research the question was raised why the contribution of pressure to composite residual stresses had been neglected in published research. The impact of dilatational residual stresses, those cause by pressure changes after sintering, was investigated and found to have a significant impact on the overall residual stresses. This finding should be considered in all future PCD residual stress research.

The manufacturing process that was developed for this material was not able to produce material at the extremes of volume fractions (0v% and 100v%) which had properties that matched the conventionally produced component material. For example, one of the 100v% PCD grades, produced with the experimental process had, on average, roughly 90% of the transverse rupture strength of the conventionally produced PCD material, and only 40% of the functional wear resistance. Despite this, the trends of the material properties indicate that this material could be further developed to reach the goal of high toughness and wear resistance. The measured wear resistance changed little until the tougher matrix made up more than 40v% of the material volume. Material with a 20-30v% matrix showed a marked increase in impact resistance over the 100v% PCD material. A field test was conducted on one grade of GDC, where the experimental drill bit inserts showed better wear resistance and toughness than the control PDC bit inserts.

References

1. Sandia National Laboratories. Polycrystalline diamond drill bits open up options for geothermal energy. https://share.sandia.gov/news/resources/news_releases /pdcs_geothermal/ (accessed Oct 26, 2012).

CHAPTER 2

BACKGROUND AND LITERATURE SURVEY

This chapter will discuss many important themes related to granular diamond composites (GDC), giving both background information and recent findings by other researchers in related fields. A possible industrial application for GDC will be selected and described. The history, properties, and uses of polycrystalline diamond (PCD) will be discussed, including design considerations. Cemented tungsten carbide, a constant companion to PCD in these applications, will also be reviewed. GDC can be considered a functionally designed hierarchically structured hard material (HSHM), so HSHM will be discussed. The functional properties of GDC will be discussed along with factors which affect these properties, such as residual stresses. Modeling is used extensively in this study and the background and current uses of modeling of residual stresses and strength of PCD will be reviewed.

Petroleum Well Drilling

Wentorf et al.[1] suggested that materials can be classified into three groups: the common materials, used for construction like organics, metallics, and some ceramics; hard materials, the oxides and particularly the carbides that are used to cut and shape the common materials; and the superhard materials which consist of diamond and cubic boron nitride, which are used to cut and shape the hard materials. The theoretical aspects of this research apply to superhard composites in general, but a specific end application is selected in order to define an optimum set of material characteristics. The chosen end application is drill bit inserts for the petroleum drilling industry, which is a good example of an important industrial application of superhard materials. In the high stress, high temperature, and highly abrasive environment of down hole drilling, only extreme materials can perform adequately.

Cobalt-cemented tungsten carbide (WC-Co) have been used for more than 50 years in drill bit inserts.[2] PCD has been used for more than 30 years.[2-4] PCD works best in high abrasive applications, typically soft to medium formations,[3] but has been shown to work in even hard formations.[5] In drilling applications, shearing the rock is more efficient than cutting. PCD works best in shearing applications.[3]

Two indicators are used in the field to evaluate the performance of drill bit inserts. Rate of penetration (ROP) and bit life.[2,3] ROP is a measure of how hard the material is pushed. A higher ROP equates to higher speeds, higher stresses and higher temperatures. The bit life, often measured in linear distance drilled, is a measure of how durable the material is at the particular ROP. The bit life ends when it is not cutting efficiently (the ROP drops) or it is not cutting effectively (the diameter of the bore hole drops below a determined threshold).[2] In the selected application of petroleum well drilling, great value is realized in being able to run at a high ROP for a large drilling distance.

There are two functional material properties which affect the ROP and bit life:

wear resistance and fracture resistance (which is related to toughness).[2] The term fracture resistance will be used to refer to the functional, or real-world, resistance to breakage under operating conditions. Generally this breakage is macroscopic and results in a sudden loss of bulk material. The service life of an insert can come to an abrupt end due to this type of catastrophic fracture. Fracture resistance is related to fracture toughness, flexural strength, fatigue properties, and other mechanical properties. Wear resistance is a measure of how well the material resists the abrasive environment. Wear is a continuous process of microscopic amounts of material removal. The drilling becomes less efficient and the bore hole size is reduced as the inserts wear, eventually ending the drill bit's service life. Wear resistance is a direct function of the material's intrinsic hardness.

There is a trade off in super hard materials between fracture resistance and wear resistance. The hardness of the material is controlled by the composition and grain size of the components. The wear resistance is enhanced as the hardness increases, but the functional toughness of the material suffers. When the hardness decreases, the fracture resistance increases but the material wears faster.[6] As shown in Figure 2.1, functionally tougher materials typically wear faster; more wear resistant materials are typically more brittle and susceptible to sudden failure.[2] If a material has a good combination of fracture resistance and wear resistance the drill can be run at a high ROP for a long distance. The ability to do this provides a high economic return for drilling companies.

Traditionally there have been two choices of drill bit inserts for extreme conditions, PCD coated inserts or full WC-Co inserts. PCD has extreme hardness, therefore inserts using PCD coatings have high wear resistance. The service life of these

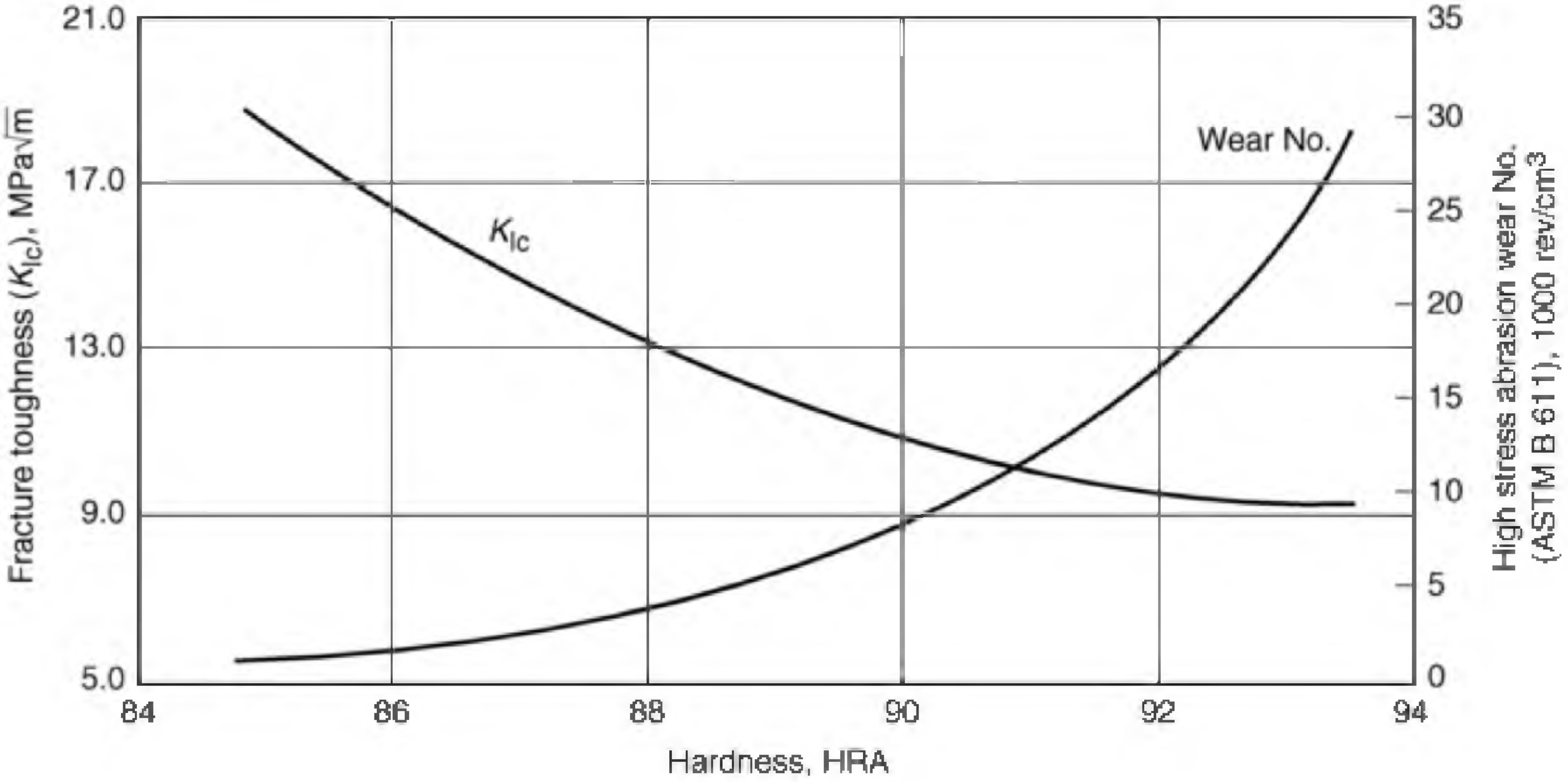

Figure 2.1. In WC-Co materials there is a distinct, inverse proportional relationship between wear resistance and fracture resistance.[7] (Reprinted with permission of ASM International. All rights reserved. www.asminternational.org.)

inserts is typically limited by the fracture resistance of the coating. WC-Co inserts, on the other hand, have good fracture resistance, but they have a much higher wear rate relative to PCD coated inserts. The service life of WC-Co inserts is typically limited by wear resistance.

By tailoring cobalt content, grain size, and other microstructural parameters, the functional properties of the materials can be adjusted to optimize the material performance for the particular rock formation to be drilled. Usually the microstructure is tweaked to enhance fracture resistance at the expense of wear resistance, or conversely, the wear resistance is enhanced while reducing the fracture resistance.

Polycrystalline Diamond

Diamond is an exceptional material from a materials science point of view. Even its name, derived from Greek meaning "unconquerable, unbreakable, unalterable,"[8] reflects its remarkable physical properties. Diamond has the highest hardness of any bulk material and is about a third harder than the next hardest material, cubic boron nitride. It also has the highest or one of the highest values for compressive strength, elastic modulus and thermal conductivity. While diamond is best known as a gemstone, these extreme properties have made diamond an invaluable industrial material.[9,10] Diamond is an allotrope of carbon and its superior properties are derived from the strong sp^3 covalent bonds of carbon arranged in a three-dimensional lattice.

Single crystal diamond has high hardness and wear resistance, but low fracture toughness.[11] Due to the random orientation of grains, PCD has a markedly improved fracture toughness with minimal hardness loss and isotropic wear resistance.[1,3,11]

Diamond is a naturally occurring material in both the single crystal form and, more rarely, the polycrystalline form. Diamond was first successfully synthesized in the 1950s, by mimicking the geological conditions in which diamond forms.[12] Today, ninety percent of the diamond used for industrial applications is synthetically produced.[13]

Synthetic diamond crystals are created from graphite under high pressure, high temperature (HPHT) conditions.[5,14,15] PCD is then synthesized by sintering together the diamond crystals in another HPHT process. A solvent, usually cobalt based, is used to facilitate the sintering. The solvent alloy melts and allows for carbon to dissolve and reprecipitate out, forming the bonds between grains.[2,5,16,17] Both the network of sintered diamond crystals and the metal matrix are continuous.[1] In practice, PCD is typically sintered on a cobalt-cemented tungsten carbide substrate. Generally, the WC-Co substrate provides the sintering alloy which infiltrates the diamond grains during the HPHT precess.[4] Figure 2.2 shows the microstructure of PCD with the diamond grains appearing dark and the cobalt-based sintering alloy appearing light.

The average diamond grain size and distribution are used to tailor PCD properties. Finer diamond has more wear resistance but lower toughness despite having higher metal content.[16] Transition layers, composed of varying amounts of WC-Co and PCD, may be used to reduce the residual stresses due to the mismatch of expansion coefficients between the PCD outer layer and the WC-Co reinforcement.[25]

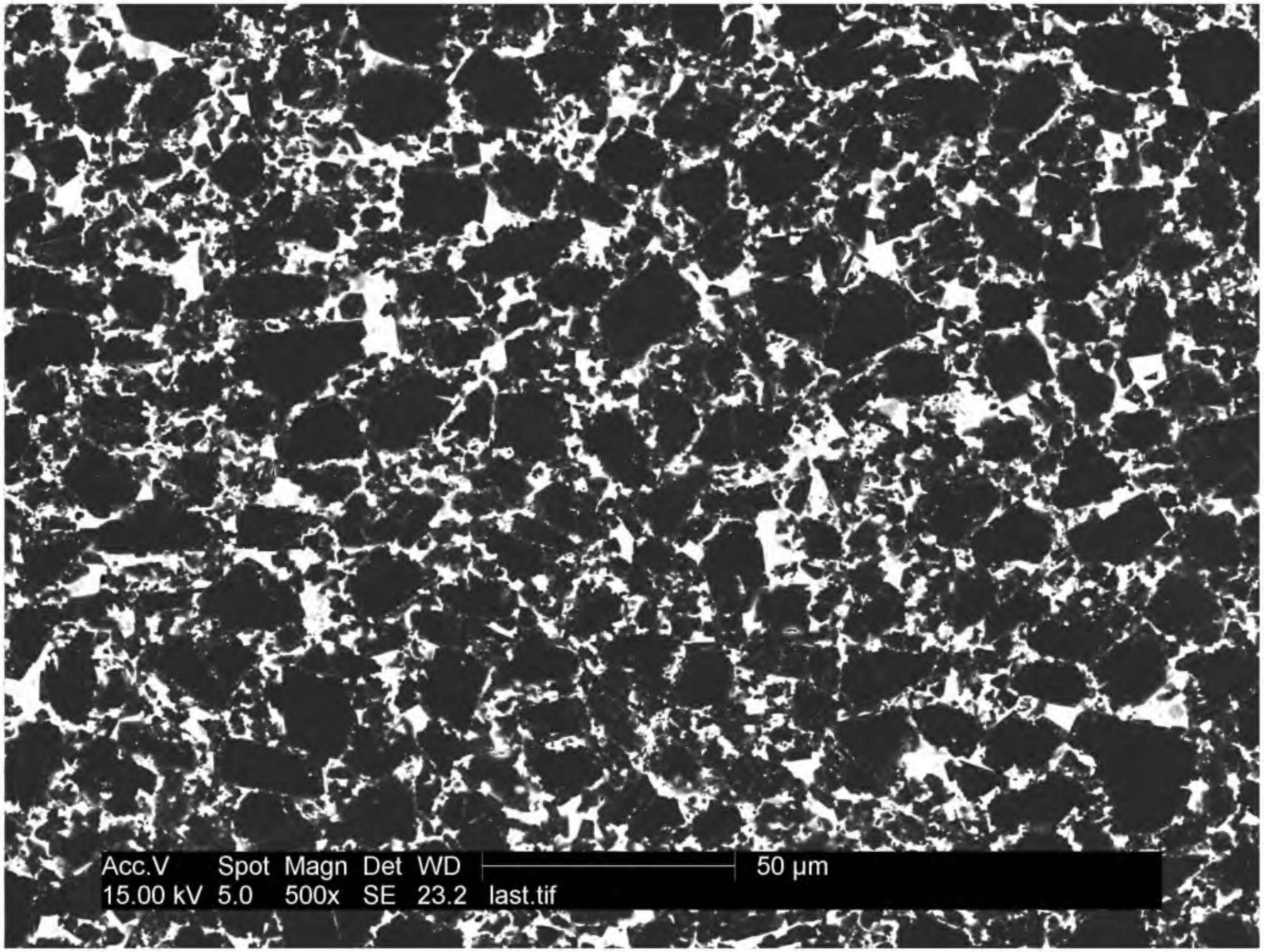

Figure 2.2. An electron micrograph revealing the microstructure of a bimodal grade of PCD. The low Z (atomic number) diamond shows dark in the micrograph and the high Z sintering alloy is bright.

Cemented Tungsten Carbide

Cobalt-cemented tungsten carbide (WC-Co) is often used along side PCD in industrial applications, particularly in petroleum well boring. Before the application of PCD in oil well boring, WC-Co was the predominate material because of its high wear resistance and fracture resistance compared with other available materials. PCD is typically made in the presence of WC-Co with the cemented carbide providing the cobalt for the diamond sintering step. Taken together, polycrystalline diamond sintered on a WC-Co substrate is called a polycrystalline diamond compact (PDC). The acronyms PDC and PCD are sometimes used interchangeably, but in this work PCD will refer to the material consisting of sintered diamond grains in a sintering alloy matrix, and PDC will refer to a component consisting of PCD sintered on a carbide substrate.

Cemented tungsten carbide is a metal matrix composite with the WC grains being the reinforcement phase and the matrix being made up of a ductile metal alloy, typically cobalt-based. The carbide grains are continuous to a degree depending on cobalt content, but are not directly bonded. The matrix phase binds, or cements, the carbide grains together,[18,19] as seen in Figure 2.3.

WC-Co is typically produced using powder metallurgy technology. The WC grains are mixed with cobalt and volatile lubricants and cold pressed to shape. The sintering step is often referred to hot isostatic pressing. [21]

As is generally the case with super hard materials, the hardness of the material is increased with a decrease in reinforcement grain size and with a decrease in the binder phase. The increased hardness increases the wear resistance and decreases the fracture

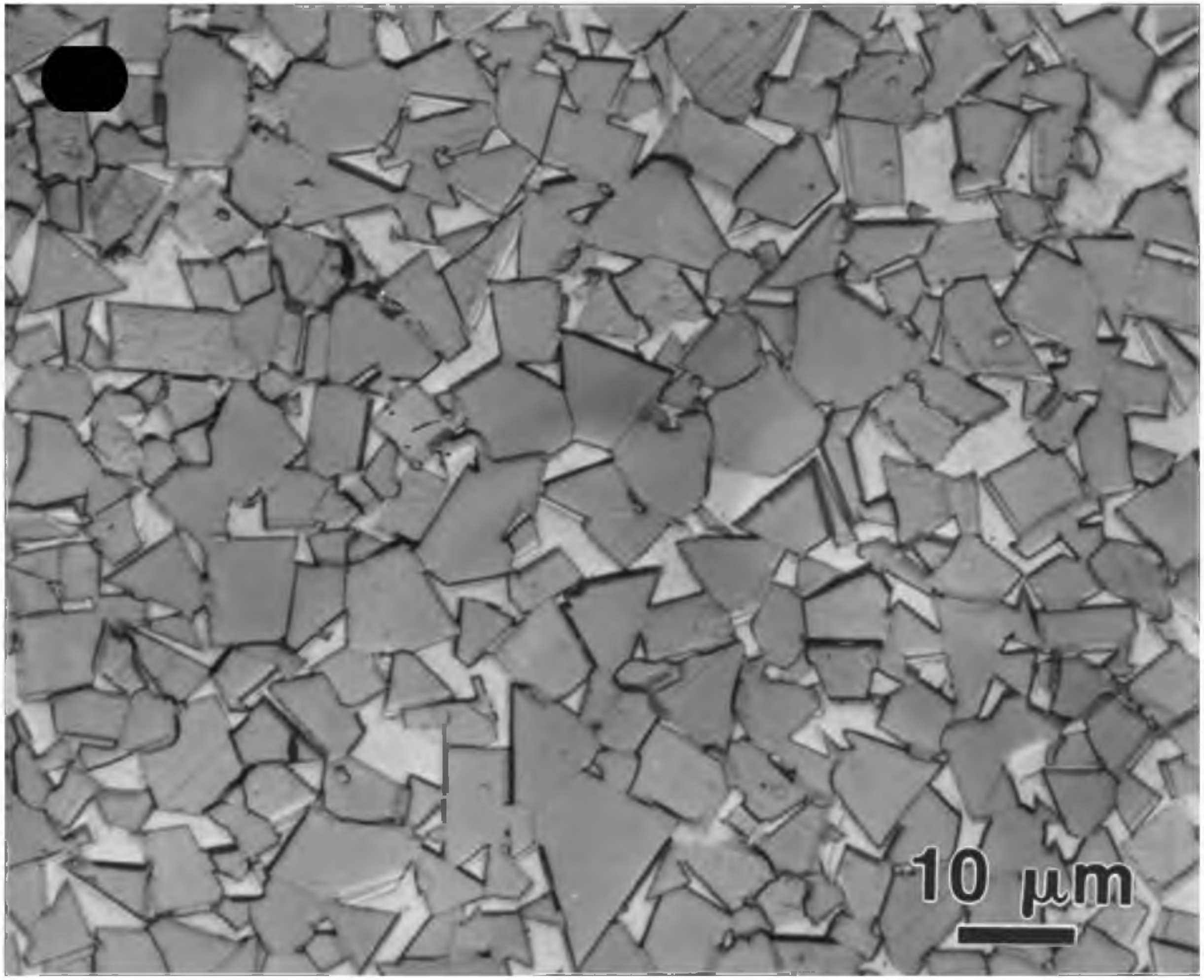

Figure 2.3. Microstructure of cobalt-cemented tungsten carbide.[20] (Reprinted with permission.)

resistance.[22]

Functionally Designed Materials

Functionally designed materials are materials which have an additional level of structure that is engineered to enhance the functional properties of the material. Functionally graded materials may be the best know subclass of functionally designed materials. The composition of functionally graded materials changes through the thickness of the material.[23] This gradation modifies the functional properties of the material through mechanisms like stress shielding or stress distributing.[24] Functionally graded materials are being actively researched in the aerospace industry, with a particular interest for heat shields.

The additional layer of structure in functionally designed materials will be referred to as the mesostructure, as the scale falls between the macrostructure and the microstructure of the material. The macrostructure can be considered as the overall geometry of the part: part thicknesses, lengths, and shapes. It is often measured in millimeters, and is produced by forging, molding, casting, machining, etc. Microstructure is a commonly used term and well understood in the materials industry. It is the structure or arrangement of a material that is visible only under magnification.[25] The microstructure is typically characterized by parameters like grain size, grain aspect ratio, texture and orientation, and fractions of different phases. It is often measured in hundreds of nanometers and is often manipulated by thermal or mechanical processing (ie. rolling, annealing, quenching, aging, etc.). Functionally designed materials have an additional layer of structure between the macro- and microstructures. It is measured in tens of micrometers and is usually not produced by either macrostructural or microstructural means, but by powder processing methods capable of producing pre-designed architectural arrangements.[22,26] Note how the gradient in functionally graded materials fits into the definition of mesostructure.

Hierarchically Structured Hard Materials

Materials which have distinct microstructures, mesostructures, and macrostructures can be considered hierarchically structured materials which include most functionally designed materials as well as many composite materials. These materials have a mesostructure composed of two or more distinctly different phases with a manipulated arrangement. Each of these phases, in turn, have their own microstructures. Both the microstructure as well as the mesostructure can be engineered to optimize various functional properties.

Hierarchically structured materials made from superhard materials like PCD and WC-Co will be referred to as hierarchically structured hard materials. Hierarchically structured hard materials have relatively large structures of super hard materials, embedded in tougher matrices. This class of material has been given much attention in the past few decades, because it can be engineered to have property combinations that are unobtainable through engineered microstructure alone.[22,26] Materials with hierarchical substructures have a broader performance range than traditional materials because in addition to modifying the microstructure, the mesostructure can also be modified by changing the volume fraction, granule shape and size distribution, and contiguity.

Double cemented tungsten carbide (DC Carbide) illustrates this principle. As shown in Figure 2.1, there is a well-defined trade off between the fracture resistance and the wear resistance in WC-Co. The fracture resistance is increased and the wear resistance is decreased by adding more cobalt matrix phase or by increasing the WC grain size, because both of these increase the mean free path of the ductile matrix phase.[6] In traditionally formed WC-Co, without a mesostructure, nothing has been found that simultaneously increases the wear resistance and the fracture resistance.

DC Carbide is a functionally designed material with a granular mesostructure. Granules of low-cobalt WC are sintered in a cobalt matrix creating a carbide composite with two levels of cementing. It can be considered a granular metal matrix composite, with the low-cobalt WC acting as the reinforcement and the pure cobalt phase acting as the metal matrix.[6] By tailoring both the mesostructure and microstructures, double cemented tungsten carbide can achieve combinations of wear and fracture resistance that are better than what can be achieved in homogeneous WC-Co (see Figure 2.4).

Particulate Composites with Brittle Matrices

The granular diamond composites studied here are made from sintered polycrystalline diamond and cobalt-cemented tungsten carbide. Both PCD and WC-Co can be considered particulate composites, with the diamond and carbide particles acting as the reinforcement phase and the cobalt alloy acting as the matrix. They have a ductile matrix that is characteristic of typical composites. On the mesostructural level, GDC fall

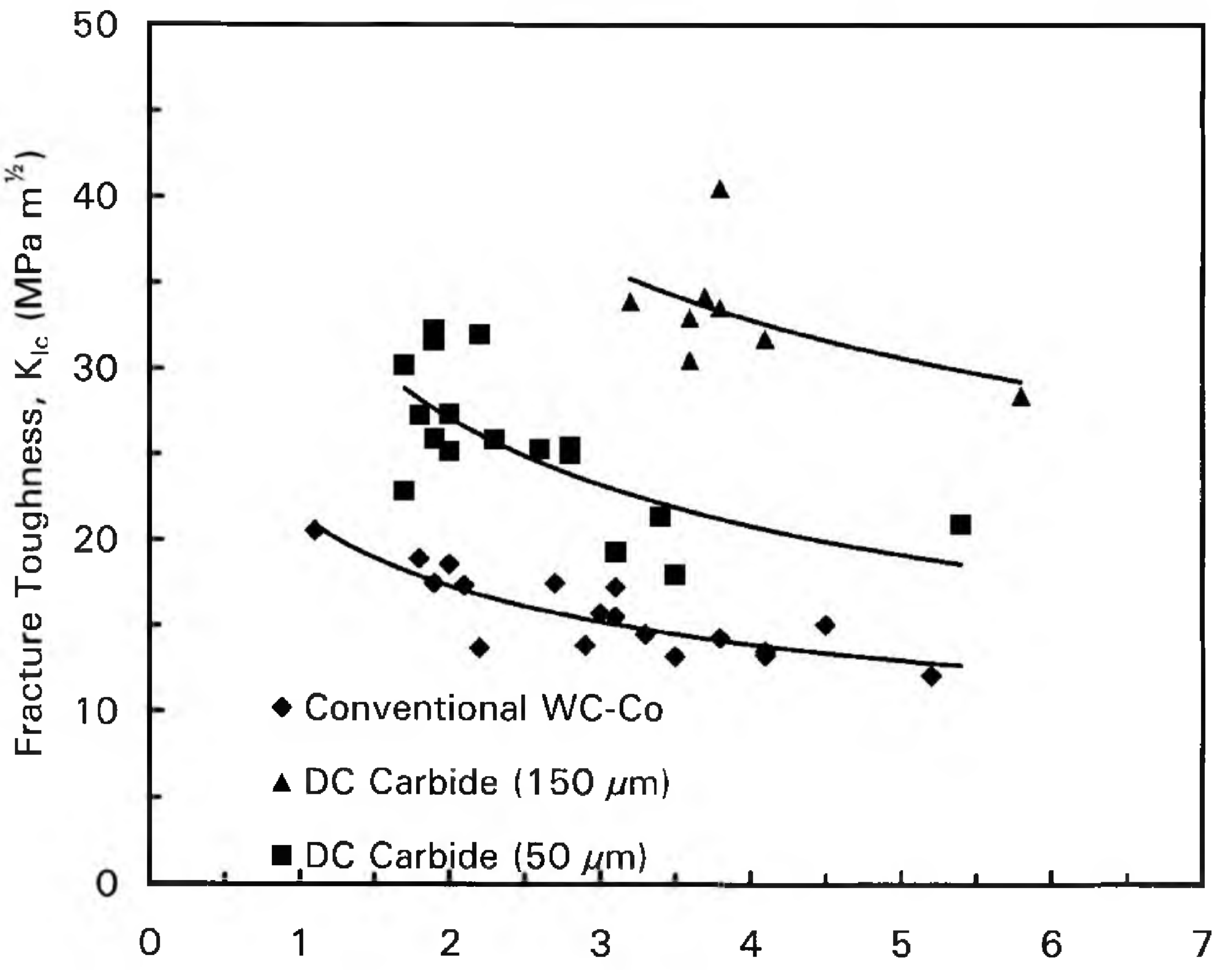

Figure 2.4. Relationship between fracture toughness and wear resistance for conventional WC-Co and DC Carbide. The additional level of structure allows the DC Carbide to simultaneously have better wear resistance and fracture toughness than conventional WC-Co.[6] (With kind permission from Springer Science and Business Media.)

under a special class of composites called brittle matrix composites. The properties and behavior of brittle matrix composites will be reviewed in this section.

Brittle matrix composites include ceramic matrix composites, glass matrix composites and intermetallic matrix composites,[27] GDC with WC-Co as the matrix would be classified as carbide matrix composites, and more generally GDC could be considered superhard matrix composites.

Brittle matrix composites have some properties that are shared with all composites, being dependent on the complex interaction of the phases. For example, the modulus of a composite usually falls between the Voight and Reuss bounds.[28]

In other aspects the complex interactions between the phases of brittle matrix composites produce properties that are not shared by more traditional composites. For example, the addition of the stronger particulates typically increases the toughness, but decreases strength.[29] This is caused by crack deflection at the interface between the reenforcement and the matrix phases.[30] Interface properties strongly affect the composite properties, as do residual stresses caused by differences in coefficients of thermal expansion (CTE). Weak interfaces are required for adequate toughening. Ceramic matrix composites are toughened by: fiber reinforcement, whisker reinforcement, ductile network, transformation toughening and microcrack toughening.[31]

Composite materials have been described using continuum models. Microstructural parameters influence the continuum model that describes the composite,[32] but continuum models have limited applicability to brittle matrix composites. For example, it is reported that fracture toughness measurements like K_{IC} and G_C have little or no meaning in brittle matrix composites with weak interfaces because the cracking stress is independent of flaw size.[31] A.G. Evans and D.B. Marshall concluded that the mechanical behavior of brittle matrix composites is sufficiently complex and coupled with sufficiently large number of independent variables to make empirical microstructural optimization not viable.[32]

One final difficulty with GDC is the particulate nature of the PCD granules. Ceramic matrix composites are most often reinforced with continuous fibers.[31] Whisker-reinforced ceramics are less effective at increasing toughness compared with continuous fibers.[31] Extrapolation to particulate materials would suggest that particulate reinforcement is even less effective at increasing toughness.

Residual Stresses in Diamond Composites

Much of the research reported in this dissertation is focused on impact and quantification of residual stresses. Analytical and numerical models are developed to simulate the accumulation of residual stresses. An attempt will be made to explain the flexural strength trends using residual stresses. Much of the literature describing the performance of PCD relies on residual stresses. A firm conceptual grasp of residual stresses and their causes is necessary to understand the current work.

Residual stresses can arise when materials with dissimilar expansion properties are bound together. The primary consideration in most material systems is thermal residual stresses, caused by a change in temperature and the differences in the coefficients of thermal expansion of the bonded materials.[33,34] This study also considers dilatational, sometimes called barometric, residual stresses, which is caused by changes in pressure and the differences in the bulk moduli of the materials.[35–38]

When two or more materials are bound together, differences in expansion properties cause residual stresses when conditions are changed. If temperatures increase, the material with the largest coefficient of thermal expansion will attempt to expand more than the other material. The bonding restricts this material from expanding as much as it would if it was not bonded, causing compressive stresses. The bonding to the first material causes the other materials to expand more than they would have otherwise expanded, creating tensile stresses in the other materials. In practice, residual stresses often result in bending which complicates the stress state of the materials.

Residual stresses in a system must always maintain equilibrium. In a two-component system, the tension formed in one component is offset by the compression in the other component. In systems with multiple components the residual stress states may become more complicated, but the summation of residual stresses must always balance.[33]

Because of the multiple levels of structure, the granular diamond composites studied in this work have multiple layers of residual stresses. Residual microstresses develop in the polycrystalline diamond because of the differences between the diamond grains and the cobalt matrix.[33,39,40] The residual microstresses in the diamond phase of PCD are compressive at room temperature.[16] This is also true of the carbide material in cemented tungsten carbide. The scale of these residual microstresses may be small, but the magnitudes can be great.[39,40]

At the mesostructural level, residual mesostresses arises between the diamond granules and the carbide matrix. The differences between these materials generate residual mesostresses which compound the residual microstresses.

Finally, the granular diamond composite material is formed on substrates in various geometric configurations. The differences in bulk material properties between the functional material and the substrate will cause residual macrostresses to form,[33,39,40] which overlay the residual mesostresses and microstresses.

The actual stress at any point is a summation of residual micro-, meso-, and macro- stresses, as well as any externally applied stresses.

Residual stresses in polycrystalline diamond compacts have been measured using neutron diffraction[33,40,41] as well as micro-Raman spectroscopy.[17,34,41–44] XRD and electron channeling methods have been used to measure residual stresses in grown films of diamond.[45]

The effect of the residual stresses on PDC cutters is substantial, Chen Feng et al.[46] blamed residual stresses for 70% of abnormal failures in cutters. Microresidual stresses can cause microcracking which can significantly reduce the performance of the material.[39,47] The modeling and mitigation of these stresses have been an area of study by empirical, theoretical, and numerical means. Much of this study has focused solely on thermal residual stresses, but recently attention has been brought to the role of dilatational residual stresses as well.

There is a host of difficulties in accurately characterizing the formation of residual stresses in PCD, leading to many sweeping general assumptions, and justification of "effective" coefficients to match modeled data to measured values. Many of the difficulties are related to the lack of measured material properties, particularly in the range of temperatures and pressures present during the formation of the residual stresses. Compounding this is the fact that PCD is a class of materials, and comes in many different grades. PCD is produced with different grain sizes and size distributions, different solvent alloy formulations and fractions, and is sintered on different equipment, with different processing parameters. All of these variables affect the material properties.[16] Yet the published residual stress models typically reuse the assumptions and material properties from previously publish papers. A.D. Krawitz et al. identified other complications including, "binder plasticity, compositional variations, a denuded Co layer in the substrate near the interface, and the possible presence of graphite below the interface."[40]

Some research has looked into the high temperature properties of WC-Co,[48] but the affects of high pressure were not investigated. No such comprehensive high temperature research has been published for sintered polycrystalline diamond.

Many of the papers on modeling residual stresses in diamond published since around the year 2000[33,35,40,42,46] rely on the paper by Lin et al.[39] for material properties (E, ν, α) regardless of the grade of PCD that is being modeled. Most recently published studies only use material properties given at 300°C, even though Lin et al. printed a table of material properties of WC-Co and PCD at various temperatures, reproduced below in Table 2.1. These studies also rely on the paper by Lin et al. for the use of 1000°C as the starting temperature, or the temperature in the model at which the material is considered

Table 2.1

Material Properties (Reprinted from Lin et Al.)[39]

Properties	Material					
	WC/Co			PCD		
	20°C	300°C	600°C	20°C	300°C	600°C
Elastic modulus (GPa)	648	579	458	890	890	890
Thermal expansion coefficient ($\times 10^{-6}$/K)	4.5	5.2	5.2	1.3	2.5	3.9
Poisson's ratio	0.22	0.22	0.22	0.07	0.07	0.07
Thermal conductivity (W/(cm·°C))	1.0	1.0	1.0	5.43	5.43	5.43
Specific heat (J/(g·°C))	0.23	0.23	0.23	0.79	0.79	0.79
Density (g/cm^3)	15.0	15.0	15.0	3.51	3.51	3.51

residual stress free. In the Lin et al. paper, the use of 1000°C was only justified by assuming that plastic deformation in diamond would occur above this temperature.

In this widely cited paper by Lin et al. it is noted that "uncertainty exists" in high temperature properties for PCD and carbide, and then cites a paper by Glowka and Stone,[49] written in 1986, for the material properties. The table reproduced by Lin et al., shown in Table 2.1, differs somewhat from the tables published by Glowka and Stone, excerpts of which are reprinted in Tables 2.2 and 2.3.

The columns for 800°C for WC-Co and 700°C for PCD may have been dropped from the paper by Lin et al. for the table to fit in the column. It is unclear if these values were used by Lin et al. It is also not clear whether the column heading change from 50°C to 20°C was intentional or an oversight. The change of the CTE for WC-Co at 300°C from 5.3 to 5.2 may have been a typographic error, and likely does not have a large impact on the results. But the change of the Poisson's ratio for PCD from 0.22 to 0.07 is a major change and yet was not explained in the paper. This is significant because so much of today's current research still uses these values, and changes to material properties can have a large effect on the modeled results, as will be shown in Chapters 5 and 6.

In summary, current academic modeling of residual stresses are relying on decades old material property values, with typos and errors propagating from one study to the next. The grades of PCD and WC-Co may be quite different from the original grades tested, and none of the data reflects properties at ultrahigh pressure. Most of these difficulties stem from the difficulty of measuring these material properties across the range of temperatures and pressures present in the sintering cycle.

Table 2.2

Select Material Properties (Reprinted from Glowka and Stone)[49]

Parameter	Water Drilling	Air Drilling
. . .		
WC/Co compact material	Grade 883 WC/Co	Grade 883 WC/Co
ρ, g/cm^3	15.0	15.0
C_c, J/kg·°C	0.23	0.23
. . .		
Diamond Layer	PDC	PDC
ρ, g/cm^3	3.51	3.51
C_c, J/kg·°C	0.79	0.79

Table 2.3

Select Temperature Dependent Material Properties (Reprinted from Glowka and Stone)[49]

	WC/Co (°C)				PCD (°C)			
Property	50	300	600	800	50	300	600	700
Elastic modulus, GPa	648	579	458	403	890	890	890	890
Thermal expansion coefficient, 10^{-6}/°C	4.5	5.3	5.2	6.4	1.3	2.5	3.9	3.9
Poisson's ratio	0.22	0.22	0.22	0.22	0.22	0.22	0.22	0.22

In 2000, a paper by Bertagnolli et al.[35] introduced an apparently novel idea that the change in pressure after sintering could also introduce appreciable residual stresses in PCD. Previously, the residual stresses from pressure changes were written off as insignificant, if they were addressed at all.[33,39,40,42] Even in some current research the residual stress contribution of the pressure change is not mentioned.[34] In the paper by Bertagnolli et al., the effect of the pressure change was used to justify using a much lower ΔT than the one assumed by Lin et al., and cited by many since then. Rather than estimating the effect of the pressure difference, Bertagnolli et al.[36] simply used an effective ΔT that gave the best agreement between the model and measured values. Ten years later this justification for using an altered ΔT is becoming more widely used.[36,38,46]

Chapter Summary

Polycrystalline diamond compacts are used in drill bit inserts for drilling petroleum wells. The combination of high hardness and fracture resistance of polycrystalline diamond gives the drill bit inserts a long service life. The hardness and fracture resistance of PCD can be adjusted by modifying grain size and material fractions, but typically any increase in hardness is accompanied by a decrease in fracture resistance, and vice versa. Diamond granular composite material is a PCD and WC-Co composite with a mesostructure designed to increase the fracture resistance with only a minimal reduction of wear resistance.

The performance, and therefore design, of polycrystalline diamond compacts is strongly affected by the residual stresses that accumulate in the material as the compact exits the sintering cycle. Residual stresses occur when materials with dissimilar expansion coefficients are bound together and undergo changes in external conditions. Historically, only thermal residual stresses have considered when estimating residual stresses. More recently the change in pressure has been used as a justification to use an "effective ΔT" to obtain FEA results that match measured residual stresses.

References

1. Wentorf, R. H.; DeVries, R. C.; Bundy, F. P., Sintered superhard materials. *Science; (United States)* **1980,** *208*, 872-880.

2. Salesky, W. J.; Payne, B. R. In *Preliminary Field Test Results of Diamond-Enhanced Inserts for Three-Cone Rock Bits*, SPE/IADC Drilling Conference, 1987.

3. Clark, I. E.; Bex, P., The use of PCD for petroleum and mining drilling. *Industrial diamond review* **1999,** *59* (580), 43-5.

4. Belnap, D.; Griffo, A., Homogeneous and structured PCD/WC-Co materials for drilling. *Diamond and related materials* **2004,** *13* (10), 1914-1922.

5. Ingmarsson, K.; Mitchell, L., Diamonds are a driller's best friend. *Quarry Management* **2000,** *27* (4), 34-38.

6. Fang, Z.; Lockwood, G.; Griffo, A., A dual composite of WC-Co. *Metallurgical and Materials Transactions A* **1999,** *30* (12), 3231-3238.

7. Fang, Z., Wear resistance of powder metallurgy alloys. *ASM Handbook* **1998,** *7*, 965-977.

8. Liddell, H. G.; Scott, R., A Greek-English Lexicon. revised and augmented throughout by Sir Henry Stuart Jones with the assistance of Roderick McKenzie. Oxford: Clarendon Press: 1940.

9. Lide, D. R., *CRC handbook of chemistry and physics*. CRC press: 2012.

10. Bauccio, M., *ASM engineering materials reference book*. ASM International: 1994.

11. Keshavan, M. K.; Liang, B.; Russell, M., Tribological Properties of Polycrystalline Diamond and its Application. *Finer Points(USA)* **1990,** *9*.

12. Bundy, F. P.; Hall, H. T.; Strong, H. M.; Wentorf, R. H., Man-made diamonds. *Nature* **1955,** *176* (4471), 51-55.

13. Olson, D. W., Diamond (industrial). *US Geological Survey. Industrial Diamonds Statistics and Information. Available at http://minerals.usgs.gov/minerals /pubs/commodity/diamond/mcs-2008-diamo.pdf* **2008**.

14. Hall, H. T., Sintered diamond: A synthetic carbonado. *Science* **1970,** *169*, 868-869.

15. Vereshchagin, L. F., The synthesis of carbonado-type diamond. *High Temperatures--High Pressures* **1971,** *3*, 239.

16. D Miess, G Rai; "Fracture Toughness and Thermal Resistance of Polycrystalline Diamond Compacts" *Materials Science and Engineering* A209 (1996) 270-276

17. Wilks, J.; Wilks, E., *Properties and applications of diamond.* Butterworth-Heinemann: Oxford ; Boston, 1991.

18. Luyckx, S.; Love, A., The dependence of the contiguity of WC on Co content and its independence from WC grain size in WC–Co alloys. *International Journal of Refractory Metals and Hard Materials* **2006,** *24* (1), 75-79.

19. Lee, P. W.; Trudel, Y.; German, R. M.; Ferguson, B. L.; Eisen, W. B.; Mover, K.; Madan, D.; Sanderow, H.; Lampman, S. R.; Davidson, G. M., ASM handbook. *Powder metal technologies and applications/prepared under the direction of the ASM International Handbook Committee, ASM Handbook* **1998,** *7*, 1146.

20. German, R. M.; Suri, P.; Park, S. J., Review: liquid phase sintering. *Journal of materials science* **2009,** *44* (1), 1-39.

21. Schwarzkopf, P.; Kieffer, R., *Cemented carbides.* MacMillan: 1960.

22. Fang, Z. Z.; Griffo, A.; White, B.; Lockwood, G.; Belnap, D.; Hilmas, G.; Bitler, J., Fracture resistant super hard materials and hardmetals composite with functionally designed microstructure. *International Journal of Refractory Metals and Hard Materials* **2001,** *19* (4), 453-459.

23. Hirai, T., Materials Science and Technology, A Comprehensive Treatment, ed. RW Cahn, P. Haasen and EJ Kramer, Chapter 20 Functional Gradient Materials. VCH Verlag. (Weinheim),(1 996): 1996.

24. Liversage, J. H.; McLachlan, D. S.; Herrmann, M., Fracture toughness enhancements through stress shielding in functionally graded SiC-TiC composites. *Key Engineering Materials* **2005,** *290*, 129-134.

25. Vander Voort, G. F., *Metallography and microstructures.* ASM International: 2004; Vol. 9.

26. Harding, D. P.; Fang, Z. Z.; Belnap, J. D. In *Hard materials with functionally designed mesostructure*, Third International Conference on Microstructology, 2005.

27. Evans, A. G.; Zok, F. W., The physics and mechanics of fibre-reinforced brittle matrix composites. *Journal of Materials Science* **1994,** *29* (15), 3857-3896.

28. Wilkinson, D. S.; Pompe, W.; Oeschner, M., Modeling the mechanical behaviour of heterogeneous multi-phase materials. *Progress in Materials Science* **2001,** *46* (3), 379-405.

29. Monette, L.; Anderson, M. P., Effect of particle modulus and toughness on strength and toughness in brittle particulate composites. *Scripta Metallurgica et Materialia; (United States)* **1993,** *28* (9).

30. Ming-Yuan, H.; Hutchinson, J. W., Crack deflection at an interface between dissimilar elastic materials. *International Journal of Solids and Structures* **1989,** *25* (9), 1053-1067.

31. Anderson, T. L., *Fracture mechanics: fundamentals and applications*. CRC: 2005.

32. Evans, A. G.; Marshall, D. B., Overview no. 85 The mechanical behavior of ceramic matrix composites. *Acta metallurgica* **1989,** *37* (10), 2567-2583.

33. Paggett, J. W.; Drake, E. F.; Krawitz, A. D.; Winholtz, R. A.; Griffin, N. D., Residual stress and stress gradients in polycrystalline diamond compacts. *International Journal of Refractory Metals and Hard Materials* **2002,** *20* (3), 187-194.

34. Erasmus, R. M.; Comins, J. D.; Mofokeng, V.; Martin, Z., Application of Raman spectroscopy to determine stress in polycrystalline diamond tools as a function of tool geometry and temperature. *Diamond and Related Materials* **2011,** *20* (7), 907-911.

35. Bertagnolli, K.; Vale, R., Understanding and controlling residual stresses in thick polycrystalline diamond cutters for enhanced durability. *Finer Points(USA)* **2000,** *12* (1), 20.

36. Bertagnolli, K. E.; Cooley, C. H. In *Polycrystalline diamond compact (PDC) design methodology utilizing strain energy capacity*, Proceedings of ETCE 2001 Energy Sources Conference and Exhibition February, 2001; pp 5-7.

37. Jia, H. S.; Ma, H. A.; Guo, W.; Jia, X. P., HPHT preparation and Micro-Raman characterization of polycrystalline diamond compact with low residual stress. *SCIENCE CHINA Physics, Mechanics & Astronomy* **2010,** *53* (8), 1445-1448.

38. Kushch, V. I.; Bondarenko, N. A.; Korostyshevskii, D. L.; Osipov, A. C., The effect of the geometry and properties of the diamond-carbide interface on the fracture strength of diamond-carbide blanks. *Journal of Superhard Materials* **2011,** *33* (1), 60-69.

39. Lin, T. P.; Hood, M.; Cooper, G. A.; Smith, R. H., Residual stresses in polycrystalline diamond compacts. *Journal of the American Ceramic Society* **1994,** *77* (6), 1562-1568.

40. Krawitz, A. D.; Winholtz, R. A.; Drake, E. F.; Griffin, N. D., Residual stresses in polycrystalline diamond compacts. *International Journal of Refractory Metals and Hard Materials* **1999,** *17* (1), 117-122.

41. Jia, H. S.; Jia, X.; Xu, Y.; Wan, L. R.; Jie, K.; Ma, H. A., Effects of initial crystal size of diamond powder on surface residual stress and morphology in polycrystalline diamond (PCD) layer. *SCIENCE CHINA Physics, Mechanics & Astronomy* **2011,** *54* (1), 98-101.

42. Catledge, S. A.; Vohra, Y. K.; Ladi, R.; Rai, G., Micro-Raman stress investigations and X-ray diffraction analysis of polycrystalline diamond (PCD) tools. *Diamond and related materials* **1996,** *5* (10), 1159-1165.

43. Evans, T.; Davey, S. T.; Robertson, S. H., Photoluminescence studies of sintered diamond compacts. *Journal of materials science* **1984,** *19* (7), 2405-2414.

44. Davey, S. T.; Evans, T.; Robertson, S. H., An investigation of plastic deformation in sintered diamond compacts using photoluminescence spectroscopy. *Journal of materials science letters* **1984,** *3* (12), 1090-1092.

45. Harker, A. B.; Howitt, D. G.; Chen, S. J.; Flintoff, J. F.; James, M. R., Residual stress measurements on polycrystalline diamond. *Window and dome technologies and materials* **1994,** *4*, 254.

46. Chen, F.; Xu, G.; Ma, C. D.; Xu, G. P., Thermal residual stress of polycrystalline diamond compacts. *Transactions of Nonferrous Metals Society of China* **2010,** *20* (2), 227-232.

47. Ortega, A.; Glowka, D., Frictional heating and convective cooling of polycrystalline diamond drag tools during rock cutting. *Old SPE Journal* **1984,** *24* (2), 121-128.

48. Novikov, N. V.; Bondarenko, V. P.; Golovchan, V. T., High-temperature mechanical properties of WC-Co hard metals (Review). *Journal of Superhard Materials* **2007,** *29* (5), 261-280.

49. Glowka, D. A.; Stone, C. M., Effects of thermal and mechanical loading on PDC bit life. *SPE Drilling Engineering* **1986,** *1* (3), 201-214.

CHAPTER 3

EXPERIMENTAL PROCEDURE

This purpose of this chapter is to explain the design of the experiment (DOE) used to measure the intrinsic and functional properties of granular diamond composites. The development of the process to produce the GDC materials is documented. The mechanical tests used to characterize the material are also described.

The goal of this investigation is to characterize superhard materials with granular mesostructures, specifically those with diamond granules, and to understand what affects their properties. The testing of the functional properties of GDC is a straightforward way of analyzing the material because the functional properties are the most important industrially. Intrinsic properties should also be measured, as they help explain the functional properties.

The experiment was designed to discover the effects of the material system and mesostructure on the functional properties of GDC materials. The material system includes the materials selected for the matrix and the granules, the volume fractions in each, and their microstructure. The mesostructure includes the morphology and contiguity of the granules, and the volume fraction of the components. Multiple material systems should be tested and multiple volume fractions should be tested within each material system. The experimental design was limited by the cost and difficulty in processing and testing PCD.

A viable process for fabricating GDC needed to be developed in order to produce the samples for testing. The process should be reproducible and as simple as effective. Some procedures were adopted from fabrication processes used in the past to produce other hierarchically structured materials. The granules should be spherical and uniformly spaced, with minimal contact with other granules. The mechanical properties of the individual components should be roughly comparable to the properties of industrially produced material.

Once GDC materials could be consistently produced, several mechanical properties including flexural strength, impact resistance, and wear resistance were experimentally measured to characterize the impact of the material system and mesostructure on the mechanical properties.

In the end, the full design of the experiment was not followed. This research was primarily funded by, and conducted in partnership with, Smith Megadiamond. They chose which materials and methods they would fund. The design of experiment was pared back to only include the material systems they felt were worthwhile testing.

Design of Experiment

The experiment was designed to investigate the relationship between the design and the mechanical properties of granular diamond composites. The material selection and material ratios are the most basic design choices. The test matrix includes two different granule materials, four different matrix materials, and varying granule to matrix ratios. The test matrix is presented in Table 3.1. The different material combinations are given letter designations, A through H. The diamond volume percentage is indicated in the grade name after the series letter. Volume fractions are typically used when working with composites, but weight fractions are typically used when discussing PCD and WC-Co compositions. Both of these conventions will be respected, volume fraction will be used when specifying component fractions in composites and weight fraction will be used when specifying the compositions of PCD and WC-Co.

Grade A100 is 100v% PCD 1, which is equivalent to B100, C100, and D100. Likewise E100, F100, G100, and E100, are all equivalents. Down at 0v% diamond, or 100v% matrix, A0 and E0 are equivalent, as is B0 and F0, etc.

The experiment was designed to demonstrate the effect of varying granule fractions within the same material system and to compare multiple material systems at the same volume fraction of granules. The design called for seven different grades of Series A to be produced ranging from diamond volume percents of 0 to 100, five grades in Series B and G and four grades in Series H. A 70v% grade in each series would be produced to allow for comparison between series. A more throughly designed experiment would have called for at least three grades in each series besides the end points.

The test plan called for the measurement of wear resistance, flexural strength, and impact resistance of the various compositions. Field testing was planned for materials which showed promising properties, to compare the performance head-to-head with an existing grade of industrial PCD.

Table 3.1

DOE Specimen Matrix

Matrix	Granules	
	PCD 1[a]	PCD 2[b]
WC-Co 1[c]	A0,[i] A40, A60, A70, A80, A95, A100[g]	E0[i], E70, E100[h]
WC-Co 2[d]	B0,[j] B40, B70, B80, B100[g]	F0,[j] F70, F100[h]
Blend 1[e]	C0,[k] C70, C100[g]	G0,[k] G30, G50, G70, G100[h]
Blend 2[f]	D0,[l] D70, D100[g]	H0,[l] H30, H70, H100[h]

[a]PCD 1 consists of 20w% Co and 3-4 μm diamond grains. [b]PCD 2 contains 95w% diamond grains (4-8 μm). [c] WC-Co 1 consists of approximately 2 μm WC grains and 14w% cobalt. [d]WC-Co 2 is presintered with 12w% Co, crushed and separated in a size range of -20 +5 μm. [e]Blend 1 is a WC-Co/PCD blend with 23.3w% diamond, 5.8w% Co, and 71w% WC-Co. [f]Blend 2 contains 57w% 80-100 μm diamond, 35w% 60-80 μm diamond, 5w% 36-54 μm diamond, 2w% 20-30 μm diamond, 2w% cobalt, and 2w% proprietary additives. [g]Grades A100, B100, C100, and D100 are all equivalents because they consist of only PCD 1. [h]Grades E100, F100, G100, and H100 are all equivalents because they consist of only PCD 2. [i]Grades A0 and E0 are equivalent because they contain no PCD granules. [j,k,l]Likewise, Grades B0 and F0, C0 and G0, D0 and H0 are equivalent because they do not contain any granules.

Starting Materials

Materials included diamond grains, WC-Co powders, sintering alloy, and hydrocarbon waxes or other binders. The materials were provided in various forms, but all were prepared according to conventional milling and drying procedures. All starting materials were existing industrial grades of diamond or carbide, provided by Smith Megadiamond.

Materials for Granules

Two different grades of PCD granules were used in this investigation. Both grades of PCD were provided by Smith Megadiamond in tape form. The tape was made from diamond powder, powdered sintering alloy, and polymer binder. A plasticiser was also added to increase the flexibility of the tape. The binder allows the otherwise loose powder to be processed as granules.

The first grade, PCD 1, is made with 20w% Co and 3-4 μm diamond grains. The second grade, PCD 2, contains 95w% diamond grains (4-8 μm) with the remainder made up of cobalt and other additives. PCD 2 has greater wear resistance than PCD 1, but PCD 1 is tougher due to the larger fraction of sintering alloy. For standard industrial diamond, 3-4 μm grained diamond is on the fine end of the spectrum. Finer diamond increases wear resistance but decreases the fracture resistance. The 20w% cobalt in PCD 1 is relatively high which will reduce the high wear resistance and increase the low fracture resistance, whereas the 95v% diamond in PCD 2 keeps it on the extreme end of the hardness spectrum. It relies on cobalt infiltrating from the matrix when it is sintered.

Materials for Matrices

There were four matrix grades tested, two composed of WC-Co, one a blend of WC-Co and PCD, and one was a mixture of PCD sizes with cobalt.

WC-Co 1 powder consisted of approximately 2 μm WC grains and 14w% cobalt. WC-Co 2 is presintered with 12w% Co, crushed and separated in a size range of -20 +5 μm. Blend 1 is a WC-Co/PCD blend with 23.3w% diamond, 5.8w% Co as the sintering alloy, and 71w% WC-Co. The grade of WC-Co used in Blend 1 is the same as WC-Co 2. Blend 2 is a blend of PCD powders of various sizes: 57w% 80-100 μm diamond, 35w% 60-80 μm diamond, 5w% 36-54 μm diamond, 2w% 20-30 μm diamond, 2w% cobalt, and 2w% proprietary additives.

The matrices listed in Table 3.1 are in order of increasing wear resistance and decreasing fracture resistance. The role of the matrix in GDC is to prevent catastrophic chipping and fracture by providing tougher areas to arrest and deflect crack propagation. With cobalt concentrations in the low teens, both WC-Co 1 and 2 would be considered fairly tough grades of industrial carbide. Being spiked with diamond, Blend 1 loses some of the toughness, but will have greater wear resistance. Blend 2 is almost completely diamond, but the large size fractions of the powders used increases the toughness of the material, compared with the relatively fine grains used in PCD 1 and 2.

At the beginning of the project the matrix materials were provided with a wax binder. This did not prove to be helpful so the powder was subjected to a dewaxing cycle to remove the wax additive. Later batches of the matrix were supplied without any wax.

Fabrication of Granular Diamond Composites

As this GDC material had never been produced before, the first step in this research was to devise a viable process to produce the test samples. Production methods of other functionally designed, hierarchically structured materials were studied and select methods were adapted and applied to produce the test samples for this study. Many of these processes were derived from powder injection molding technologies.

The manufacturing process is outlined in the flowchart shown in Figure 3.1. The starting materials were obtained from Smith Megadiamond and then processed in the Powder Metallurgy Lab at the University of Utah. The materials were carefully mixed under controlled conditions designed to uniformly coat each diamond granule with the matrix material. The coated granules were returned to Smith Megadiamond to be shaped and sintered. After sintering, Smith Megadiamond cut the material into test specimens.

Table 3.2 lists all of the materials which were produced for this investigation. Each batch in a grade was designated by a sequential letter. Only mixtures which were further processed are listed here. Early in the process, several attempts were made before a mixture was deemed promising enough to move onto the next step. For example, grade A80 was the first to be produced and it took eleven attempts to produce A80k which was the first batch to be deemed good enough to process further.

Granule Processing

Several steps were taken to produce the diamond granules from the PCD tape. The objective was to produce clean, spherical granules of polymer bound diamond

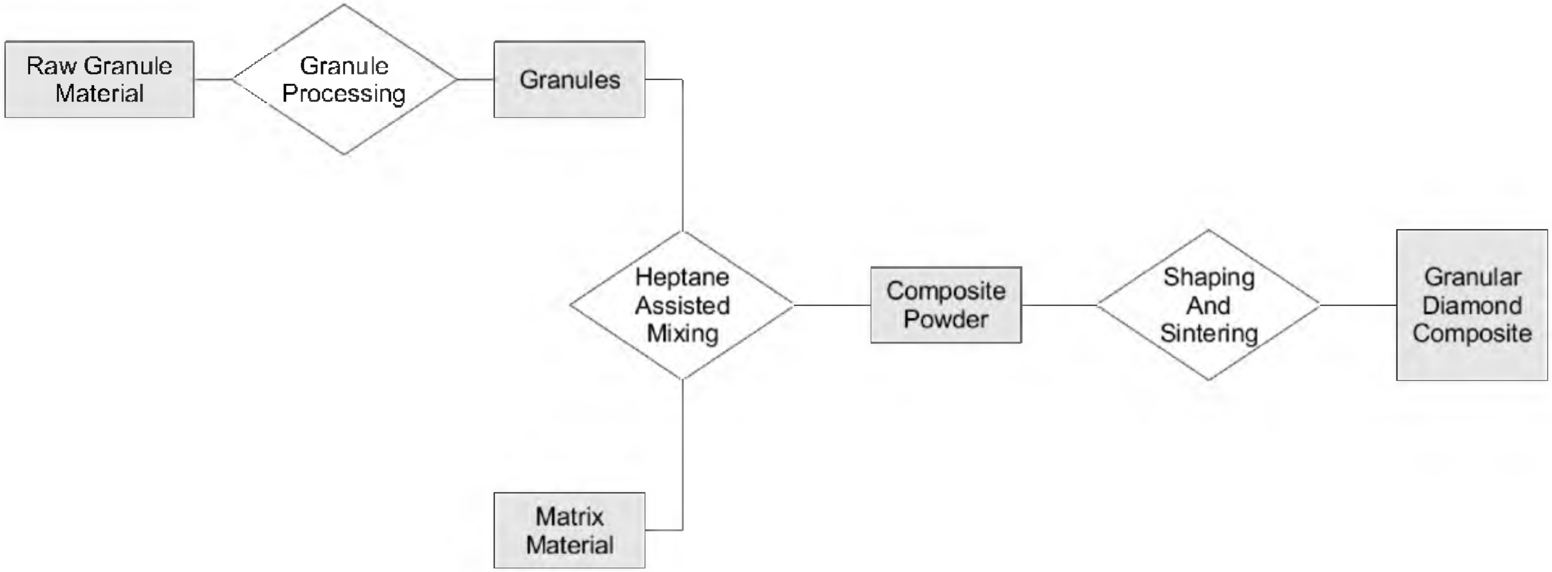

Figure 3.1. Flow chart outlining the major steps used to produce granular diamond composites. Shaded boxes signify materials, white rhombuses signify processes.

Table 3.2

Composite Grades Produced

Materials Produced
A0a, A0b, A40b, A40c, A60b, A60c, A70a, A70b, A70c, A80k, A80l, A95b, A95c, A95d, A100a, A100b
B0a, B40a, B40b, B70a, B70b, B70c, B70d, B80a, B80b
C70a
D70a, D70b
E70a
F70a, F70b, F70c, F70d
G30a, G30b, G30c, G30d, G30e, G30f, G50a, G50b, G70a
H30a, H30b, H30c, H70a, H70b

powder in the correct size range. A large amount of time and effort was expended to develop the final method, and the objectives were never fully met. Three main processing steps were used to prepare the granules to be coated with matrix material. First, the tape was ground into granules. Second, granules in the correct size range were separated out from the oversized and undersized granules. Third, the granules were washed to remove the fine diamond grains that loosely adhere to the larger granules.

The starting material was supplied by Smith Megadiamond and was almost always in a tape form. The tape is composed of diamond grains, powdered sintering alloy, and a polymer binder, with or without a plasticizer. The amount of plasticizer in the binder was varied at the beginning of the investigation until it was decided that tape with no plasticizer yielded the best results. The plasticizer made the tape gummy which made it difficult to break the tape up into granules. The tape with plasticizer would smear inside the grinding equipment until the machine was too encumbered to continue operating. Figure 3.2 is a closeup of a granule which shows the various ingredients glued together.

Several grinding techniques were tried and grinding with a grain mill gave slightly superior results. Other tested techniques included grinding by hand using a mortar and pestle, processing in a lab sized hammer mill, and using a consumer grade coffee grinder. Cooling the tape with liquid nitrogen was combined with each of these techniques, but the effect was short lived as the tape quickly warmed, and the main outcome was the increased production of undersized granules. Granulation directly from diamond powder by tumbling the diamond powder and binder in solvent atmosphere was briefly attempted but was unsuccessful. The particles stuck to each other and the walls of

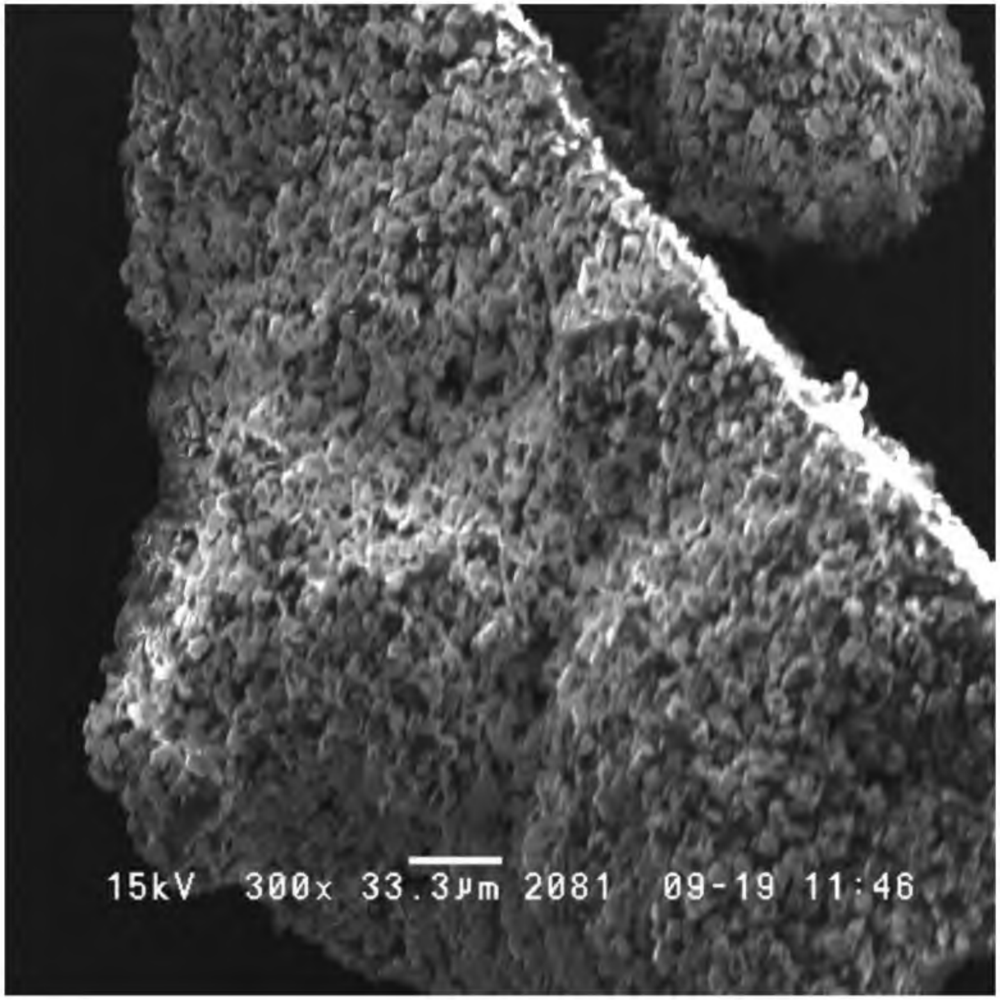

Figure 3.2. Scanning electron micrograph of single granule of PCD 2 material. The individual diamond grains are visible.

the flask and tumbling quickly ceased.

The polymer bound granules of desired size were then separated from the rest of the ground material. In this investigation, two different sizes were used: 250 to 355 μm, and 180 to 250 μm. The finer size fraction was used for Series A - D, and the coarser size range was used for Series E - H. Three inch screens were used to separate the granules into size classes. A large amount of time and energy was required to properly separate the granules. Mechanical vibration, swishing, and knocking were used, but manual shaking was found to be more effective in separating the material, despite the tedium and decrease in reproducibility. Figure 3.3 is a micrograph of freshly ground and separated PCD granules.

No grinding method was found which produced a high yield of granules in the desired size range. The oversized material was cycled directly back into the grinding step. The volume of undersized granules necessitated a reprocessing method. The binder is soluble in acetone, so it was used to reform tape out of the undersized granules. The reformulated tape was then reprocessed by grinding. An example of the grinding results is shown in Figure 3.4.

It is likely that there are better methods for generating PDC granules, either through grinding or through agglomeration, but a better method was not determined in this study.

After separation, the granules were washed in heptane, a solvent which does not dissolve the binder. The screening step left small granules and unbound diamond grains adhering to the sides of the granules. During the mixing and sintering steps this debris

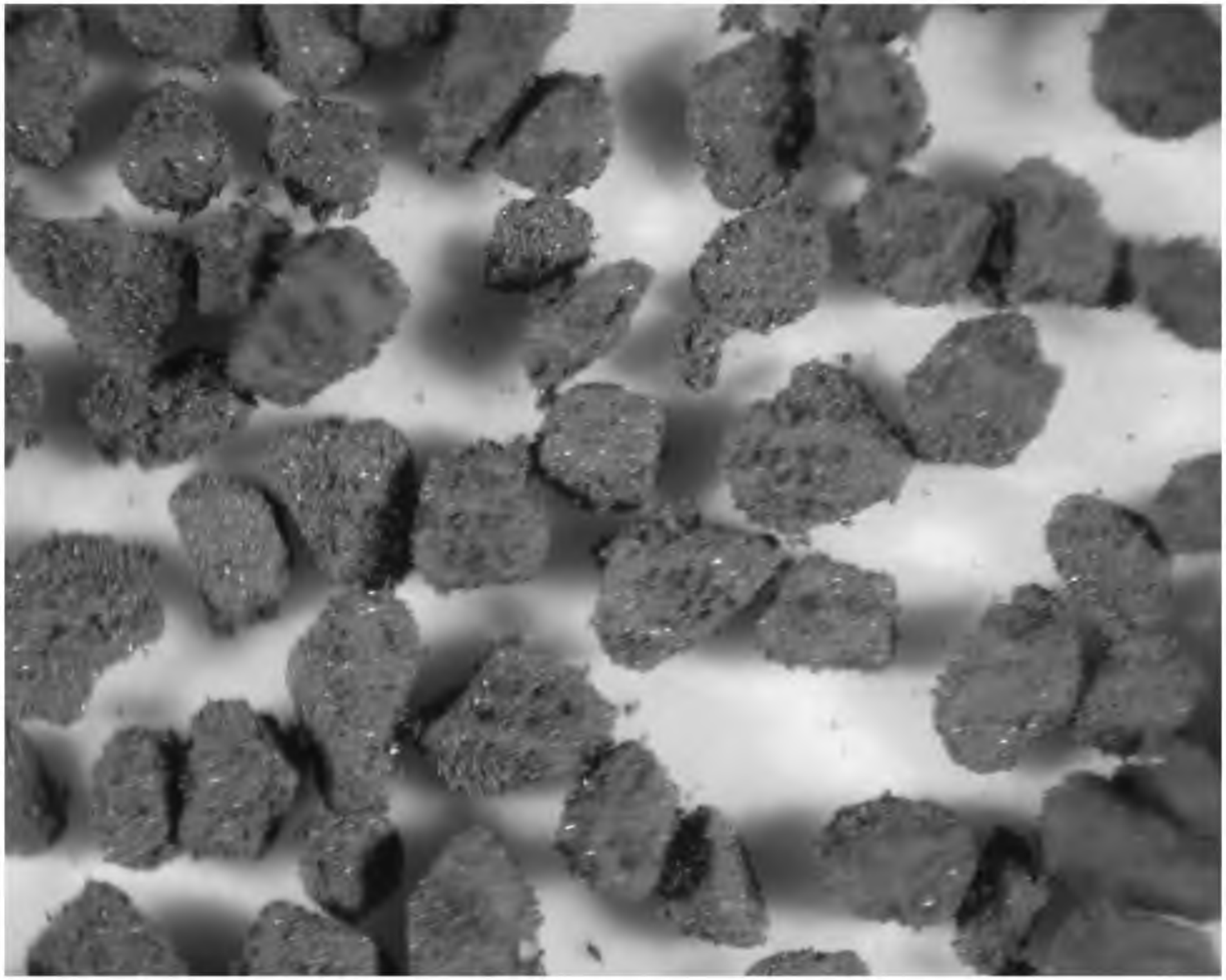

Figure 3.3. Stereoscopic light micrograph of PCD granules in the -250 +180 μm size range.

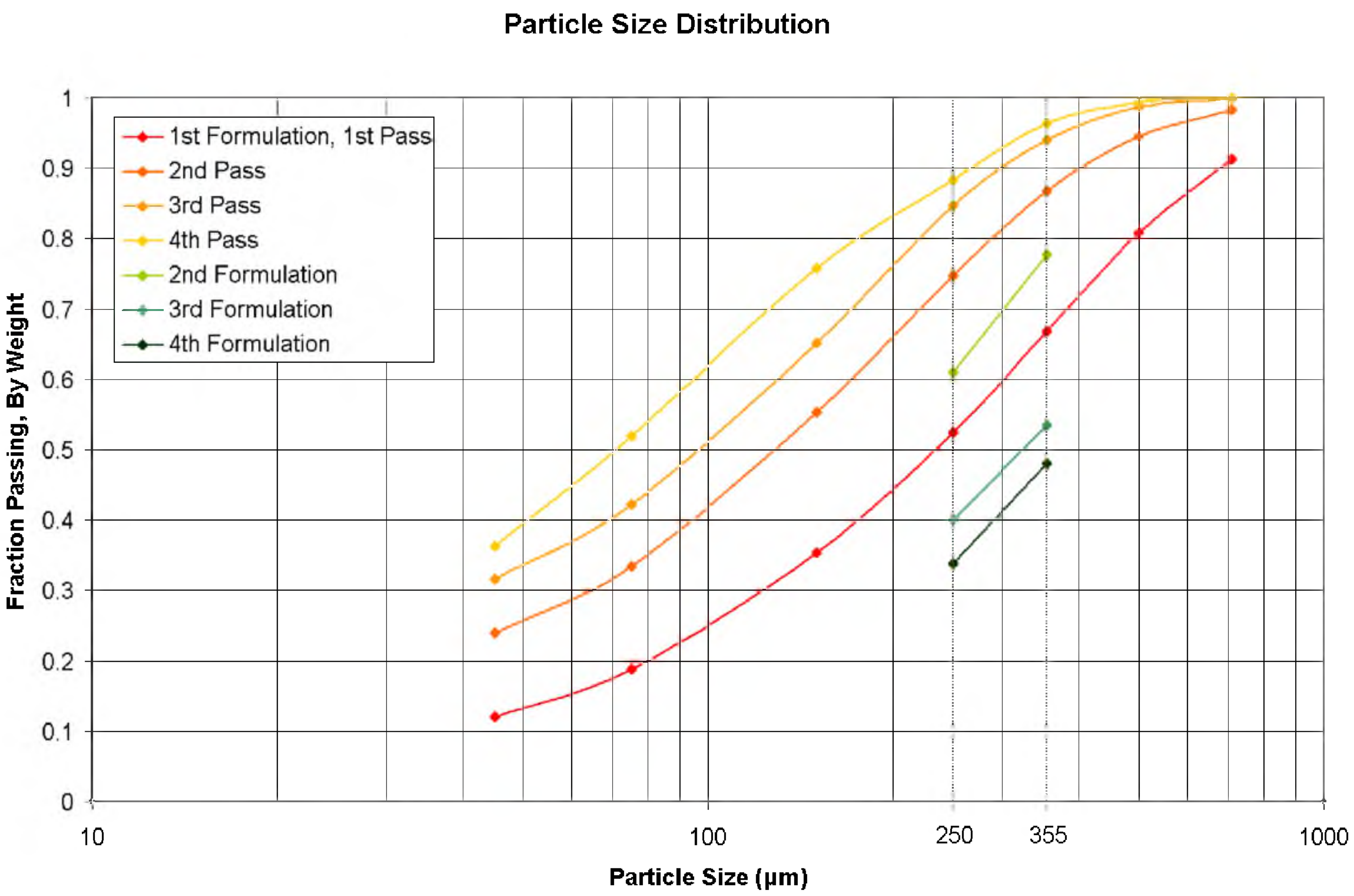

Figure 3.4. Particle size distribution after grinding. A curve higher on the graph indicates a finer result because more of the material is passing through the screen of a particular size. A steep section of the line indicates that a large portion of the particles is in that range. Multiple passes through the grinder results in finer and finer material. Reducing the amount of plasticizer (later formulations)

would migrate into the matrix affecting its properties. Figure 3.5 is a micrograph of washed PCD granules. Compare the appearance of the washed granules to the unwashed granules shown in Figure 3.3.

Heptane Assisted Mixing

The objective of the mixing step is to uniformly coat the granules with matrix material.

The matrix powder was weighed out in a glass beaker. The granules were weighed out and added to the beaker. Heptane was added so that the mixture was saturated and a small amount of heptane pooled at the top. The mixture was stirred by hand with a glass rod until it was nearly dry. Air was blown across the top of the beaker to increase the evaporation rate. The end of stirring needed to be carefully timed. If the material was not stirred while it was wet, the constituents would settle out and the mixture would dry into a solid clump. When the clump was later broken into pieces it would preferentially break along the powder/granule interface resulting in non coated granules. If the mixture was stirred excessively after drying the powder coating would be rubbed off.

This processing step was originally developed using a small amount of Lucant 2000, a synthetic oil which is soluble in heptane, as a binder to promote a more uniform or more robust coating. While searching for the optimum binder amount it was shown that mixes with no Lucant had the best outcome.

Figure 3.6 presents images from a stereomicrograph showing three grades after processing. The grades are a) A0b (WC-Co 1), b) B0a (WC-Co 2), c) A100a (PCD 1).

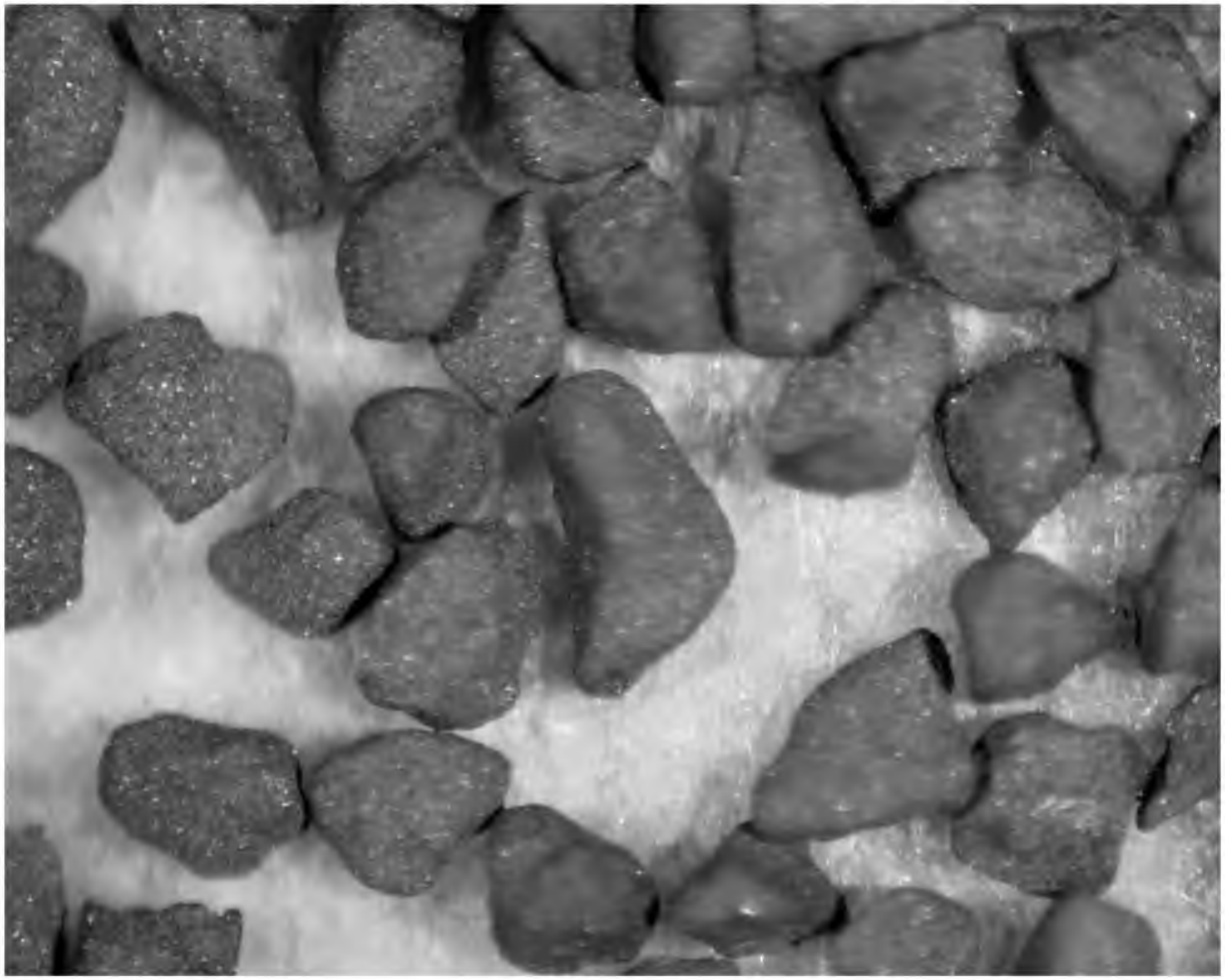

Figure 3.5. Stereographic light micrograph of washed PCD granules. Compare the appearance of these granules to the unwashed granules shown in Figure 3.3

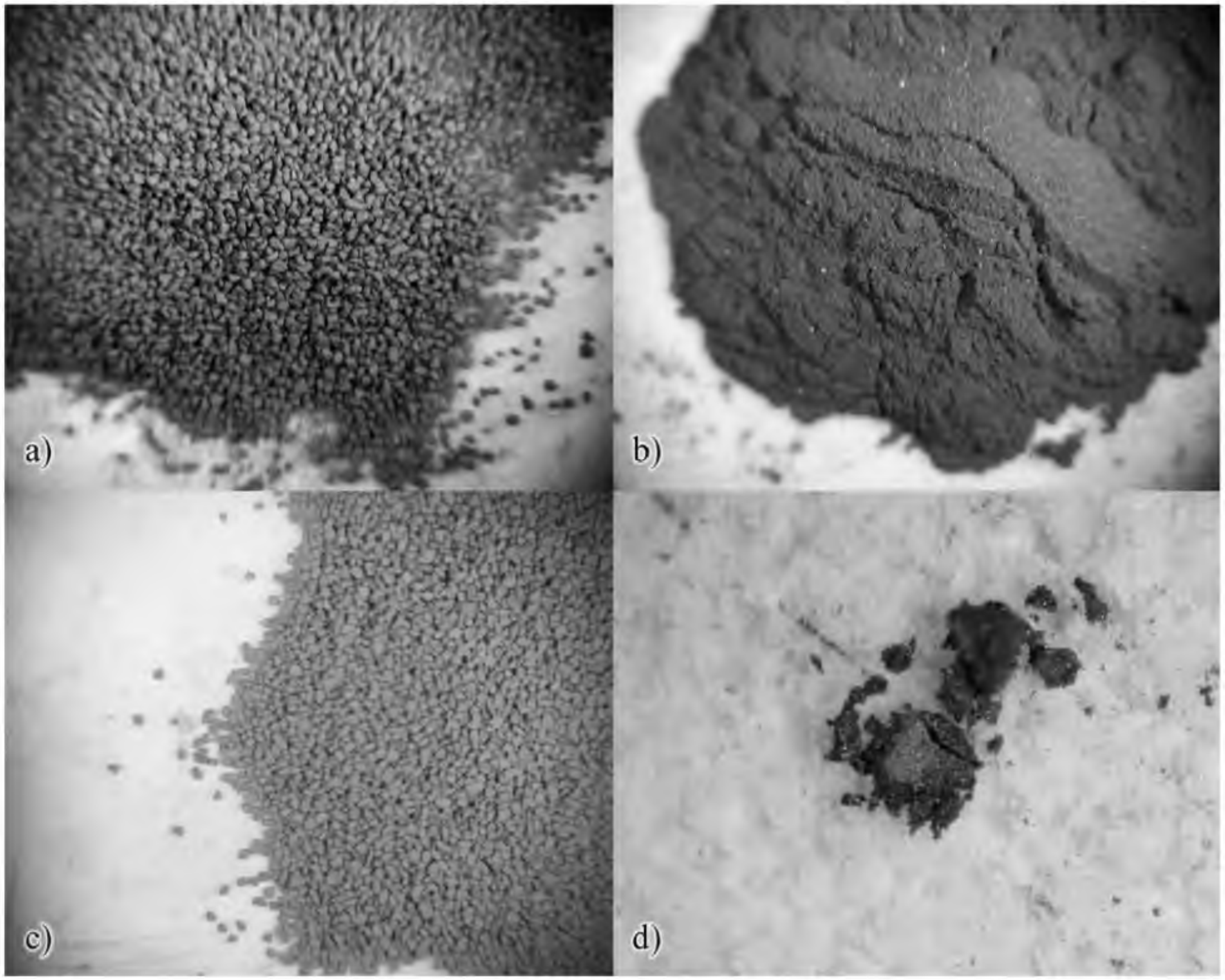

Figure 3.6. Images from a stereoscope of mixed GDC grades after processing but before shaping and sintering, a) A0b b) B0a c) A100a. d) A stereomicrograph of a coated granule of A40c that has been sectioned to reveal the lighter granule inside the darker matrix coating.

Though these grades are made up of only one constituent, they were treated in the same way as the rest of the grades. A0b (a) even balled up to resemble the mixes with granules. B0a (b) remained as a loose powder. Figure 3.6d shows a coated granule from mix A40c which has been crushed open to reveal the lighter granule inside the darker matrix coating.

The 70v% diamond grades of the series with PCD 1 (Series A - D) are shown in Figure 3.7. The first three images, a) A70c, b) B70a, and c) C70a show well coated granules. Figure 3.7d shows D70b which is not uniformly coated because the size of matrix grains is so large that the volume fraction of matrix is not sufficient to coat the granules.

The same thing is seen in Figure 3.8 which shows the 70v% diamond grades of the PCD 2 series (Series E - H). The series with WC-Co 1, WC-Co 2, and Blend 1 are all well coated, but Series H with Blend 2 (Figure 3.8d) is not well coated.

Shaping and HTHP Sintering

After the granules have been coated in matrix, the material is shaped and sintered. Both of these steps were conducted at the Smith Megadiamond laboratories.

The material was formed into two different shapes, flat discs and domes. Most of the mechanical test specimens were cut from flat discs. The impact resistance and the field testing were conducted on dome shaped specimens. The mixes are shaped by loading into shaped refractory metal cans along with shaped WC-Co substrates.

All of the hydrocarbons need to be removed from the material before sintering.

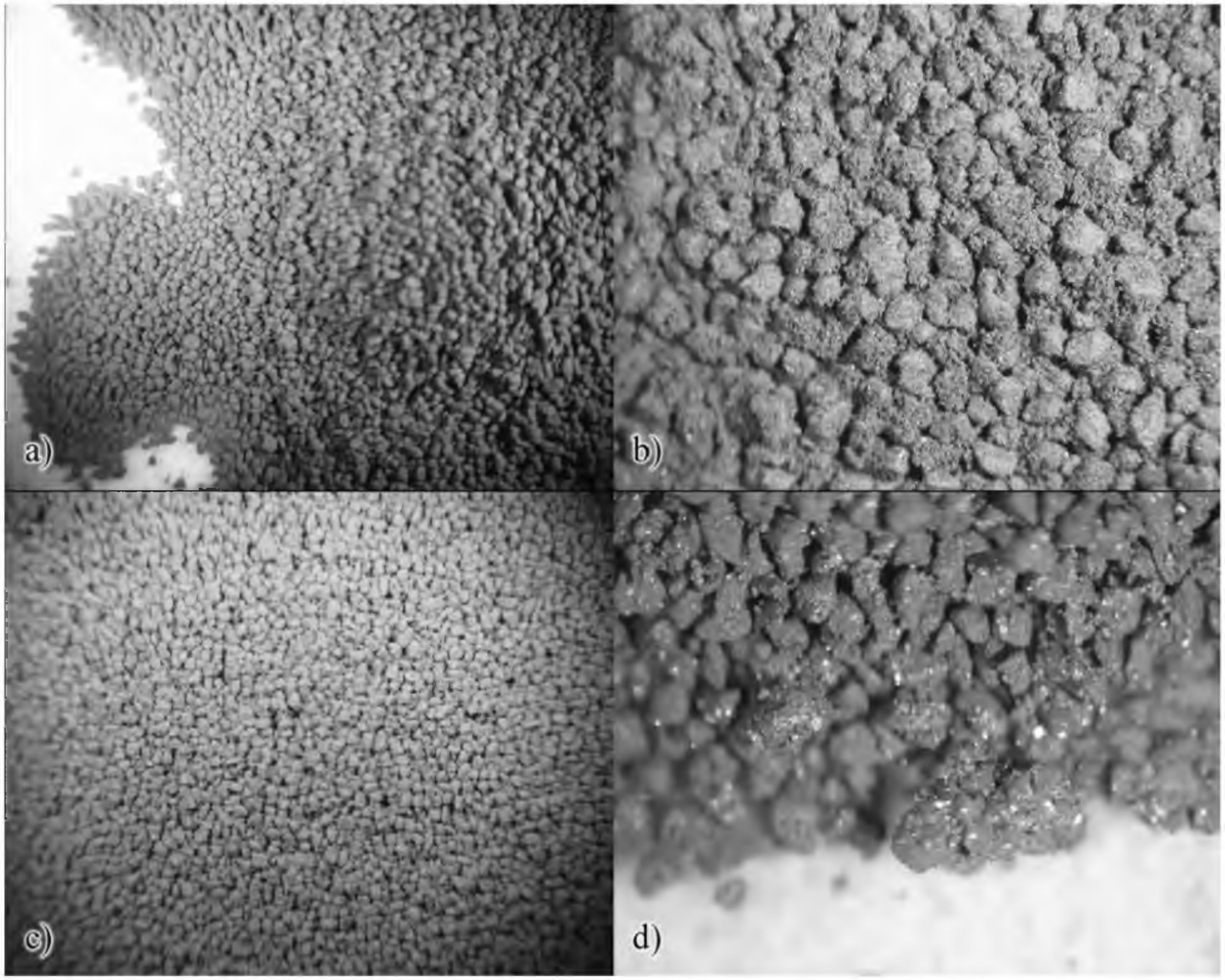

Figure 3.7. Images from a stereoscope of mixed GDC grades after processing but before shaping and sintering, a) A70c b) B70a c) C70a d) D70b

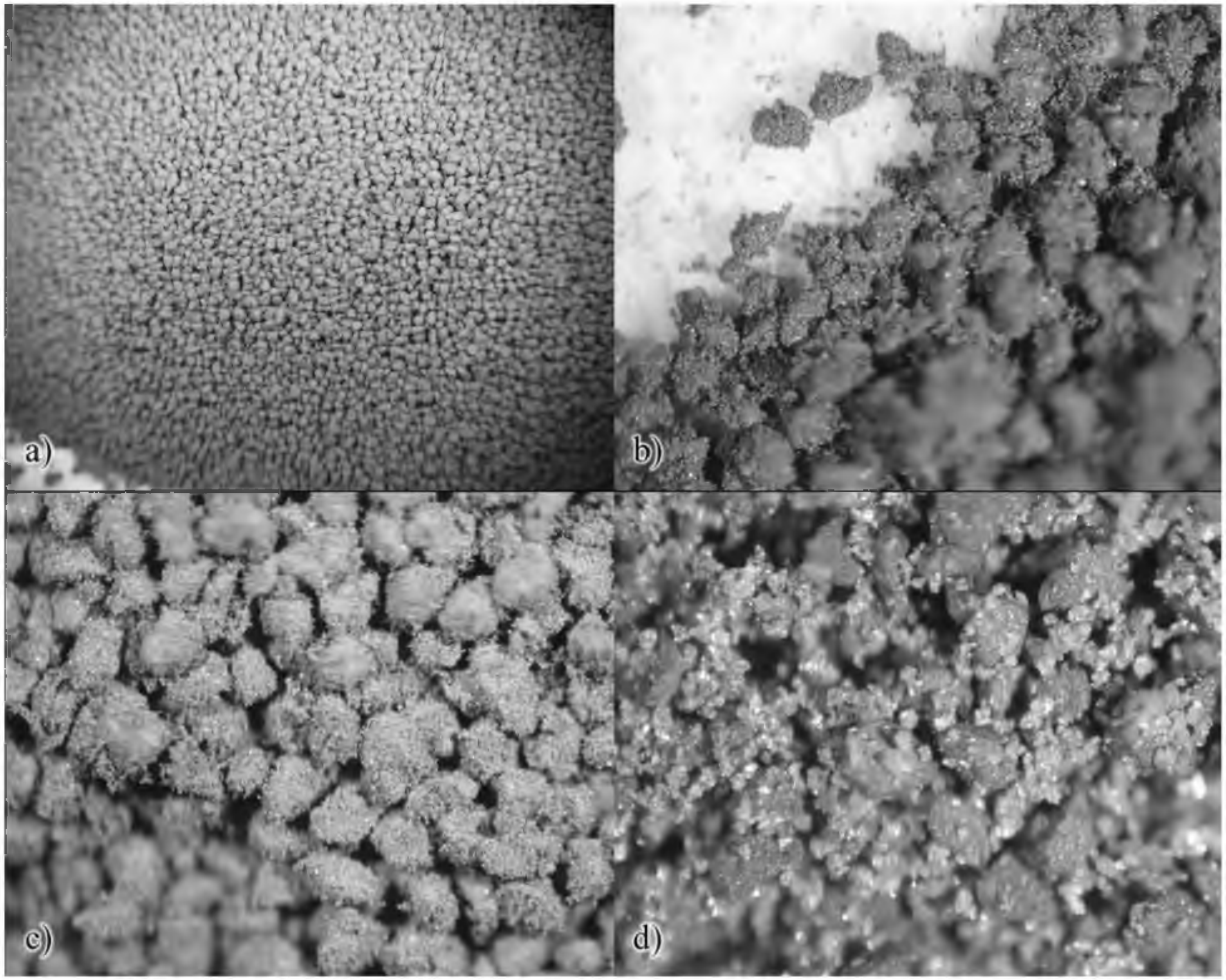

Figure 3.8. Images from a stereoscope of mixed GDC grades after processing but before shaping and sintering, a) E70a b) F70b c) G70a d) H70b

Hydrocarbons may be present in the form of binders, plasticizers, or waxes. The hydrocarbons are removed by heating in a vacuum furnace for an extended amount of time. Also in preparation for sintering, the oxygen that has reacted to the surface of the diamond needs to be driven off. This is done at a higher temperature in an inert, flowing atmosphere.

At this stage, the loaded cans are assembled into the cell, which includes salt, pyropholite, heating components, and components to transfer the power to the heaters. The cell is then loaded into the diamond press.

The diamond press takes the internal pressure up to around 5500 MPa and the internal temperature to roughly 1400°C. At these conditions the diamond grains in the granules sinter together to form an integral mass. The carbide and/or diamond in the matrix also fuses together and the matrix and granules react into a single mass.

Mechanical Property Testing of Granular Diamond Composites

Four functional properties were tested to characterize the mechanical properties of granular diamond composites. This includes flexural strength, wear resistance, impact resistance, and field testing.

Flexural Strength

Flexural strength, or transverse rupture strength, is one of the most important characteristics of brittle materials as it is related to other properties such as hardness, intrinsic strength, and toughness, and it is readily measurable and sensitive to manufacturing defects. The overall strength of the super hard material can be approximated by measuring the transverse rupture strength.

For the flexural strength experiments the specimens were prepared by having the carbide substrate removed and the sintered GDC material cut, using EDM, into rectangular bars, with cross-sectional dimensions of 2.00 mm by 0.75 mm, as illustrated in Figure 3.9. The size of the test specimens is much smaller than typical ASTM size[1] due to the expense and difficulty in producing PCD at larger sizes. The two sides with the largest surface area (the top and the bottom of the sample) were then polished with diamond slurries ranging down to 1 μm.

The fixture uses three 3.1 mm cylinders. This test is quick and easy when compared to other strength tests of brittle materials. The specimens were tested using a screw driven testing frame (Alliance RT/30, MTS, Eden Prairie, MN). The bottom span is 8.13 mm. The top pin is held by a fully articulating support. The testing was done at 0.2 mm/min. The flexural strength, σ_u, was calculated using equation 3.1, where F is the load, L is the span, w is the width of the specimen, and t is the thickness of the specimen.

$$\sigma_u = \frac{3FL}{2wt^2} \tag{3.1}$$

Wear Resistance

Wear resistance is a functional property which directly relates to the service life of the drill bit inserts.

The wear resistance of the material was measured using a granite-log test at the

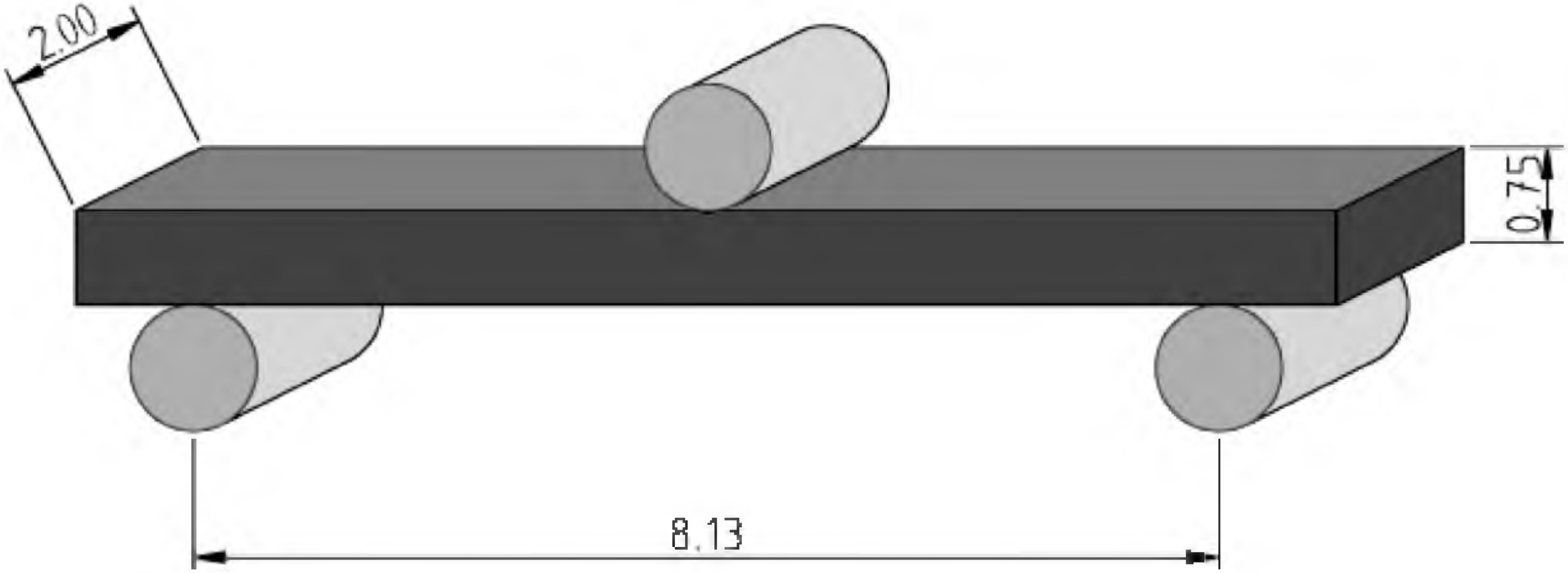

Figure 3.9. Three point bend test set-up and specimen dimensions.

Smith Megadiamond lab. A schematic of the granite log test is shown in Figure 3.10. In this test a cylinder of granite is turned on a lathe and a shear cutter is used to cut the granite. The test measures the ratio of tool wear volume, V_R, to granite wear volume, V_d, see equation 3.2. Test parameters include rotation speed, feed rate, rake angle and depth of cut. The presented values of wear ratio are normalized against the wear ratio of the industrially produced PCD 1.

$$G = \frac{V_R}{V_d} \tag{3.2}$$

Impact Resistance

Impact resistance testing was conducted on the Series A material at the Smith Megadiamond laboratories. Quarter inch, hemispherical enhanced inserts were loaded into a test fixture so that the tip of the insert is protruding from the bottom. The fixture is dropped from increasing heights into a tungsten carbide plate until fracture is observed on the material. The average height required to fracture the material is a relative measure of its impact resistance.

Field Testing

Smith Megadiamond arranged for one of the GDC grades to be tested in an actual drilling application. Smith Megadiamond selected the G30 grade to be field tested. In the field test GDC inserts were placed in the heel row alternating between inserts made from a standard PDC material, as shown in Figure 3.11.

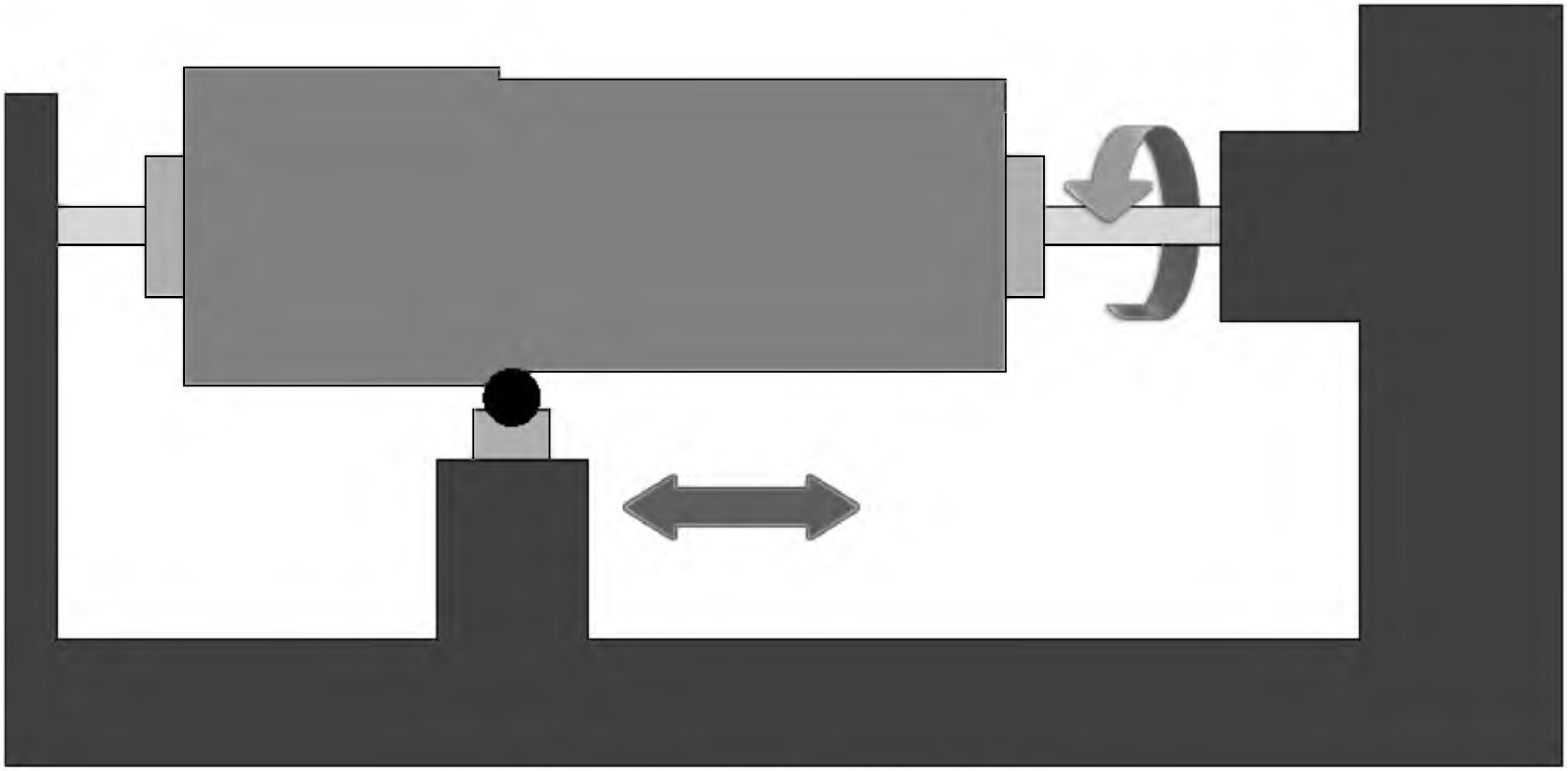

Figure 3.10. Schematic of the granite log test.

Figure 3.11. A field tested roller cone with GDC inserts in every other position in the heel row (top row in the picture), indicated by the yellow marks.

Chapter Summary

A fairly exhaustive experimental plan was devised to compare the mechanical properties of granular diamond composites made from different constituents in different ratios. The design of the experiment was limited by the cost and difficulty of processing and testing PCD. A method was developed which produced granular diamond composites. The granules were well separated by matrix material, but the granule shape was not as spherical as desired. Several mechanical test methods to characterize the functional and intrinsic properties of GDC materials were outlined in this chapter. The results of these tests are presented in the next chapter.

References

1. "Standard Test Method for Flexural Strength of Advanced Ceramics at Ambient Temperature" ASTM Designation: C 1161-90

CHAPTER 4

EXPERIMENTAL RESULTS

This chapter presents the mechanical test results and discusses the implications arising from these studies. Only a selection of the GDC grades that were produced was tested. The number of GDC grades tested varied depending on the specific mechanical test employed. Fourteen grades were tested for flexural strength, seven grades were tested for wear resistance, impact resistance was measured in six grades, and only one grade was field tested. Funding and partnership considerations limited the extent of testing, making it necessary to deviate from the original experimental design. More testing would have allowed for a clearer picture from the experimental results, but much was learned from the tests conducted, including the need for further study.

Flexural Strength

Flexural strength tests were conducted on Series A, B, G and H material as listed in Table 4.1. The number of specimens tested for each grade ranged from 6 to 39. The experiment was designed with an N, the number of samples, of 20. The number of samples for some grades fell below 20 because some of the specimens had to be rejected due to cracks, dimensional deviations, and test errors. Grades B0 and B60 were added at

Table 4.1

Composite Grades Tested for Flexural Strength

Material	# of Specimens	Material	# of Specimens
A0	19	B0	6
A40	19	B40	14
A60	20	B60	6
A70	21	B80	20
A80	20	G30	15
A95	17	G50	13
A100	39	H30	9

the end of the testing using surplus material. There was not enough surplus material to produce 20 specimen, but it was decided that there was value in having more data points even if the confidence in those points is lower. The low number of B0 samples is not as important because this grade should be equivalent to A0. Two separate batches of A100 were tested with 20 samples each to compare the differences between batches of the same grade.

The results from the transverse rupture strength testing are presented in Table 4.2, and are graphed in Figure 4.1. With the design of the experiment trimmed back, some of the planned comparisons could not be made, like a direct comparison between PCD 1 and PCD 2. Other aspects of the methods and material system are evaluated below.

Two batches of WC-Co 1 (A0 and B0) were tested and had a good agreement on transverse rupture strengths. Two batches of PCD 1 (A100a and A100b) were tested with a difference about 7% of the values. Comparing the strengths of Series A to Series B, the Series A was consistently stronger than Series B at all volume fractions. It can be concluded that PCD 1 performs better TRS-wise with WC-Co 1 than WC-Co 2. Series G, with PCD 2 and Blend 1 has higher strength than Series H, with PCD 2 and Blend 2. By not testing C, D, E, or F grades, no comparison can be made between PCD 1 and PCD 2, or between the WC-Co and Blend matrices.

It is important to note that the samples at the end points of the volume fraction spectrum all have lower measured flexural strengths than the published or accepted values. Single component grades, like A0, A100, B0, etc., are made up of either 100v% PCD or WC-Co. Theoretically they could have the same flexural strength as the

Table 4.2

Flexural Strength Results

Material	Flexural Strength	Standard Deviation
A0	1961	97
A40	1460	162
A60	1333	117
A70	1340	177
A80	1186	97
A95	1308	156
A100a	1589	223
A100b	1479	139
B0	1933	141
B40	1144	152
B60	1059	89
B80	996	143
G30	1125	104
G50	942	159
H30	639	69

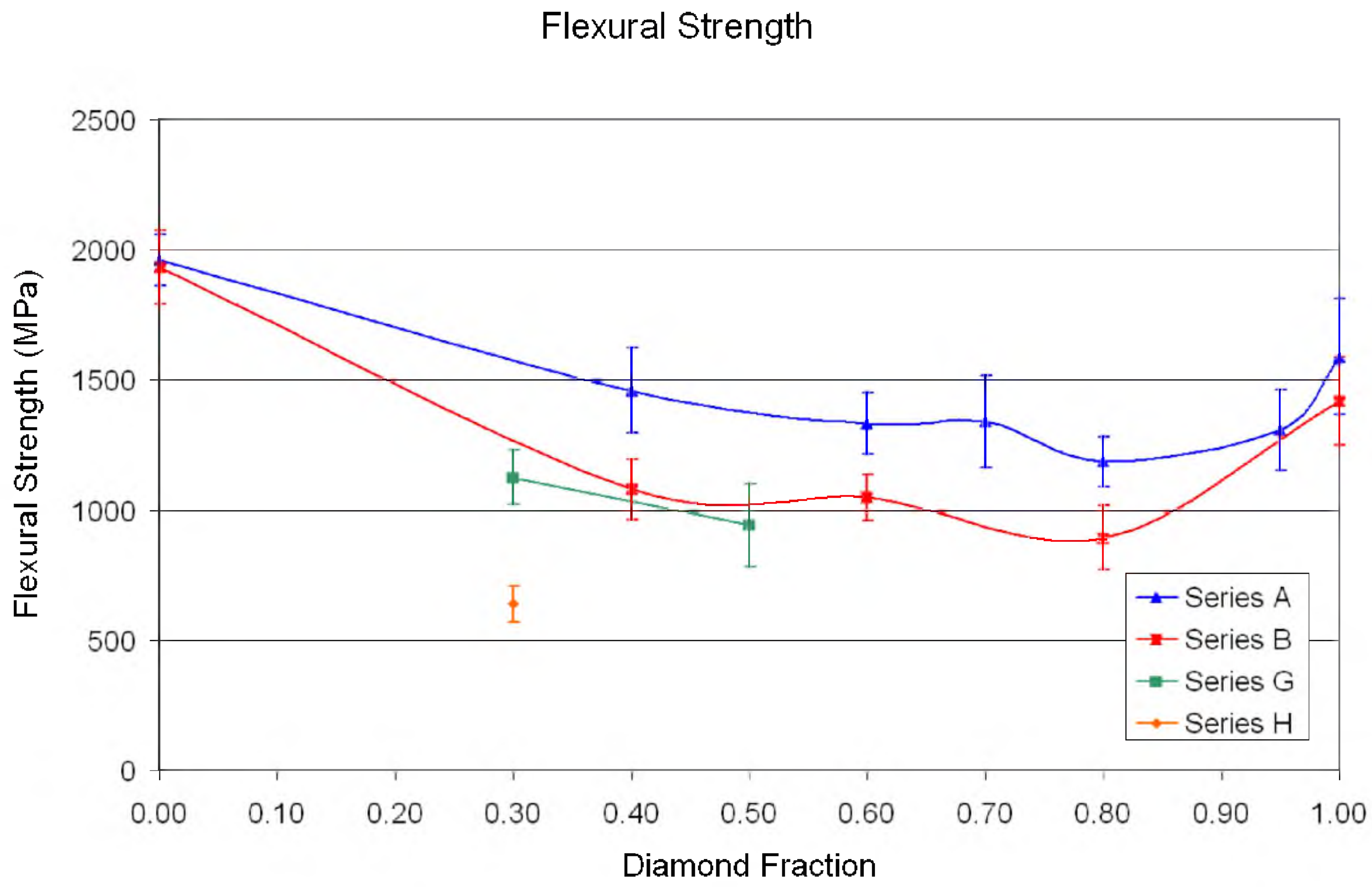

Figure 4.1. Flexural strengths of Series A, B, G, and H. The data points represent the average flexural strength and the error bars indicate the standard deviation for the grade.

industrially produced material. For example, the TRS of the PCD 1 grade conventionally processed is 1714 MPa[1], but A100 which is made of 100v% PCD 1 had an average measured flexural strength of 1534 MPa, or 10% lower strength. For the carbide grades this can at least partly be attributed to the fact that it is being sintered at pressures and temperatures optimized for sintering PCD, which is quite different from the carbide sintering conditions. The lower strength of the PCD sample has not been fully explained, but it is also likely attributable to the differences in processing conditions from conventional PCD processing. It is also possible that slight differences in flexural strength testing methodology is partly responsible for the variances.

Another interesting trend is that the end points (0v% and 100v%) of Series A and B have higher flexural strength measurements than any of the composites of these materials. Because WC-Co has a higher measured strength than PCD, it might be expected that by adding WC-Co to PCD the strength of the material would be improved. The strength properties of most composites fall somewhere between the strengths of its constituents, as illustrated by the shaded area in Figure 4.2.

One possibility is that the material strength may be limited by the strength of the interface between the PCD granules and the WC-Co matrix. If the interfacial strength is less than the components, the composite will fail before the critical stress in either component is reached. This possibility was studied by examining the fracture surfaces of the various grades.

The micrographs in Figure 4.3 compare the two sides of a fracture surface. Notice that all of the granules appear in both images indicating that the crack grew

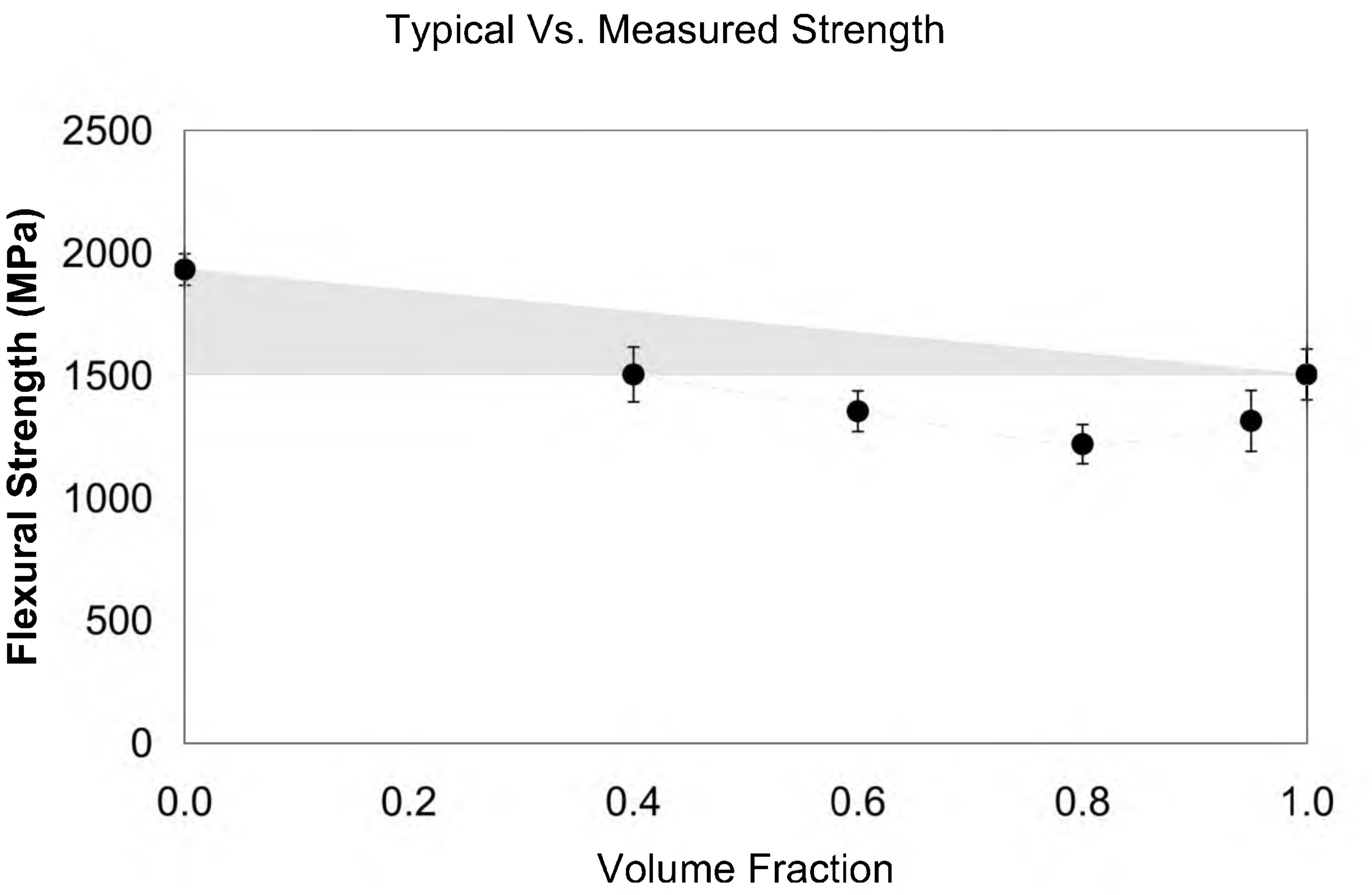

Figure 4.2. Flexural strengths of the Series A plotted along with a shaded area representing the anticipated strengths of most composites with similar component strength.

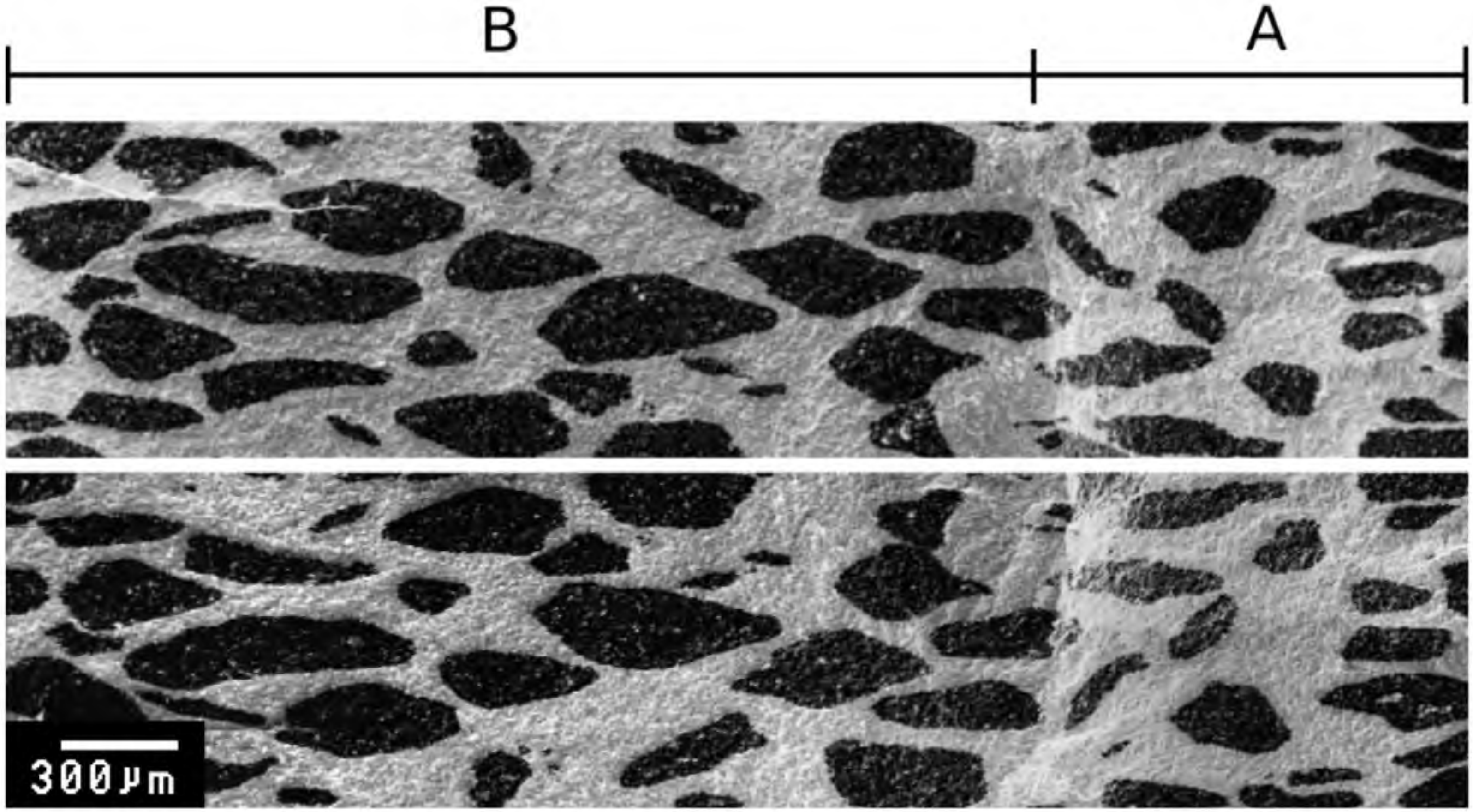

Figure 4.3. The two faces of a fracture surface, positioned to create a vertical mirror image. Section A was created during slow fatigue crack growth. Section B was created during a sudden catastrophic failure.

intragranularly, rather than propagating along the interface. The crack shown in Figure 4.3 was grown in two stages, catastrophic growth in section B, and fatigue growth in section A. The lack of preferential crack growth along the interfaces in section A in particular suggests that the interface between the two materials is not the weak link causing fracture.

This phenomenon will be revisited in subsequent chapters that focus on analytical and numerical models of this material. The explanation of this trend through the use of models illustrates the value of the models in understanding the behavior of complete material systems.

The Weibull probabilities of failure versus the calculated tensile stress are plotted in Figures 4.4 through 4.7 for the four material series tested. Each sample has an equation displayed. The coefficient in the equation is the Weibull modulus. The Weibull modulus is a measure of the variation in the property of the materials. A higher modulus indicates a lower amount of variation in the data. The all WC-Co specimens showed the least data scatter. The composites showed a moderate amount of scatter, comparable to the all-PCD specimens. This can be explained by recognizing that the composites have all of the defect distribution found in their constituents, but also have variation due to nonuniformity in the mesostructure. This point will be illustrated later when reviewing the numerical models.

Flexural strength testing was conducted on roughly half of the prepared GDC grades. The testing was shown to be moderately reproducible between different batches of the same material. The testing showed that WC-Co 1 performed better than WC-Co 2

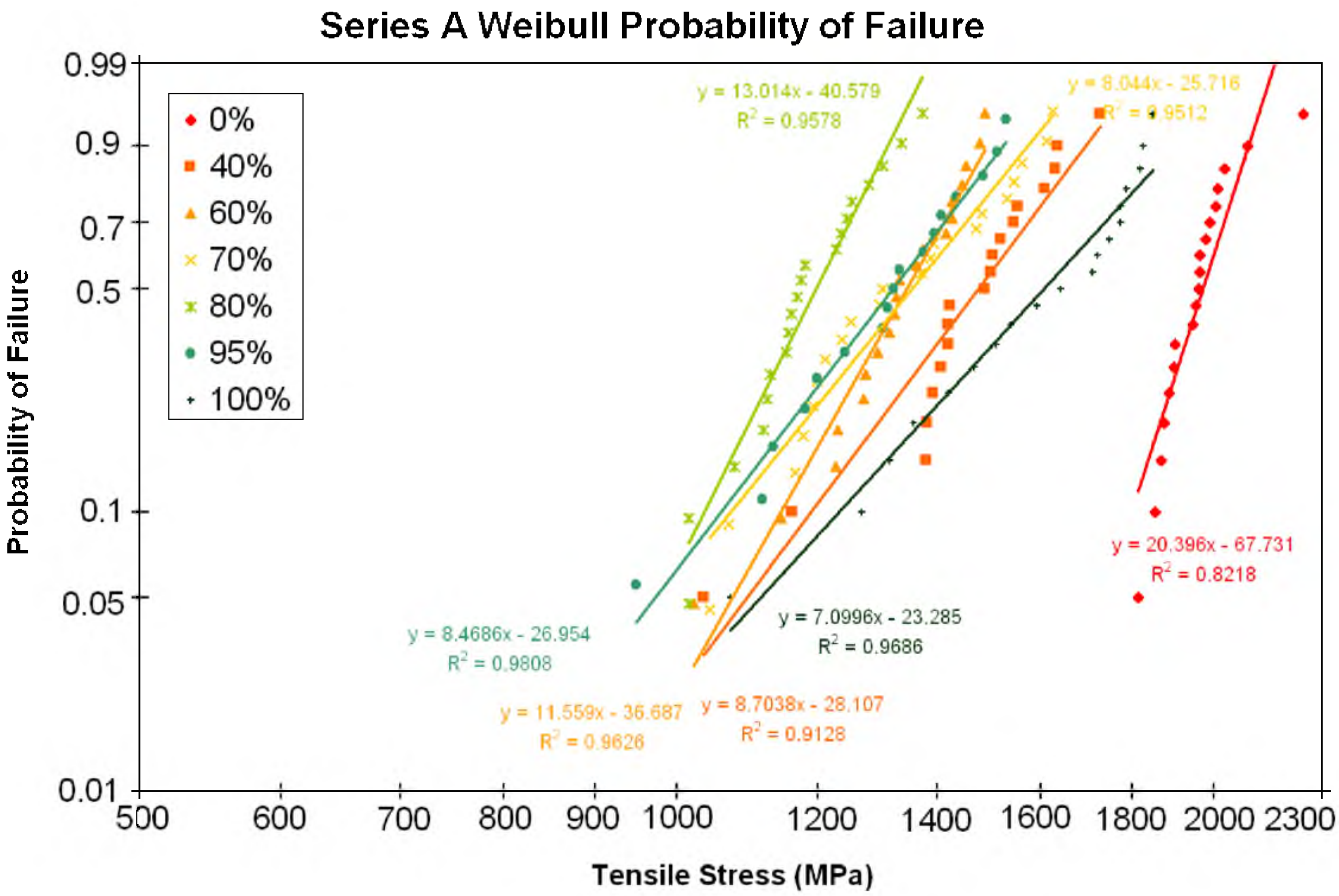

Figure 4.4. Weibull probability of failure for Series A materials.

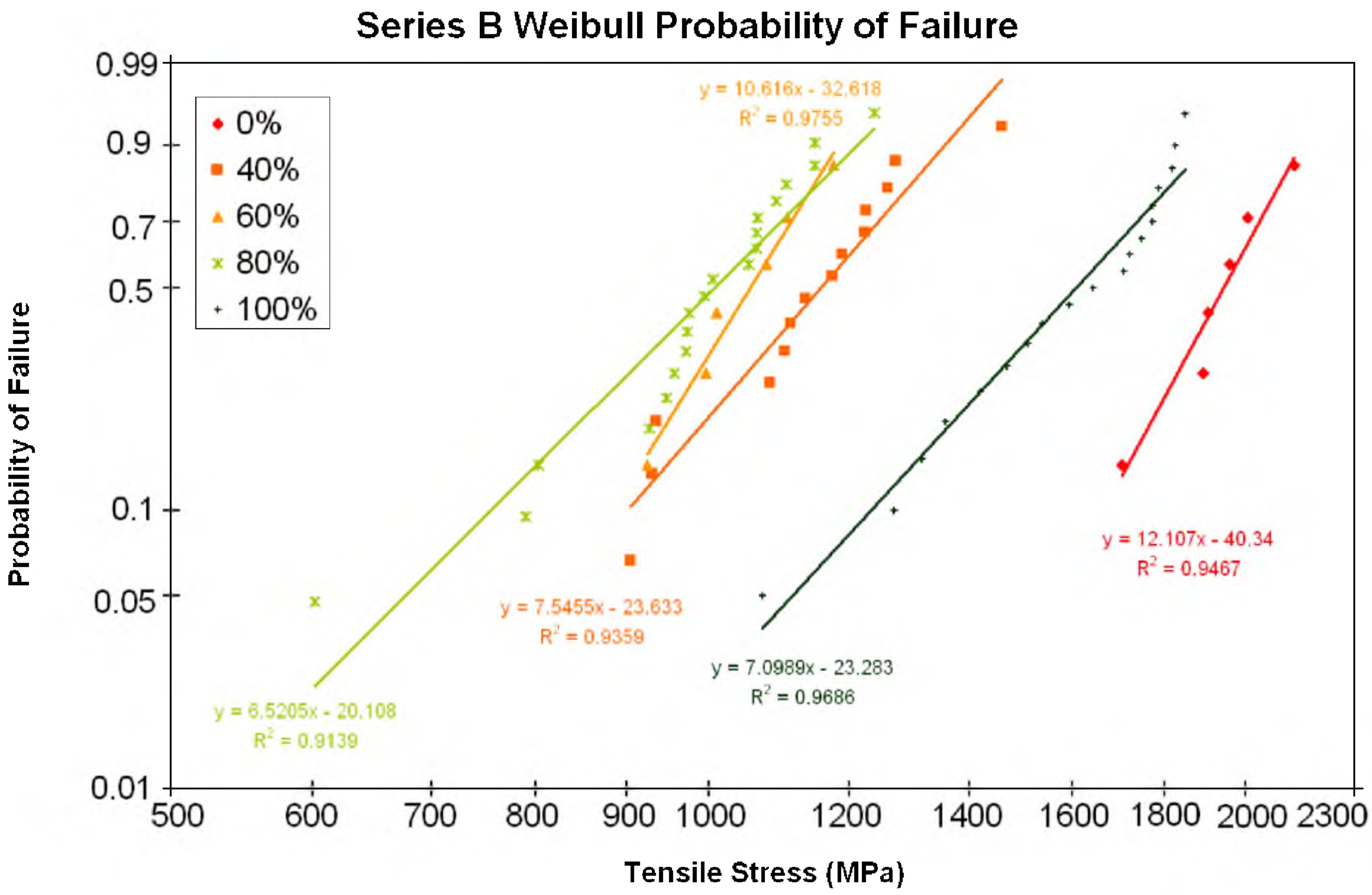

Figure 4.5. Weibull probability of failure for Series B materials.

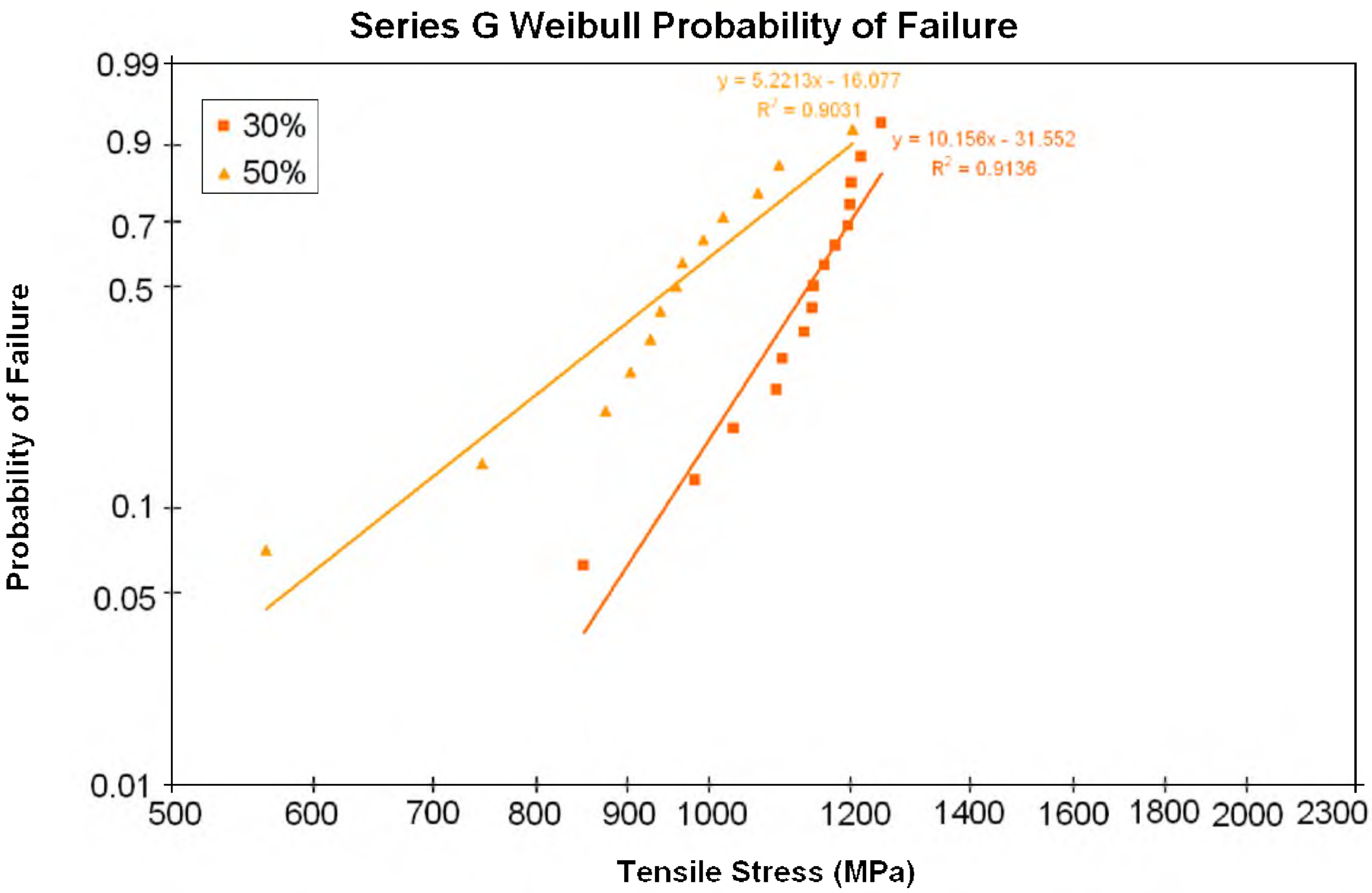

Figure 4.6. Weibull probability of failure for Series G materials.

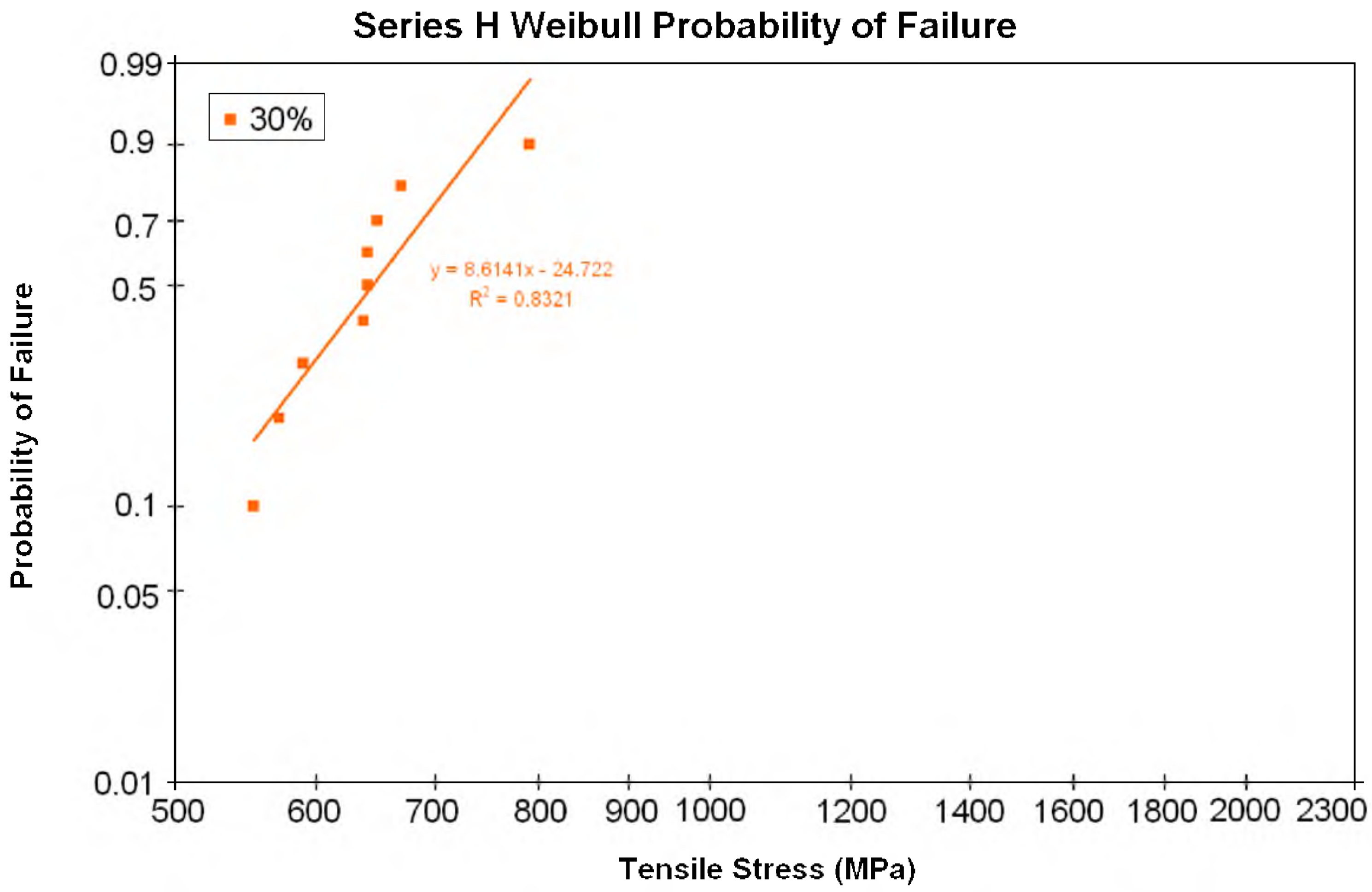

Figure 4.7. Weibull probability of failure for Series H materials.

and Blend 1 better than Blend 2 in flexural strength tests. Because of the limited grades selected for testing, PCD 1 could not be compared with PCD 2. The constituents processed and sintered using the developed procedure had lower flexural strengths than the typical strengths for the material. Composites had lower measured strengths than either constituent, which is not typically seen in composites. The materials have relatively low Weibull moduli, indicating a large variation in material strengths.

Wear Resistance

The Series A materials listed on the first line of Table 4.3 were wear tested and the results are plotted in Figure 4.8. The wear is measured as a ratio of granite material removed per composite material removed. It is presented as a normalized wear number, relative to the wear resistance of PCD 1.

The promising aspect of the results is that the wear resistance didn't drop significantly until more than 40v% of carbide had been added to the composite. This suggests that there may be design space where the fracture resistance may be raised, without substantially reducing the wear resistance of the material. The negative aspect of the results is that even at high diamond fractions, the wear resistance of the series is much lower than wear resistance of PCD 1.

The grades with WC-Co were expected to have a lower wear resistance because carbide is less wear resistant than diamond. A100 has no carbide, and is 100v% PCD 1, so it could be expected to have roughly the same wear resistance as the industrially produced PCD 1. Instead, the wear tests showed that A100 had roughly 40% of the wear

Table 4.3

Composite Grades Mechanically Tested

Experiment	Materials Tested
Wear Resistance	A0, A40, A60, A70, A80, A95, A100
Impact Resistance	A40, A60, A70, A80, A95, A100
Field Testing	G30

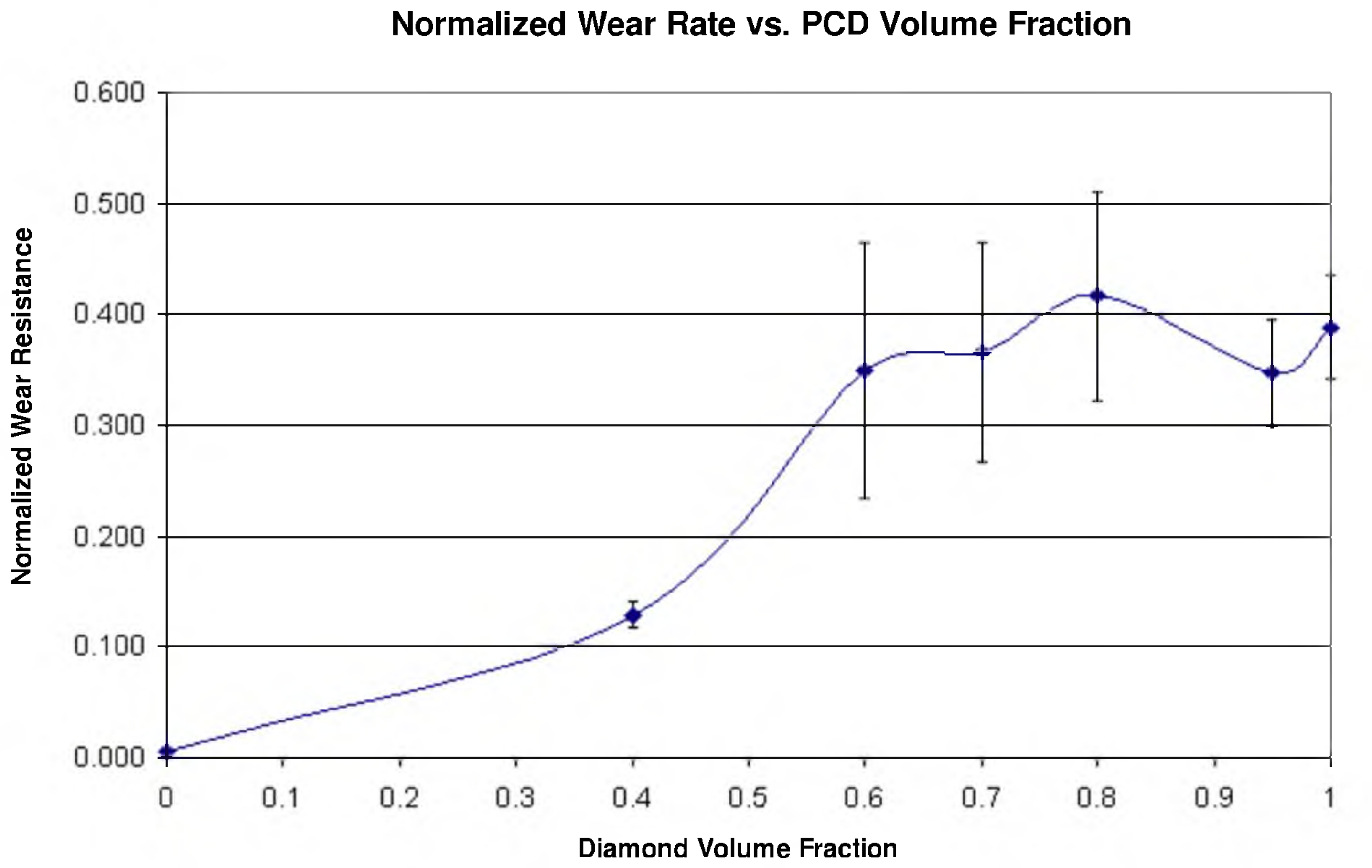

Figure 4.8. Normalized wear resistance as a function of PCD granule fraction.

resistance of PCD 1. This suggests that the manufacturing process that was developed is not producing properly sintered material. The applicability of GDC would be severely limited unless an improved manufacturing process is developed which allows grades like A100 to perform more like industrial PCD 1.

Impact Resistance

The second line of Table 4.3 lists the grades that were tested for impact resistance. The individual test results are plotted in Figure 4.9 as the probability of failure versus the drop height. The average drop heights for failure for the various diamond concentrations are shown in Figure 4.10. The intuitive assumption that increasing the tougher phase will increase the impact resistance is challenged by the results. While the material with 20v% WC-Co has significantly improved impact resistance when compared with 100v% PCD, the impact resistance steadily drops from 80v% PCD to 40v% PCD. It is difficult to explain why the 95v% PCD tested lower than 100v% PCD and 80v% PCD.

Field Testing

The G30 grade was field tested by Smith Megadiamond and showed better resistance to long range fracture and better wear resistance, when compared to coated inserts with a grade of conventional 30v% Co PCD.

Figure 4.11a compares the long range fracture experienced by a PCD-30v% Co coated insert (right) and a G30 coarse GDC insert (left). While both inserts experienced fractures, the tougher matrix in the GDC insert has prevented any long range damage.

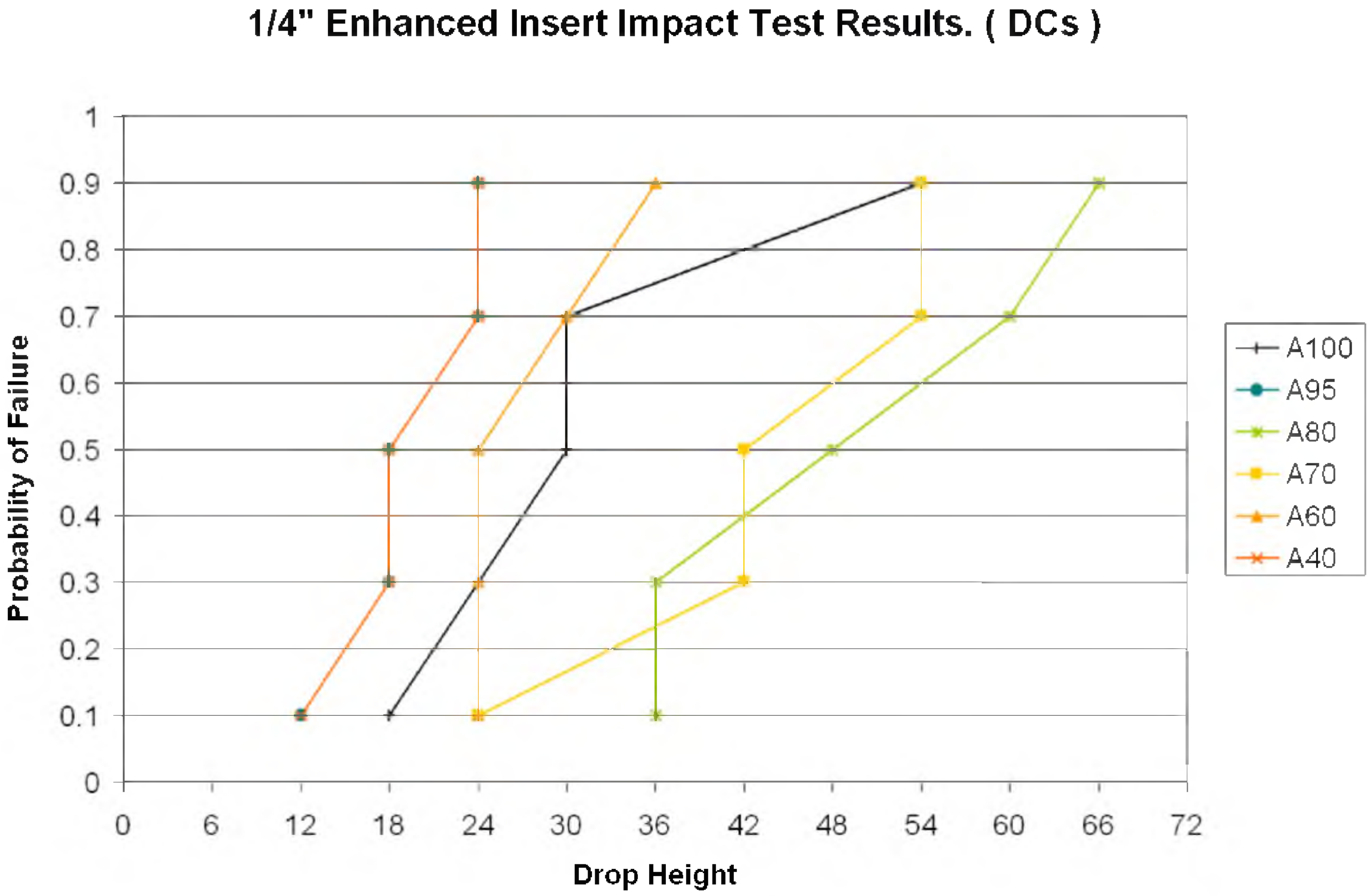

Figure 4.9. Probability of fracture as a function of drop height.

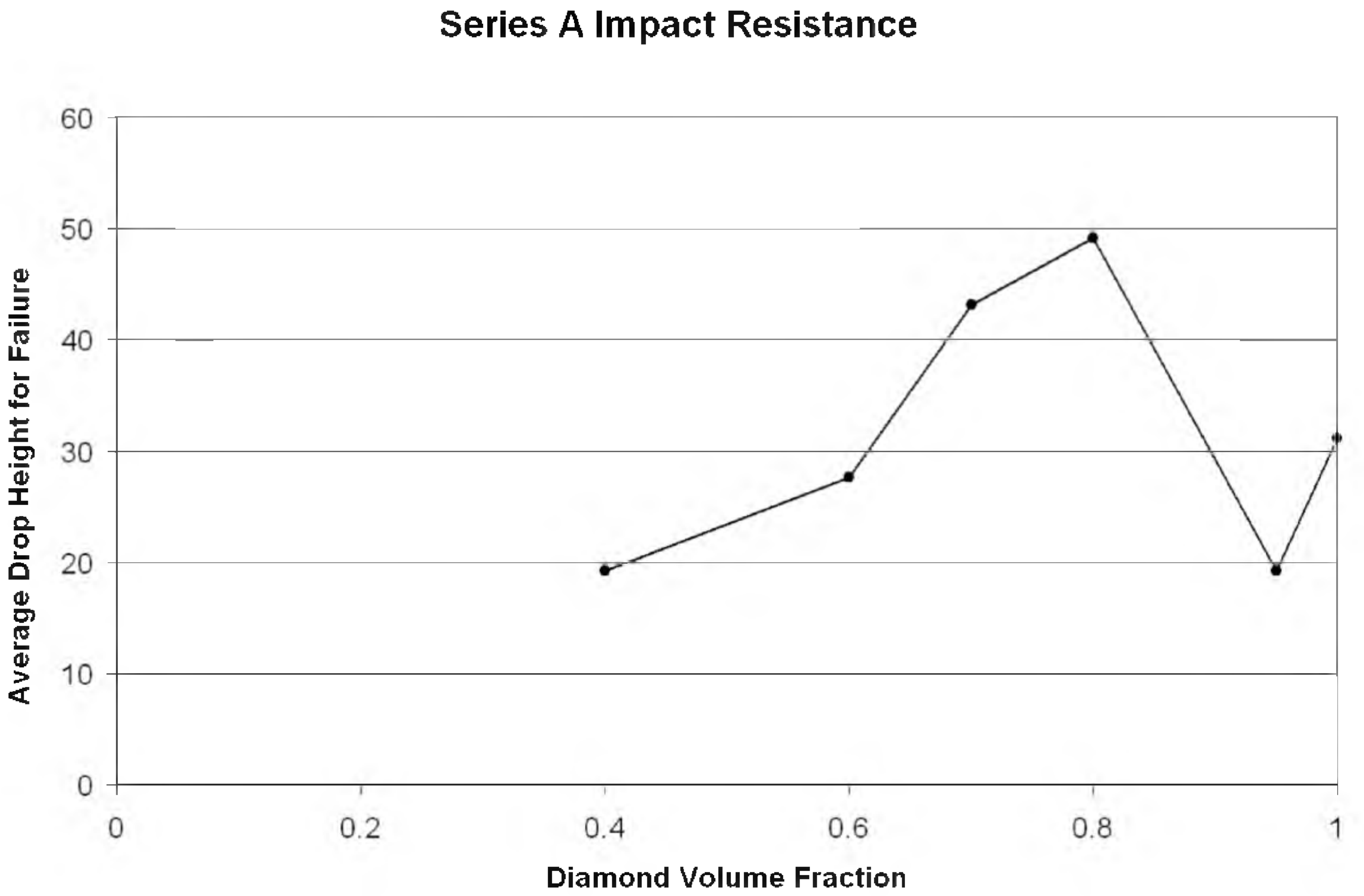

Figure 4.10. Impact resistance as a function of diamond content. It was expected that the 80v% diamond grade would have better impact resistance than 100v% diamond, but it was not expected that the impact resistance would trend lower as more of the tougher carbide phase was added.

Figure 4.11. Field test results comparing G30 coated drill bit inserts to drill bit inserts coated with an industrial PCD grade. The G30 inserts are on the left. The standard PCD inserts are on the right. a) Comparison of damage to field tested inserts. b and c) Comparison of insert profiles.

Figure 4.11b compares the profiles of a G30 insert (left) at a PCD coated insert (right). Even though the GDC insert suffered some short range damage, it held its radius much better than the fracture-free PCD coated insert. Figure 4.11c White circles are superimposed over the image which makes the material removal easier to assess.

Chapter Summary

This investigation tested several functional and intrinsic material properties of GDC grades. The original test plan turned out to be too expensive and needed to be pared back significantly. Most testing was performed only on Series A. Flexural strength testing was also conducted on Series B, G and H. Only G30 was field tested. In general, granular diamond composites performed worse in testing than expected. Previous to testing, it was assumed that the all-diamond grades would perform similarly to the conventionally produced component material. Instead, the all-diamond grades performed significantly worse, particularly in the wear resistance test. The all-carbide grades produced using the GDC procedure also performed worse than conventionally produced grades, but this was more expected. The poor performance is likely due to deficiencies in the production method. The mechanical properties of the GDC materials were mixed compared with the end points. Often the data trends defied explanation. One identified trend was that the A95 grade typically did not follow the trend of the rest of the composites. These trends, or lack thereof, will be explored in subsequent chapters.

There are several factors that complicate the characterization of GDC materials. PCD is expensive and difficult to work with. The capacity of the diamond sintering press limits the specimen size to smaller than is typically used in the mechanical tests. The manufacturing process appears to be producing material with less than optimal sintering, which degrades its mechanical properties. Analytical and numerical modeling can be used to further investigate these materials and can assist in developing a better understanding to the mechanisms which influence their mechanical properties. The modeling work will be presented in Chapters 5 and 6.

References

1. Belnap, J. D. Smith Megadiamond, Provo, UT. Personal communication, 2004.

CHAPTER 5

ANALYTICAL MODELING OF COMPONENT STRESSES AND COMPOSITE STRENGTH

An analytical model approximating the flexural strength of granulated diamond composites is developed in this chapter. The simplifying assumptions are presented and discussed. The interactions between the components are examined. The role of residual stresses, created in the material upon exiting the high-temperature/high-pressure (HTHP) sintering cycle, will be considered. A case will be made for the inclusion of dilatational residual stresses.

Models can assist in understanding material systems. Models allow for the rapid exploration of different parameters and theoretical designs. Analytical models are particularly helpful because they can relate functional properties to intrinsic properties and describe how the properties are related. The added insight and understanding gained from the models will assist in designing optimal mesostructures.

The Voigt and Ruess models, derived from a slab model, are used to develop the analytical model. These models better approximate long-fiber composites than particulate composites, but have been used to establish upper and lower bounds of various composite properties in a wide range of composites.[1] Hooke's law of elasticity will be reduced from its full 3-D form by assumptions made in these models.

Dilatational residual stresses are the residual stresses which arise between materials of different stiffnesses when there is a change in the applied pressure. Historically, only thermal residual stresses have been considered when modeling sintered materials, including sintered PCD.[2–5]

Many disciplines are incorporated in this analysis. Different disciplines may use different symbols. Occasionally, the meaning of symbols conflicts with each other where they overlap. There is a List of Symbols on Page ix with the meaning of the symbols as used in this analysis.

Fundamentals and Assumptions

The analytical model is based on the slab model and is derived from Hooke's Law. There are several simplifications and assumptions that provide a model that is simple enough to obtain an analytical solution. The material properties listed here are themselves best approximations based on limited data.

Hooke's Law of Elasticity

The foundational analytical model is Hooke's law, shown in the compliance form in three dimensions in equation 5.1, where ϵ is normal strian, γ is shear strain, E is Young's Modulus, S is compliance tensor, σ is normal stress, and τ is shear stress. The first assumption is that granular diamond composites behave linear-elastically in the modeled scenarios. Considering the high strength and brittle nature of both diamond and carbide, this is a reasonable assumption at room temperature.

$$\begin{bmatrix} \epsilon_x \\ \epsilon_y \\ \epsilon_z \\ \gamma_{yz} \\ \gamma_{zx} \\ \gamma_{xy} \end{bmatrix} = \frac{1}{E} \begin{bmatrix} S_{11} & S_{12} & S_{13} & S_{14} & S_{15} & S_{16} \\ S_{21} & S_{22} & S_{23} & S_{24} & S_{25} & S_{26} \\ S_{31} & S_{32} & S_{33} & S_{34} & S_{35} & S_{36} \\ S_{41} & S_{42} & S_{43} & S_{44} & S_{45} & S_{46} \\ S_{51} & S_{52} & S_{53} & S_{54} & S_{55} & S_{56} \\ S_{61} & S_{62} & S_{63} & S_{64} & S_{65} & S_{66} \end{bmatrix} \begin{bmatrix} \sigma_x \\ \sigma_y \\ \sigma_z \\ \tau_{yz} \\ \tau_{zx} \\ \tau_{xy} \end{bmatrix} \tag{5.1}$$

The second assumption is that the material behaves isotropically. Both diamond and tungsten-carbide are anisotropic as single crystals, but in randomly-oriented polycrystalline form they can be considered isotropic.[2,6,7] The stress-strain relationship for isotropic materials is shown in equation 5.2.[1,8]

$$\begin{bmatrix} \epsilon_x \\ \epsilon_y \\ \epsilon_z \\ \gamma_{yz} \\ \gamma_{zx} \\ \gamma_{xy} \end{bmatrix} = \frac{1}{E} \begin{bmatrix} 1 & -\nu & -\nu & 0 & 0 & 0 \\ -\nu & 1 & -\nu & 0 & 0 & 0 \\ -\nu & -\nu & 1 & 0 & 0 & 0 \\ 0 & 0 & 0 & 1+\nu & 0 & 0 \\ 0 & 0 & 0 & 0 & 1+\nu & 0 \\ 0 & 0 & 0 & 0 & 0 & 1+\nu \end{bmatrix} \begin{bmatrix} \sigma_x \\ \sigma_y \\ \sigma_z \\ \tau_{yz} \\ \tau_{zx} \\ \tau_{xy} \end{bmatrix} \tag{5.2}$$

Equal Stress and Equal Strain Conditions

The slab model is used to approximate the GDC material and is a simple enough form to allow for an analytical solution. The slab model consists of two hexahedral slabs of material, perfectly bonded along one face. Figure 5.1 is a conceptual illustration of the slab model. Only normal stresses are applied and the faces of the model are not allowed to shear.

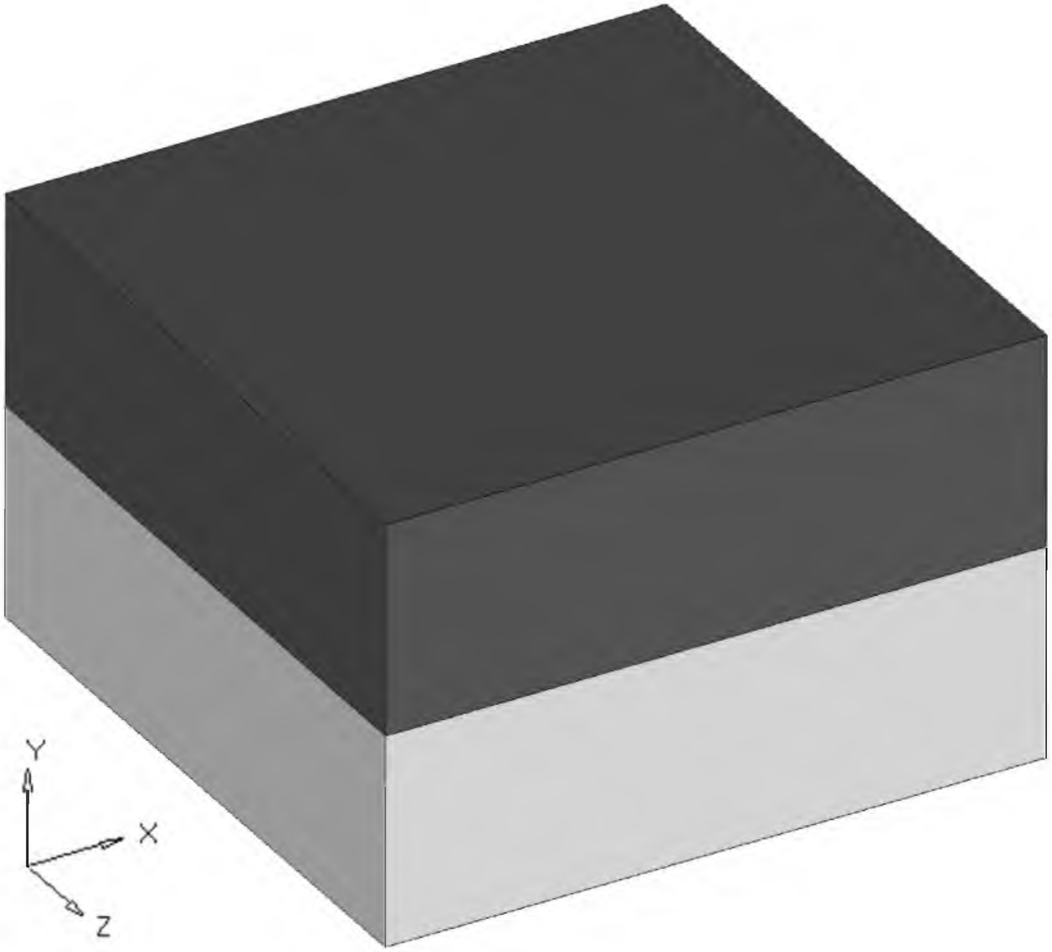

Figure 5.1. Conceptual illustration of the slab model. The materials are perfectly bonded along their interface and no shear is allowed.

The slab model is used to develop both the equal stress and equal strain models. The equal strain model, also called the Voigt model, is applied when a stress is applied in the axial (X) direction. Because the material is not allowed to shear, both materials will undergo the same strain, creating different stresses in components with different stiffnesses. The equal strain model, shown in Figure 5.2, is a good approximation of a long fiber-reinforced composite stressed along the direction of the fiber.

When a stress is applied to the slab model in the transverse direction, it is called the Ruess, or equal stress model. The equal stress model is illustrated in Figure 5.3. This model is similar to equal strain except the stresses are applied perpendicularly, rather parallel to the interface. Both components are unconstrained in the transverse direction and will freely strain in response to the applied stress. The equal stress model is a good approximation of a long fiber reinforced composite stressed in the transverse direction.

While the equal stress and equal strain models best approximate long-fiber reinforced composites, they are often used to establish the upper and lower bounds of responses for other composite types and are published in introductory composite books. Equations 5.3 through 5.5 are taken from a book by Hull and Clyne[1]. V_f is the volume fraction of the reinforcement phase and V_m is the volume fraction of the matrix phase.

$$\epsilon = \epsilon_f = \epsilon_m \tag{5.3}$$

$$\sigma = V_f \sigma_f + V_m \sigma_m \tag{5.4}$$

$$E = V_f E_f + V_m E_m \tag{5.5}$$

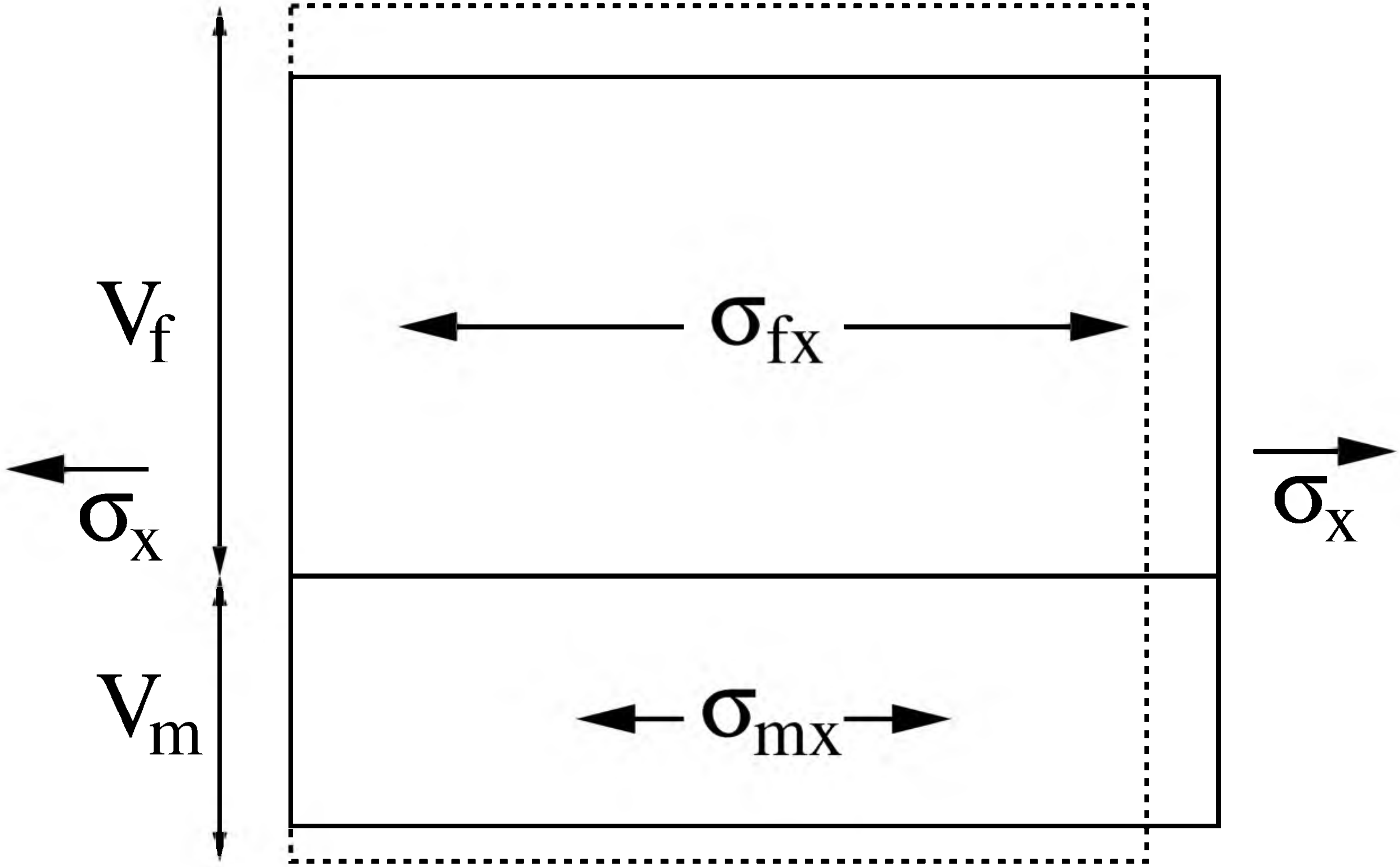

Figure 5.2. This is a representation of the ideal equal strain condition using the slab model. The dashed outline indicates the prestressed geometry. The solid outline shows the geometry after a stress, σ_x, has been applied.

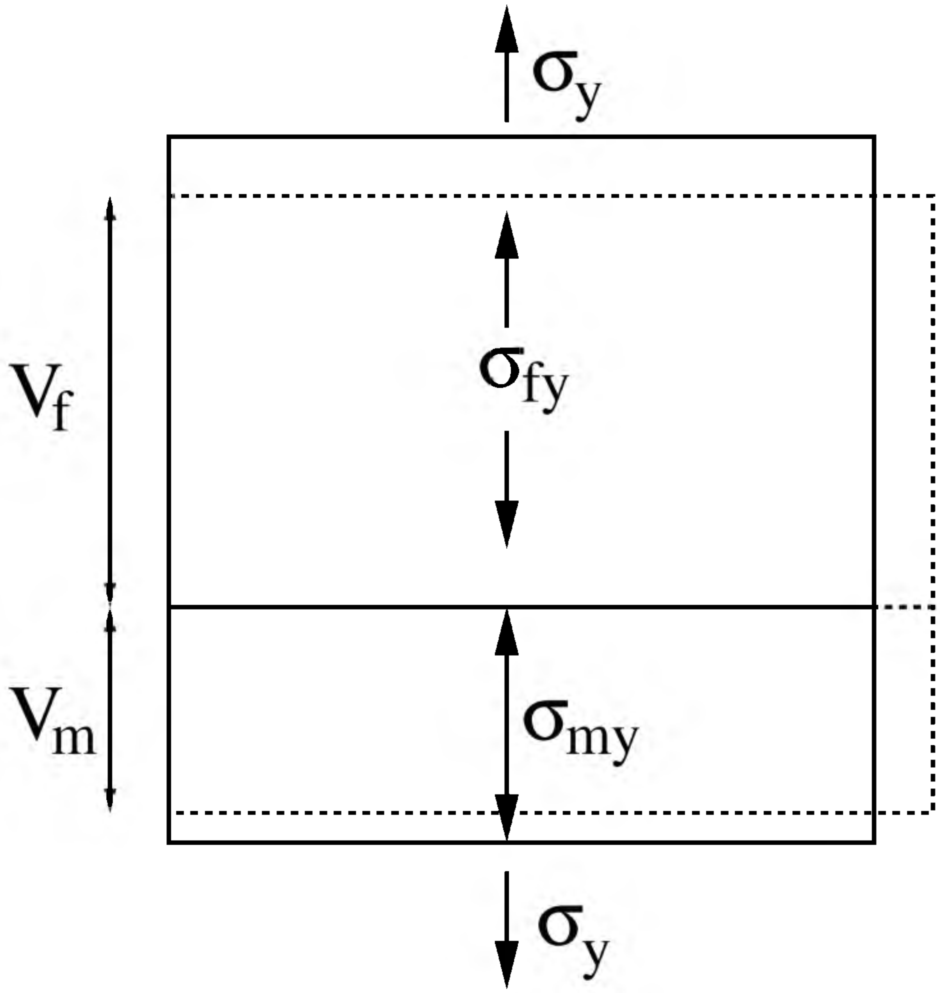

Figure 5.3. This is a representation of the ideal equal stress condition using the slab model. The dashed outline indicates the prestressed geometry. The solid outline shows the geometry after a stress, σ_y, has been applied.

Equations 5.3 and 5.4 are straightforward descriptions of the equal strain model. Equation 5.5 is the well known "Rule of Mixtures" for the equal strain model. It has been shown to be very accurate when modeling materials that are well approximated by the equal strain model, even though it neglects differences in the Poisson's ratio (nu;between materials.[1]

The equal stress model is characterized by equation 5.6. Equation 5.7 is the "Rule of Mixtures" for the equal stress model.

$$\sigma = \sigma_f = \sigma_m \tag{5.6}$$

$$E = \frac{E_f E_m}{E_m V_f + E_f V_m} \tag{5.7}$$

Hooke's Law in Equal Stress

Hooke's stress-strain equation can often be simplified for particular states. Two well known examples of this are the plane stress and plane strain states. The equation can also be simplified for application to the equal strain model. Because shear strain is not allowed in the equal strain model and because shear stress depends only on shear strain, three rows and three columns can be removed from the stiffness matrix. There are no applied stresses in the transverse or thickness directions in the equal strain model, further simplifying the equation. The resulting simplified equation is shown as equation 5.8.

$$\begin{bmatrix} \epsilon_x \\ \epsilon_y \\ \epsilon_z \end{bmatrix} = \frac{1}{E} \begin{bmatrix} 1 & -\nu & -\nu \\ -\nu & 1 & -\nu \\ -\nu & -\nu & 1 \end{bmatrix} \begin{bmatrix} \sigma_x \\ 0 \\ 0 \end{bmatrix} \tag{5.8}$$

For a given axial stress, σ_x, the strain in the axial direction, ϵ_x, can be determined by using equation 5.5 to estimate the Young's modulus of the composite, E. The strains in the other two directions can be determined when the overall Poisson's ratio of the composite, ν is estimated. Like stiffness, there are several "Rule of Mixture" estimates for Poisson's ratio in a composite, but these estimates are unnecessary in this study.

Equation 5.8 can also be applied to the two components that make up the composite. The only difference between the composite and its components is that the components also can have stress in the thickness direction. These stresses arise from the differences in Poisson's ratio between the materials. No stresses will accumulate in the transverse direction because it is perpendicular to both the direction of stress and the material interface and are therefore not constrained. If the stresses caused by the difference in Poisson's ratios are neglected, as they were in the "Rule of Mixture" equation 5.5, then the simplified Hooke's equation for each component (equation 5.9) will have the same form as equation 5.8. The error that is introduced by this assumption will be evaluated in the next chapter.

$$\begin{bmatrix} \epsilon_{cx} \\ \epsilon_{cy} \\ \epsilon_{cz} \end{bmatrix} = \frac{1}{E_c} \begin{bmatrix} 1 & -\nu_c & -\nu_c \\ -\nu_c & 1 & -\nu_c \\ -\nu_c & -\nu_c & 1 \end{bmatrix} \begin{bmatrix} \sigma_{cx} \\ 0 \\ 0 \end{bmatrix} \tag{5.9}$$

In the case of the components, the stresses in the axial direction must balance between the components be to equal the stress in the composite. This is represented in equation 5.10.

$$\sigma_x = V_f \sigma_{fx} + V_m \sigma_{mx} \tag{5.10}$$

Material Properties

The material properties that will be used in the models are listed in Table 5.1. The material strength is taken from the flexural strength measured in the experiments described in Chapter 3. The moduli of elasticity and the Poisson's ratios were supplied by the manufacturer. As discussed in Chapter 2, there are many difficulties in obtaining accurate material properties that describe PCD and WC-Co across the range of pressures and temperatures present in the HTHP sintering cycle. These values should be understood to be rough estimates. A sensitivity analysis is presented at the end of this chapter which illustrates the impact of small changes to these values.

Modeling of Applied Stresses

Using the conceptual framework of the Voigt model and the material properties of the components, the behavior of the composite can be modeled. Using this model, the composite stiffness is estimated, the distribution of stresses within the composite is modeled, and ultimately, the strength of the composite is predicted, based on the strengths of the components and the distributions of stresses. This prediction is compared to the

Table 5.1

Component Material Properties

Property	Value	Unit
E_f	841,000	MPa
E_m	543,000	MPa
ν_f	0.20	
ν_m	0.23	
σ_{fc}	1589	MPa
σ_{mc}	1961	MPa

measured material strengths found in Chapter 4.

Unless otherwise specified, stresses and strains that are discussed and used in equations should be assumed to be in the axial direction.

Composite Stiffness

The equation for the Young's modulus of the composite, E, is given in equation 5.5, and is a function of the volume fraction. It is graphed against the volume fraction of diamond in Figure 5.4 using the material properties listed in Table 5.1.

The stiffness of the composite increases linearly with volume fraction of the reinforcement phase from the stiffness of the matrix to the stiffness of the reinforcement.

Compliance is the inverse of the stiffness, and combined with the stress-strain relationship in equation 5.8, is simply the amount that a material will strain under a given stress.

$$\frac{1}{E} = \frac{\epsilon}{\sigma} = \frac{1}{V_f E_f + V_m E_m} \tag{5.11}$$

This equation is graphed in Figure 5.5 with the diamond fraction, V_f, ranging from 0 to 1.

As is expected, the compliance of the material is reduced as the volume fraction of the stiffer reinforcement phase is increased. This is typical for composites.

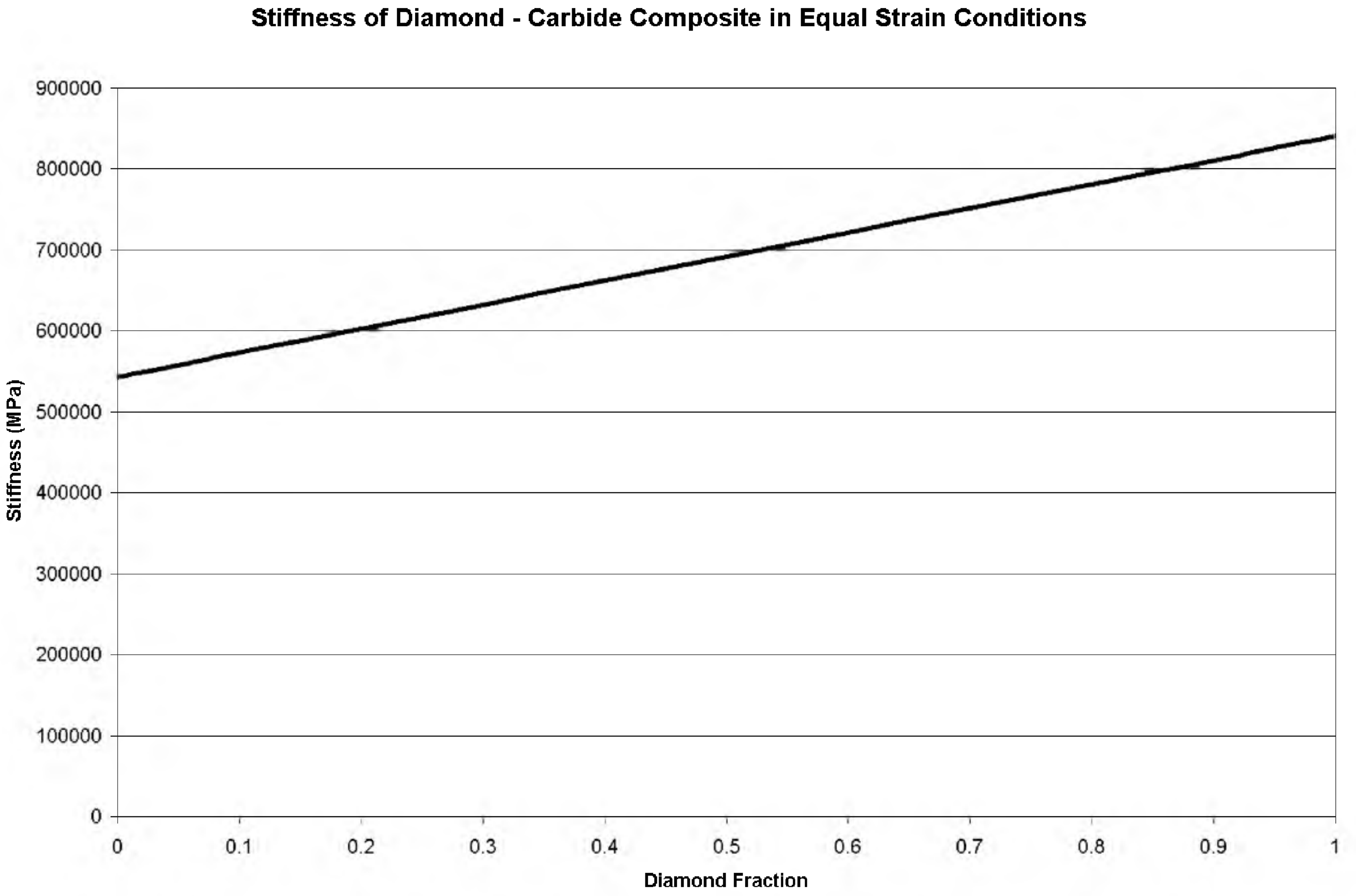

Figure 5.4. Composite stiffness as a function of V_f. The stiffness linearly increases with the addition of the stiffer diamond phase.

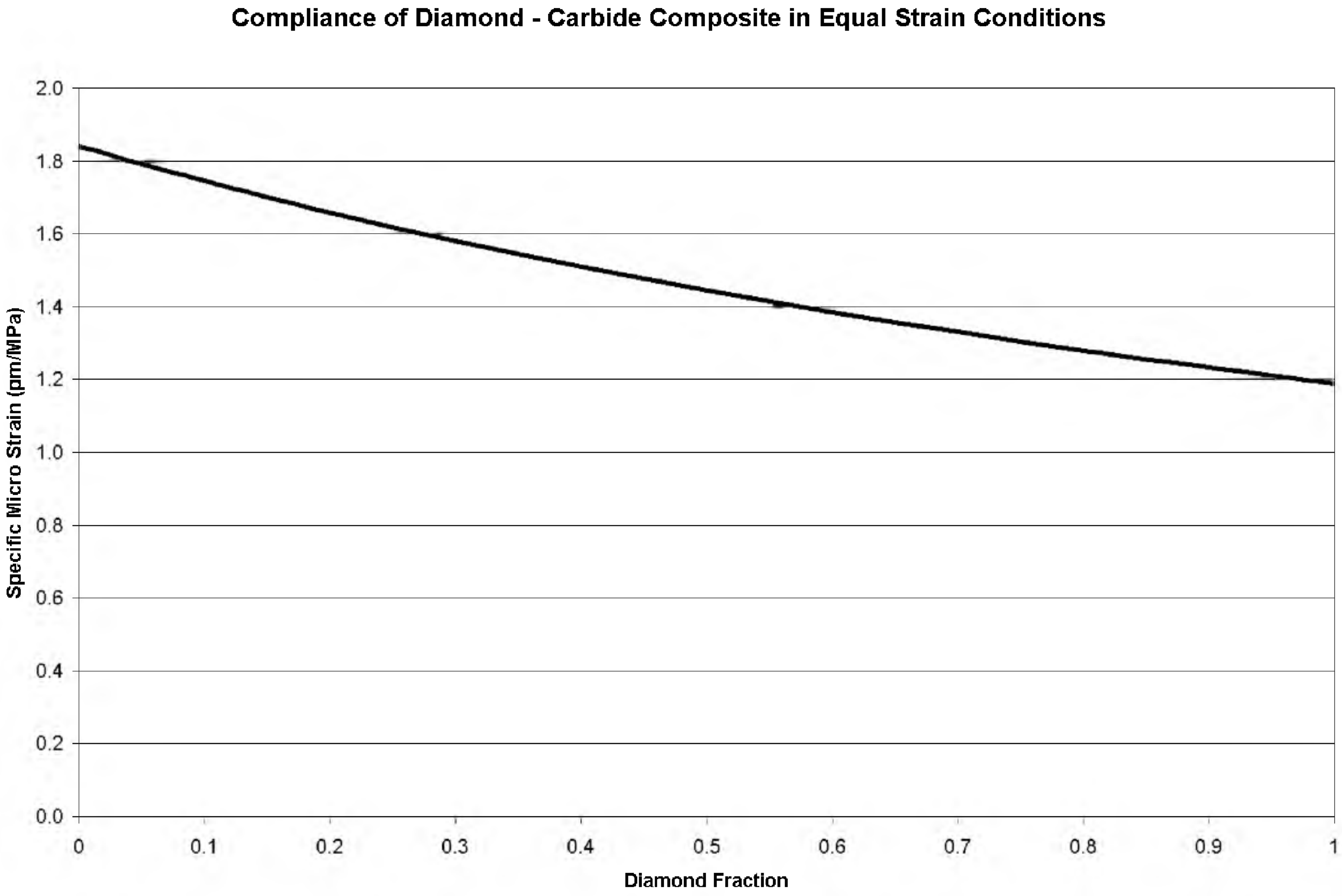

Figure 5.5. Composite compliance as a function of V_f. The compliance decreases the amount of PCD increases.

Stress Intensification

From equations 5.8 and 5.9, the ratio between the stress in a component and the stress applied to the composite can be found using equation 5.12:

$$\frac{\sigma_c}{\sigma} = \frac{E_c \epsilon_c}{E \epsilon} \tag{5.12}$$

In the equal strain model, the strain of the composite is equal to the strain in each of the components (see equation 5.3), therefore:

$$\frac{\sigma_c}{\sigma} = \frac{E_c}{E} \tag{5.13}$$

The stress intensification factor, $\frac{\sigma_c}{\sigma}$, estimates how much a component will stress, σ_c, for a given amount of average stress in the composite, σ. It is equal to the ratio between the Young's modulus of the component and the Young's modulus of the composite.

Because the Young's modulus of the composite, E, is a function of the volume fraction, the amount of stress intensification in each phase will vary with the composition. Equation 5.13 is plotted in Figure 5.6 for both the matrix phase and the reinforcement phase.

At 0v% of PCD, the stress in the carbide phase is equal to the applied stress. This should be obvious because the composite wholly consists of WC-Co. The same is true of the stress in the diamond phase at 100v% PCD. At $V_f = 0.1$, the material is slightly stiffer

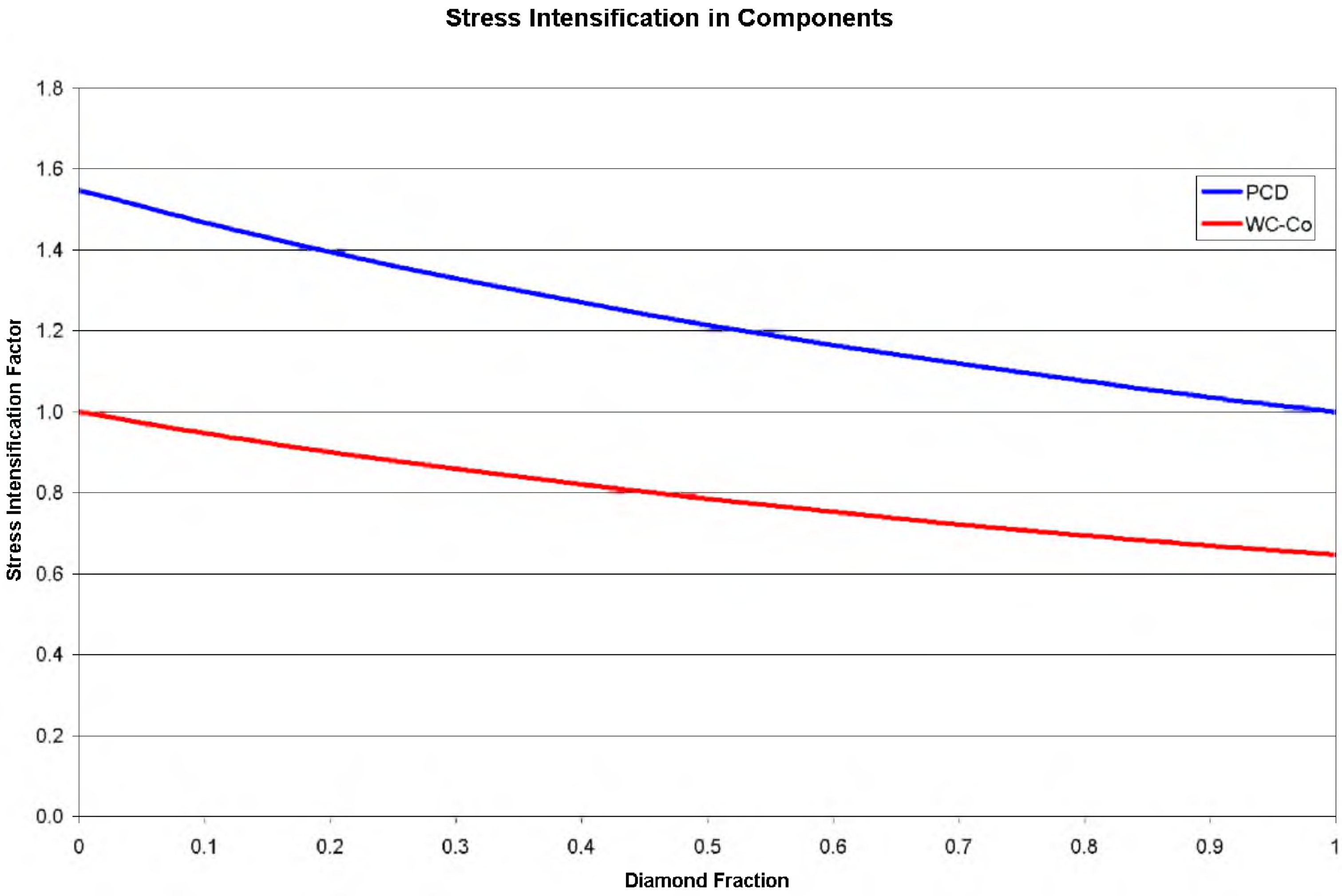

Figure 5.6. Stress intensification in WC-Co (red) and PCD (blue). The stress concentrates in the diamond because PCD is stiffer than WC-Co.

than an all carbide material but quite a bit more compliant than an all diamond material (see Figure 5.4). The stress in the carbide is reduced slightly because the material isn't quite as strained as an all WC-Co material. The diamond must be stressed significantly more because the material is strained substantially more than it would be if it was all PCD. This behavior is also typical of composites and results from the reinforcement phase being stiffer than the matrix phase.

Note that the ratio between the stress intensification factors for the two components remains constant over all volume fractions, as it is not a function of composition. For the material properties listed in Table 5.1, $\frac{\sigma_f}{\sigma_m}$ turns out to be 1.55. From equation 5.13:

$$\frac{\sigma_f}{\sigma_m} = \frac{E_f}{E_m} \tag{5.14}$$

Stress Distribution

While the stiffer component will always have a higher stress, at low volume fractions the more compliant phase may carry more of the load.

The total stress is a volume-weighted average of the component stresses (see equation 5.4). The component's fractional contribution to the overall stress is:

$$\frac{V_c \sigma_c}{\sigma} \tag{5.15}$$

Figure 5.7 plots the distribution of the overall stress in the components. This

Figure 5.7. Fraction of the load being taken by the diamond phase (blue) and the carbide phase (red).

model of the PCD/WC-Co system estimates that at a V_f of a little less than 40%, both components would be sharing the load equally. The larger the difference in stiffness between the reinforcement and matrix phases, the closer the intersection will occur to the left. With equal parts diamond and carbide, ($V_f = 0.5$), WC-Co takes about 40% of the total stress and PCD takes the other 60%. The ratio of the stress distribution is roughly 60%/40% or 1.5, as seen in the previous section.

Composite Strength

With the equation for stress intensification in the components (equation 5.13), it is possible to calculate the applied composite stress that will cause each component to fail (σ_{auf} and σ_{aum}).

$$\sigma_{auc} = \frac{E}{E_c} \sigma_{uc} \tag{5.16}$$

Figure 5.8 is a graphical representation of how the stress intensification factors affect the strength of the composite. It plots equation 5.16 for both carbide and diamond at 80v% PCD. The solid lines correlate the stress in the components to the stress applied to the composite ($\sigma_f = \frac{E_f}{E} \sigma$, see equation 5.13). The slope of the PCD line is greater than one, indicating that stress is concentrated in the PCD phase. Conversely, the slope of the WC-Co line is less than one. The long-dashed lines represent the intrinsic strength of the components, or the stress at which they will fail. The short-dashed lines indicate the applied composite stress at which the components will reach their critical stress.

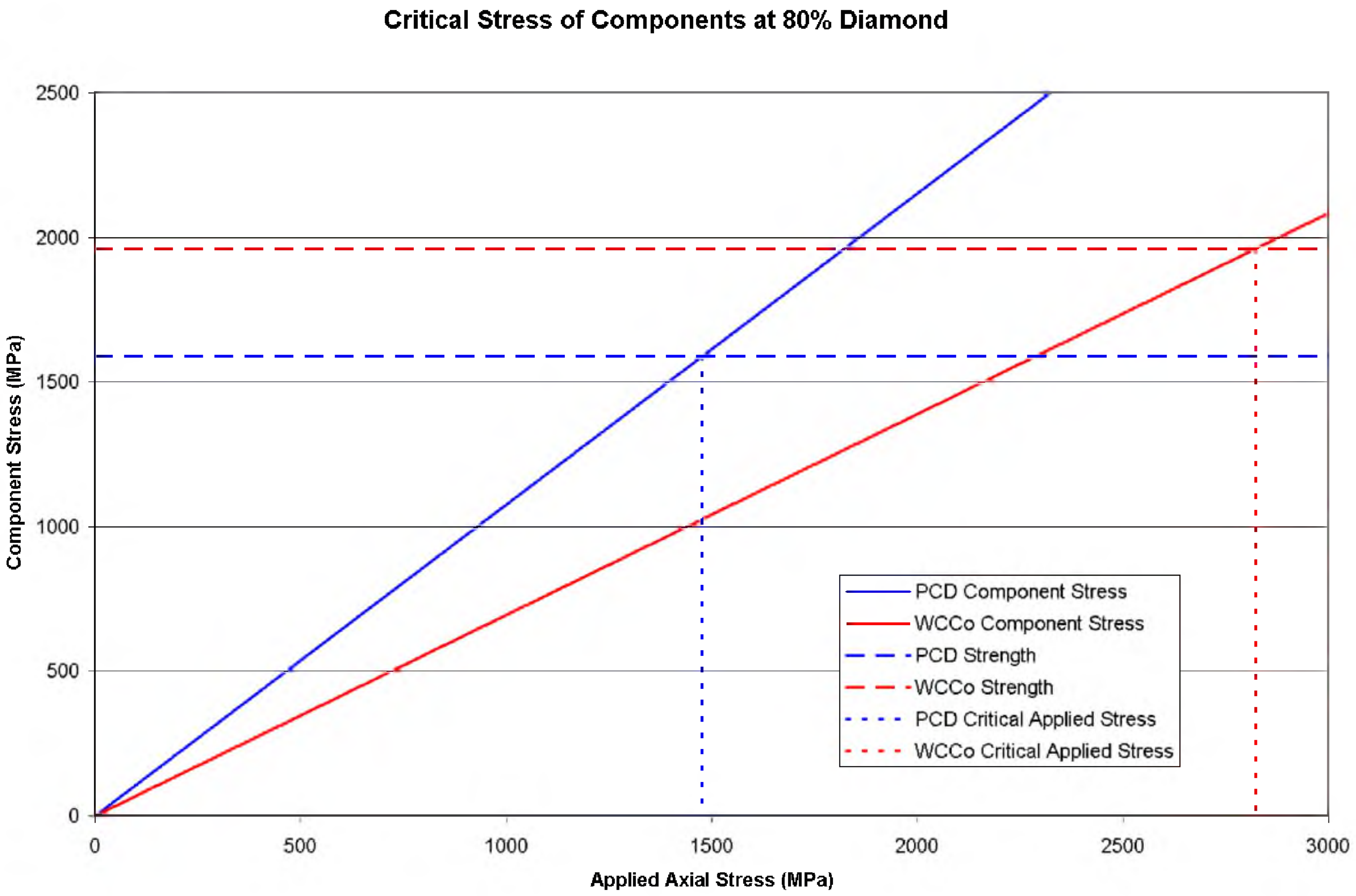

Figure 5.8. Illustration of how the stress concentration due to differences in stiffness affects the stress at which a component will fail. The minimum stress that causes any component to fail is considered the strength of the composite. The diamond volume percent for this graph is 80v%.

At 80v% diamond it only takes 1476 MPa of external applied stress for the diamond phase to reach its critical stress of 1589 MPa. Whereas an external applied stress of 2822 MPa is needed for the carbide to reach its critical stress of 1961 MPa.

Because the PCD/WC-Co system can be assumed to be perfectly brittle, the external applied stress that cause the weaker component to fail can be taken as the stress which causes composite failure, which should be considered the strength of the composite. A brittle composite is only as strong as its weakest component.

$$\sigma_u = \min\left(\frac{E}{E_f}\,\sigma_{uf}, \frac{E}{E_m}\,\sigma_{um}\right) \tag{5.17}$$

As measured in the experimental portion of this investigation, the diamond has a lower strength compared to WC-Co. This strength difference is exacerbated by the stress concentration in diamond due to its stiffness. Graphically, this is observed by noting that the steeper the solid line (i.e., stress concentration) the lower the applied stress necessary to cause component failure. This behavior is not typical of composites. Traditional composites have reinforcement phases that are stiffer *and* stronger than the matrix phase. The stress will concentrate in the reinforcement phase, as it does in this system, but unlike this system, the reinforcement phase is typically stronger so the composite is strengthened. In this system, the stiffness in diamond is predicted to caused that phase to fail earlier than if it was alone. Graphically, the difference in slopes has caused the short-dashed lines in Figure 5.8 to separate. In typical composites the difference in slopes would cause the short-dashed lines to converge. In effect, the stronger phase typically takes more of the load than the weaker phase. In the PCD/WC-Co system, the weaker phase is predicted to take more of the load.

Figure 5.8 is valid at 80v% PCD. Because E is a function of V_f, the amount of stress concentration and therefore the slope of the solid lines will change at different volume fractions. Figure 5.9 plots the applied stress at which the components reach their critical stresses as a function of volume fractions of the PCD. In Figure 5.9 the thick lines show the component's critical applied stress in the equal strain case, and the thin lines are for the equal stress case. Because there is no stress concentration in the equal stress case, the critical applied stress for each component is simply the component's strength.

There was a discussion in chapter 4 about the expectation that the strength of a composite would fall somewhere between the strengths of its components (see Figure 4.2). This expectation was based on the behavior of typical composites. Typical composites have stiffer reinforcement phases which are stronger than the matrix. In the PCD/WC-Co system the diamond phase is stiffer, but it is also weaker. This analytical model predicts that stresses will preferentially accumulate in the weaker component, causing it to fail at even lower applied stresses.

Comparison of Modeled Strengths and Measured Strength

The experimentally measured values of GDC flexural strength are compared in Figure 5.10 with the analytically predicted strengths. The model correctly predicts that the diamond phase will fail below the strength of either diamond or carbide. The strengths of the composites were experimentally measured less than the experimental

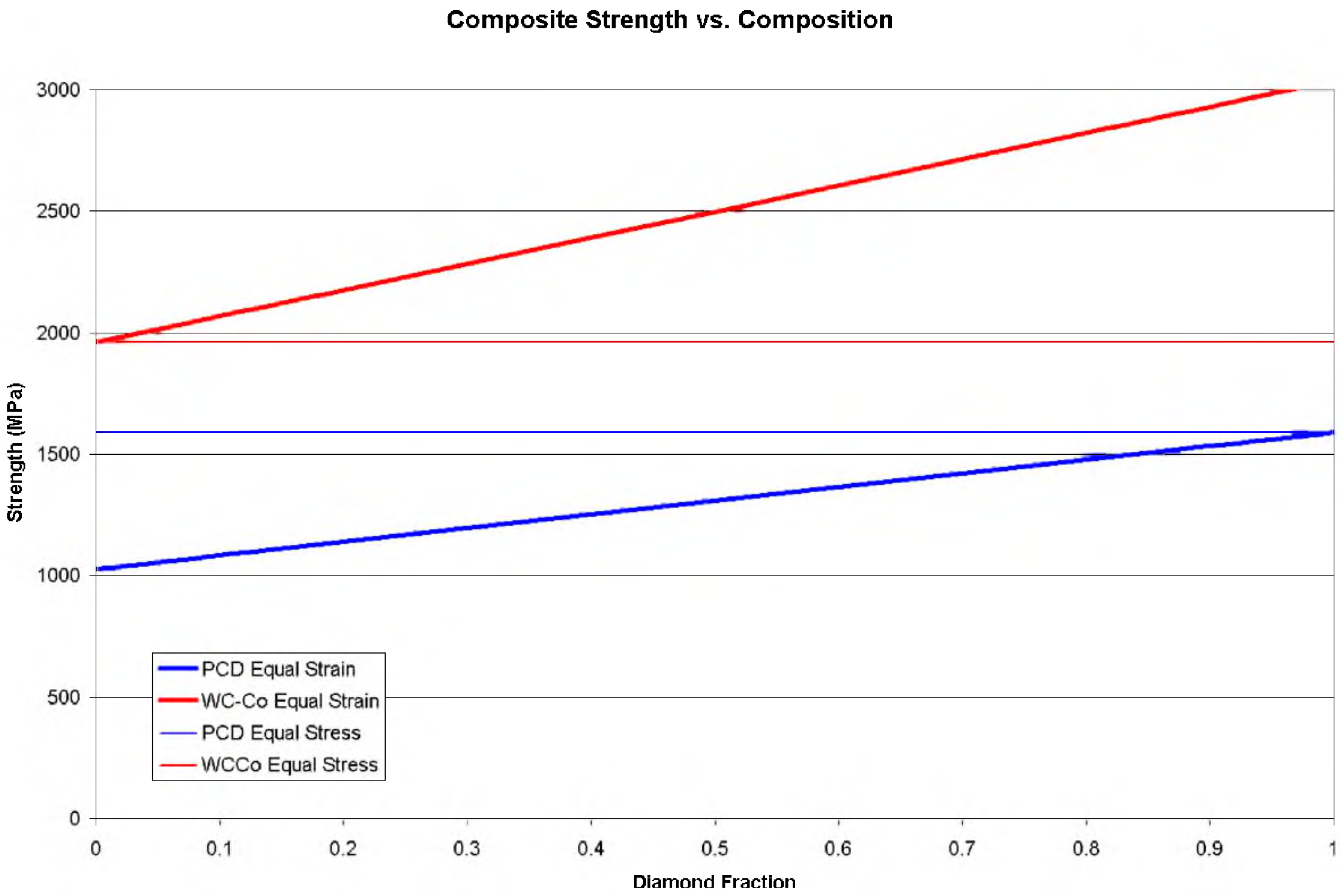

Figure 5.9. The external applied stresses to cause failure (strengths) are plotted for both PCD (blue) and WC-Co (red), in both equal strain and equal stress configurations.

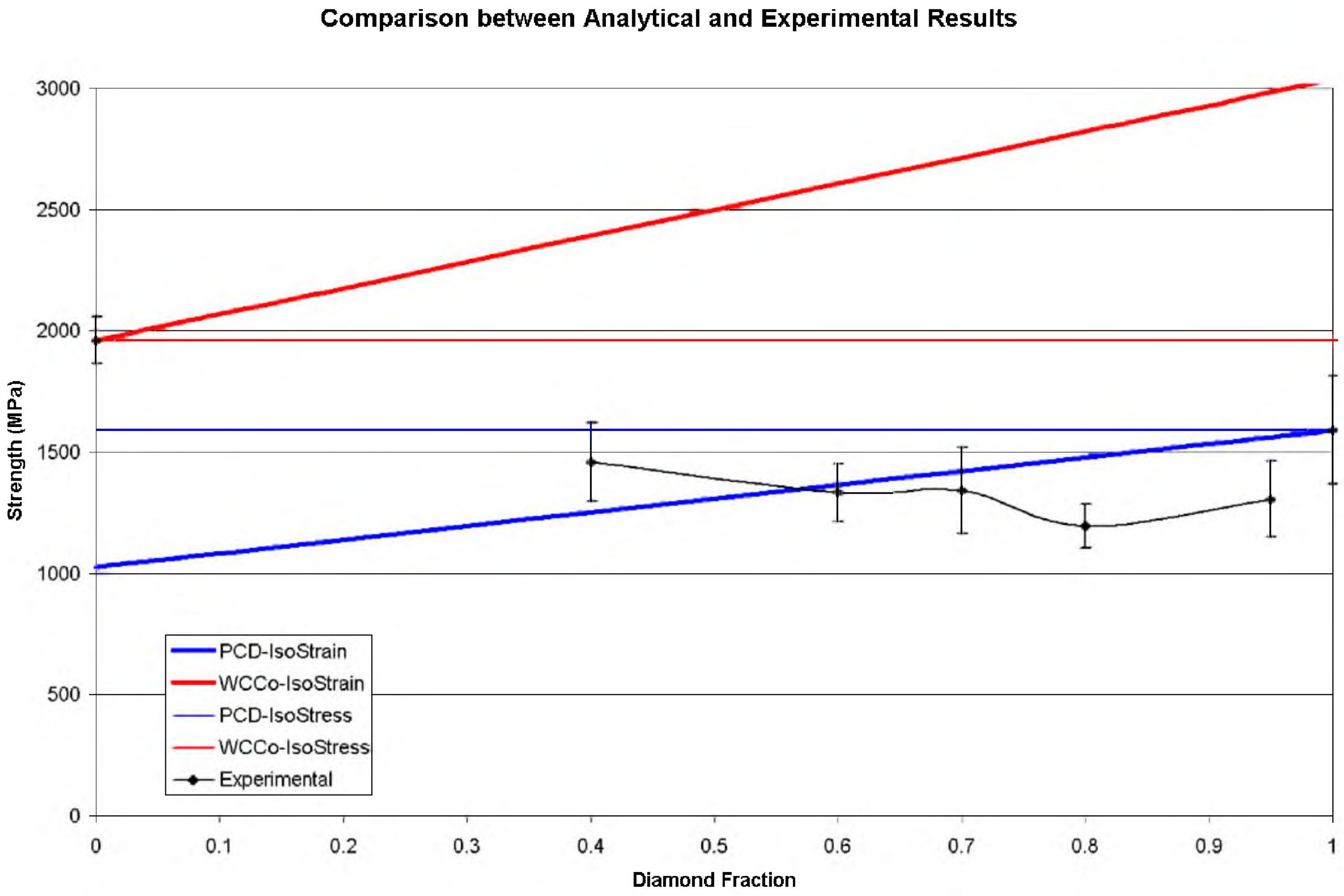

Figure 5.10. The composite strength, as predicted by the analytic model, is compared with the experimentally measured strength.

strengths of either component. The model predicts that the composite strength will increase with the addition of PCD until it reaches the flexural strength of an all PCD material. The experimental data shows the opposite trend. Composites with larger amounts of PCD generally had lower strengths.

Modeling of Residual Stresses

Residual stresses occur because of the differences in responses to environmental changes in materials that are bound together. When PCD is sintered in the presence of another phase, often in the role of a substrate, residual stresses will form as the material cools and is decompressed at the end of the sintering process. These residual stresses can be significant and will influence the behavior of the material.

Residual stresses strongly affect the strength of PCD composites and therefore are important to understand and control. The residual stresses in PCD composites, and any hot pressed composite, arise from the differences in expansivity of the constituents. The material will change size due to cooling (thermal contraction), as well as the release of pressure (dilatational expansion) after consolidation. Residual stresses arise when the materials are constrained from their desired dimensional change.

By analytically deriving equations for residual stresses and considering both temperature and pressure change, the importance of including the dilatational expansion in diamond materials can be readily shown. The results challenge assumptions that were made in the previous research into PCD material that pressures changes did not need to be considered.

The residual stresses are made up of two components, thermal residual stresses and dilatational residual stresses. Assuming that the materials behave linear-elasticly, the two components are independent of each other.

$$\sigma_{rc} = \sigma_{rTc} + \sigma_{rDc} \tag{5.18}$$

In addition to the material properties listed in Table 5.1, thermal material properties and sintering parameters need to be included to model the residual stresses that develop as the material exits sintering conditions. These parameters are listed in Table 5.2.

As discussed in Chapter 2, past researchers used 1000°C as the starting point for residual stress accumulation. It was rationalized that any stresses generated above 1000°C would be annealed due to the plastic nature of the materials above that temperature. It was assumed that diamond behaves linear-elastically below that temperature so all stresses generated below that temperature would be accumulated.

In most sintering cycles, included sintering conducted in this research effort, the pressure is reduced after the system temperature has been lowered close to room temperature. Therefore, the full difference in pressure is included in the modeling.

Thermal Residual Stresses

Thermal residual stresses arise when a phase is constrained so that it cannot fully expand or contract in response to a temperature change. In the Voigt model, the

Table 5.2

Thermal Component Properties and Process Parameters

Property	Value	Unit
$\boldsymbol{\alpha_f}$	1.75×10^{-6}	/°C
$\boldsymbol{\alpha_m}$	5.48×10^{-6}	/°C
$\boldsymbol{\Delta T}$	-973	°C
$\boldsymbol{\Delta p}$	5500	MPa

components are constrained by each other, and residual stresses will arise because each component will respond differently to a change in temperature. The change in length that a material undergoes in response to a change in temperature, ϵ_T, is related to the change in temperature, ΔT, and its coefficient of thermal expansion (CTE), α, as described in equation 5.19.

$$\epsilon_T = \alpha \Delta T \tag{5.19}$$

Equation 5.19 can be applied to the individual components of a composite, as well as to the composite assuming that α accurately describes the CTE of the composite.

Any residual stresses which arise in a component will also affect the strain in the component. Once again, the relationship is governed by Hooke's law (equation 5.9). Equation 5.20 is the thermal strain of a component due to a change in temperature.

$$\epsilon_{Tc} = \alpha \Delta T + \frac{\sigma_{rTcx} - \nu_c \sigma_{rTcy} - \nu_c \sigma_{rTcz}}{E_c} \tag{5.20}$$

Unlike applied stresses, temperature changes are non-directional; an isotropic material will tend to expand or contract uniformly in all directions. In the equal strain model, the residual stresses in both the axial and thickness directions are equivalent due to the symmetry of material constraint. And in the transverse direction there are no residual stresses because the material is not constrained in that direction. Equation 5.20 can therefore be simplified to equation 5.21.

$$\epsilon_{Tc} = \alpha_c \Delta T + \frac{(1-\nu_c)\sigma_{rTc}}{E_c} \tag{5.21}$$

To solve for the thermal residual stresses and strains in a component, two relationships will be exploited. First, the thermal residual strains in both components must be equal in the equal strain model (see equation 5.3).

$$\alpha_f \Delta T + \frac{(1-\nu_f)\sigma_{rTf}}{E_f} = \alpha_m \Delta T + \frac{(1-\nu_m)\sigma_{rTm}}{E_m} \tag{5.22}$$

Second, the thermal residual stresses must balance each other out. If there are any net residual stresses, composite wide, then the composite is not at equilibrium and will continue to change size until the component residual stresses balance and there are no longer any net residual stresses (see equation 5.4).

$$\sigma_{rT} = 0 = V_f \sigma_{rTf} + V_m \sigma_{rTm} \tag{5.23}$$

With the two equations 5.22 and 5.23, the two unknowns, σ_{rTf} and σ_{rTm}, can be solved.

$$\sigma_{rTf} = \frac{E_f E_m V_m \Delta T(\alpha_m - \alpha_f)}{V_m E_m (1-\nu_f) + E_f V_f (1-\nu_m)} \tag{5.24}$$

$$\sigma_{rTm} = \frac{E_m E_f V_f \Delta T(\alpha_f - \alpha_m)}{V_f E_f (1-\nu_m) + E_m V_m (1-\nu_f)} \tag{5.25}$$

Equations 5.24 and 5.25 are plotted in Figure 5.11 as a function of the diamond volume fraction using the parameters listed in Table 5.2.

Diamond has a much lower coefficient of thermal expansion, as compared to carbide. As the composite cools, the carbide phase will intrinsically contract more than the diamond phase. Being constrained to have the same dimensional change, the carbide will put the diamond into compression while it is forced into tension.

Similar to the stress intensification discussed in the last section (Figure 5.6), when a component dominates in a volume fraction, its stress is small relative to that of the minor constituent. In a composite with equal parts of both components, the thermal residual stresses are equal but opposite.

Having solved for the thermal residual stresses, it is possible to solve for the change in length in the composite (and therefore each component) using equation 5.21. Equation 5.21 is plotted in Figure 5.12 versus diamond volume fraction. Diamond has a much smaller CTE, therefore composites with more diamond will shrink less during the cooling portion of the sintering cycle.

Dilatational Residual Stresses

The diamond-carbide composite experiences a drastic change in pressure as it exits the high temperature/high pressure sintering cycle. Pressure is a particular type of stress and materials change dimensions in response to changes in stress (see equation 5.2). Stresses and strains due to changes in pressure will be referred to as dilatational stresses and dilatational strains. Due to the uniform application of pressure and the

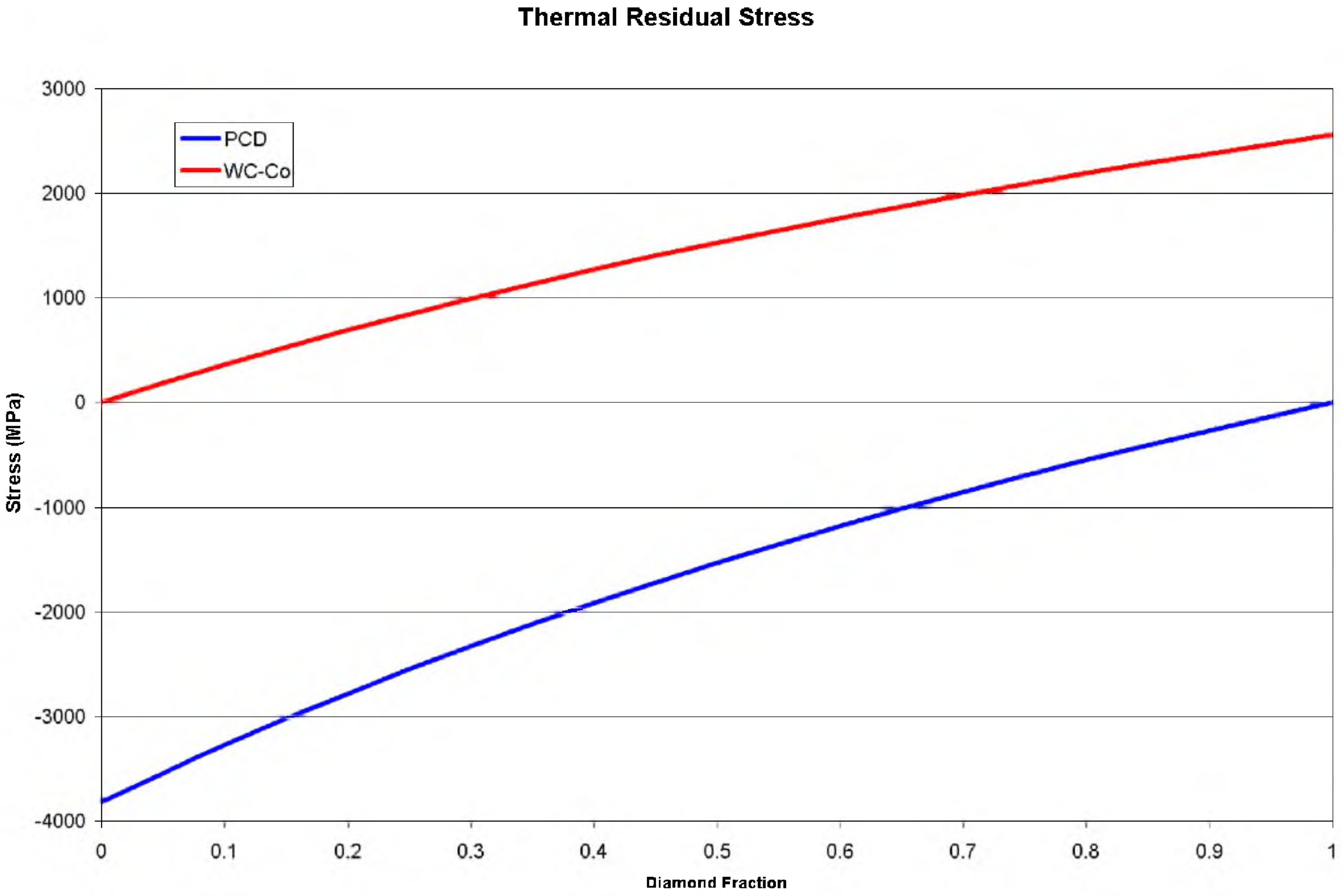

Figure 5.11. Estimated thermal residual stresses in the diamond (blue) and carbide (red) components.

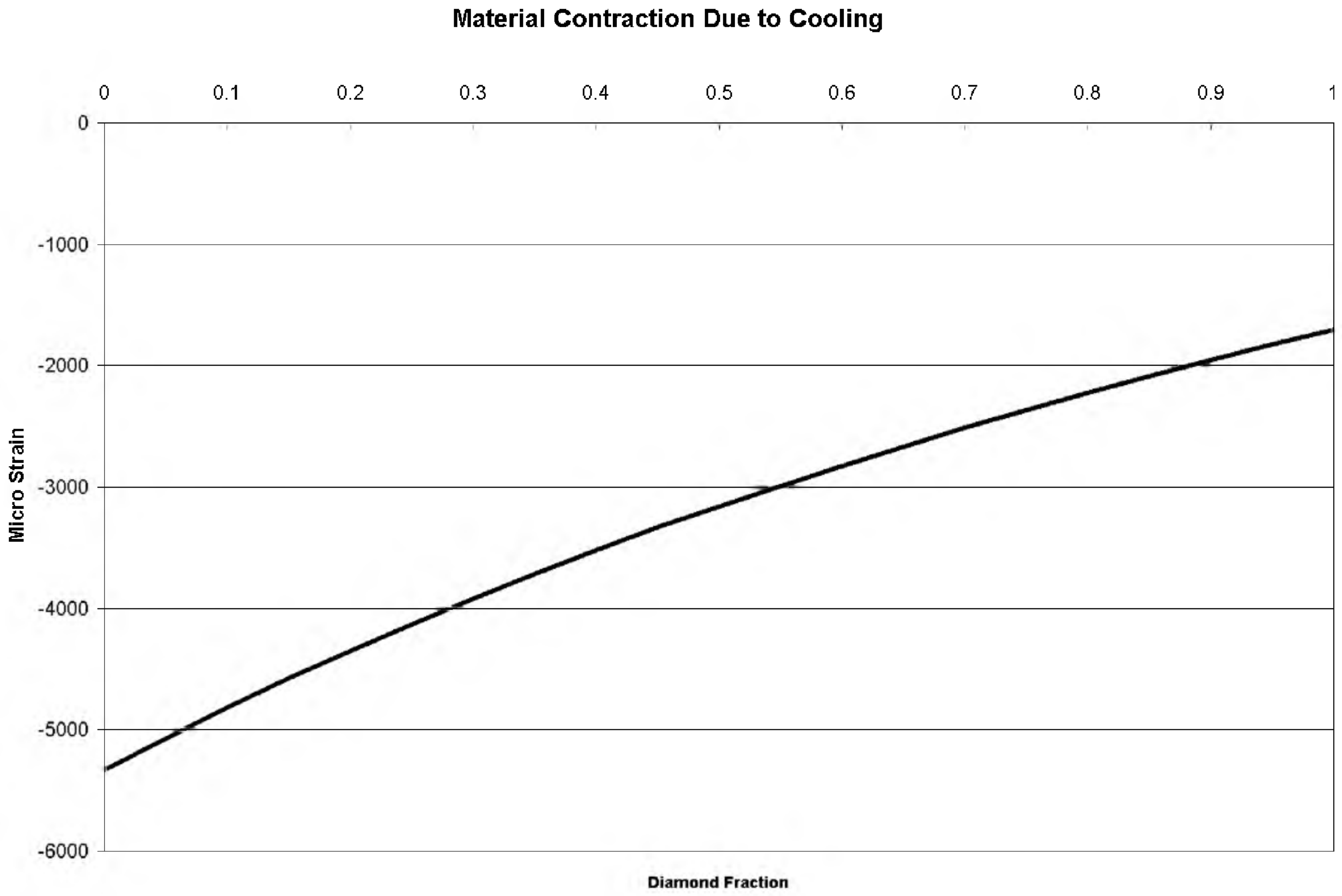

Figure 5.12. The change in dimensions parallel with the material interface of the composite, as a function of diamond volume fraction. The strain in both components is equal to the composite strain.

isotropy of the material, and independently due to the assumptions of the slab model, dilatational stresses are hydrostatic and do not produce any shear stresses or strains. Though the applied dilatational stress will sometimes be referred to as pressure, the standard stress sign conventions will be used; A reduction in pressure causes a reduction in compressive stress, which is a net positive change.

In this model, the composite is assumed to be residual stress free at the height of the sintering cycle. The stresses in the components are in equilibrium. It is often more useful to refer to stress relative to atmospheric pressure. Therefore, stresses relative to the high-pressure, stress-free state will be denoted with a prime, and will later be converted to stresses relative to atmospheric pressure which will not be marked with the prime symbol.

Analogous to the thermal strain in the last section, the dilatational strain is caused by the change in pressure and the dilatational residual stresses. From equation 5.2:

$$\epsilon_{Dc} = \frac{\sigma'_{Dcx} - \nu_c \sigma'_{Dcy} - \nu_c \sigma'_{Dcz}}{E_c} \tag{5.26}$$

The overall dilitational stress in a component is equal to the residual dilitational stress and the applied stress (pressure change).

$$\sigma'_{Dc} = \Delta p + \sigma'_{rDc} \tag{5.27}$$

Again, the stress in the axial and thickness directions are equivalent. There are no residual stresses in the transverse direction, but there is still the change in stress due to the pressure change.

$$\epsilon_{Dc} = \frac{(1-\nu_c)\sigma'_{Dc} - \nu_c \Delta p}{E_c} \tag{5.28}$$

The solution to the dilatational residual stresses follows the same pattern used to solve for thermal residual stresses. The residual strain in each component must be equal (see equation 5.3).

$$\frac{(1-\nu_f)\sigma'_{Df} - \nu_f \Delta p}{E_f} = \frac{(1-\nu_m)\sigma'_{Dm} - \nu_m \Delta p}{E_m} \tag{5.29}$$

The volume weighted component stresses must still balance (equation 5.4), but in the dilatational case they must also balance against the pressure change.

$$\sigma'_D = \Delta p = V_f \sigma'_{Df} + V_m \sigma'_{Dm} \tag{5.30}$$

With the two equations, the two unknowns can be solved.

$$\sigma'_{Df} = \frac{E_f(1-\nu_m) + V_m E_m \nu_f - V_m E_f \nu_m}{V_f E_f(1-\nu_m) + V_m E_m(1-\nu_f)} \Delta p \tag{5.31}$$

$$\sigma'_{Dm} = \frac{E_m(1-\nu_f) + V_f E_f \nu_m - V_f E_m \nu_f}{V_m E_m(1-\nu_f) + V_f E_f(1-\nu_m)} \Delta p \tag{5.32}$$

Equation 5.33 is used to convert the stresses related to sintering conditions to the residual stresses related to atmospheric conditions.

$$\sigma_{rDc} = \sigma'_{Dc} - \Delta p \tag{5.33}$$

The resulting dilatational residual stress equations, related to atmospheric conditions, are:

$$\sigma_{rDf} = \frac{E_f(1-\nu_m)+V_mE_m\nu_f-V_mE_f\nu_m}{V_fE_f(1-\nu_m)+V_mE_m(1-\nu_f)}\Delta p - \Delta p \tag{5.34}$$

$$\sigma_{rDm} = \frac{E_m(1-\nu_f)+V_fE_f\nu_m-V_fE_m\nu_f}{V_mE_m(1-\nu_f)+V_fE_f(1-\nu_m)}\Delta p - \Delta p \tag{5.35}$$

Equations 5.34 and 5.35 are plotted in Figure 5.13 as functions of diamond volume fraction.

Diamond has a considerably larger bulk modulus than carbide. As the pressure is released at the end of the sintering cycle, the diamond phase will intrinsically dilatate less than the carbide phase. This difference in dilatation adds tensile residual stresses to the diamond phase and compressive stresses to the carbide phase. Because these stresses are opposite to the effects of cooling temperatures, the reduction in pressure counteracts the effects of the reduction in temperature (see Figure 5.11).

Figure 5.14 plots the strain due to the change in pressure versus the volume fraction of diamond. The slope and magnitude of the dilatational strain is opposite of the

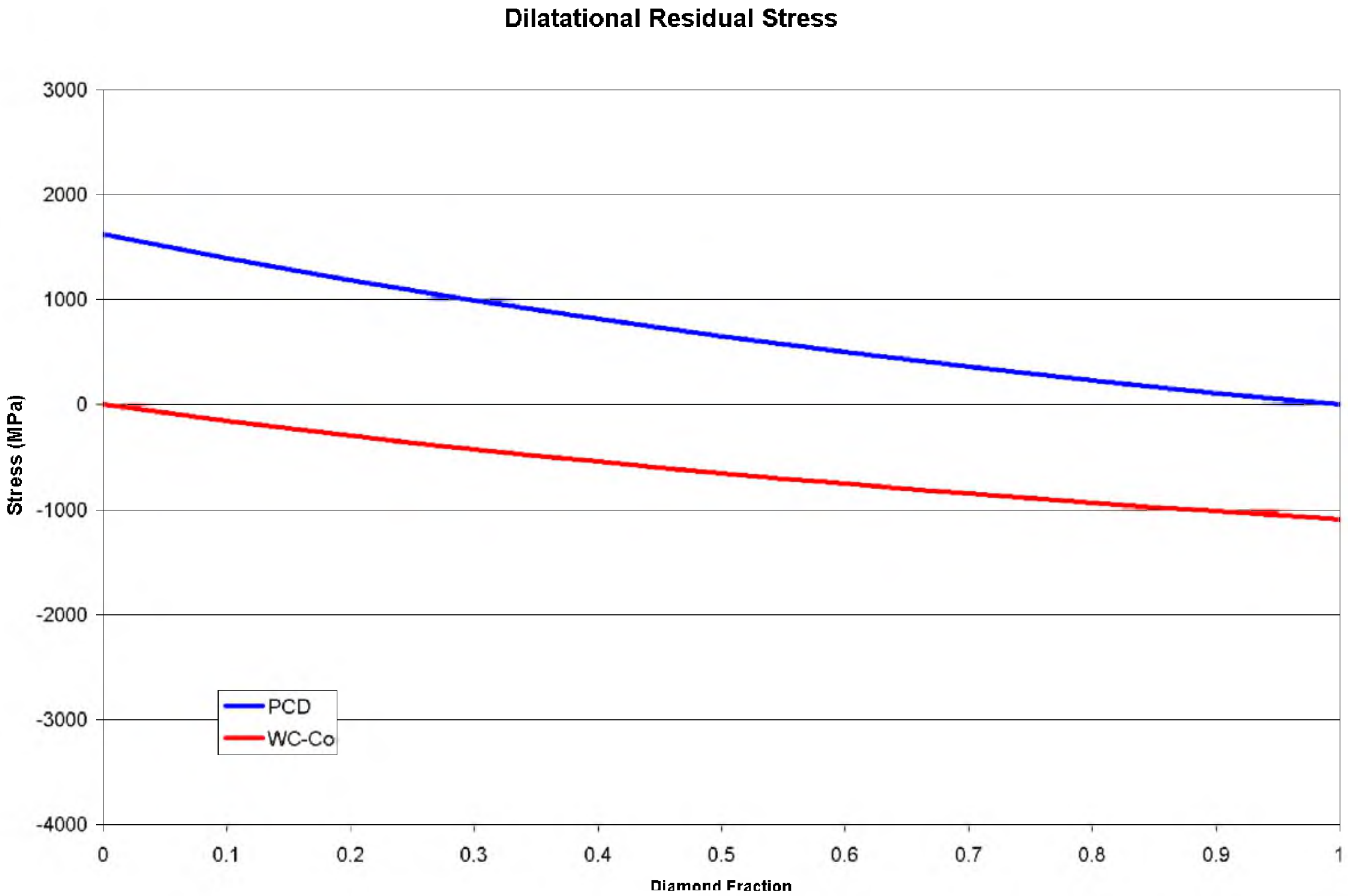

Figure 5.13. Estimated dilatational residual stresses in the diamond (blue) and carbide (red) components.

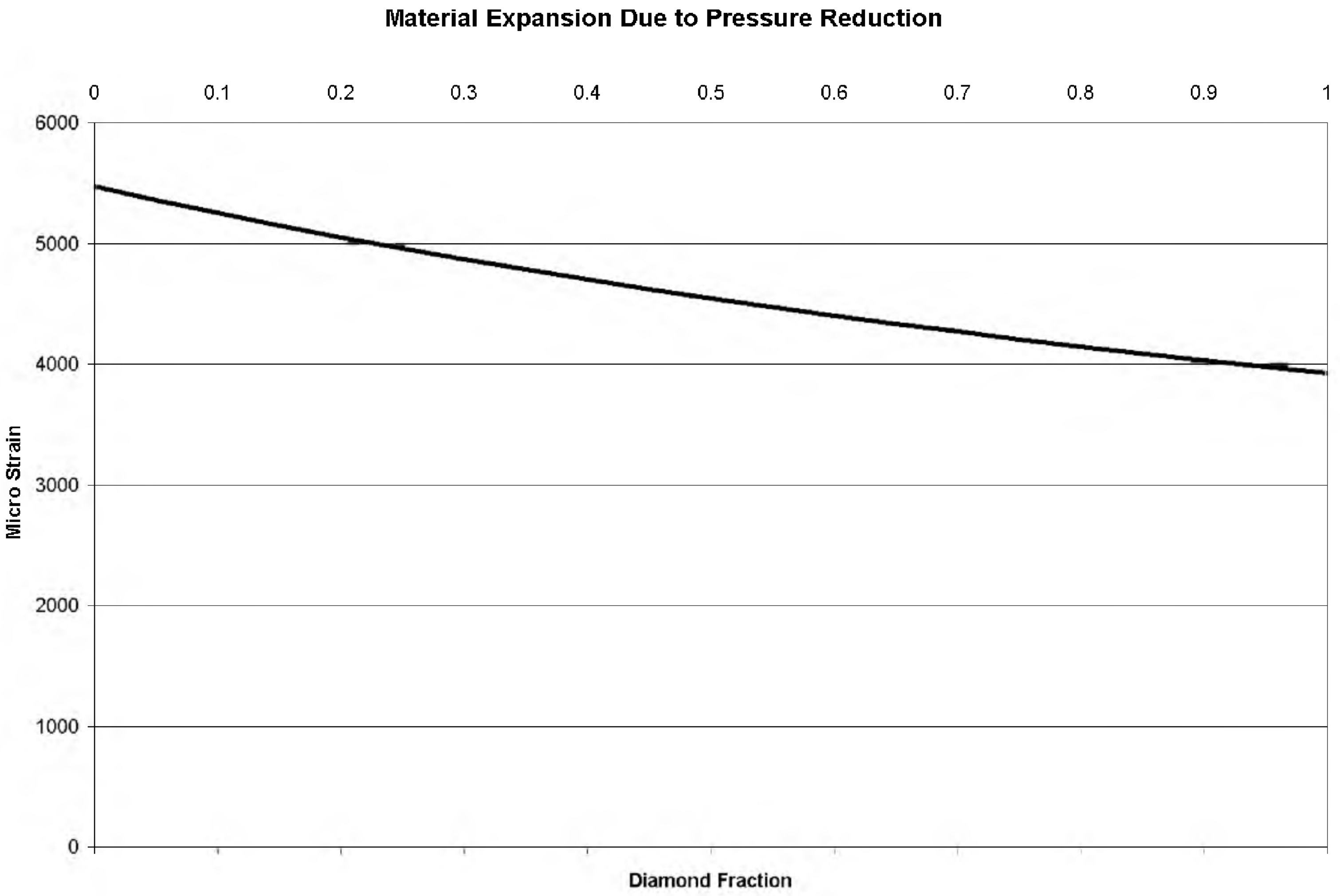

Figure 5.14. Material dilatation due to the reduction in pressure, as a function of the volume fraction of diamond in the composite. In the equal strain model (not shown), both components experience the same strain as the composite.

thermal strain (see Figure 5.12).

Total Residual Stresses

The overall residual stresses in the components after the sintering cycle is a linear combination of the thermal and the dilational residual stresses (see equation 5.18). Equation 5.36 is the summation of equations 5.24 and 5.34, and equation 5.37 is the summation of equation 5.25 and equation 5.35.

$$\sigma_{rf} = \frac{E_f E_m V_m \Delta T(\alpha_m - \alpha_f)}{V_m E_m(1-\nu_f) + E_f V_f(1-\nu_m)} + \frac{E_f(1-\nu_m) + V_m E_m \nu_f - V_m E_f \nu_m}{V_f E_f(1-\nu_m) + V_m E_m(1-\nu_f)} \Delta p - \Delta p \tag{5.36}$$

$$\sigma_{rm} = \frac{E_m E_f V_f \Delta T(\alpha_f - \alpha_m)}{V_f E_f(1-\nu_m) + E_m V_m(1-\nu_f)} + \frac{E_m(1-\nu_f) + V_f E_f \nu_m - V_f E_m \nu_f}{V_m E_m(1-\nu_f) + V_f E_f(1-\nu_m)} \Delta p - \Delta p \tag{5.37}$$

These equations are plotted on Figure 5.15.

Because the thermal residual stresses are dominant, the total residual stress graph has the same form as the thermal residual stress graph (see Figure 5.11). The diamond phase is pushed into an overall compressive state and the carbide is in a tensile state. The larger the diamond fraction, the less the compressive residual stresses in the diamond. And likewise, the greater the carbide fraction, the smaller the tensile stresses in the carbide.

The compressive residual stresses in the diamond will increase the externally applied stress at which the diamond phase will fail. Conversely, the tensile residual stresses in the carbide phase will reduce its flexural strength.

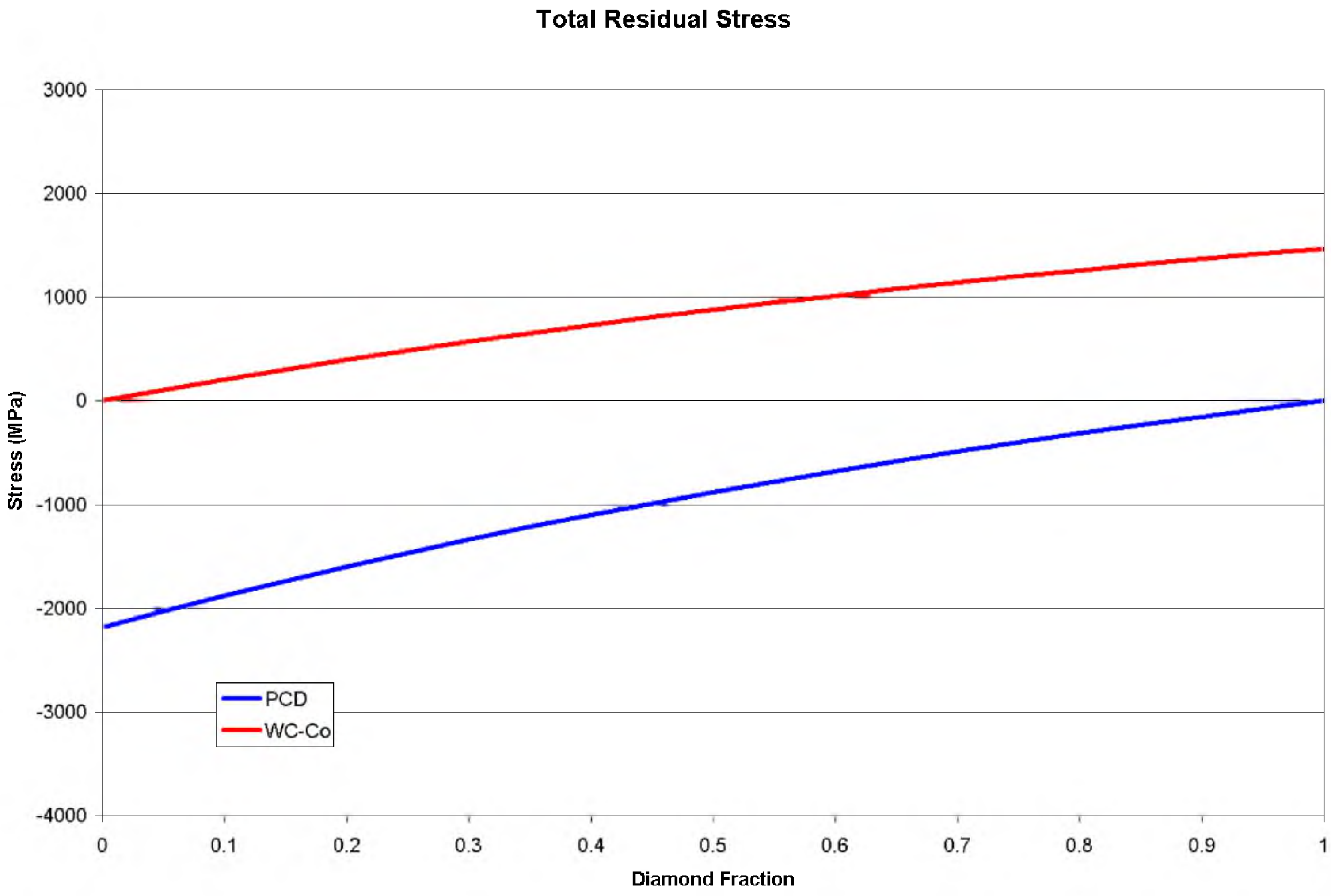

Figure 5.15. Estimated total residual stresses in the diamond (blue) and carbide (red) components.

Figures 5.16 and 5.17 plot the two halfs of equations 5.36 and 5.37 respectively and illustrate how the thermal and dilatational residual stresses interact in the diamond and carbide phases. The thermal residual stresses dominate the total residual stresses in each component.

Figure 5.18 plots the overall strain of the composite (which is also the strain of either component, see equation 5.3), and the thermal and dilatational components of the total strain. The thermal strain is calculated using equation 5.21 and the dilatational strain is calculated using equation 5.28.

Compared to carbide, diamond has a smaller CTE and bulk modulus. Intrinsically diamond has smaller dimensional changes to either temperature changes or pressure changes. But the black line in Figure 5.18 indicates that diamond rich composites have a larger overall strain than carbide rich composites. This is because the changes are better balanced and offset each other despite the fact that carbide has larger dimensional changes (note the green and orange lines).

Figures 5.16 and 5.17 illustrate the dominance of the temperature effect on residual stresses. On the other hand, Figure 5.18 indicates that the effect of pressure dominates the dimension change. This is because the strain is a function of the volume weighted *average* of the expansion coefficients whereas the residual stresses are controlled by the *difference* between the expansion coefficients.

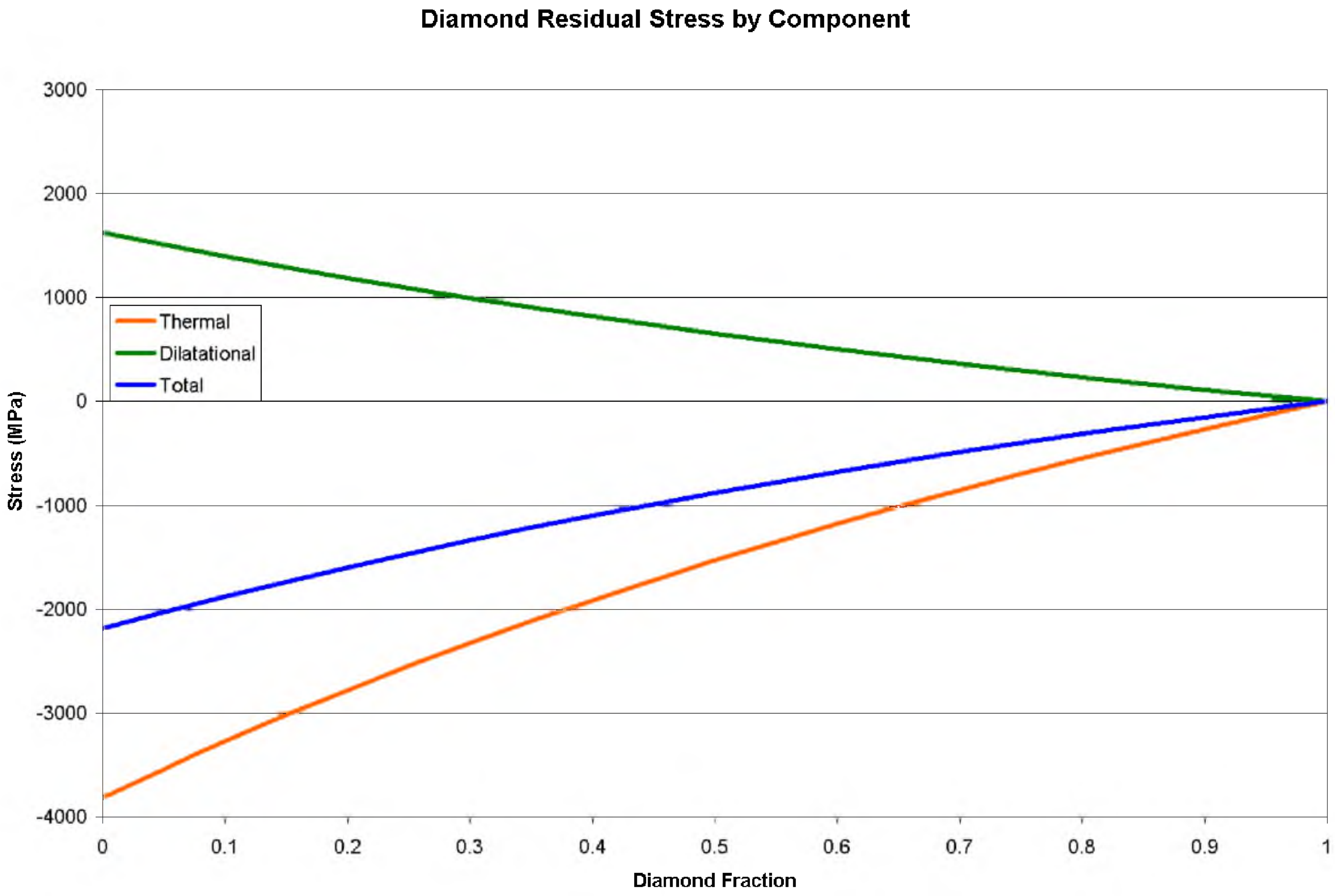

Figure 5.16. Thermal, dilatational, and total residual stress estimates in the diamond phase as a function of diamond volume fraction. The tensile dilatational residual stresses mitigate but do not completely offset the compressive thermal residual stresses.

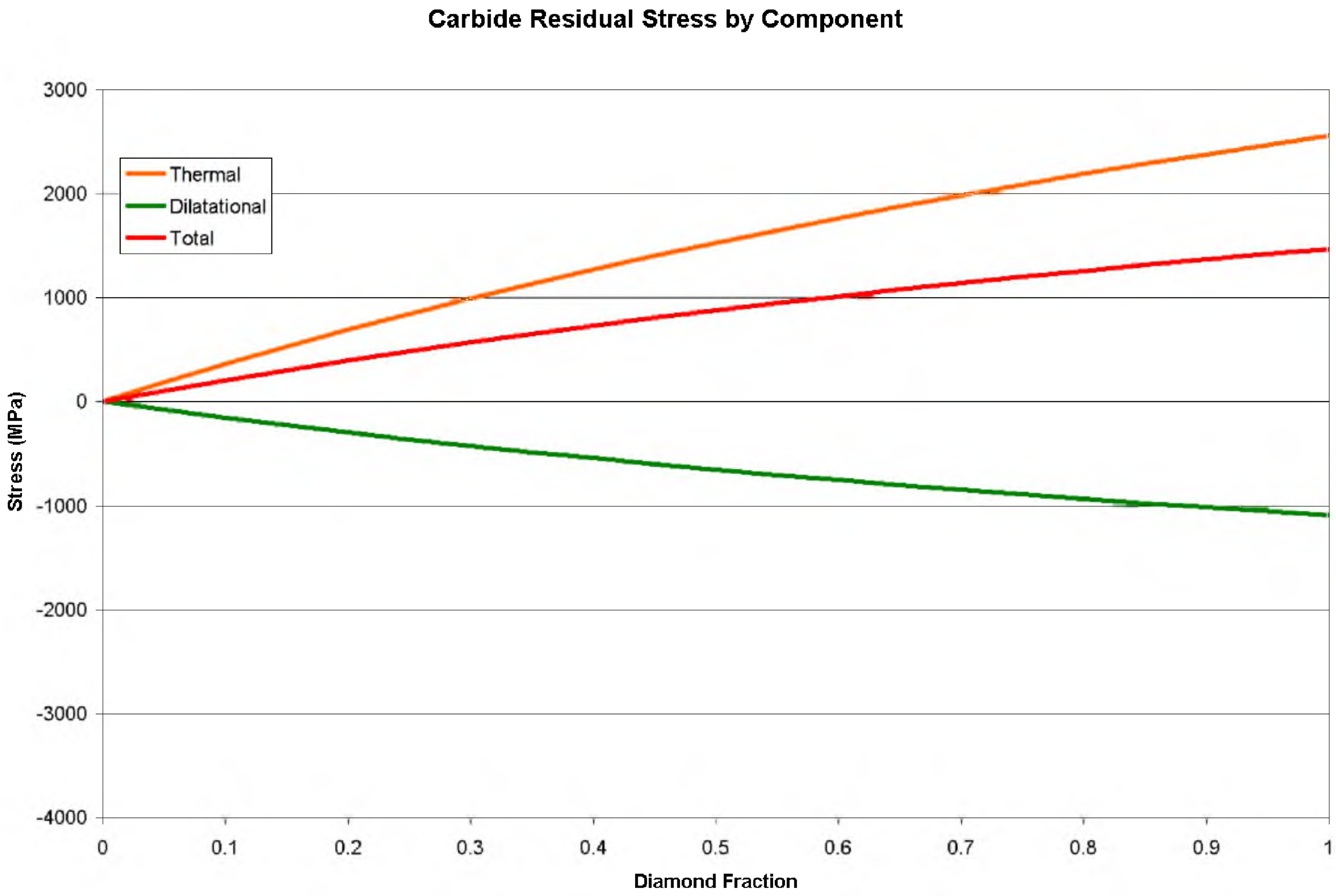

Figure 5.17. Thermal, dilatational, and total residual stress estimates in the carbide phase as a function of diamond volume fraction. The residual stresses in the carbide phase must offset the diamond residual stresses.

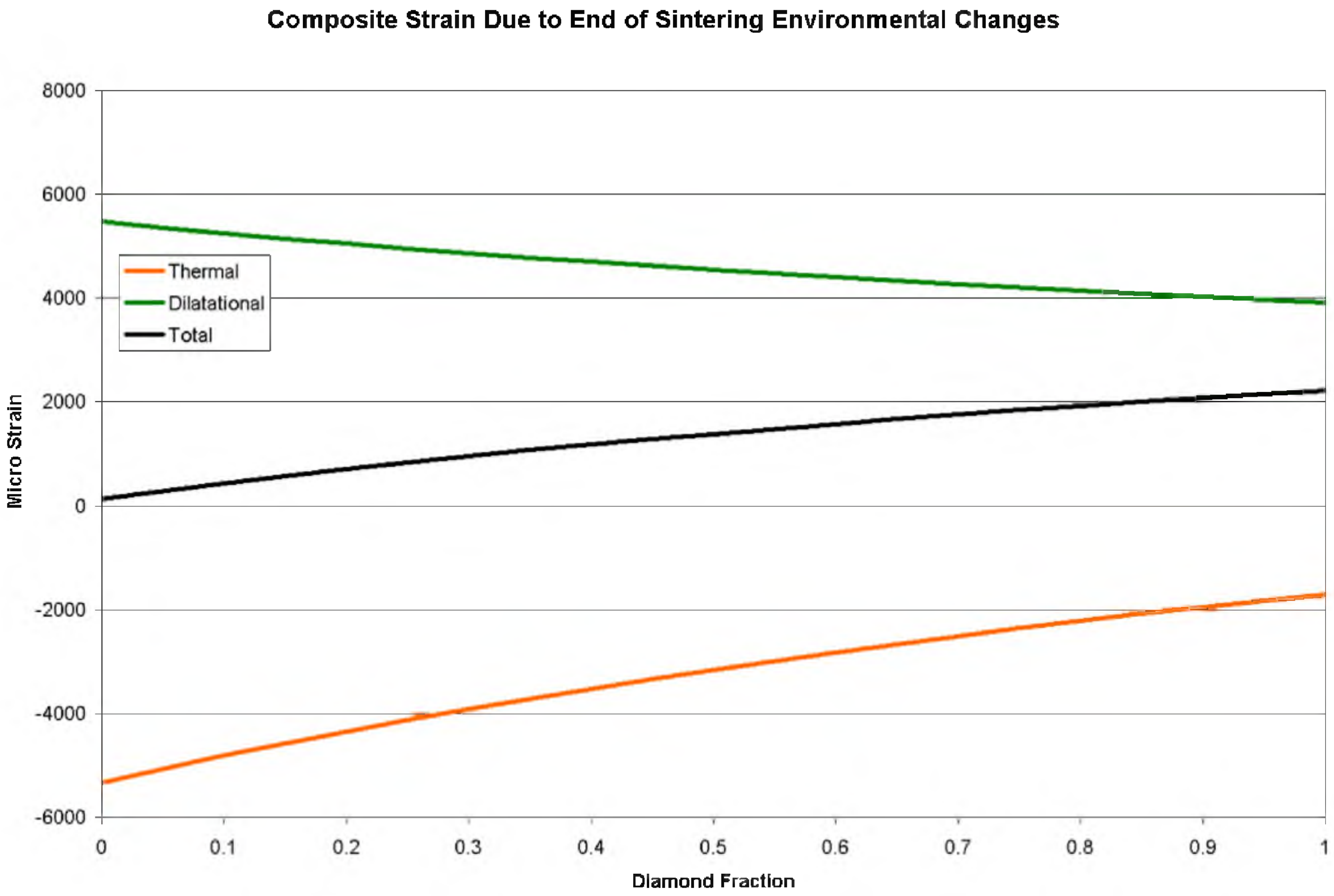

Figure 5.18. Thermal, dilatational, and total strain in both the components and the overall composite due to the reduction of pressure and temperature at the end of the sintering cycle.

Analytical Estimation of the Dilatational Effect on Residual Stresses

With a working model of the residual stresses due to both temperature and pressure changes it is possible to quantify the importance of including dilatational residual stresses in the model. Table 5.3 compares the residual stresses and strain of a 80v% diamond composite using the material properties from Table 5.2.

With errors of 78% and -216%, the effect of dilatation due to pressure change should not be neglected when calculating the residual stresses and overall strain associated with PCD and WC-Co sintered composites. In other types of hot pressing technologies the dilatational effect would be much less, because the pressures are usually less than 1/20 of HTHP pressures, while the temperatures are roughly equivalent. Therefore, it may be appropriate to neglect dilatation in those cases.

As it was noted in the previous subsection, the effect of pressure only partly offsets the effect of temperature on residual stresses but it reverses temperature's effect on the overall strain.

Using the idealized equal stress and equal strain models, equations were derived to estimate the residual stresses arising from both temperature and pressure changes that occur at the end of the HTHP sintering cycle. These estimates will be used to refine the model of flexural strength of the composites.

Modeling of Strength

Thermal and dilatational residual stresses were modeled in the previous section. In the section before that, the intensification of stress in the stiffer component was

Table 5.3

Impact of Neglecting Pressure Changes on Residual Stress and Strain

Model	Residual Stress		Micro Strain
	Diamond	Carbide	Composite
Temperature Only	-548	2192	-2224
Temperature and Pressure	-315	1258	1922
Temperature Only Error	78%	78%	-216%

Based on 80v% Diamond.

modeled, along with its effect on the overall flexural strength of the composite. In this section the two models will be combined to estimate the flexural strength of the composite when accounting for residual stresses.

The strength of the composite, σ_u, is the lesser of the applied stresses that will cause the components to fail.

$$\sigma_u = min(\sigma_{auf}, \sigma_{aum}) \tag{5.38}$$

The external applied stress that will cause a component to fail is equal to the strength of the component, reduced by the residual stresses in the component, multiplied by the stress intensification factor.

$$\sigma_{auc} = \frac{E}{E_c}\left(\sigma_{uc} - \sigma_{rc}\right) \tag{5.39}$$

These equations are illustrated in Figures 5.19 and 5.20 at different diamond fractions.

The solid lines in Figures 5.19 and 5.20 have the form $y = mx + b$ The variable y is the stress in the component, x is the stress applied to the composite, m is the stress concentration factor, $\frac{E_c}{E}$, and b is the residual stress in the component.

Compare Figure 5.20 to Figure 5.8, which does not take residual stresses into account. The stress intensification in diamond still causes the slope of the stress correlation line to be steeper for diamond than for carbide, but because the carbide begins

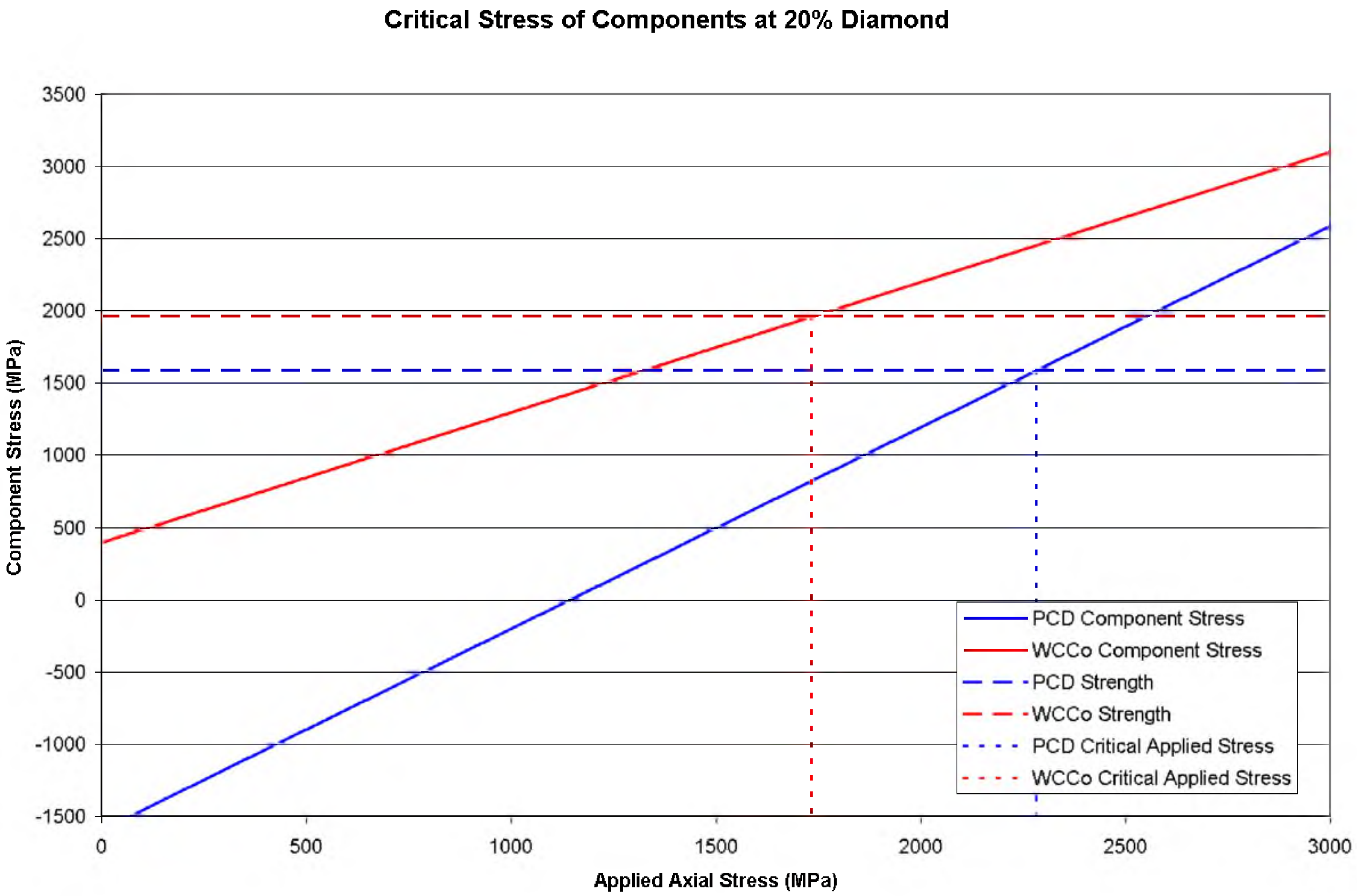

Figure 5.19. Relationship between applied composite stresses and the stresses experienced by each component in a 20v% diamond composite. Stress intensification factors, as well as residual stresses, are taken into account.

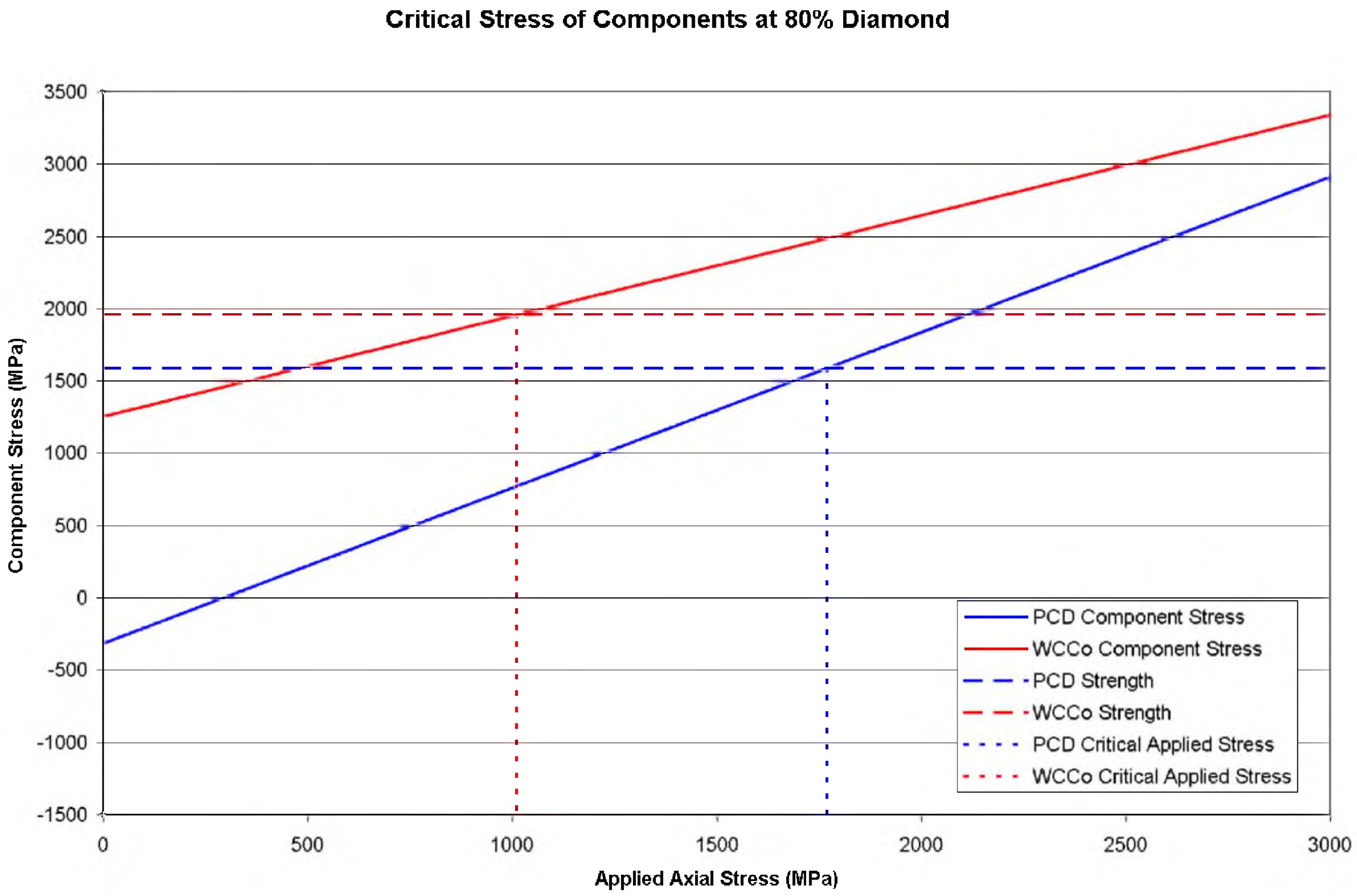

Figure 5.20. Relationship between applied composite stress and the stress experienced by each component in an 80v% diamond composite. The flexural strength of the composite is the lesser of the applied stresses that cause component failure.

in tension due to the residual stresses, carbide has become the first component to fail, despite having the larger intrinsic strength.

Composites with a smaller fraction of diamond have greater stress intensification in the diamond, but the diamond phase also begins with a larger amount of compressive residual stress which has to be overcome before the diamond component will fail. Conversely, only a small fraction of the applied stresses will accumulate in the carbide, but because the carbide begins with so much tensile stress, it is still predicted to fail first.

After all the discussion regarding the implications of the stiffer phase being the weaker phase, the residual stresses in this system are such that the stronger, more compliant phase is predicted to fail before the weaker and stiffer phase.

The applied stresses to cause component failure (see equation 5.39) are plotted in Figure 5.21 as a function of diamond fraction, along with the experimental results.

Considering the uncertainty of the input parameters, the fit between the experimental and analytical results is surprisingly good. This is especially true because of the sensitivity of the results to small changes to the system, as will be discussed in the next section.

While it was unexpected that the model prediction that WC-Co would be the component to fail first, the slope and position of the experimental data points can only be explained by this fact. Assuming the experimental data, including the end points, are accurate reflections of the intrinsic properties of the composite, and not adversely affected by improper processing, the only way to explain the experimental data is for WC-Co to be the phase to fail. If the PCD strength slope matches the slope of the data

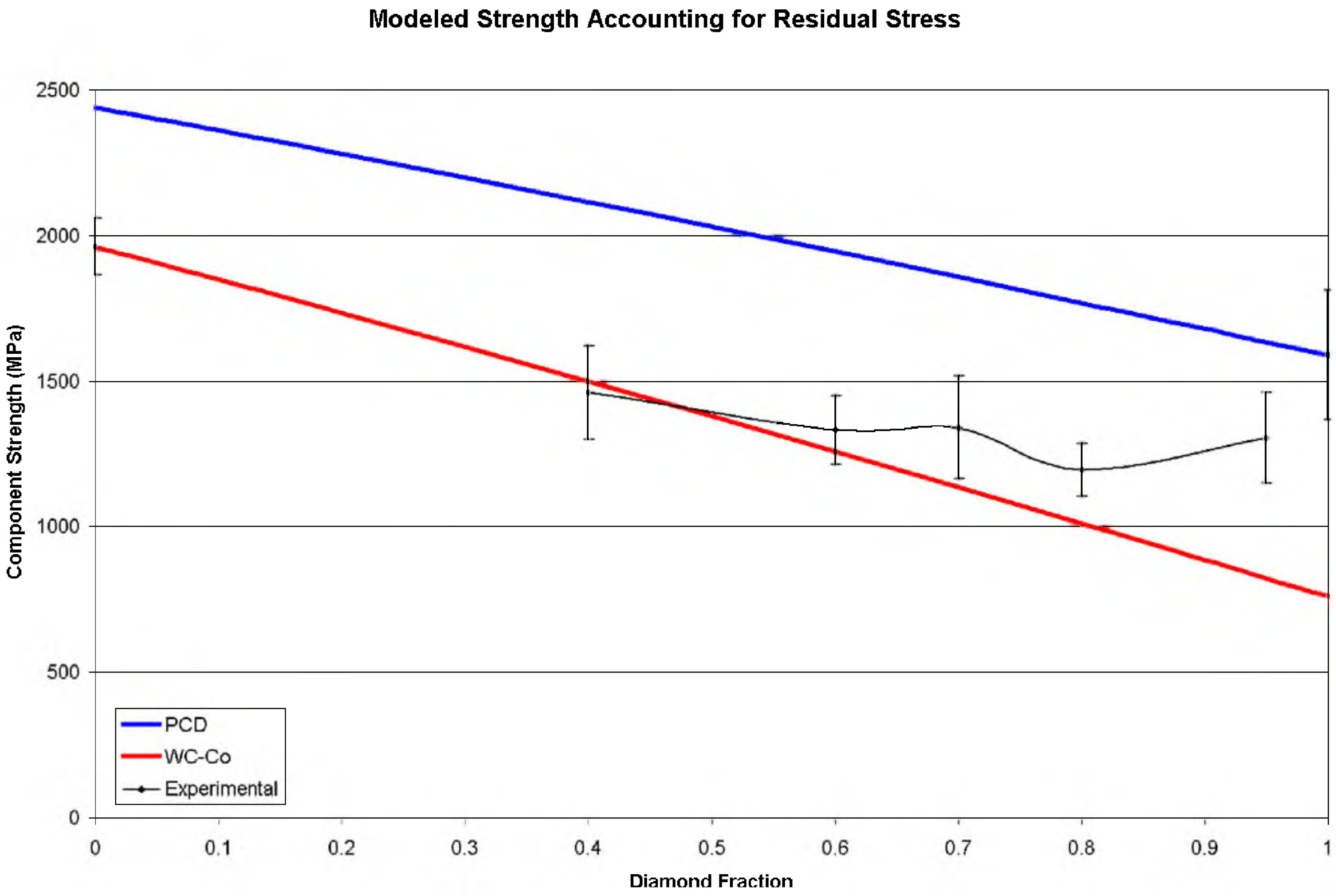

Figure 5.21. Modeled flexural strength of GDC as a function of diamond fraction, accounting for both thermal and dilatational residual stresses. The composite will fail at the lower of the component stresses. There is good correlation between the experimentally measured flexural strengths and the model.

then the strength would be too high. If the predicted strength of PCD is near the measured values then the slope would be in the wrong direction (see Figure 5.10).

The flexural strength of 95v% diamond appears to be an outlier as it doesn't follow the trend of decreasing strength with increasing diamond fraction. It is possible that at this low carbide concentration, the carbide phase is found in isolated pools rather than an interconnected network. If this is the case, the slab model would poorly approximate the pools of carbide which would be shielded from the applied stresses by the surrounding diamond material.

Impact of Neglecting Pressure Changes

At the end of the last section, the impact of neglecting pressure changes on residual stresses was evaluated. Figure 5.22 illustrates the impact of neglecting dilatational residual stresses on the flexural strength predictions.

The reduction of pressure at the end of the sintering cycle reverses some of the impact of the thermal residual stresses. Without this correction, the calculated tensile residual stresses in the carbide phase are too high, and the model will predict the premature failure of the composite. Table 5.4 tabulates the penalty for neglecting dilatational residual stresses as a function of volume percent diamond.

Parameter Sensitivity

There are several input variables which affect the estimated flexural strength of GDC materials, including material properties such as Young's modulus, Poisson's ratio,

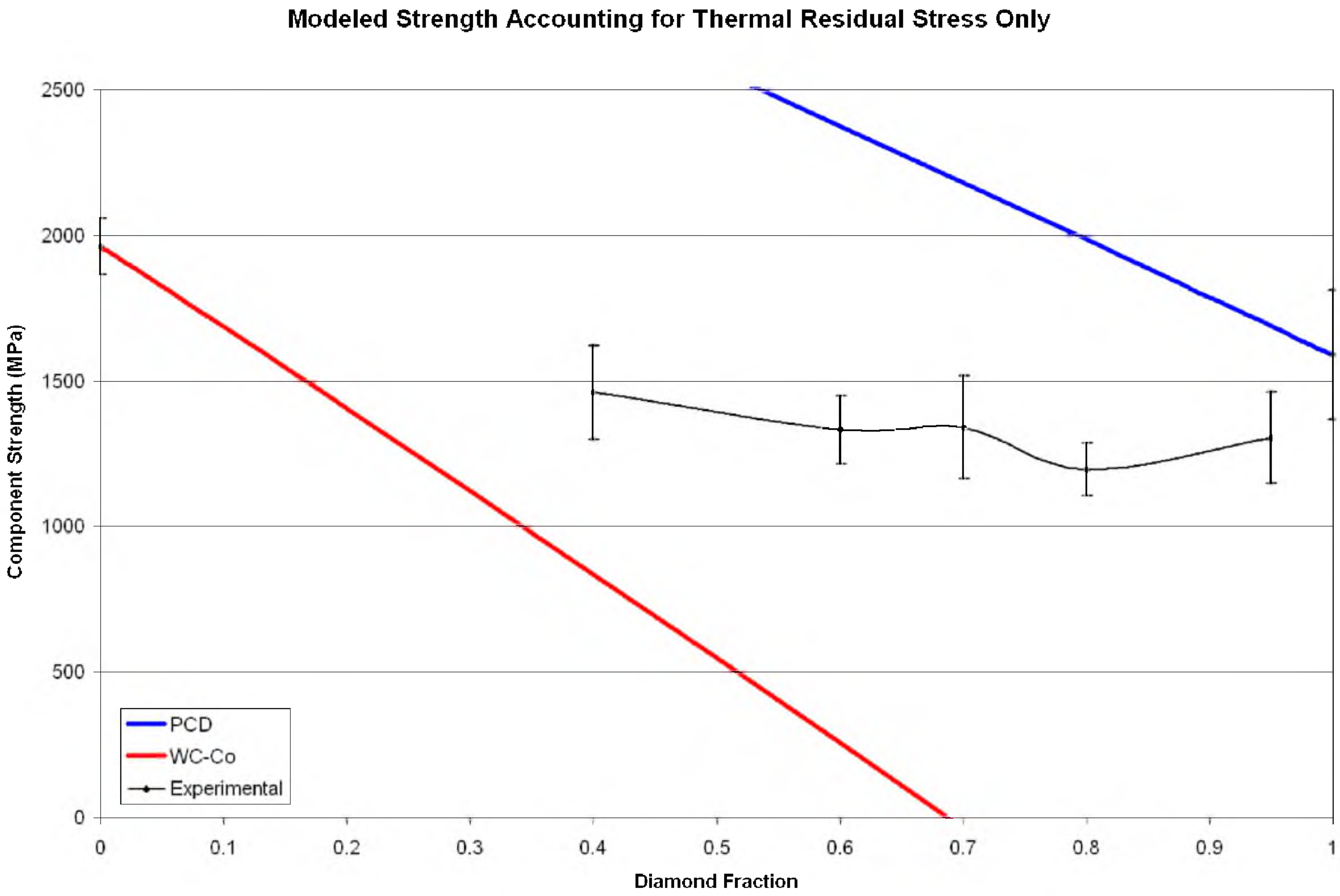

Figure 5.22. Flexural strength prediction of GDC materials of varying diamond fraction considering only thermal residual stresses. The strength of the carbide is underestimated due to an overestimate of residual tensile stresses in the phase.

Table 5.4

Impact of Neglecting Dilatational Residual Stresses on Strength

Volume Percent Diamond	0%	10%	20%	30%	40%	50%	60%	70%	80%	90%	100%
Strength (MPa) Accounting for Dilatation	1961	1848	1734	1617	1498	1378	1257	1135	1011	887	762
Strength (MPa) Neglecting for Dilatation	1961	1685	1405	1122	836	547	256	-37	-332	-629	-927
Error	0%	-9%	-19%	-31%	-44%	-60%	-80%	-103%	-133%	-171%	-222%

thermal expansion coefficient, and strength, and process parameters including pressure and temperature changes.

Figures 5.23 through 5.31 demonstrate the sensitivity of the flexural strength predictions to magnitude changes of +/- 5% for these parameters.

The overall calculated strength of the composite is very sensitive to changes in material properties and process parameters. This is particularly important because of the uncertainty in many of the input parameters used in this model. Some of the parameters were taken from literature, but the origin and accuracy is suspect. Additionally, different grades of carbide and diamond will have different properties. These material properties are difficult to measure, particularly across the range of conditions that are included in the model. The change in temperature and pressure, and the elastic contributions to the stresses are particularly difficult to assess. Any of these limitations have the potential to greatly affect the accuracy of the model.

Finally the analytical model is based on the idealized equal strain model, which does not closely approximate the actual structure of the test specimens. Numerical modeling will be used in the next chapter to more closely simulate the mesostructure of GDC materials.

Chapter Summary

In this chapter an analytical model was developed to estimate the flexural strength of granular diamond composites. The slab model that was selected does not closely approximate the complex spatial structure of the material, but is simple enough to make

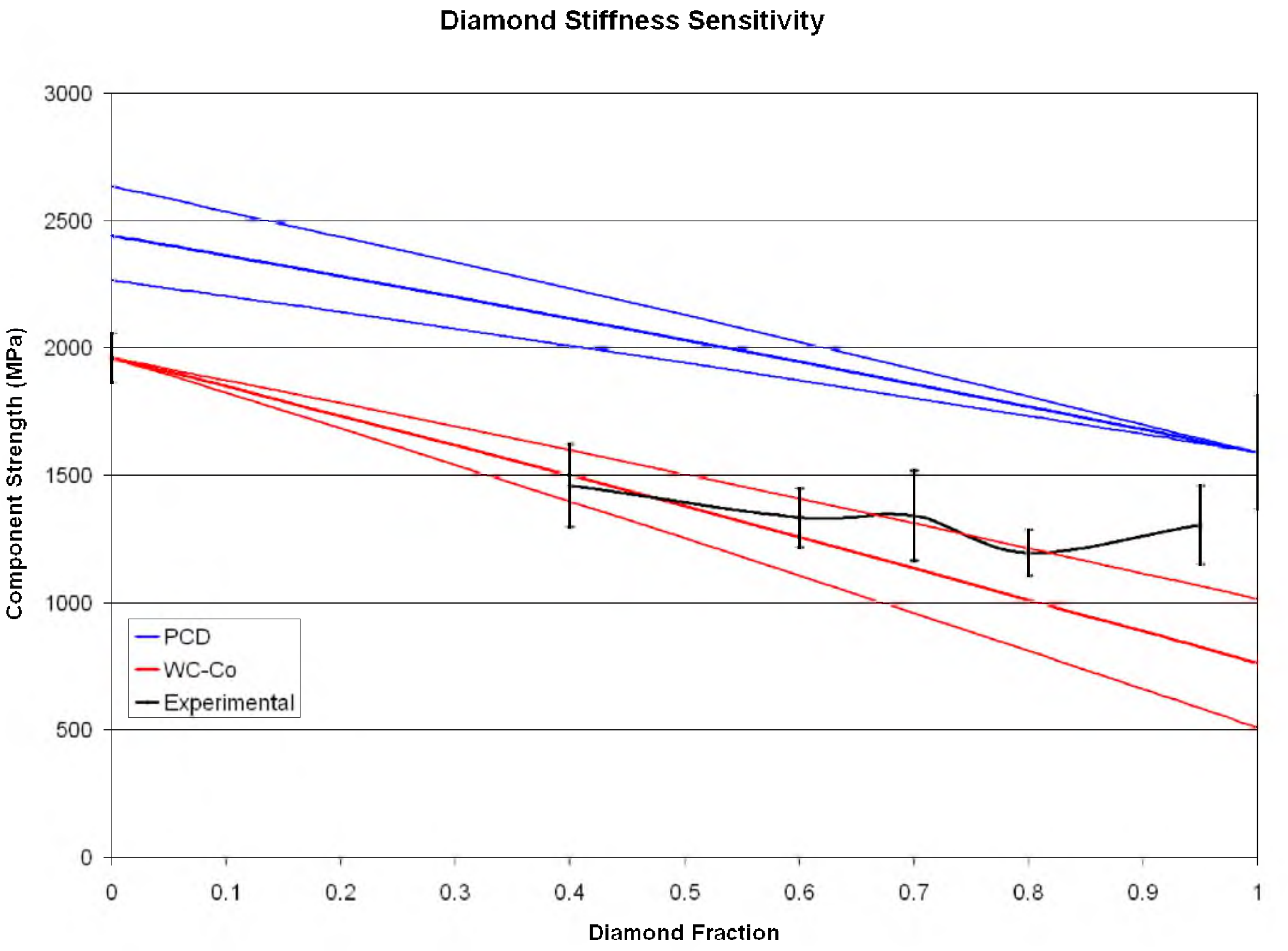

Figure 5.23. Variation of predicted component strengths due to a +/- %5 change in the value of Young's modulus of PCD.

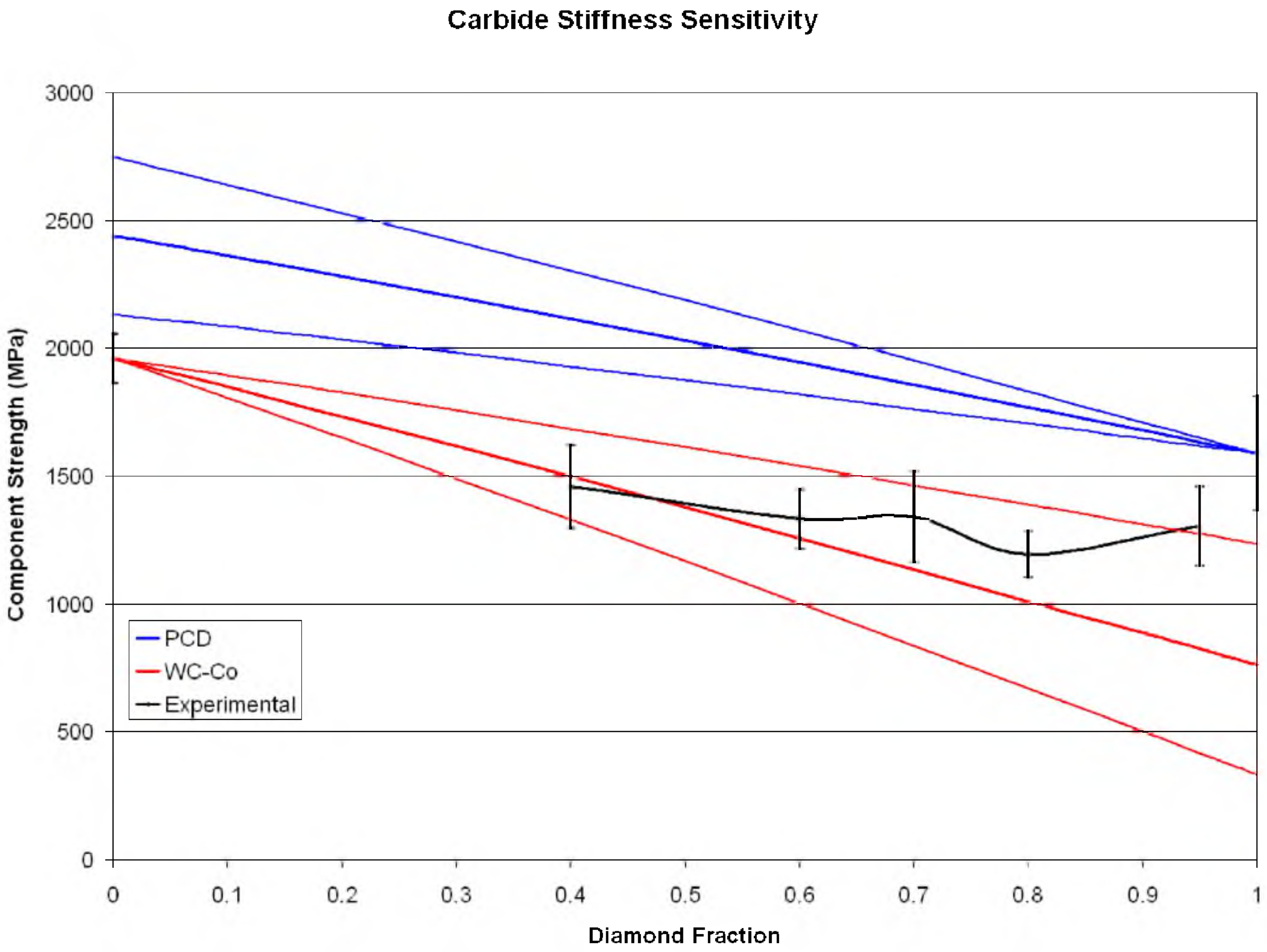

Figure 5.24. Variation of predicted component strengths due to a +/- %5 change in the value of Young's modulus of WC-Co.

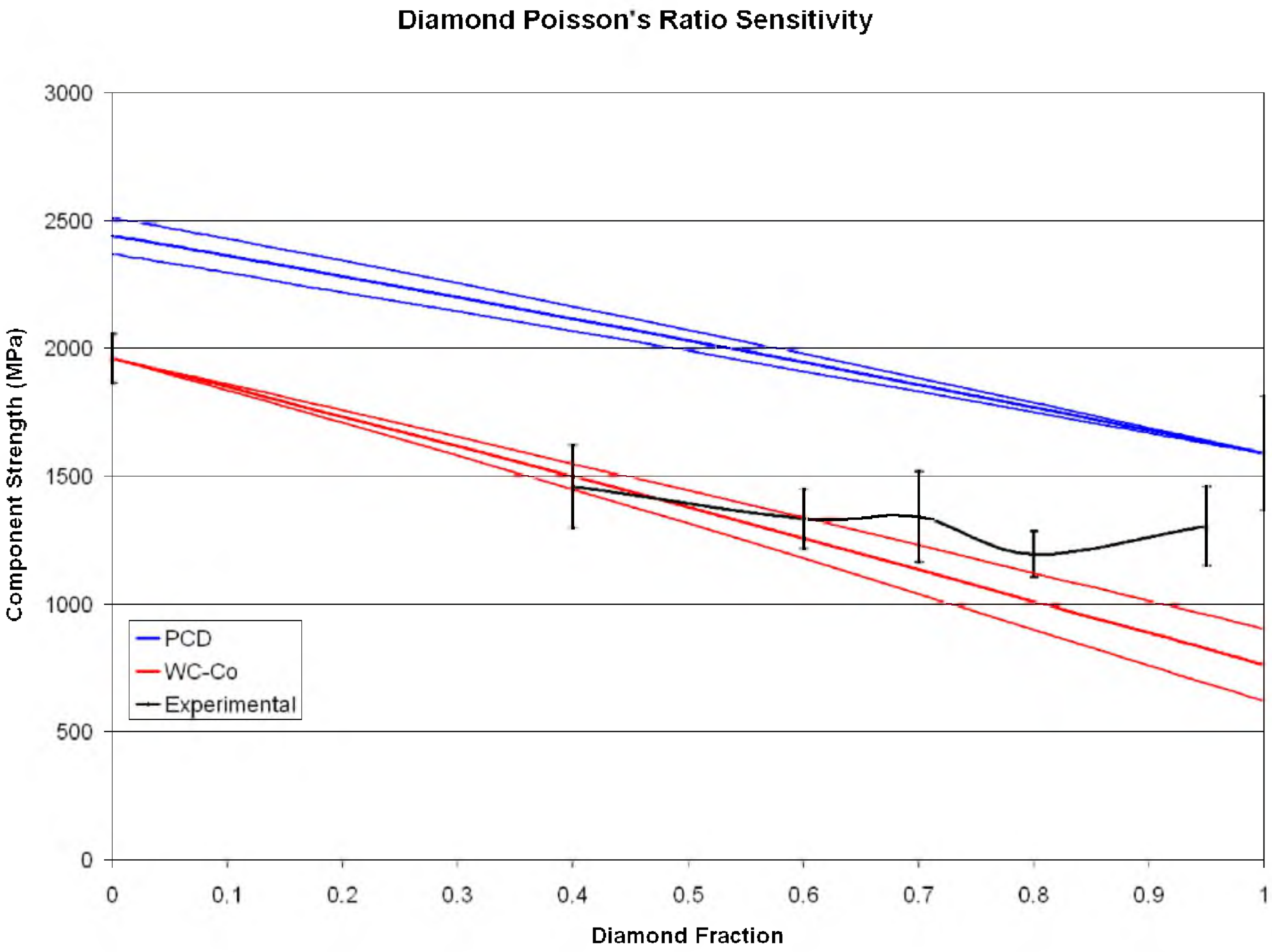

Figure 5.25. Variation of predicted component strengths due to a +/- %5 change in the PCD Poisson's ratio.

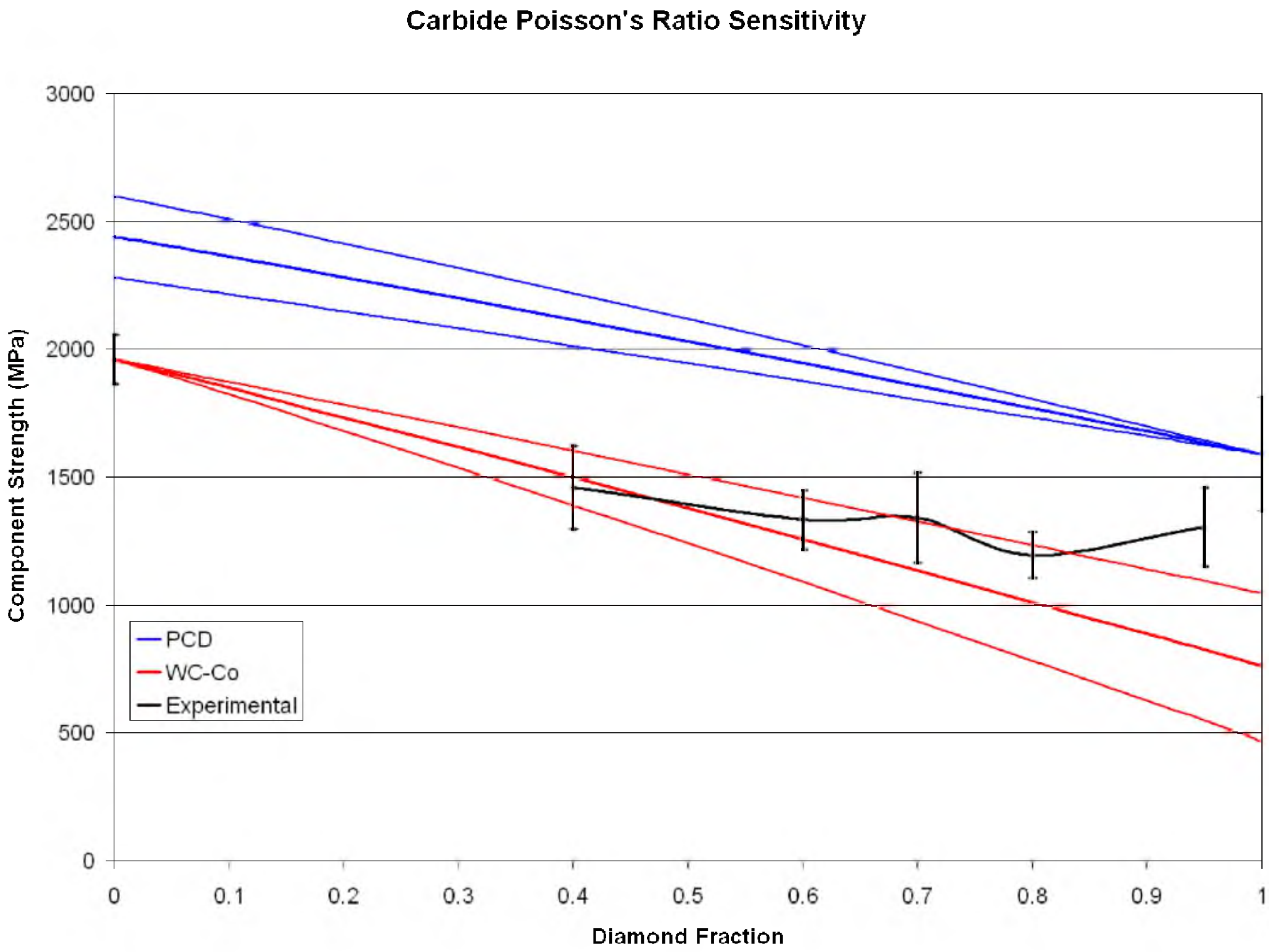

Figure 5.26. Variation of predicted component strengths due to a +/- %5 change in the WC-Co Poisson's ratio.

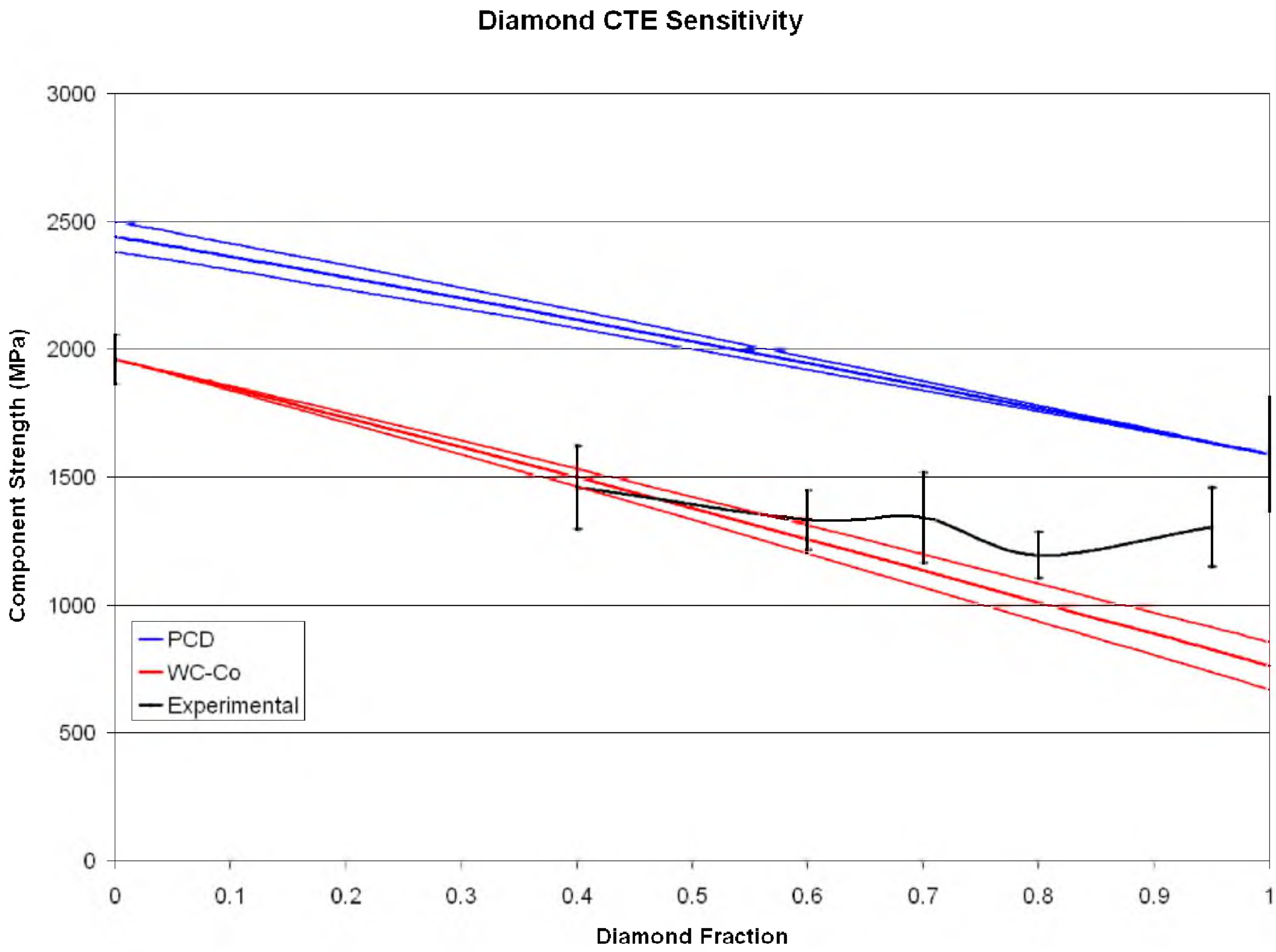

Figure 5.27. Variation of predicted component strengths due to a +/- %5 change in the PCD coefficient of thermal expansion.

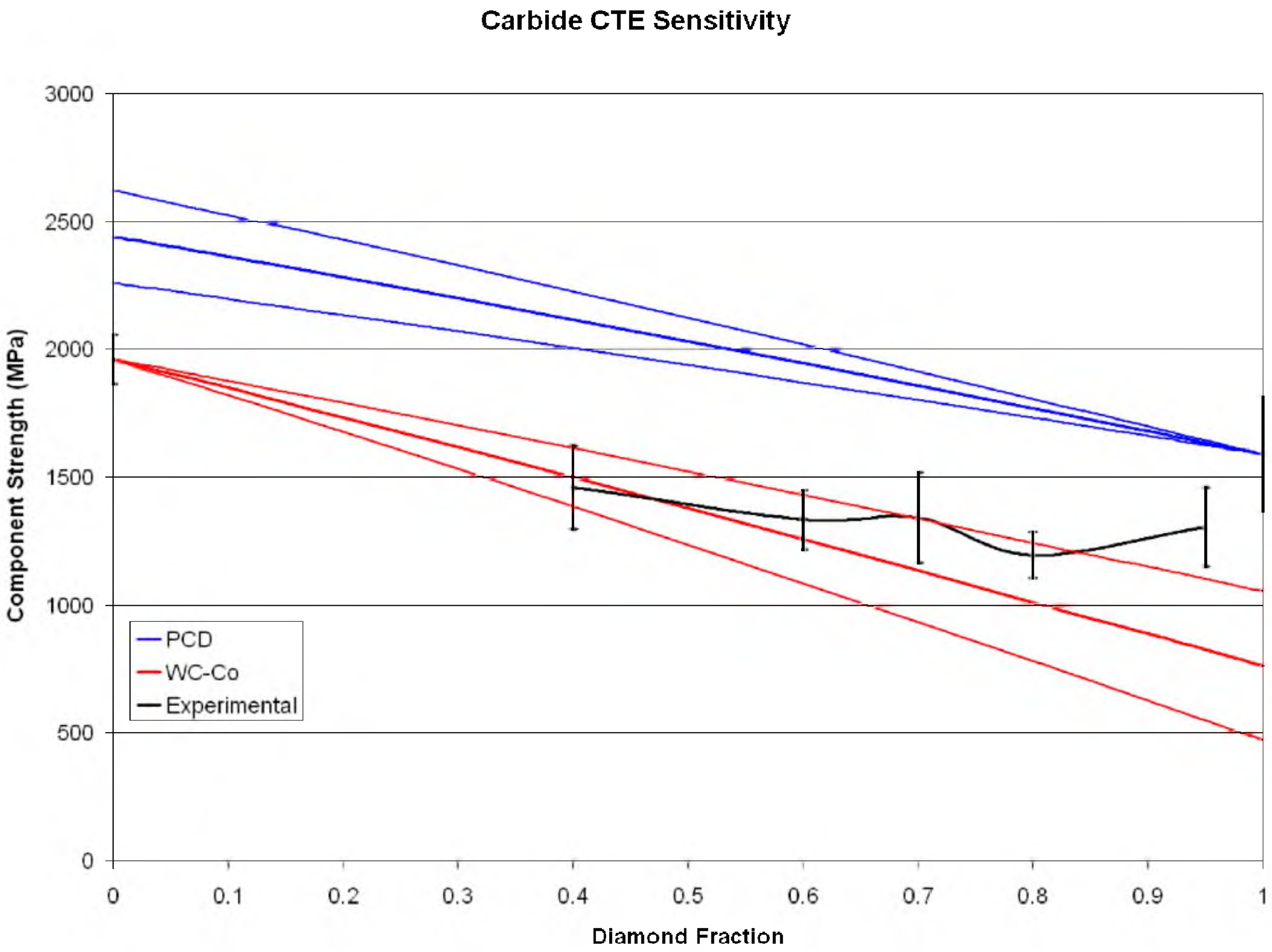

Figure 5.28. Variation of predicted component strengths due to a +/- %5 change in the WC-Co coefficient of thermal expansion.

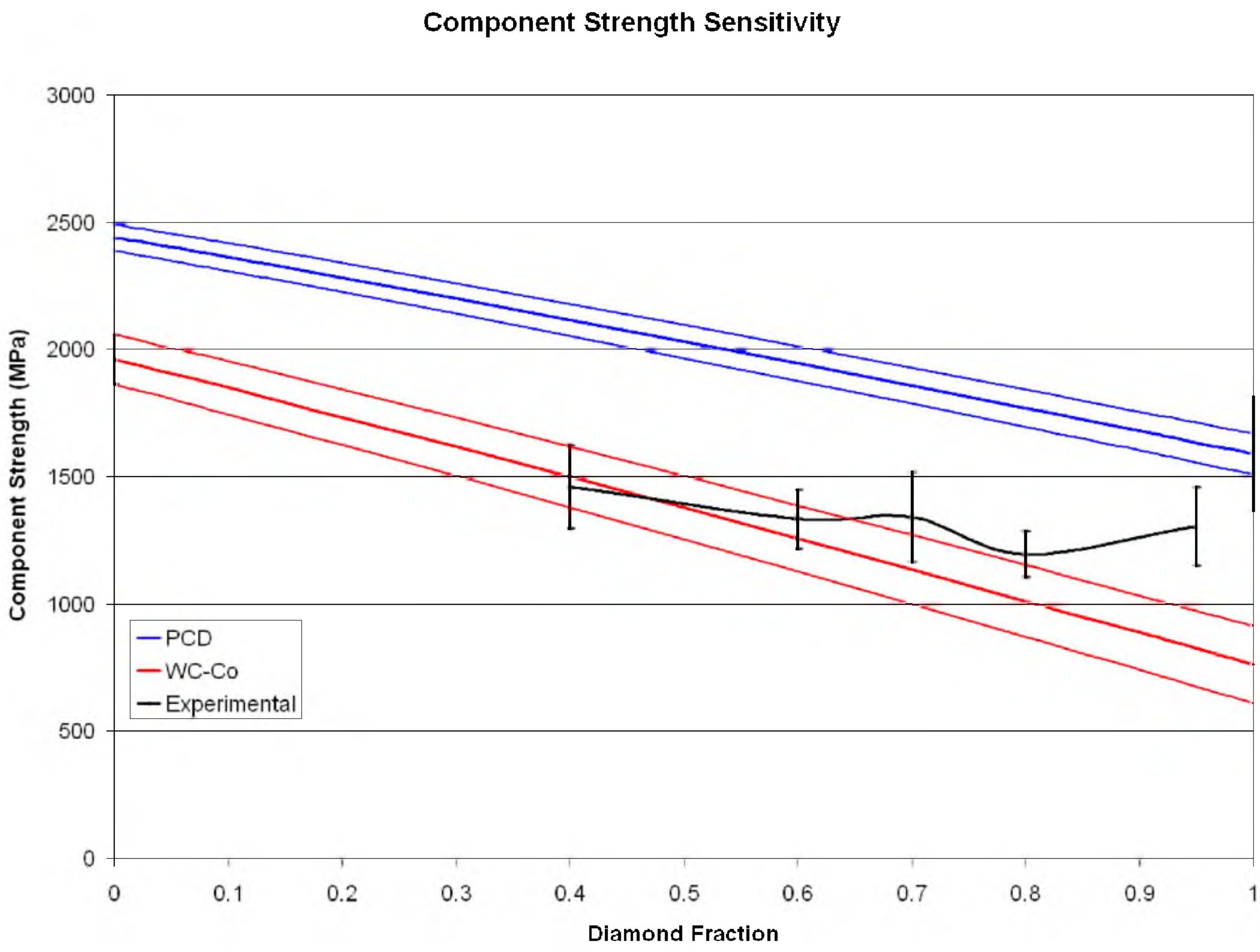

Figure 5.29. Variation of predicted component strengths due to a +/- %5 change in the PCD and WC-Co flexural strength values.

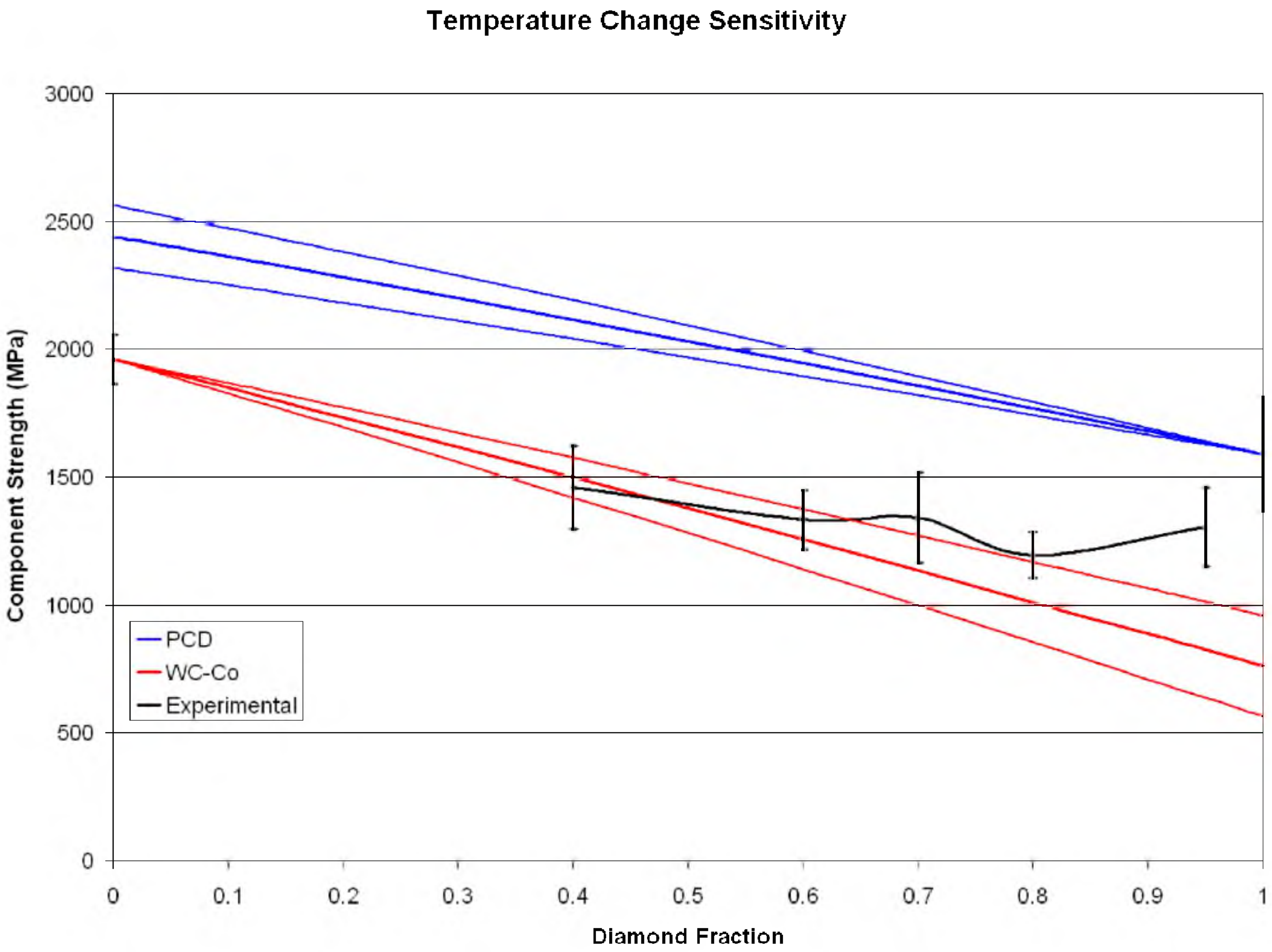

Figure 5.30. Variation of predicted component strengths due to a +/- %5 change in the ΔT used to calculate thermal residual stresses.

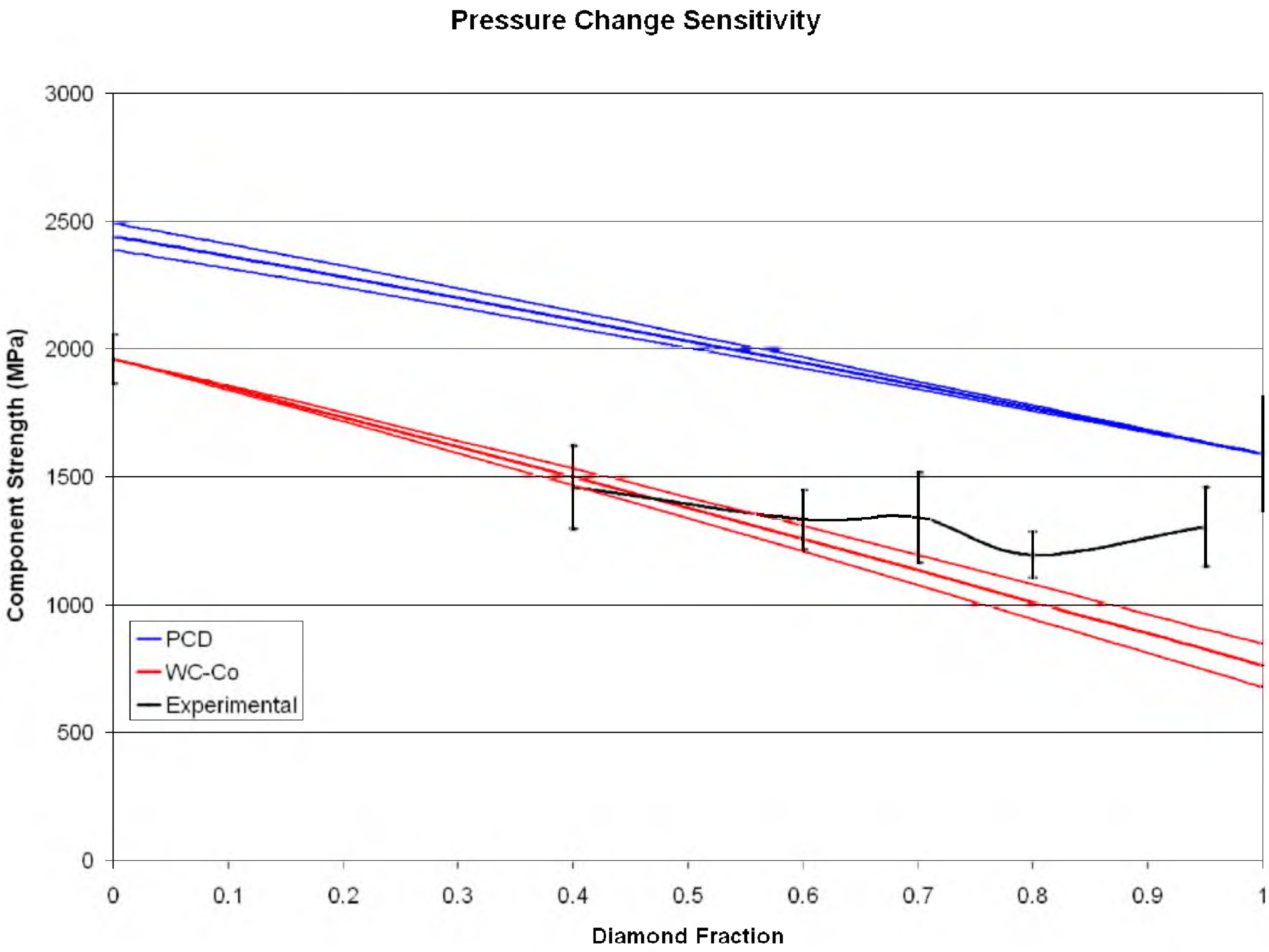

Figure 5.31. Variation of predicted component strengths due to a +/- %5 change in the Δp used to calculate dilatational residual stresses.

the analytical solution feasible, and was able to illustrate the interactions between the different materials and the applied and residual stresses. The strength was estimated by modeling the distribution of the applied stress between the components and the residual stresses that accumulate as the material exits the high temperature/high pressure sintering cycle.

The input parameters used in the model were taken from various sources. The intrinsic material properties were supplied by the material manufacturer. The flexural strength values that were used for the components were experimentally measured, as reported in Chapter 4. The temperature and pressure changes were taken from the sintering process parameters, but were modified using assumptions that are generally accepted in the literature regarding PDC residual stress modeling.

The analytical model predicted the measured flexural strength values for the GDC with surprising accuracy. It is the author's opinion that the close correlation between experimental and analytical values is at least in part a fortunate coincidence. The relatively high uncertainty in the material properties and process parameters, along with the high sensitivity of the strength estimates to small changes in the input parameters lowers the confidence in the precise solution. The model is valuable in illuminating the interaction between the materials and the role of the various material and system properties. Even with the uncertainty of input parameters and simplifications, it is evident that there is a set of parameters within the acceptable range which describes the strength values that were experimentally measured.

It is worth noting once more in this chapter the important role that dilatational residual stresses plays in the overall strength model for PCD composites. By neglecting to consider the impact of pressure, past efforts to properly estimate residual stresses were flawed.

References

1. Hull, D.; Clyne, T. W., *An introduction to composite materials*. Cambridge university press: 1996.

2. Paggett, J. W.; Drake, E. F.; Krawitz, A. D.; Winholtz, R. A.; Griffin, N. D., Residual stress and stress gradients in polycrystalline diamond compacts. *International Journal of Refractory Metals and Hard Materials* **2002,** *20* (3), 187-194.

3. Krawitz, A. D.; Andrew Winholtz, R.; Drake, E. F.; Griffin, N. D., Residual stresses in polycrystalline diamond compacts. *International Journal of Refractory Metals and Hard Materials* **1999,** *17* (1), 117-122.

4. Lin, T. P.; Hood, M.; Cooper, G. A.; Smith, R. H., Residual stresses in polycrystalline diamond compacts. *Journal of the American Ceramic Society* **1994,** *77* (6), 1562-1568.

5. Catledge, S. A.; Vohra, Y. K.; Ladi, R.; Rai, G., Micro-Raman stress investigations and X-ray diffraction analysis of polycrystalline diamond (PCD) tools. *Diamond and related materials* **1996,** *5* (10), 1159-1165.

6. Bertagnolli, K.; Vale, R., Understanding and controlling residual stresses in thick polycrystalline diamond cutters for enhanced durability. *Finer Points(USA)* **2000,** *12* (1), 20.

7. Jia, H. S.; Ma, H. A.; Guo, W.; Jia, X. P., HPHT preparation and Micro-Raman characterization of polycrystalline diamond compact with low residual stress. *SCIENCE CHINA Physics, Mechanics & Astronomy* **2010,** *53* (8), 1445-1448.

8. eFunda. Hooke's Law: Isotropic Materials. http://www.efunda.com/formulae /solid_mechanics/mat_mechanics/hooke_isotropic.cfm (accessed Jun 28, 2005)

CHAPTER 6

NUMERICAL MODELING OF COMPONENT STRESSES AND COMPOSITE STRENGTH

In this chapter, finite element analysis (FEA) will be used to investigate how the interaction between the components of granular diamond composite material leads to residual stresses and determines the material strength. Numerical models, using finite elements, are able to simulate the behavior of materials in complex arrangements. Harnessing the computational power of modern computers, numeric models can solve systems that are many orders of magnitude more complex than those solved using analytical means.

A simple numerical model which approximates the slab model used in Chapter 5 will be employed to evaluate the analytical model and to estimate the error caused by some of the assumptions in the analytical model. A similar numerical model will be applied to a simple shear cutter. Next, a two-dimensional (2-D) model will be used to estimate the impact of the mesostructure on the residual stresses and strength of GDC using actual SEM images of the mesostructure. Finally, a three-dimensional (3-D) model will be used to model the residual stresses and the composite strengths along the volume fraction spectrum using simulated 3-D mesostructures. This 3-D model will also be used to evaluate how changes to the mesostructure might affect composite strength.

The slab FEA validates the equations derived in the last chapter and finds only small errors, less than 1%, due to the simplification of not accounting for differences in Poisson's ratio in the thickness direction.

A simple shear cutter is similar to the slab model in several respects. The shear cutter has also been the subject of previous residual stress studies, with both empirical measurements and numerical modeling. With this model the effect of pressure on residual stresses will be calculated, and the results will be compared to the past published studies.

The 2-D micrograph-based FEA results follow the trend of experimental data reported in the last chapter. The strengths are predicted high and low depending on whether plane stress or plane strain assumptions are used. The plane strain model is in better agreement with the analytical model. This model highlights the interactions between the diamond and carbide phases which control the strength of the overall composite. The Weibull analysis assesses the distribution of strengths due only to the inhomogeneity of the mesostructure because the distribution of flaws is not modeled.

The 3-D FEA finds an even closer agreement with the experimental data. It predicts the same mechanisms will control the composite strength as the 2-D FE model. The 3-D model agrees with the plane strain 2-D model and the analytical model that the carbide is the limiting phase for flexural strength.

The 3-D FE analysis also predicts that smoother, more uniform, and better separated mesostructures will provide higher flexural strengths.

Analytic Model Evaluation

A 3-D model was developed to approximate the slab model that was used in the last chapter. It was used to evaluate the analytical model and to estimate the error introduced by the assumption that there are no stresses in the thickness direction. The stresses in the thickness direction arise from differences in the Poisson's ratios of the materials. Because of the trivial nature of the results of the equal stress (Ruess) model, only the Voigt, or equal strain model was incorporated in this study.

The HyperWorks FEA software suite by Altair was used to create and solve the Voigt model. As shown in Figure 6.1, the model uses hexahedral elements to create the slab of two materials. The length of each side is 1 mm, giving a surface area of 1 mm^2 to each face and a total volume of 1 mm^3. On the near face normal to the X axis, the nodes are constrained to have no displacement in the axial (X) direction. On the far face the nodes are constrained to move uniformly in the axial direction. Nodes on both faces normal to the Z axis are also constrained to move in unison in the thickness (Z) direction. The constraints also assume zero shear in the model. Volume fractions of 20%, 50%, and 80% were modeled.

Modeling Applied Stress

A single force is applied to the X-normal, uniformly constrained, face of the slab model to model the stress response of the composite in the equal strain model. The force is represented by the red arrow in Figure 6.1. A force of 1 N was used in this model. The rest of the modeling parameters are the same as those used before, presented in Table 5.2.

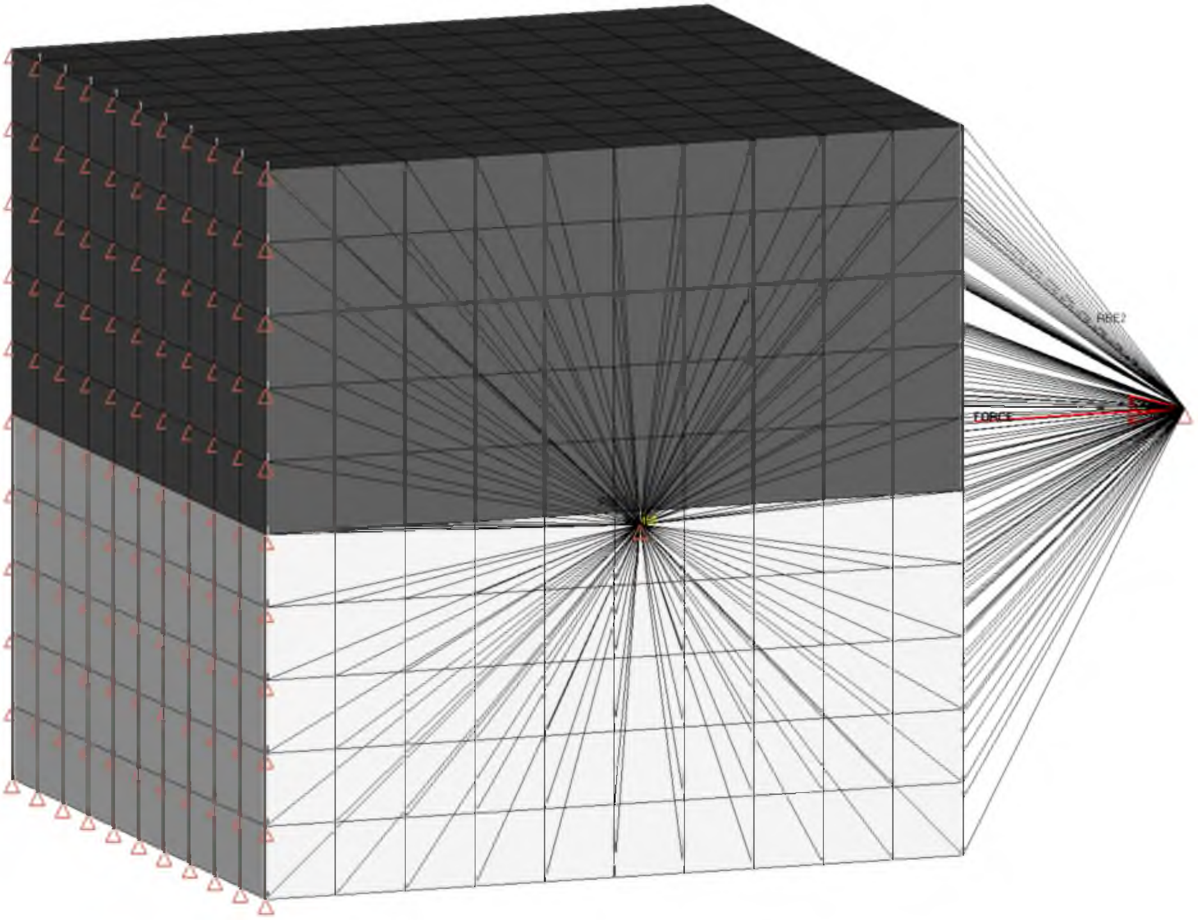

Figure 6.1. The finite element model is composed of hexahedral elements. All of the nodes on the cube's faces are constrained to move uniformly in the normal direction. This figure shows a 50v% diamond composite. Diamond is represented in the darker gray. A single force, represented by the red arrow is applied in the axial direction in the applied stress model.

The interface between the diamond and carbide phases is perpendicular to the transverse direction. The lack of shear and uniform normal displacements at the faces cause the material to displace uniformly in the axial and thickness directions. Both materials are free to displace in the transverse direction. This displacement will be uniform within each of the materials. The diamond has a lower Poisson's ratio than the carbide (see Table 5.1), therefore the diamond will displace less in the transverse direction than the carbide when a force is applied in the axial direction. This phenomenon is illustrated in Figure 6.2, a displacement map of a 50v% composite. In Figure 6.2a and Figure 6.2c (respectively, the displacement in the axial and thickness directions), the color bands are of uniform thickness, indicating uniform displacement. Displacement in the transverse direction is shown in Figure 6.2b and the displacement bands in the upper (diamond section) are broader than the displacement bands in the carbide, indicating that the carbide displaces more in the transverse direction than the diamond when a force is applied in the axial direction.

Because all the nodes on the face are constrained to displace uniformly, the force will not be uniformly distributed across the face. The stiffer elements will be stressed greater than the more compliant elements. Figure 6.3 is a stress map of an 80v% diamond composite. The stiffer diamond is colored red, indicating a higher stress than the more compliant carbide, shown in blue. Because of the no-shear assumption, the stress within each component is uniform. There is no stress gradient with in the components so there is no color gradient either.

The numerical results for both microstrain and component stresses are listed in

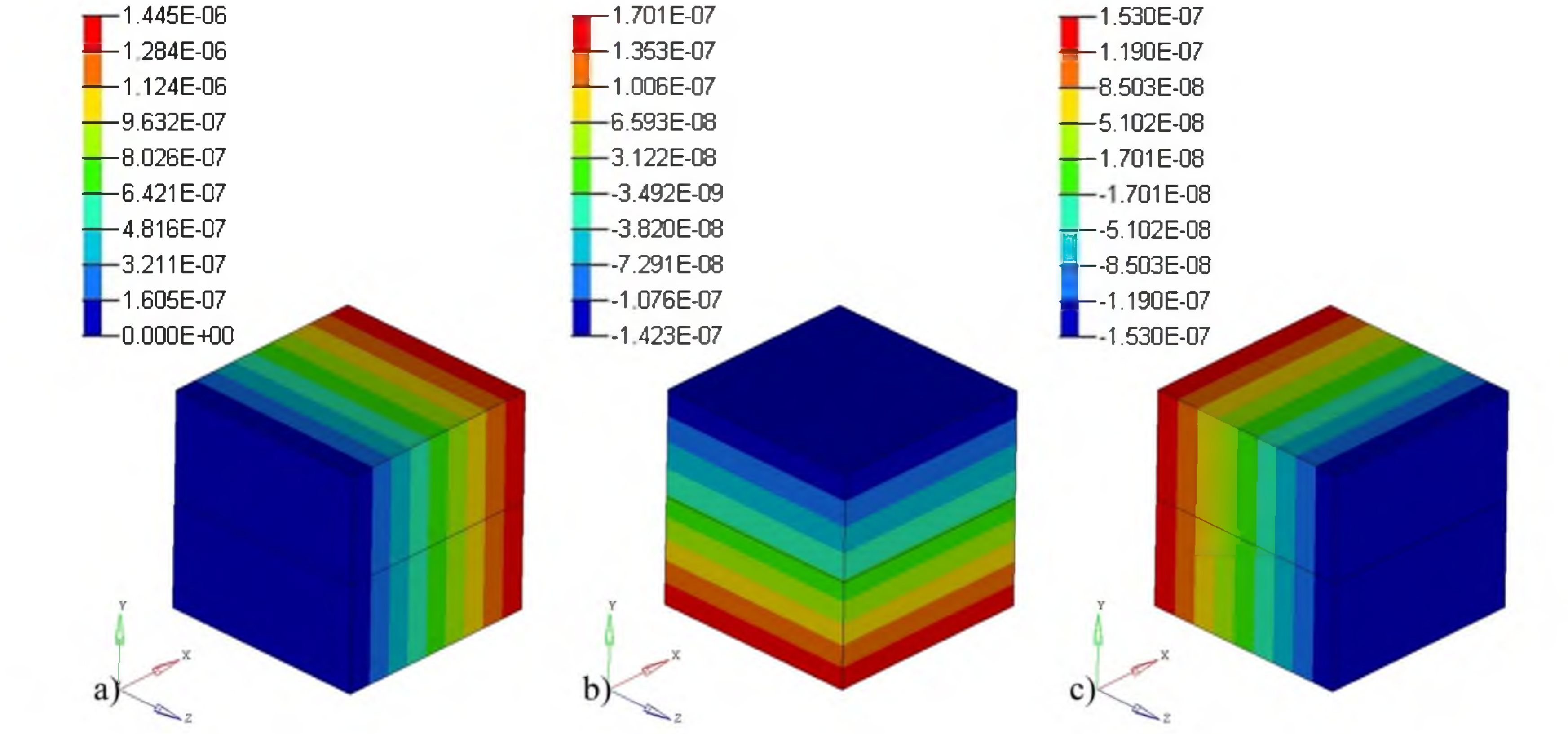

Figure 6.2. Displacement in the three orthogonal directions due to the application of a stress in the axial direction. Note that the displacement is uniform in the axial and thickness directions as required by the definition of the slab model. The carbide phase has greater displacement than the diamond phase in the transverse direction.

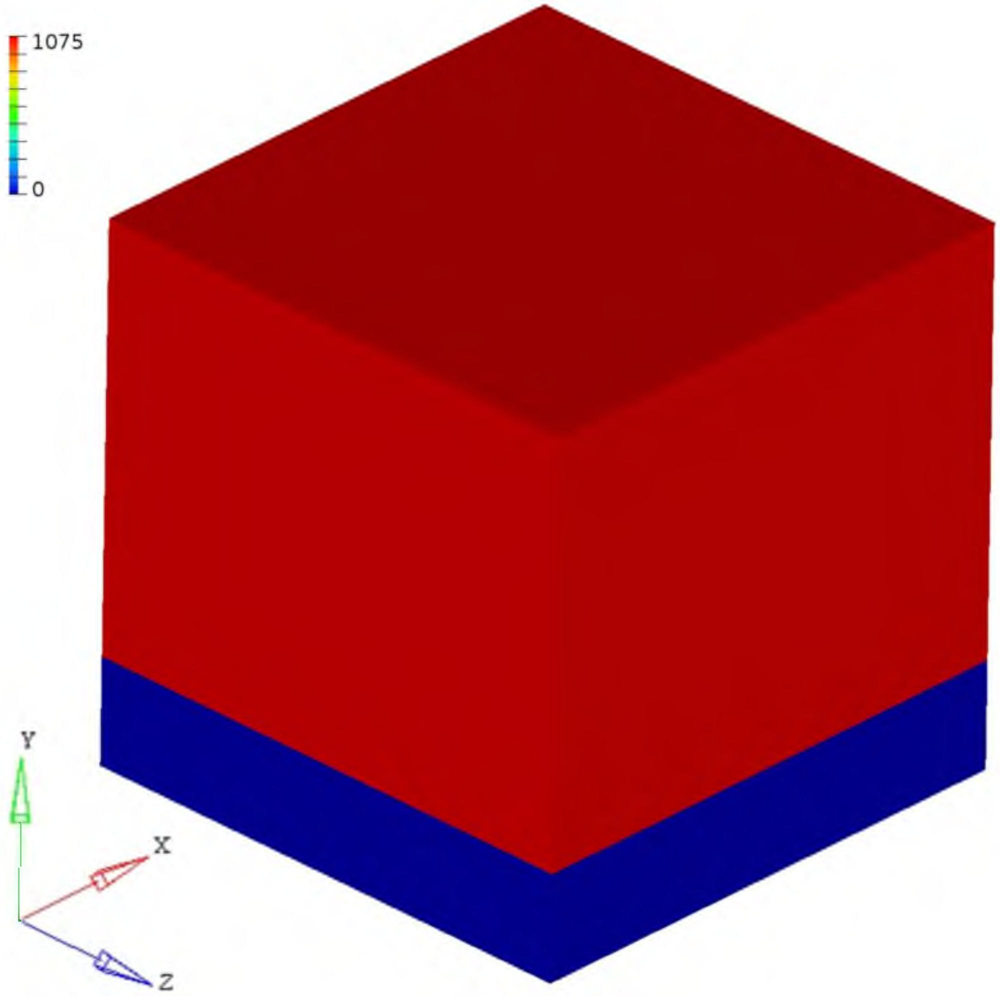

Figure 6.3. Axial stress results for an 80v% diamond composite. The equal strain model causes the stresses to be uniform within the components.

Table 6.1. In this table the numerical results are also compared to the analytical results found in Chapter 5. In the analytical model presented in Chapter 5 the stresses in the thickness direction that arise from differences in the material's Poisson's ratios were neglected. This accounts for the discrepancies between the results of the numerical model and the analytical model. Table 6.1 calculates the error associated with this assumption.

The simplification of neglecting the differences in the Poisson's ratios, used in Chapter 5, does not greatly impact the results as the error never exceeds 1%. The error reported in the stress results is greater than the error found in the strain results. The error in the diamond phase is positive, meaning the stresses in the analytical results was slightly overestimated, and the error in the carbide phase is negative. The error is greater in the phase with a lower diamond volume fraction.

Modeling Residual Stresses

The residual stresses that the composite accumulates as it exits the sintering conditions were modeled by applying a temperature change to all of the nodes and a pressure change to exterior nodes. A ΔT of -973°C was used along with -5500 MPa for the Δp (see Table 5.2).

Figure 6.4 is a stress map showing the residual stresses in a 20v% diamond composite. The diamond is shown in blue, indicating that the residual stresses in the diamond are lower than the residual stresses in the carbide, shown in red. In the case of 20v% diamond, the magnitude of the residual stresses in the diamond are greater in magnitude than in the carbide, but are negative, meaning the diamond is in a compressed

Table 6.1

Applied Stress Model – Analytical vs. Numerical Result Comparison

	Numerical	Analytical	Error
20v% PCD			
$\mu\epsilon_x$	1.659	1.660	0.06%
σ_f (MPa)	1.389	1.396	0.50%
σ_m (MPa)	0.9027	0.9011	-0.18%
50v% PCD			
$\mu\epsilon_x$	1.445	1.445	0.00%
σ_f (MPa)	1.212	1.215	0.25%
σ_m (MPa)	0.7880	0.7847	-0.42%
80v% PCD			
$\mu\epsilon_x$	1.280	1.280	0.00%
σ_f (MPa)	1.075	1.076	0.09%
σ_m (MPa)	0.6992	0.6949	-0.61%

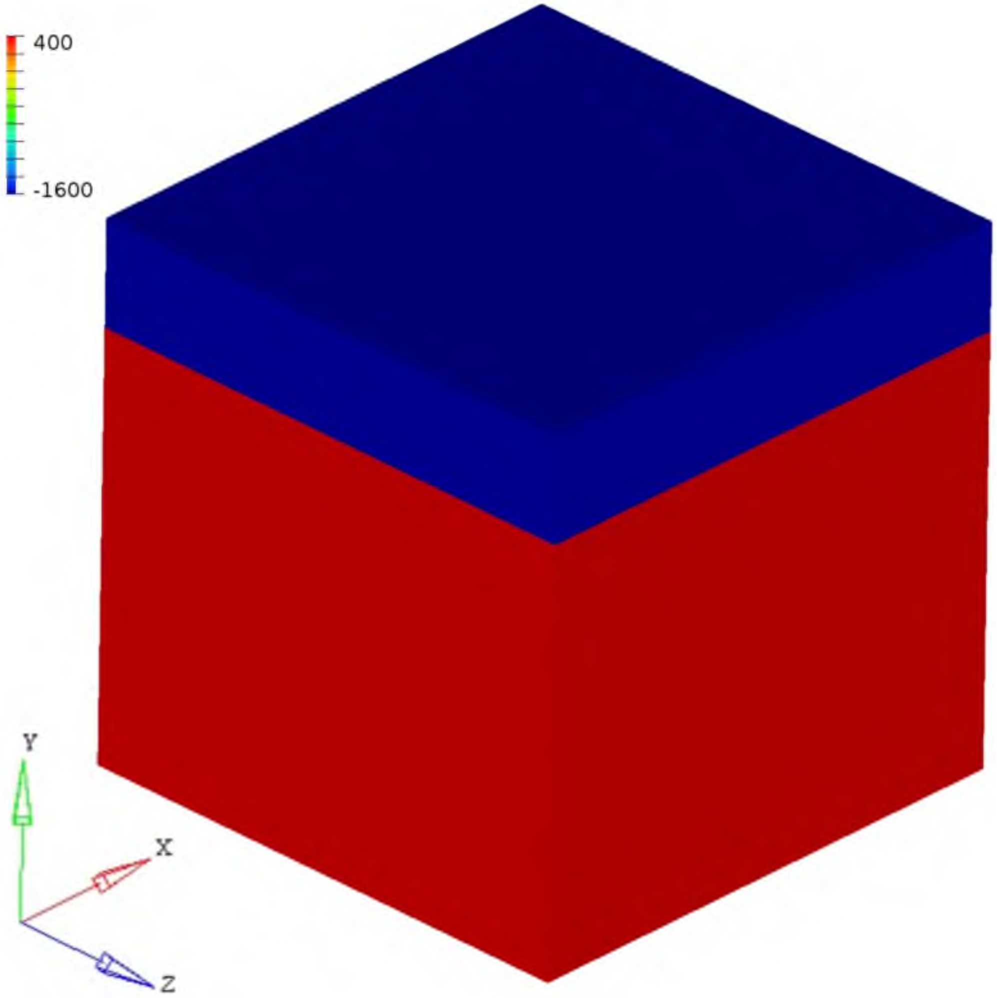

Figure 6.4. Residual stresses in a 20v% diamond composite. The stresses shown in the legend are relative to the sintering pressure rather than atmospheric pressure.

state.

The residual stresses presented in Figure 6.4 are relative to the starting pressure. This is the sintering pressure and not the atmospheric pressure. To convert the starting pressure to the ending or atmospheric pressure, the Δp must be subtracted from the results.

The numerical results from the 20v%, 50v%, and 80v% models are listed in Table 6.2. The analytical results from the model used in Chapter 5 are also listed in the table. Because the numerical model closely approximates the analytical model and uses the same assumptions, there are no discrepancies found and the calculated error is therefore zero.

Strength Modeling with Residual Stresses

The previous two models will be merged to model the strength of the composite. The ΔT, Δp, and single force in the axial direction are incorporated into the same model. Solving this model will produce stresses in each component, which can then be used to calculate the external applied stress at which either component of the composite will fail. The lower of the applied stresses that will cause component failure becomes the strength of the composite due to the brittle nature of this material system.

The variable σ_{auc} represents the external applied stress that causes a component to reach its critical stress (σ_{uc}). This variable can be found by dividing the stress needed to push the component to its breaking point, equation 6.1, by the stress intensification factor, equation 6.2 (see equation 5.13), as shown in equation 6.3.

Table 6.2

Residual Stresses Model – Analytical vs. Numerical Result Comparison

	Numerical	Analytical	Error
20v% PCD			
σ_{rf} (MPa)	-1596	-1596	0.00%
σ_{rm} (MPa)	399	399	0.00%
50v% PCD			
σ_{rf} (MPa)	-879	-879	0.00%
σ_{rm} (MPa)	879	879	0.00%
80v% PCD			
σ_{rf} (MPa)	-315	-315	0.00%
σ_{rm} (MPa)	1258	1258	0.00%

$$\sigma_{uc} - \sigma_{rc} \tag{6.1}$$

$$\frac{\sigma_{ac}-\sigma_{rc}}{\sigma_{a}} \tag{6.2}$$

$$\sigma_{auc} = \frac{\sigma_{a}(\sigma_{uc}-\sigma_{rc})}{\sigma_{ac}-\sigma_{rc}} \tag{6.3}$$

The σ_{auc} for both components were calculated for 20v%, 50v% and 80v%. The results are presented in Table 6.3. The strength results from the analytical model used in Chapter 5 are also presented here. The differences are caused by ignoring the stresses in the thickness direction due to differences in Poisson's ratio, as discussed earlier in this chapter. The error caused by this assumption is calculated in the third column. Notice that the magnitudes of error are equivalent to the errors presented in Table 6.1, but the signs are reversed. This is because Table 6.1 presents the stresses and Table 6.3 presents the strengths.

Shear Cutter Modeling

The shear cutter is a common drill bit insert used in the petroleum extraction industry. It has a cylindrical shape, as illustrated in Figure 6.5. A simple PDC shear cutter has a top layer of PCD sintered onto a WC-Co substrate, with a flat interface between the two. Shear cutter residual stresses have been studied in the past and several reports have been published. A shear cutter will be modeled, both with and without considering dilatational residual stresses and the results will be compared to the published data.

A simple shear cutter is geometrically similar to the slab model, with two layers

Table 6.3

Strength Model – Analytical vs. Numerical Result Comparison

	Numerical	Analytical	Error
20v% PCD			
σ_{auf} (MPa)	2293	2282	-0.48%
σ_{aum} (MPa)	1730	1734	0.23%
50v% PCD			
σ_{auf} (MPa)	2036	2031	-0.25%
σ_{aum} (MPa)	1373	1378	0.36%
80v% PCD			
σ_{auf} (MPa)	1770	1769	-0.06%
σ_{aum} (MPa)	1005	1011	0.60%

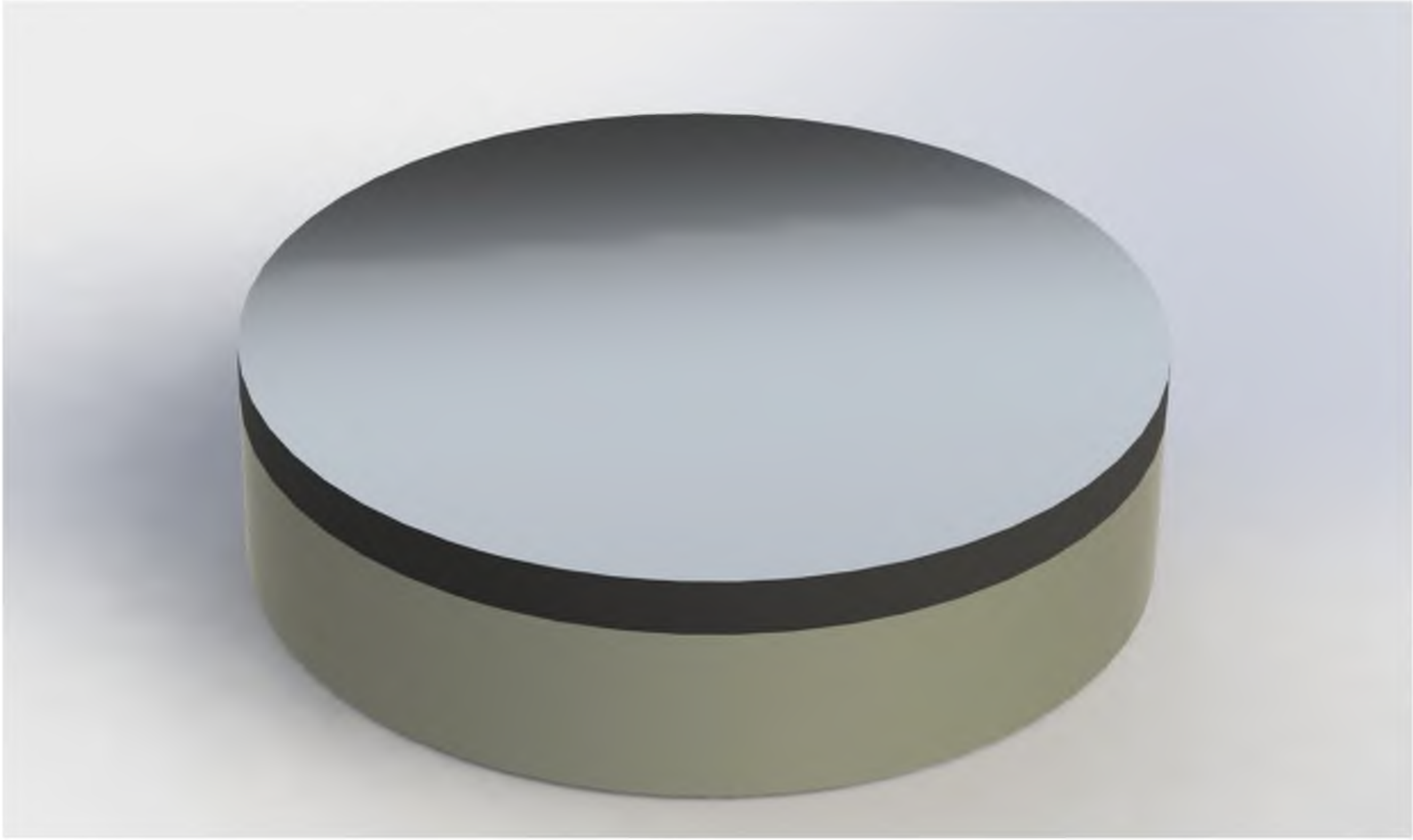

Figure 6.5. A simple shear cutter consists of a layer of PCD sintered onto a WC-Co substrate. Shear cutters are an important drill bit insert in the petroleum drilling industry.

bonded across a single flat interface. There are some important differences though. The slab model assumes the material has infinite length and depth. The model is therefore less and less applicable as the material in a shear cutter approaches its edge. Also, the slab model doesn't allow for shear stresses, but residual shear stresses are important in shear cutters.

In a study on residual stresses and stress gradients Paggett et al.[1] measured the residual stresses in PCD using neutron diffraction. The measurements were then compared to the residual stress numerical model predictions as developed by Lin et al.[2] The dimensions of the studied shear cutters are listed in Table 6.4.

The results from the study by Paggett et al.[1] are presented in Figure 6.6. The square data points represent neutron diffraction residual stress measurements in the WC-Co. The triangular data points represent neutron diffraction measurements in the PCD. The solid lines represent the residual stress predictions calculated in the paper by Paggett et al., based on the model from Lin et al.[2]

In the current study a model was built for a shear cutter of the same dimensions listed in Table 6.4. The model was solved twice. In the first calculation, the change in pressure was ignored. In the second, the pressure change was considered. The model results are listed in Table 6.5. By neglecting the pressure change, the model predicts the residual stresses to be larger by a factor of two, and once again incorrectly predicts a negative strain. It should be noted that the model found the residual stresses relative to the starting point, σ' (at the peak of sintering), but the table lists the residual stresses relative to the ending point, σ (in atmospheric pressure). The difference between the

Table 6.4

Modeled Shear Cutter Dimensions

Dimension	Value
Cutter Diameter	13.5 mm
Cutter Thickness	0.85 mm
WC-Co Thickness	2.65 mm

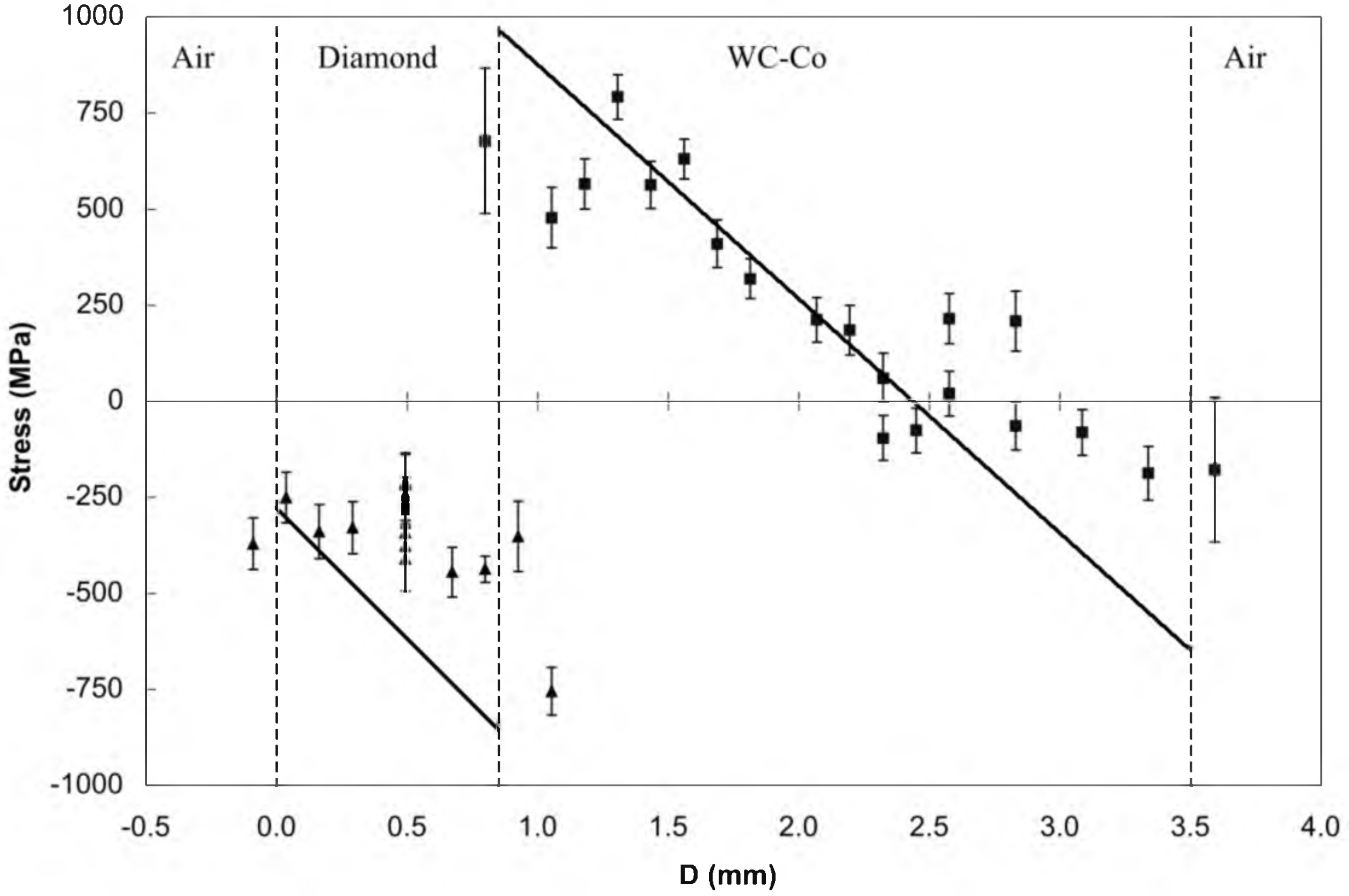

Figure 6.6. Measured and modeled residual stresses in PDC shear cutters. Square data points are neutron diffraction measurements in WC-Co. Triangular data points are neutron diffraction measurements in PCD. The solid lines are the model predicted residual stresses. Figure was compiled from data published by Paggett et al.[1] (Reprinted with permission.)

Table 6.5

Residual Stress and Strain Results of the Shear Cutter Model

	Residual Stress		Strain
	PCD	WC-Co	
3-D Finite Element (maximum along central axis)			
Neglecting Pressure	-1604	1531	-0.00454
Considering Pressure	-786	750	0.000657
% change	-51%	-51%	-114%

sintering pressure and atmospheric pressure is 5500 MPa.

Figure 6.7 compares the data presented in the paper by Paggett et al. with the current residual stress predictions taking pressure into account. The predictions including the dilatational residual stresses are shown in red.

The current model that includes the dilatational residual stresses more closely matches the empirical data than the previously published model. However, the results of the previously published model are not as far off as those currently predicted by the model that does not account for dilatational residual stresses. This discrepancy is due to differences in the material properties of the samples used in the different models. The model in this study uses properties in Table 5.2, whereas the Paggett et al. model uses the parameters discussed in Chapter 2 (see Table 2.1).

Solving the current model using the parameters found in Table 2.1 and neglecting the dilatational residual stresses confirms the results shown in Table 6.6. Interestingly, the results showed no change when accounting for pressure. Upon investigation it was found that when using the parameters in Table 2.1 PCD and WC-Co, coincidentally, have the same bulk modulus. Because dilatational residual stresses arise from differences in bulk moduli, no dilatational residual stresses will arise between materials having the same bulk modulus. The bulk modulus, κ, can be calculated from Young's modulus, E, and Poisson's ratio, ν, as shown in equation 6.4[3]:

$$\kappa = \frac{E}{3(1-2\nu)} \tag{6.4}$$

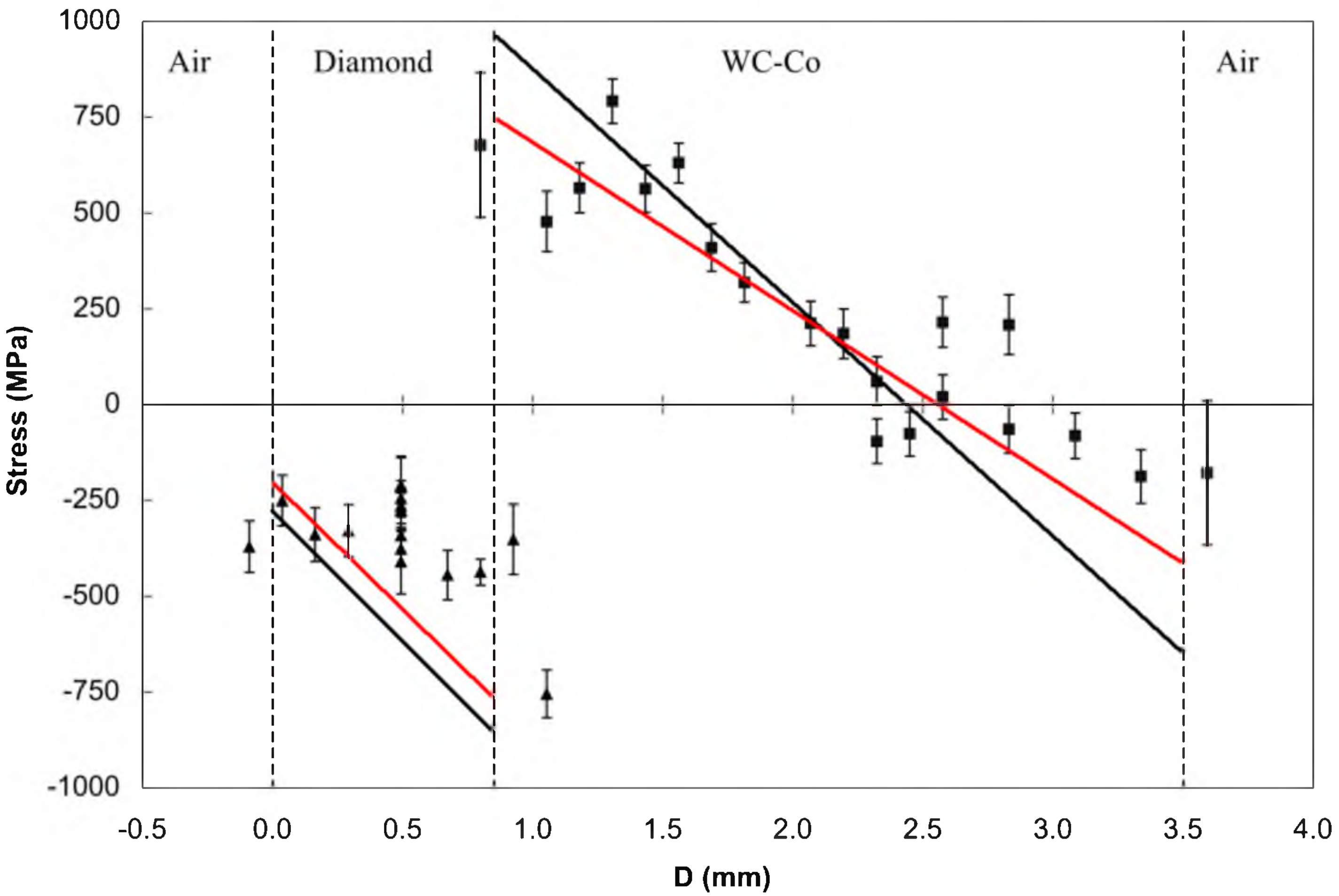

Figure 6.7. Reprint of Figure 6.6 with the addition of model results that account for dilatational residual stresses (in red).

Table 6.6

Differences in Bulk Moduli of PCD and WC-Co Using Various Material Property Data Sources

Material Property Source	PCD	WC-Co
Glowka and Stone[4]	530 GPa	345 GPa
Lin et al[2]	345 GPa	345 GPa
Current Model (see Table 5.2)	467 GPa	335 GPa

Table 6.6 presents the calculated bulk moduli of PCD and WC-Co based on different sets of material property data. The Paggett et al. model used the parameters given by Lin et al. Lin et al. cited Glowka and Stone as the source for the parameters, but there were some discrepancies, as discussed in Chapter 2. The difference between the calculated bulk moduli using a Poisson's ratio of 0.07 instead of 0.22 is significant and would lead to large differences in the calculation of overall residual stresses. The point is not that a Poisson's ratio of 0.07 is wrong, but that the material properties used by Lin et al. happened to negate the dilatational residual stresses. Perhaps, this coincidence is responsible for the general neglect of dilatational residual stresses over the past two decades. Even when the bulk moduli happen to coincide, neglecting to account for the pressure change can lead to highly inaccurate strain estimates. Other material data sets that have been used in modeling PCD and WC-Co result in significant differences in bulk moduli.

2-D Numerical Modeling

The slab model used to this point is a very simplistic model. Despite the simplicity, it has been helpful to gain insight into how the properties of the diamond and carbide phases interact. This insight can only go so far, because this simplicity does not allow consideration of the mesostructure of the hierarchically structured materials being researched here. In order to investigate the impact of the mesostructure on stresses and strengths, numerical modeling was used.

The 2-D numerical modeling of the flexural strength of the PCD/WC-Co composite was performed using Object Oriented Finite Element Analysis (OOF), a finite element analysis package available from the US National Institute of Standards and Technology (NIST, Gaithersburg, MD).[5] OOF is designed to analyze microstructural stresses based on real micrographs. OOF can generate a 2-D mesh based on a micrograph and can then analyze 2-D stresses assuming linear-elastic behavior. Because both PCD and WC-Co are hard materials, the linear elastic behavior assumption is reasonable for both materials, up to the point of fracture. Because the behaviors of the functionally designed composites depend strongly on their mesostructure, OOF is particularly well suited for modeling this composite material.

Micrographs of the material were obtained using a scanning electron microscope (SM-300 TopCon) at 50X using a backscattered electron detector (System 47 GW Electronics, Inc.). The micrographs were then processed into binary images, examples shown in Figures 6.8 and 6.9, using an open source image processing program (GIMP, the GNU Image Manipulation Program). Different image analysis procedures were used on the same image and the modeling results were compared. Image smoothing procedures decreased the data scatter but had no statistical effect on average strength numbers. Several images were taken from the same specimen and from different specimens in the same batch. These images were processed and compared for consistency. The strength numbers remained very consistent, indicating that even though the granules are irregularly shaped and spaced the mesostructure behavior is almost uniform.

The processed micrographs were then loaded into the OOF program. Each phase,

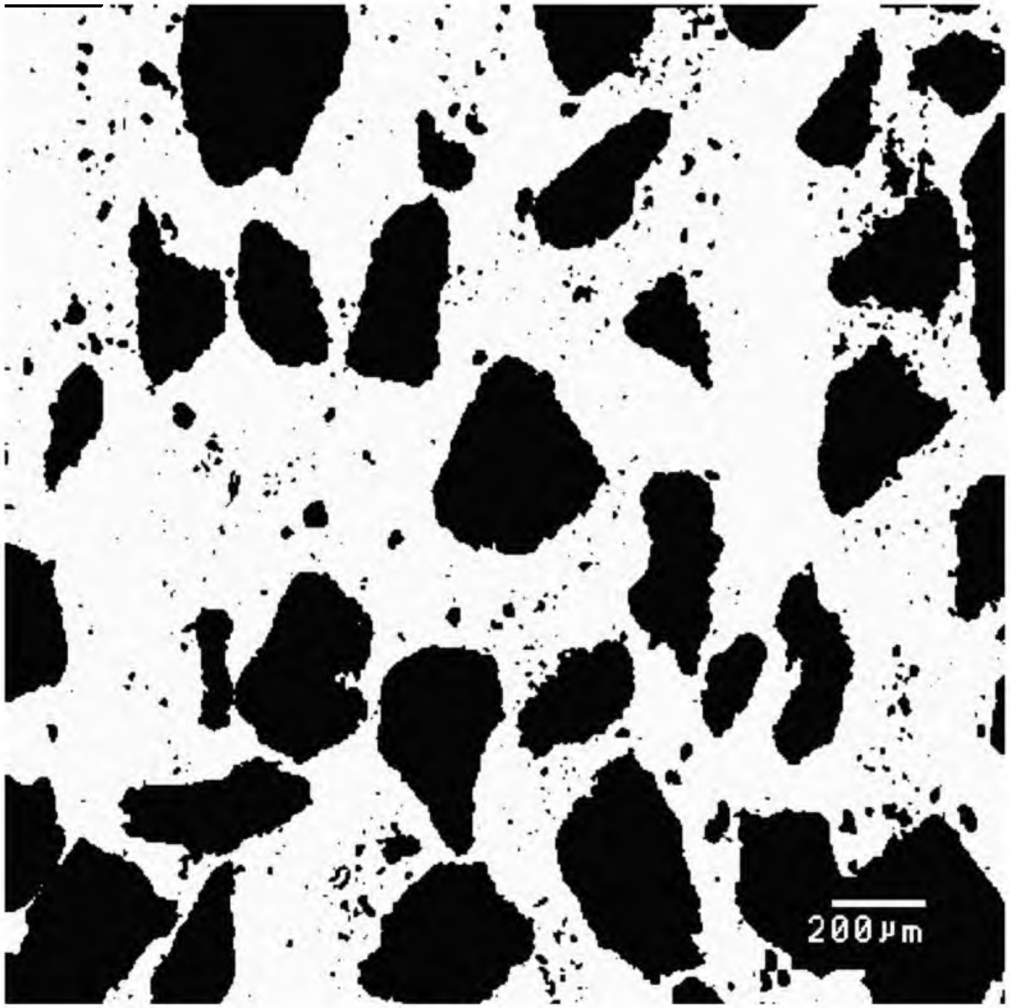

Figure 6.8. A processed micrograph of a 40v% diamond composite. A threshold algorithm has been used to create a binary image where black represents the diamond phase and white represents the carbide phase.

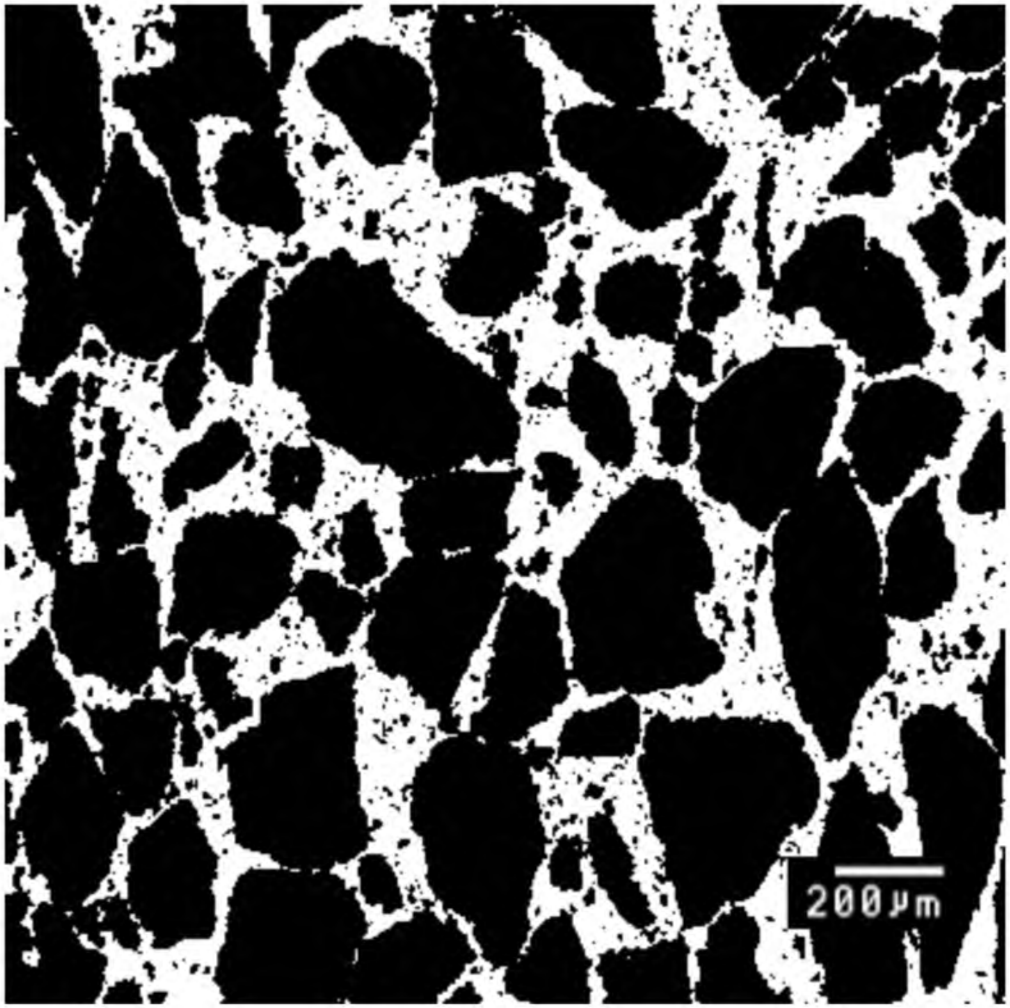

Figure 6.9. A processed micrograph of a 70v% diamond composite. Compared to the 40v% mesostructure, there is less carbide matrix and the PCD granules are beginning to touch their neighbors.

designated by the different gray levels, is assigned material properties, found in Table 6.7. The material was modeled using both plane stress and plane strain conditions and the results were compared.

Inside of OOF, a mesh is applied to the image. OOF only allows for the use of triangular elements. The standard work flow in OOF is to apply a relatively coarse mesh to the micrograph and then to use several built in algorithms to adjust the mesh to better fit the microstructure. It often took a full day to produce a coarse mesh that properly represented the mesostructure and contained no malformed elements. Even using a relatively high-speed, work-station class computer, the mesh needed to be fairly coarse for all the mesh optimization algorithms to complete in a reasonable amount of time. The process was judged to be subjective and not very repeatable. Once a quality mesh had been produced, OOF could solve the models in under a minute. An alternative workflow was attempted. The resolution of the micrograph was reduced to 400 × 400 pixels and a finer mesh was applied so that each pixel was split into two triangular mesh elements. The solution time was increased dramatically but the overall processing time decreased because the time to optimize the mesh was eliminated. This process also reduces subjectivity and increases repeatability. A quick data processing method was applied later to minimize pixelization effects. As mentioned above, the results from this method were compared to the results from a larger micrograph that used an optimized mesh and no smoothing algorithm on the data. The results were statistically indistinguishable. The fine, unoptimized mesh method was used to generate the data analyzed here. Figure 6.10 illustrates the application of the fine mesh.

Table 6.7

2-D Modeling Parameters

	Diamond	Carbide	Model
Gray level	0.1	0.9	
Young's modulus (MPa)	841,000	548,000	
Poisson's ratio	0.2	0.23	
Coefficient of thermal expansion /°C	1.75×10^{-6}	5.48×10^{-6}	
Temperature change °C			-973
Pressure change (MPa)			-5500

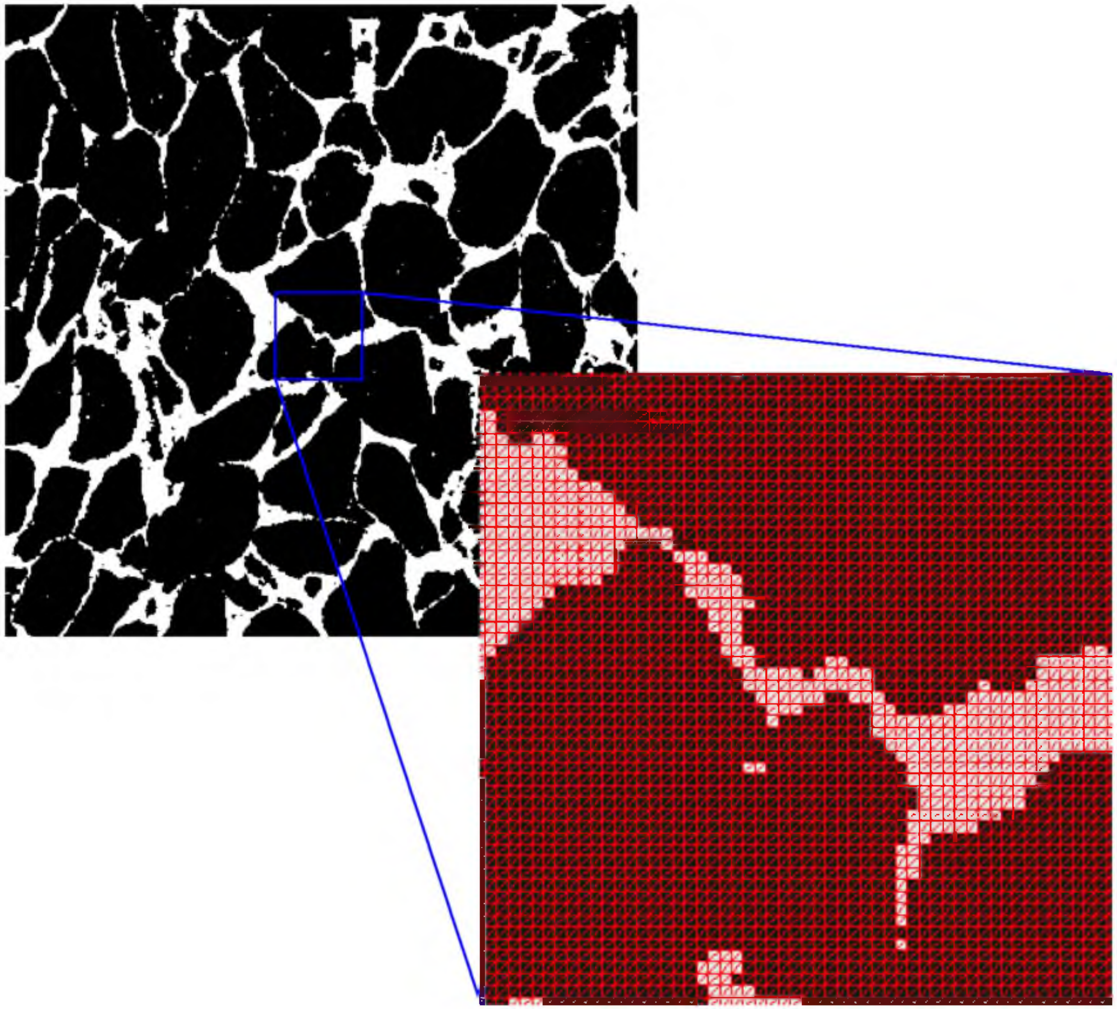

Figure 6.10. The 2-D mesh is applied to a 80v% diamond micrograph so that each pixel is bisected by two triangular mesh elements.

Modeling Applied Stress

The nodes on the lower border were constrained to not move in the vertical direction. The nodes on the left border were constrained so that their lateral displacement was zero. The nodes on the top and right borders were constrained to move uniformly in the perpendicular direction. All border nodes were free to move in the parallel direction and no node displacement was allowed in the out-of-plane direction. Both plane stress and plane strain methods were alternately applied.

A lateral force of 2000 N was placed on the right border. The stress map of lateral stresses when solving using plane stress conditions is shown in Figure 6.11. Figure 6.12 is the results from a similar set up except that plane strain conditions were assumed. In order to increase the results from each processed micrograph, and because the mesostructure is isotropic, additional results are produced by removing the lateral force and applying a 2000 N force in the vertical direction on the top border of the model. The vertical stress results using plane stress and plane strain are shown in Figures 6.13 and 6.14, respectively.

In these four graphs two things are apparent. First, the diamond is stressed more than the carbide. This phenomenon was also seen in the slab model. Second, the stresses are more concentrated in the narrow necks connecting grains in the direction of loading. These stress risers, in the weaker and more loaded phase, would drastically reduce the strength of the composite.

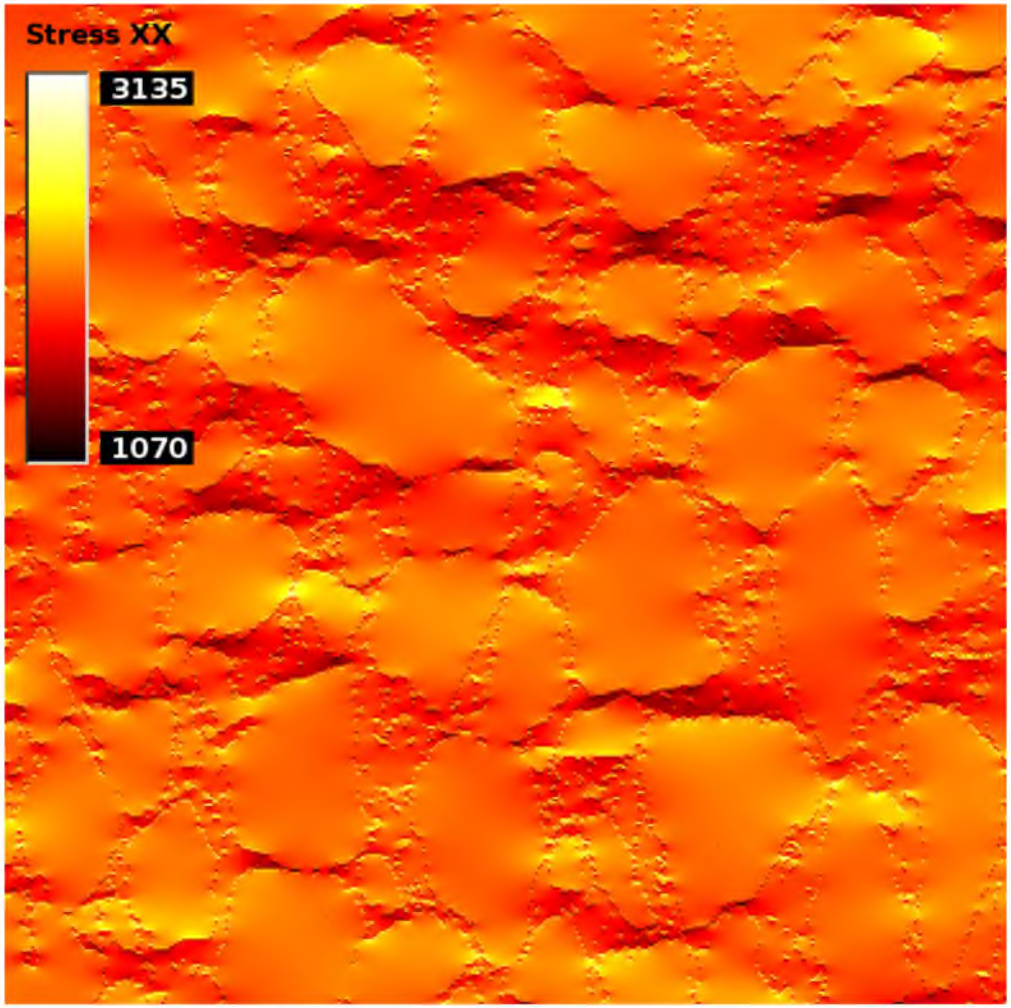

Figure 6.11. A stress map of the lateral stresses when a lateral load is modeled on an 80v% diamond micrograph, using plane stress assumptions. The stresses are represented on a thermal color gradient. The tensile stress concentrates in the stiffer diamond phase, particularly where granules are touching in the lateral direction.

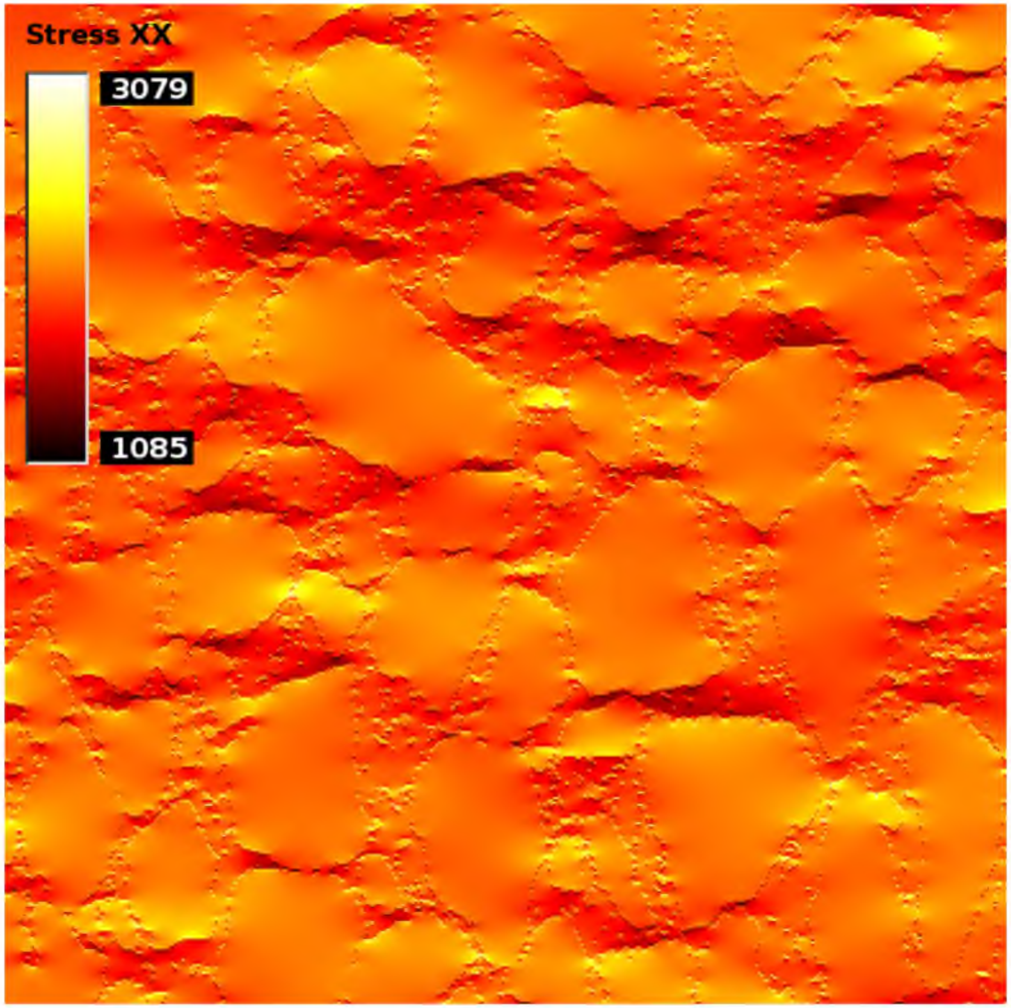

Figure 6.12. A stress map of the lateral stresses when a lateral load is modeled on an 80v% diamond micrograph, using plane strain assumptions. The stresses are very similar to the plane stress results.

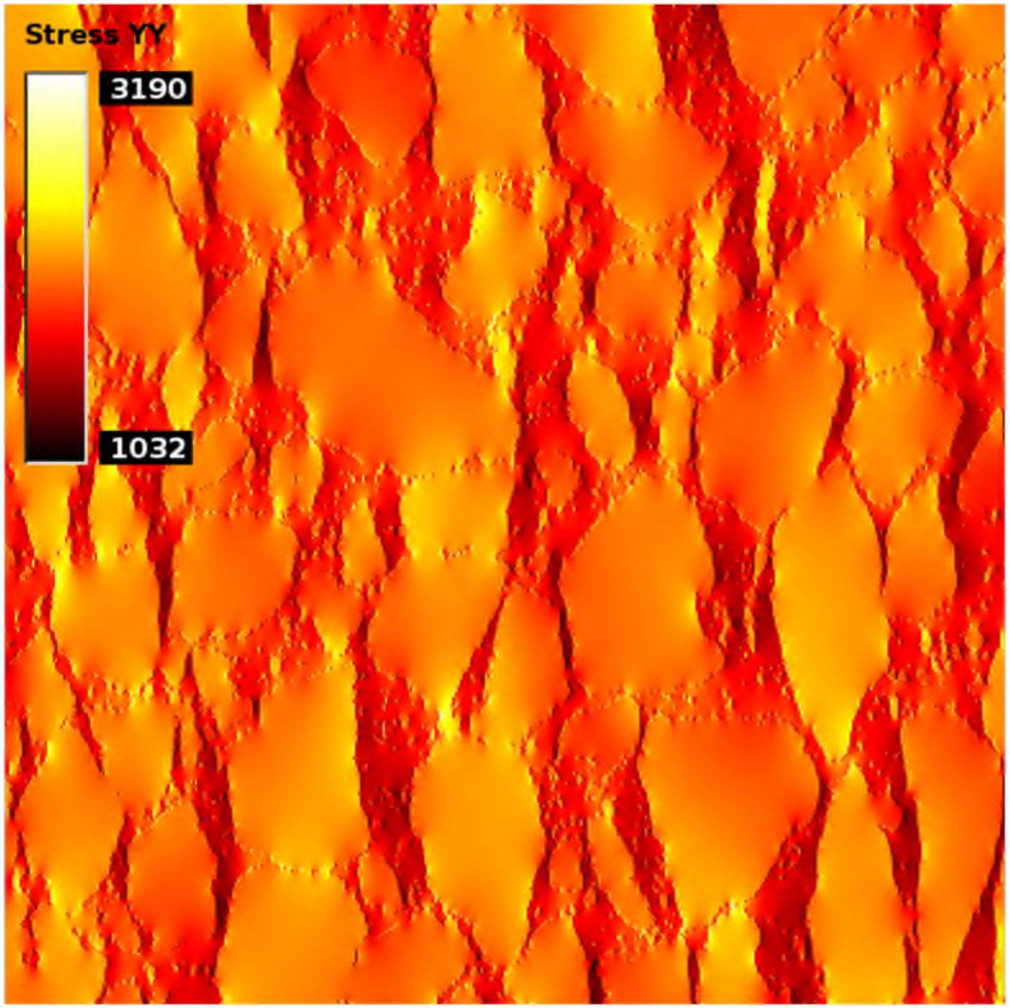

Figure 6.13. A stress map of the stresses in the vertical direction when a vertical load is modeled on an 80v% diamond micrograph, using plane stress assumptions. The stress concentrations are now oriented vertically. The contact points between vertical granules are now the points where stresses concentrate.

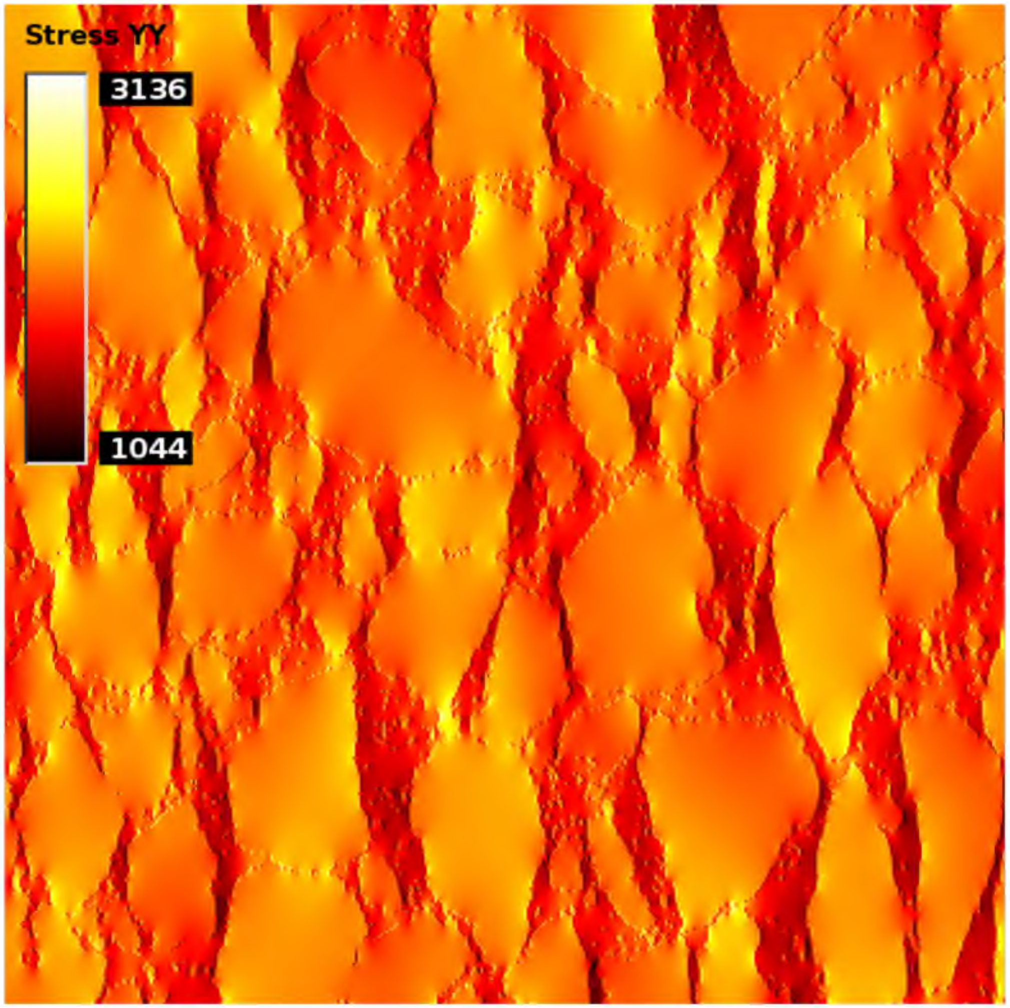

Figure 6.14. A stress map of the stresses in the vertical direction when a vertical load is modeled on an 80v% diamond micrograph, using plane strain assumptions.

Modeling Residual Stresses

Following the routine established in past models, the residual stresses developed post-sintering were modeled on these micrographs. The pressure and temperature changes listed in Table 6.7 were applied. Figures 6.15 through 6.18 show the residual stress maps for a 70v% diamond composite in both the lateral and vertical directions and for both plane stress and strain conditions. Notice that the diamond phase is put into compression by the residual stress, as is expected. Also note that the areas of the mesostructure which were stress risers in the applied stress maps are also stress risers in the residual stress maps. The areas where applied stresses will concentrate are the areas that are compressed the most by residual stresses. This has the effect of strengthening the weakest points in the mesostructure.

There is little difference in stress pattern between the plane stress and plane strain model, but the magnitude of the stresses in the plane strain model is greater.

Strength Modeling with Residual Stress

The stress maps including the residual stresses as well as the applied stresses are shown in Figures 6.19 through 6.22. The plane stress maps exhibit an interesting stress pattern. The stress orientation seems to be turned 45°. The magnitude of the stresses may appear high, but it is important to remember that these stresses are relative to the highly compressed sintering conditions. Taking the 5500 MPa pressure release and the 2000 N applied load into account, the stresses vary less than +/- 300MPa between the components and different areas of the mesostructure. The diamond granules are less

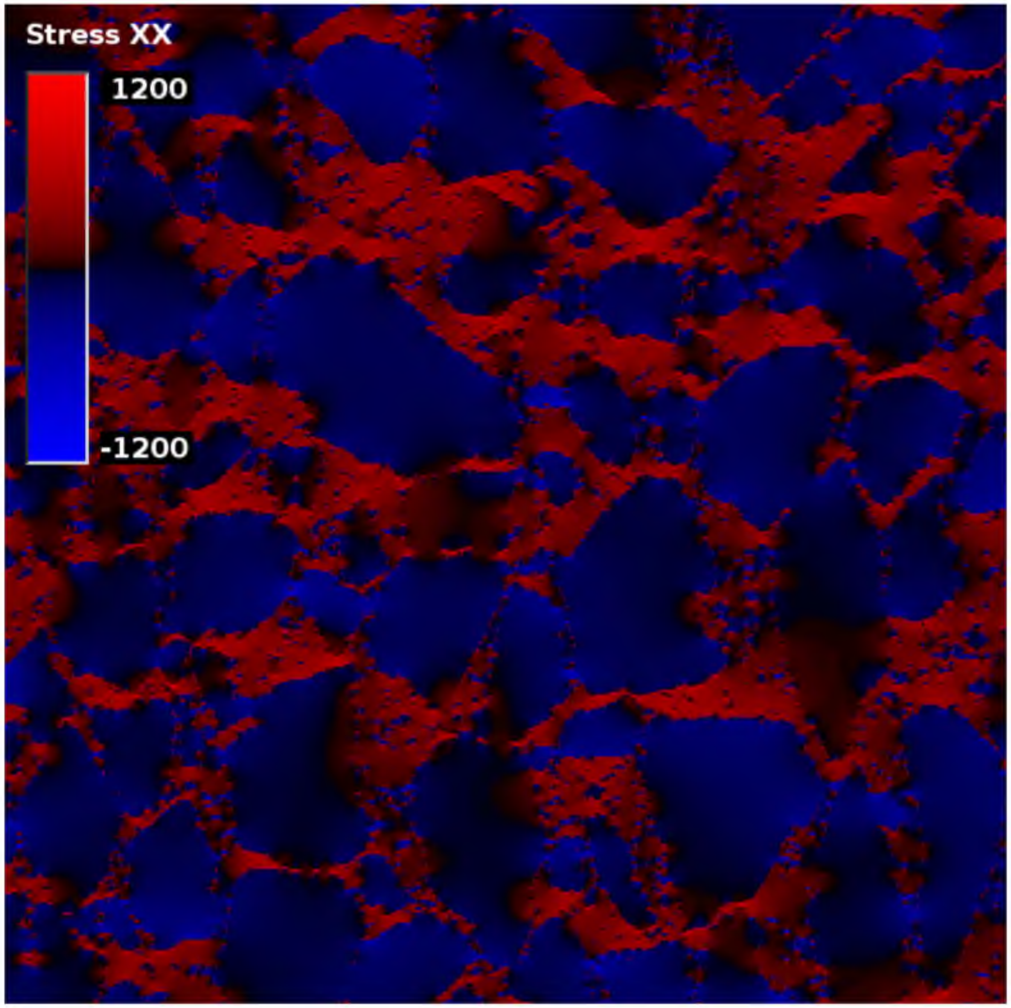

Figure 6.15. A map of lateral residual stresses (relative to sintering pressure) of an 80v% diamond micrograph, using plane stress assumptions. The color gradient shows tensile stresses in red and compressive stresses in blue. The areas of concentrated stress seen in the applied stress model are also the areas of stress concentration in the residual stress model

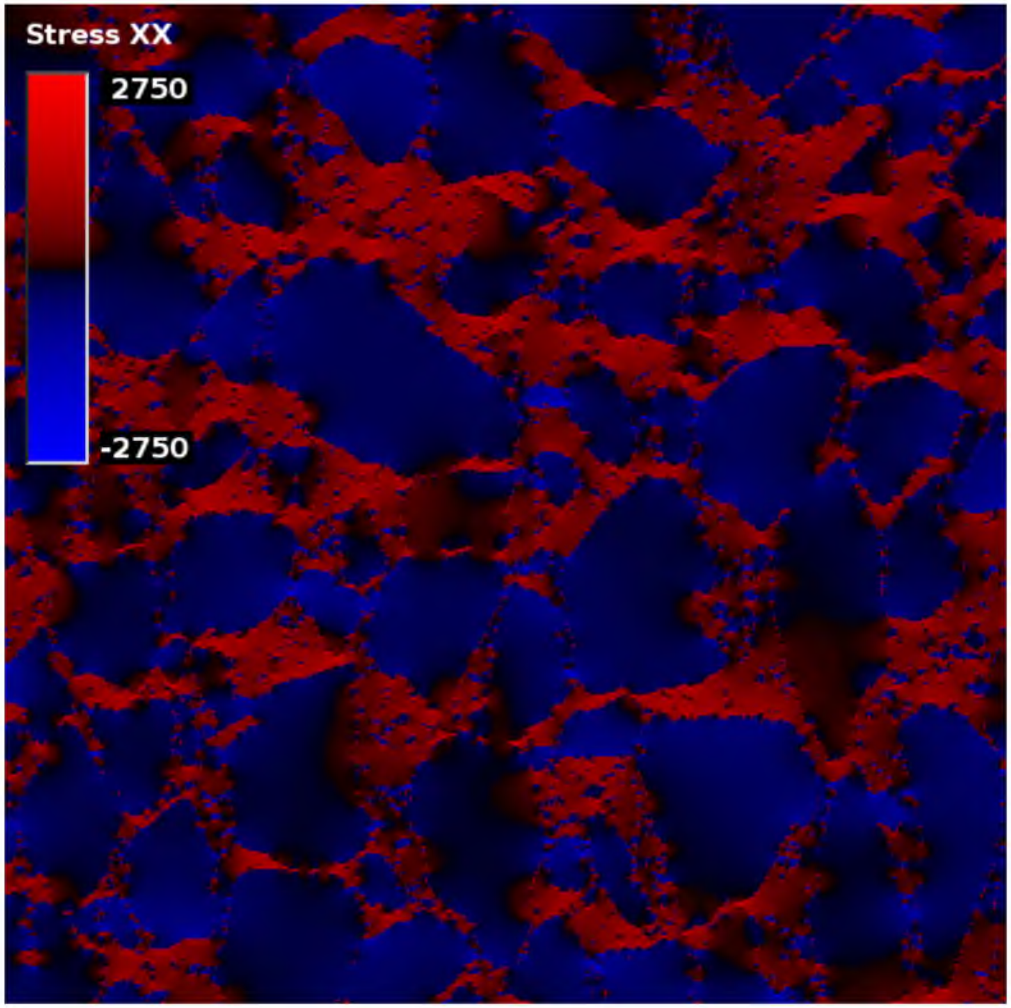

Figure 6.16. A map of lateral residual stresses (relative to sintering pressure) of an 80v% diamond micrograph, using plane strain assumptions. The stresses follow the same pattern as the plane stress model, but the magnitude of the residual stresses is greater in the plane strain model.

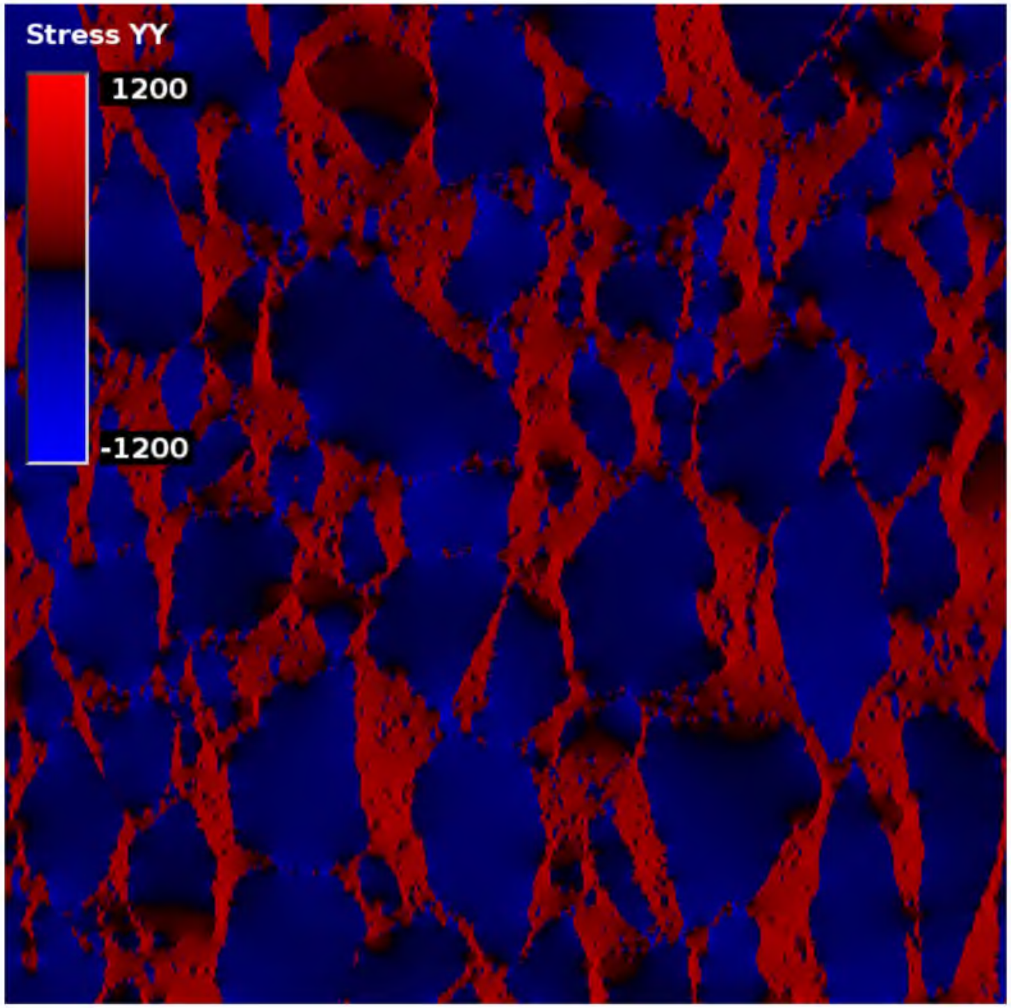

Figure 6.17. A stress map (relative to sintering pressure) of residual stresses in the vertical direction of an 80v% diamond micrograph, using plane stress assumptions.

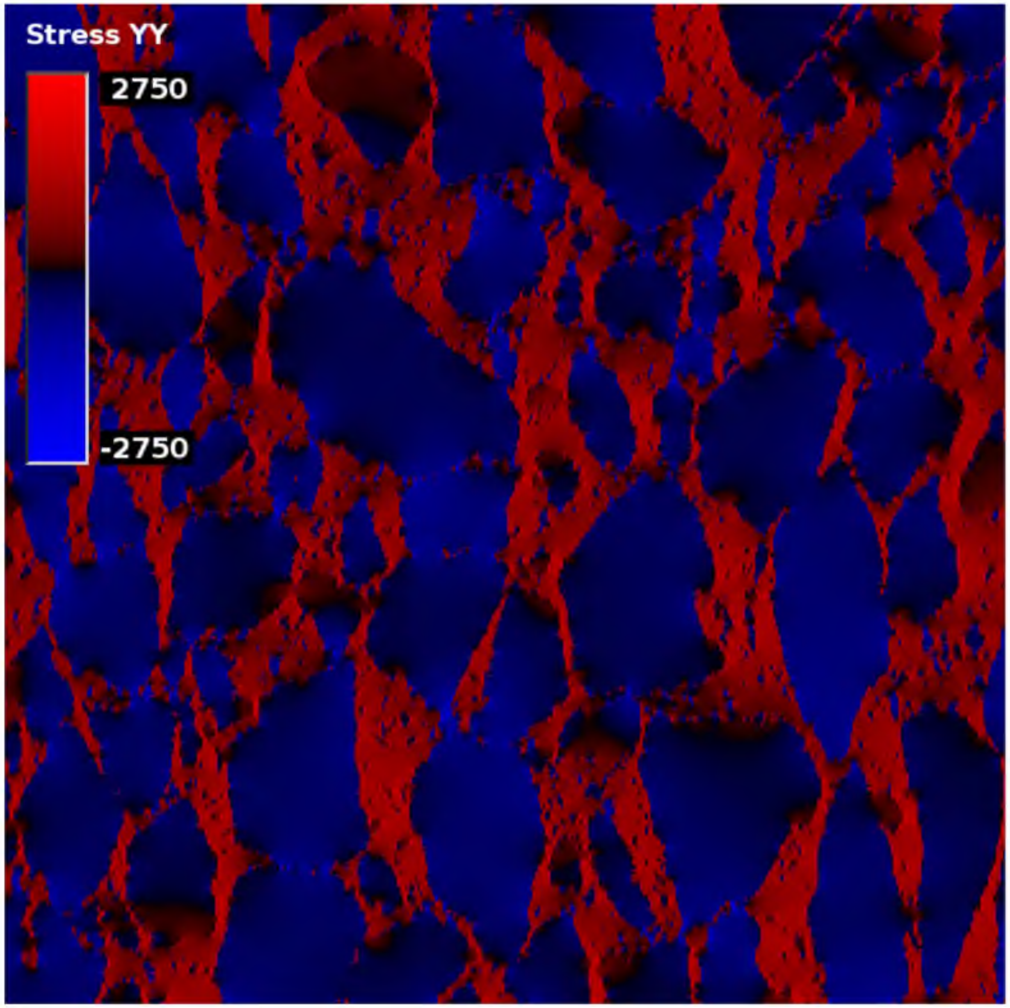

Figure 6.18. A stress map (relative to sintering pressure) of residual stresses in the vertical direction of an 80v% diamond micrograph, using plane strain assumptions.

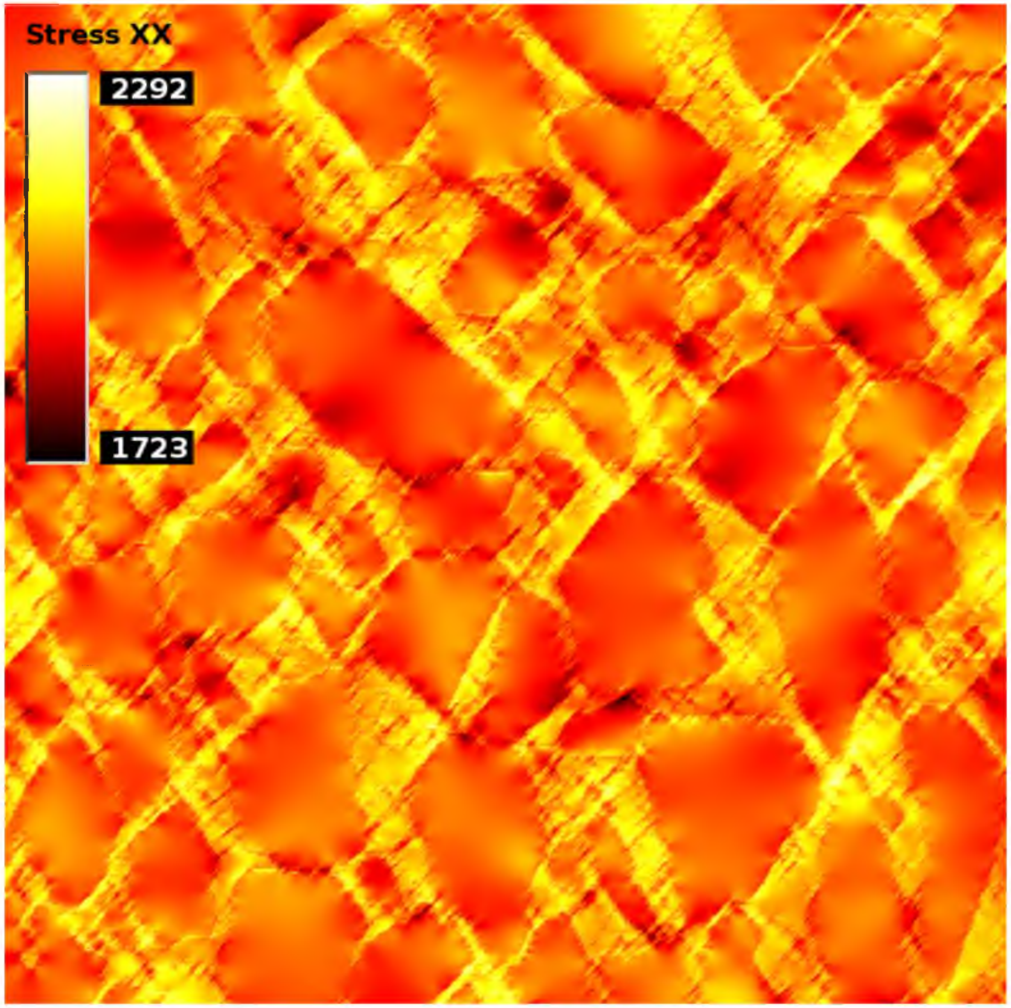

Figure 6.19. A stress map (relative to sintering pressure) showing the summation of the residual stresses and the applied stresses in the lateral direction, using plane stress assumptions. The stress is preferentially concentrated in the carbide matrix, but the range of the stresses is relatively low.

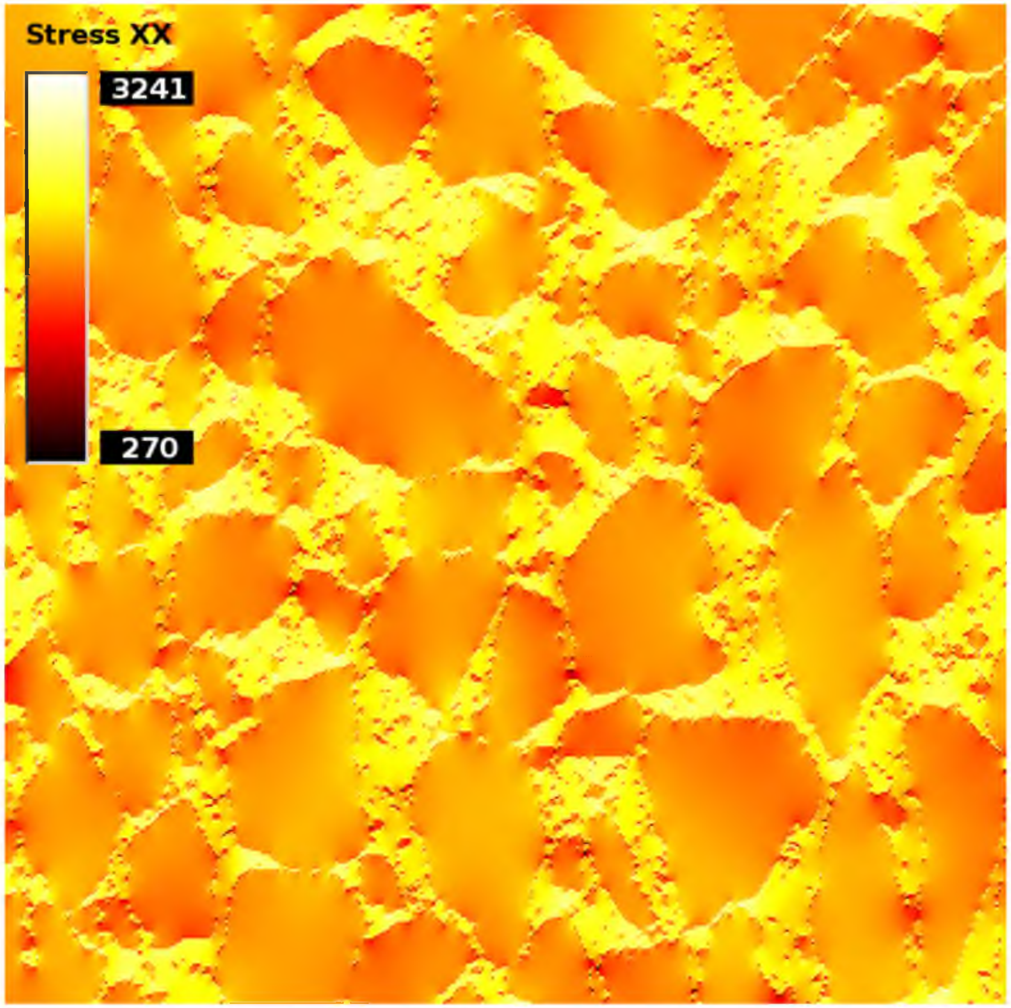

Figure 6.20. A stress map (relative to sintering pressure) showing the summation of the residual stresses and the applied stresses in the lateral direction, using plane strain assumptions. The range of stresses is relatively high. The areas of highest stress are in channels of matrix that run parallel to the applied load.

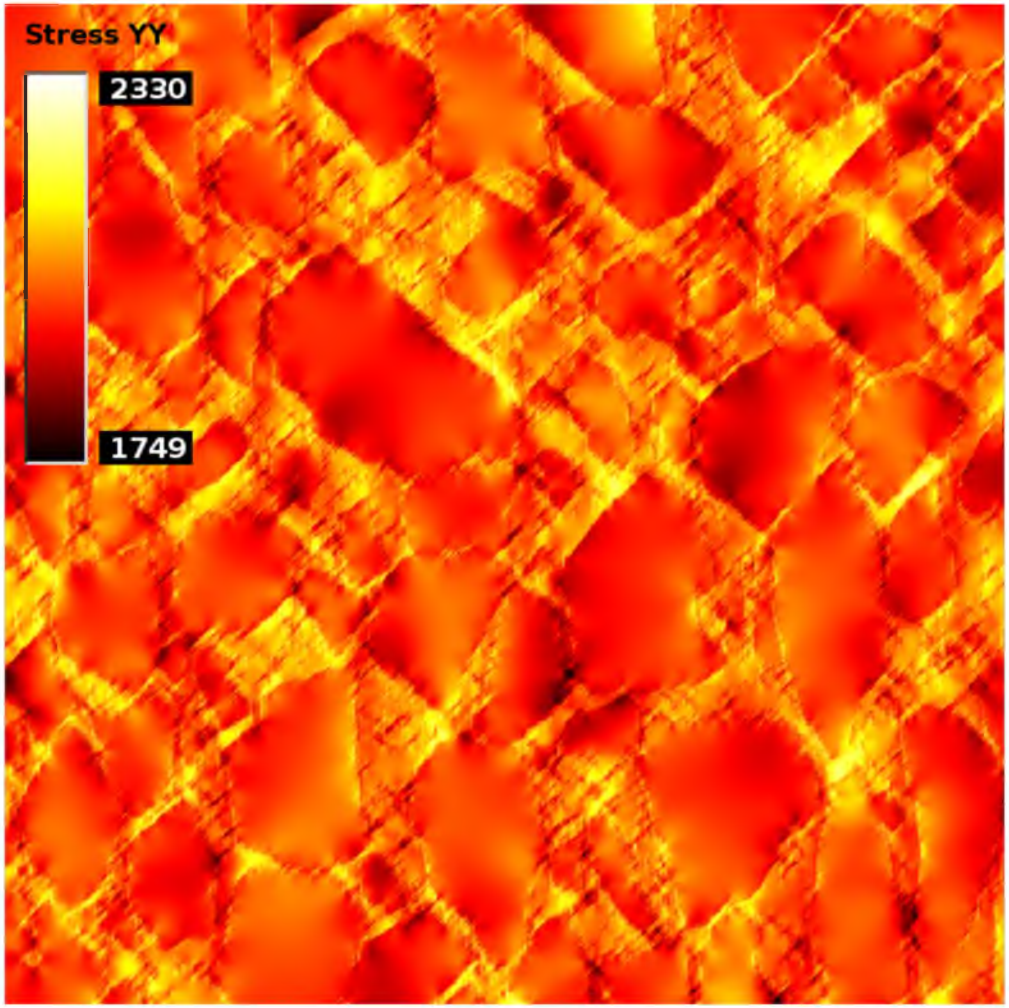

Figure 6.21. A stress map (relative to sintering pressure) showing the summation of the residual stresses and the applied stresses in the vertical direction, using plane stress assumptions. The stress is preferentially concentrated in the carbide matrix, but the range of the stresses is relatively low.

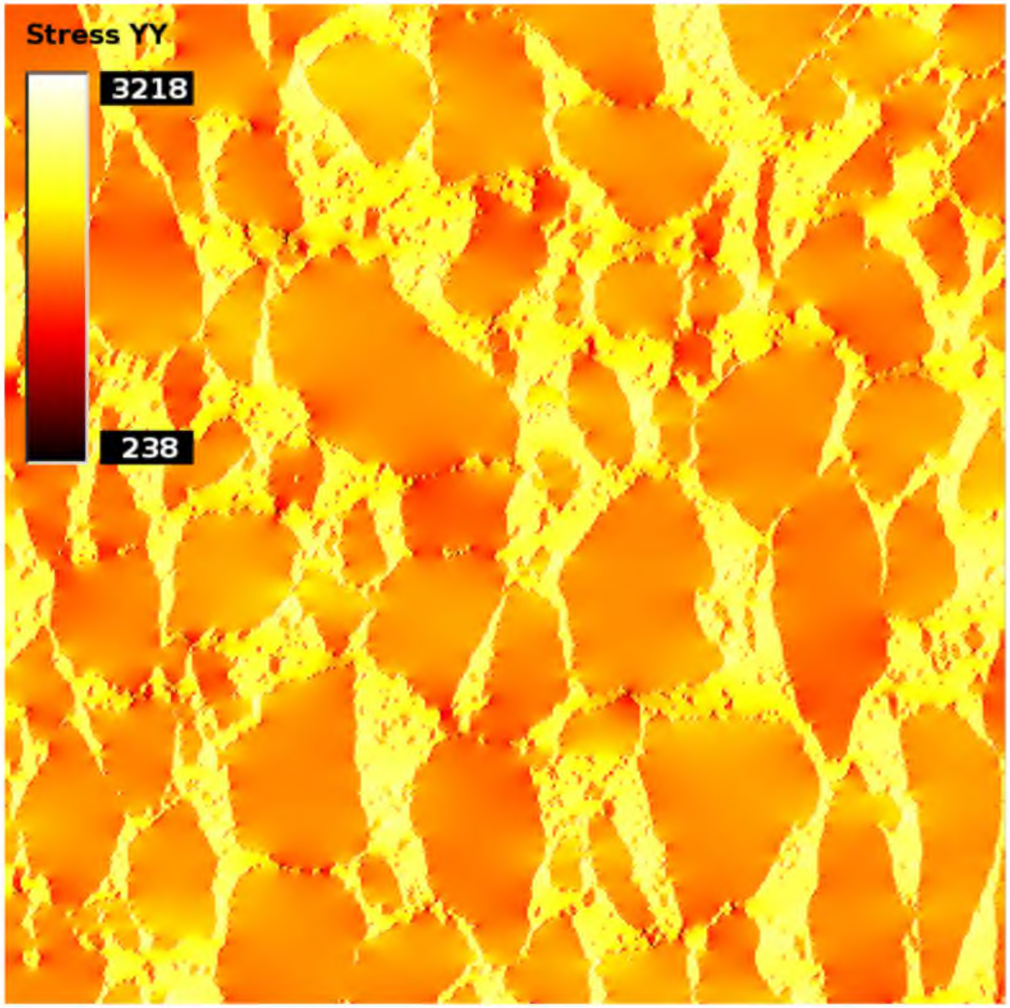

Figure 6.22. A stress map (relative to sintering pressure) showing the summation of the residual stresses and the applied stresses in the vertical direction, using plane strain assumptions. The range of stresses is relatively high. The areas of highest stress are in channels of matrix that run parallel to the applied load.

stressed than the matrix, but not by a large amount.

The stress pattern differences between the plane stress and plane strain simulations were relatively small when looking at the residual stress and the applied stress separately. But put together, the plane strain maps look quite different from the plane stress maps. If anything, the stress orientation appears to be perpendicular to the direction of applied stress. The areas of the highest stress are in the areas that showed the lowest amount a stress in the applied stress analysis. But these are the same areas which had the highest residual stresses. These areas of high stress all occur in the carbide matrix and the range of stress is more than five times larger than in the plane stress analyses.

Before considering the residual stresses, it appeared that the weakest points of the mesostructure would be where the diamond granules contact each other in the direction of the applied load. When considering the residual stresses alone, the areas of highest stress concentration occur in thin channels of carbide matrix running parallel to the applied load. The combined analysis shows that the residual stresses are more than sufficient to protect the narrow necks between diamond granules, but the high stress points in the carbide matrix remain.

When using the slab model there was one stress in the diamond phase and one stress in the carbide phase. In the 2-D OOF models, the mesostructure causes large variations of stresses throughout the phases. Instead of having one strength for the entire phase, each pixel in the model has its own strength. A method was used to simulate the flexural strength measurement obtained in a three-point bend test. In a three-point bend test, tensile stresses are maximal along the center line between the two supports, opposite the single support (refer to Figure 3.9). It is assumed that the specimen will fail along this line of maximum tension. To represent this, the material models were subjected to axial tensile loads along with the residual stresses and the resulting stress was recorded along a line perpendicular to the applied stress. In the 2-D OOF model the whole face experiences the same load, rather than only a single line of maximum load. This allows multiple lines of stress to be recorded from each image. The stress lines were recorded after the residual stresses were applied and again after both the residual stresses and the test loads were applied. This is illustrated in Figure 6.23.

The flexural strength of each stress line can be calculated separately, much like the testing of several specimens in a batch. The flexural strength of the material at the stress line is taken to be the lowest applied stress which will cause any element along the line to fail. An element is assumed to fail if the stress in the element exceeds the critical stress for the element's material. The applied stress which causes the element to fail is calculated by equation 6.3. The critical stress of PCD and WC-Co were taken to be the flexural strength experimentally measured in the three-point bend tests of the all WC-Co (0% PCD granules) and all PCD (100% granules) specimens respectively, which is shown in Table 6.7. The stress can be applied in the vertical direction and data can be collected in lateral lines to increase the samples collected from each micrograph. Nine lines were recorded perpendicular to the laterally applied load and nine lines were taken perpendicular to the vertically applied load for a total of 18 simulated transverse rupture strength (TRS) measurements from each micrograph.

The OOF results of the plane stress and plane strain models are shown in Figure

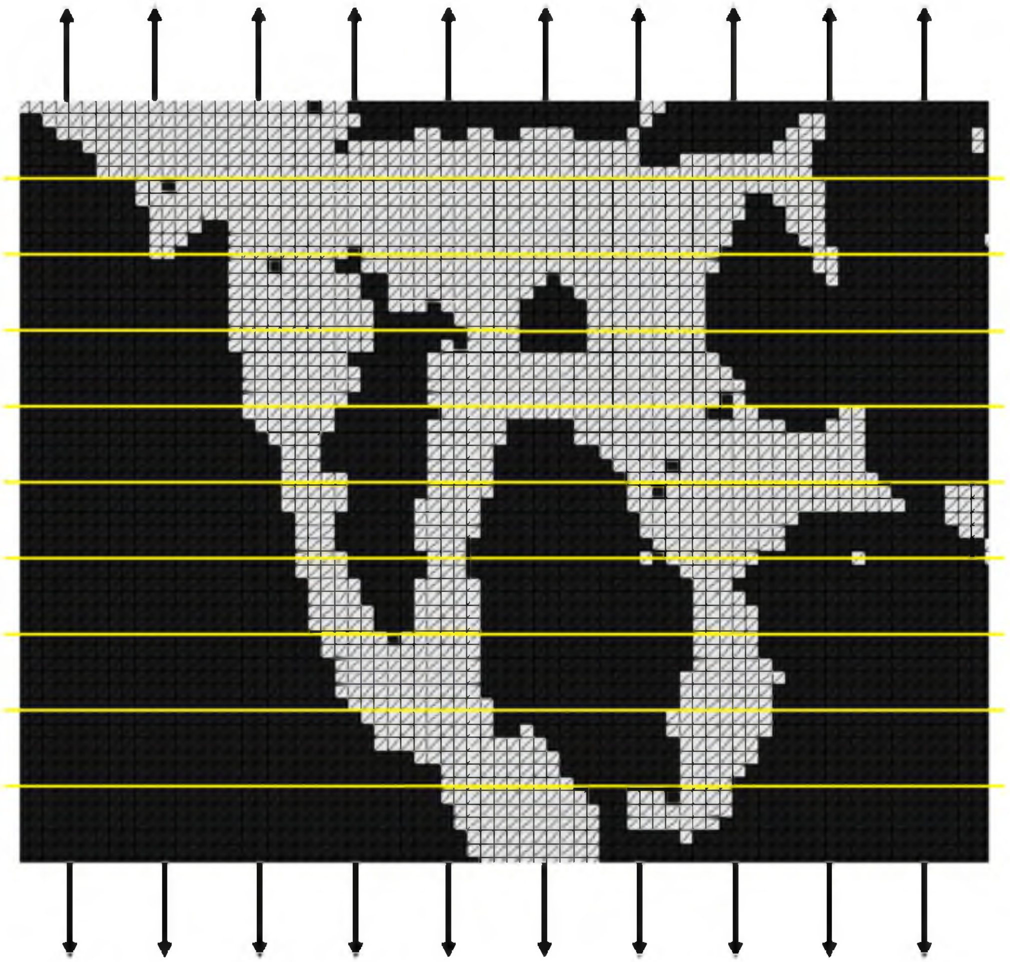

Figure 6.23. Depiction of the nine lines where stresses are recorded to simulate TRS tests.

6.24 along with the experimental and analytical results.

The results from the plane stress model are shown in red. The PCD phase failed first when using plane stress assumptions. The WC-Co phase was more heavily loaded, but the higher strength of the carbide was sufficient to keep it from failing before the diamond. The error bars plot +/- one standard deviation. This shows that there was relatively little variation in the strength measurements. This is because of the small variation in stresses seen in Figures 6.20 and 6.22.

The results from the plane strain model are shown in blue. Under plane strain assumptions, the carbide matrix fails first. This is because the residual stresses are so high in the carbide phase that the applied stresses exceed the strength of the stronger phase before the weaker diamond fails. The trend and the variance in the plane strain model resemble the experimental results, but the 2-D model predicts lower strengths across the spectrum. This may suggest that the residual stresses are being over estimated.

The multiple simulated TRS measurements can be used to create simulated Weibull plots, as shown in Figure 6.25 and Figure 6.26. These graphs should be compared to the Weibull plots of the experimental data which is found in Figure 4.4. Typical Weibull variation includes contributions from the distribution of flaws, experimental errors, and other factors. The composite strength will also vary due to the inhomogeneity of the mesostructure. The data scatter from the numerical model is due solely to this inhomogeneity, therefore the 0 and 100v% materials have no scatter at all in the numerical model. The method of modeling employed in this study can be used to study the contribution of mesostructural inhomogeneity to the variation in the flexural

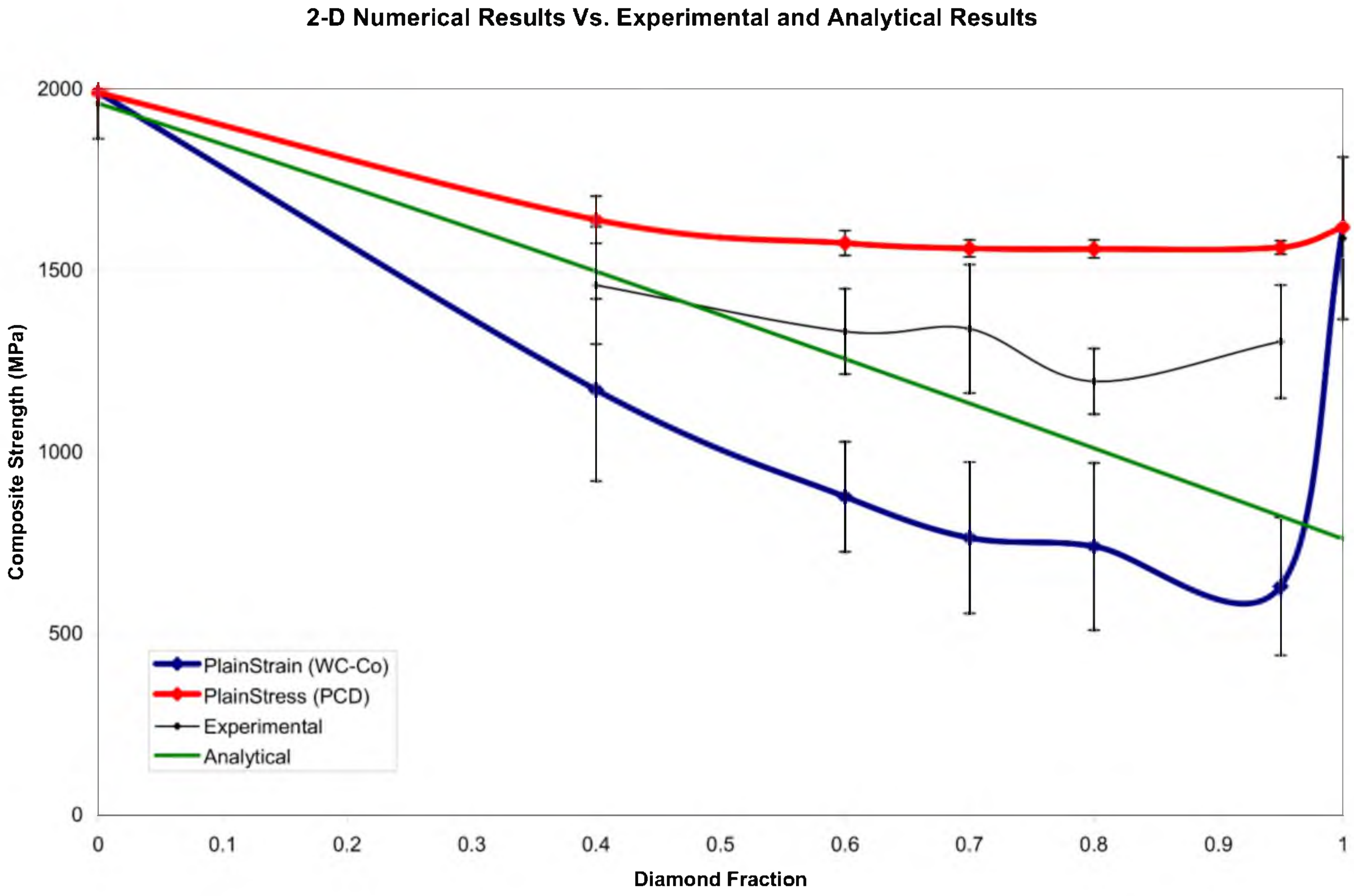

Figure 6.24. Flexural strengths of granular diamond composites estimated in a variety of methods. The plane stress 2-D strength estimates are high compared to the analytical and experimental results. The plane strain results are low compared to the other methods, but closely follow the measured trend.

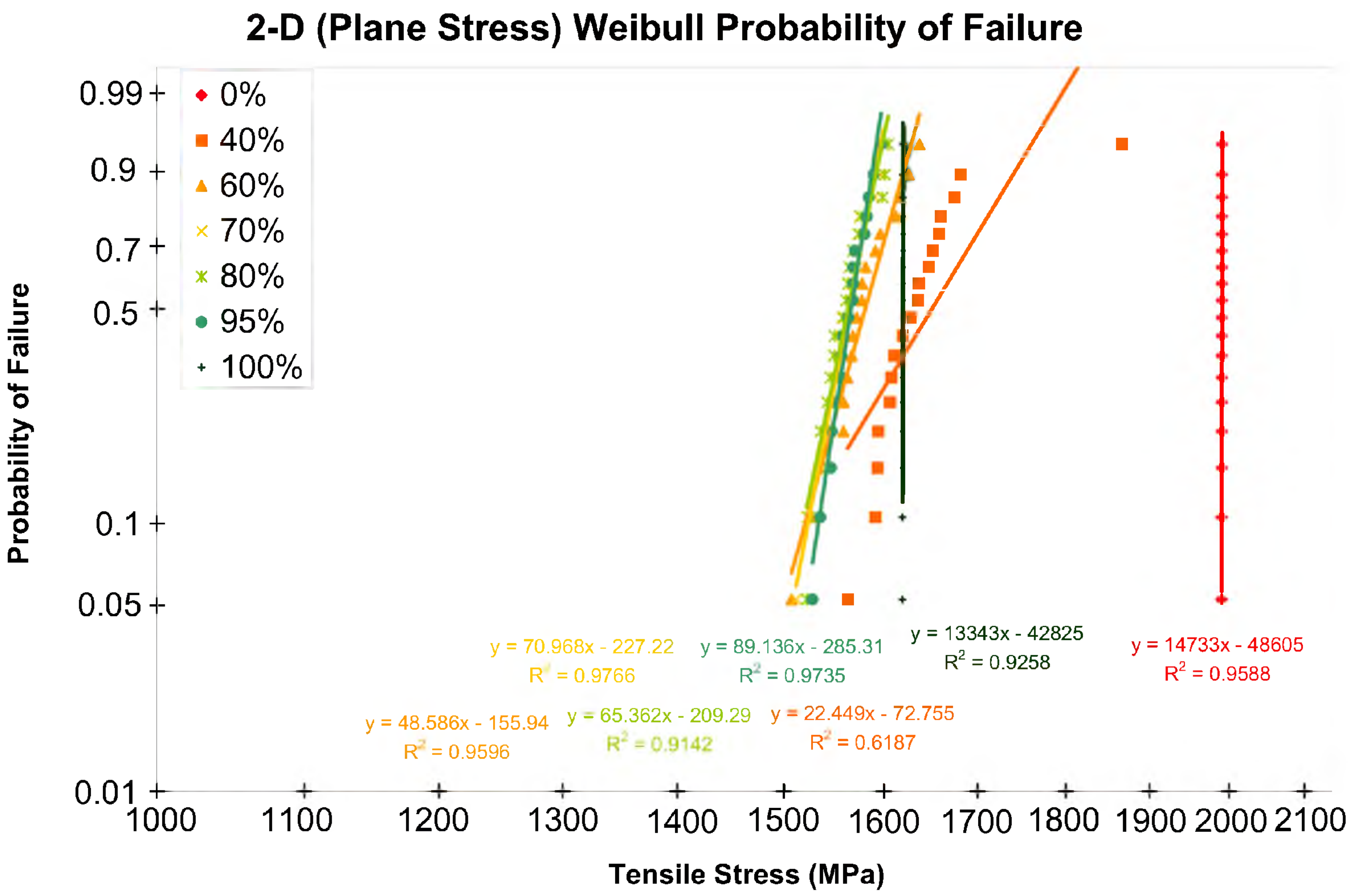

Figure 6.25. Weibull plot of the 2-D strength data using plane stress assumptions. The data has higher Weibull moduli than the experimental data. The variations are due to the inhomogeneities in the mesostructure. The 0v% and 100v% diamond composites do not have a mesostructure and therefore do not have any variation.

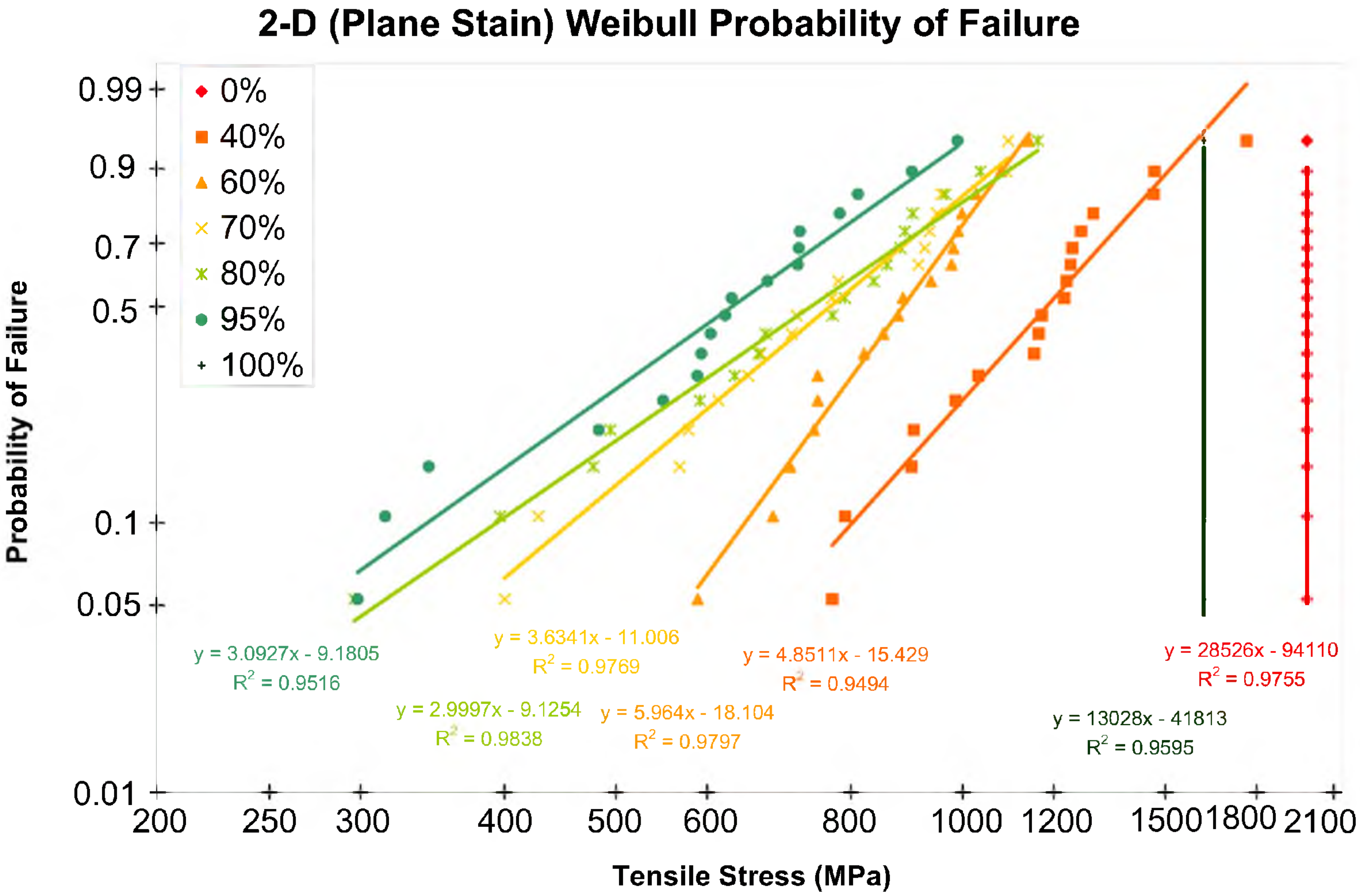

Figure 6.26. Weibull plot of the 2-D strength data using plane strain assumptions. The data has lower Weibull moduli than the experimental data. The variations are due to the inhomogeneities in the mesostructure. The 0v% and 100v% diamond composites do not have a mesostructure and therefore do not have any variation.

strength.

The plane stress 2-D model Weibull graph shows only a small amount of variation, less than the variation measured in the experiment. This error is due only to the mesostructure. If this model were assumed to be accurate, the majority of the strength variation in the empirical data would be attributed to traditional Weibull factors, like flaw distribution, rather than the inhomogeneity of the mesostructure.

The plane strain data, on the other hand, shows more variation than the experimental data. This model would suggest that most of the variation in strength is due to the inhomogeneity of the mesostructure.

3-D Numerical Modeling

Three-dimensional modeling was also used to explore the impact of mesostructure on the predicted behavior of granular diamond composites. Three-dimensional modeling trades off larger data sets and more intense computing for a reduction in the number of assumptions that are needed, most notably, the plane stress or plane strain assumptions that were required using the 2-D OOF model.

In general, the results of the 3-D modeling coincided with the results from the other models. Less assumptions were used and this helped validate the assumptions used in previous models. The calculated strength values were even closer to the values measured in actual laboratory experiments. The 3-D modeling provided even greater insight into the mechanisms that control the flexural strength of granular diamond composites.

Obtaining a 3-D Mesostructure Representation

The first difficulty in modeling the stresses and strengths of a 3-D mesostructure was obtaining a 3-D representation of the mesostructure. The initial intent was to collect microCT data on each of the grades in Series A. This proved to be too costly and difficult. The modeling, therefore, was conducted using simulated 3-D mesostructures. A program was written to generate the simulated mesostructures as closely as possible to the actual mesostructures observed in micrographs of Series A material.

One data set was collected of a 80v% diamond composite, A80k, using a 3-D microCT scanner. The high average atomic number of tungsten carbide made the collection of X-rays difficult. It limited the size of the specimen and increased the scan times required to obtain a usable resolution. Further processing of this data set was complicated by the relatively low resolution of the data set in comparison to the feature sizes of the mesostructure and by the fineness of the mesh required to capture the tomography. The feature sizes and fineness of the mesh limited the size of subsample that could be processed because of limitations in computational power.

Figure 6.27 is several 2-D views of the scanned 3-D microCT data for the A80k grade of GDC. Figure 6.27a shows one-quarter of the total scanned volume. The bright phase is the denser carbide and the gray phase is the diamond. Figure 6.27b is a subsample that was isolated for further processing. Note that most of the grains are clipped by the boundary of the subsample. This would have made the quantitative volume analysis less accurate. Figure 6.27c is the same subsample that has been converted to a binary data set, which each phase being assigned a uniform gray value. Figure 6.27d is a

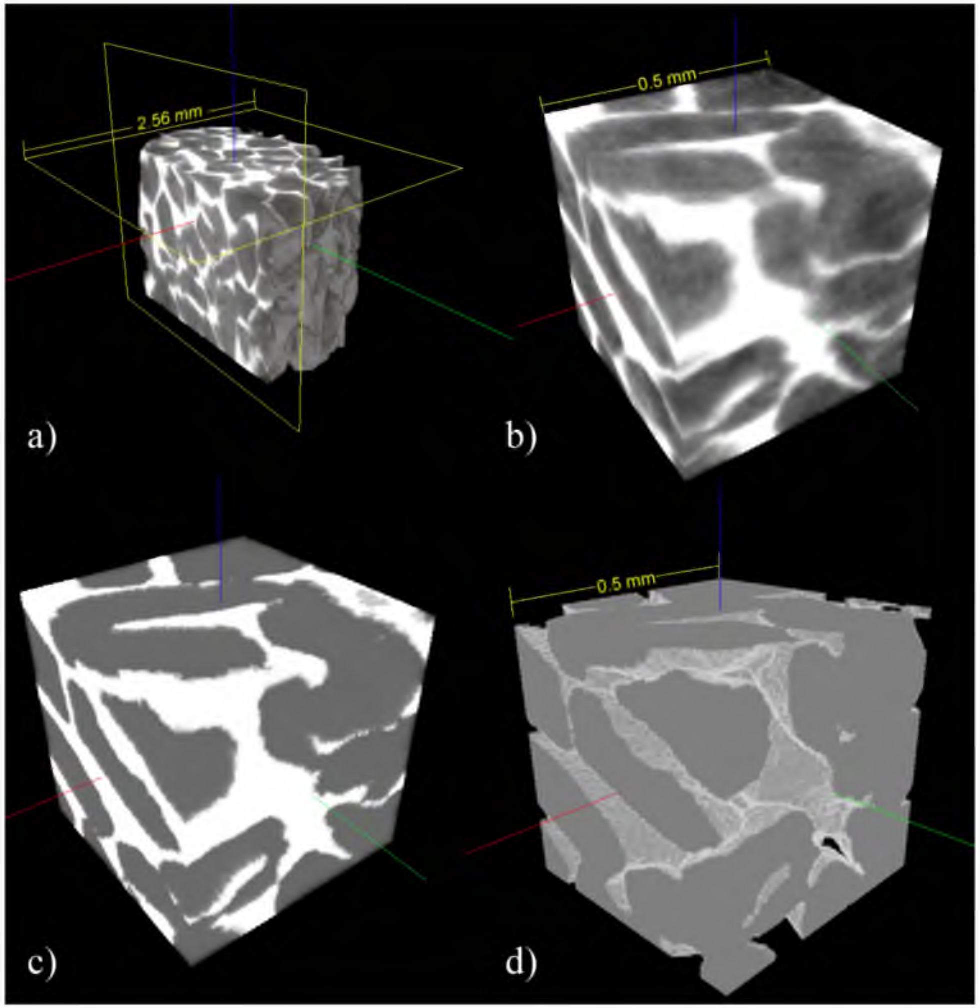

Figure 6.27. a) One-quarter of the total scanned volume. The bright phase is the denser carbide and the gray phase is the diamond. b) Subsample that was isolated for further processing. c). The same subsample that has been converted to a binary data set. d) The same subsample with the carbide matrix hidden.

view of the subsample with the carbide matrix removed.

Due to the difficulties in obtaining usable microCT data of actual mesostructures, a program was written to produce simulated 3-D mesostructures similar to the mesostructure seen in GDC SEM micrographs. Given the 3-D nature and the size of the datasets, manually creating the mesostructures was not practical. The program was written in the Java programming language and the input parameters were adjusted to produce mesostructures which resembled the mesostructures produced in the laboratory. Simulated mesostructures were created for eight volume fractions between 28v% and 95v%. Code for the program is given in Appendix A.

A 3-D array of voxels was created of the dimensions 64 × 64 × 64, measuring 1 mm on each side. Seeds were randomly distributed throughout. The seeds were grown into granules by evaluating the probability of each vacant voxel becoming part of a granule at each time-step. The probability was affected by the number and proximity of neighbor voxels which are part of existing granules. In order to maintain some separation between granules, individual granules retarded the growth of other granules nearby.

Figure 6.28 is an image of a 67v% simulated mesostructure. Compare this mesostructure to that shown in Figure 6.29, which is a micrograph of a 70v% GDC produced in the laboratory, A70a. One obvious difference is that the simulated mesostructure is blocky or "pixelated." This is due to the nature of how the mesostructure was produced. Significant efforts were made to convert a blocky mesostructure into a smooth representation. This was accomplished for a few mesostructures yielding acceptable results, but these smoothed mesostructures proved to be extremely difficult to

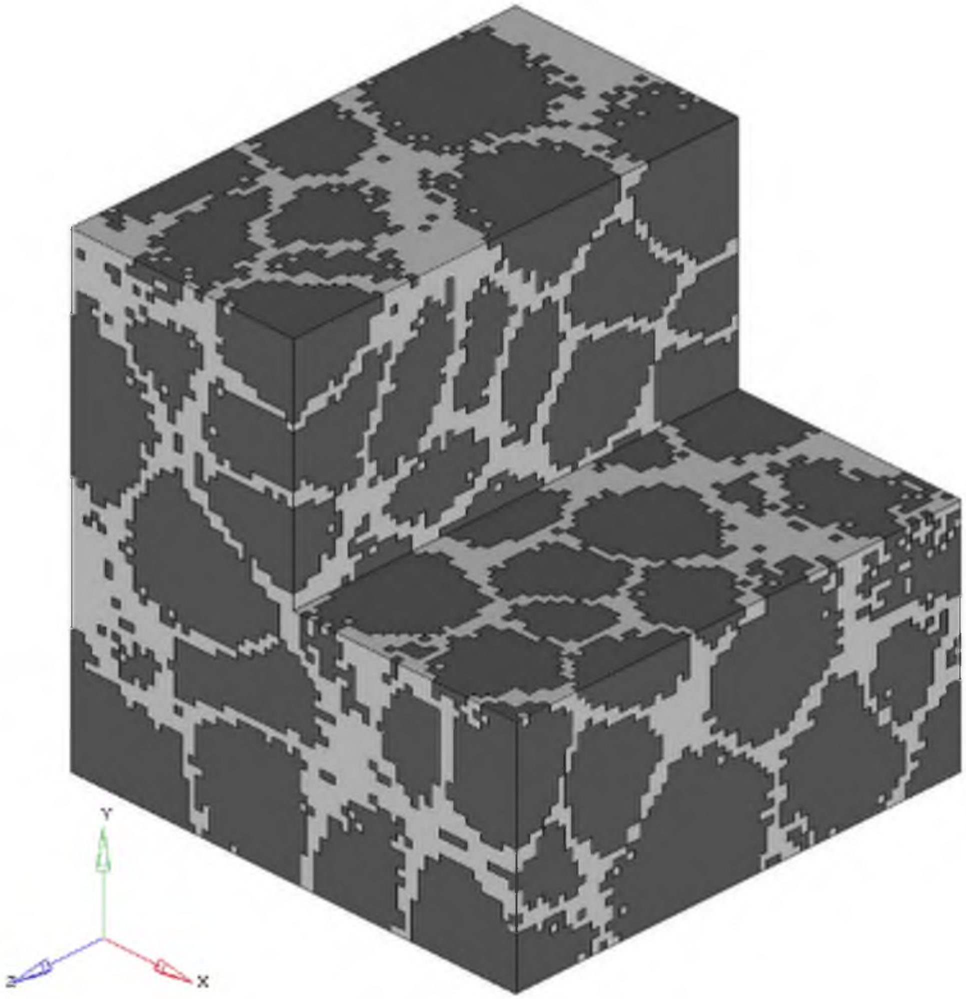

Figure 6.28. Image of the simulated 67v% mesostructure. A section of the model has been removed to reveal part of the interior. Each voxel of the simulated mesostructure has been converted into a hexahedral finite element.

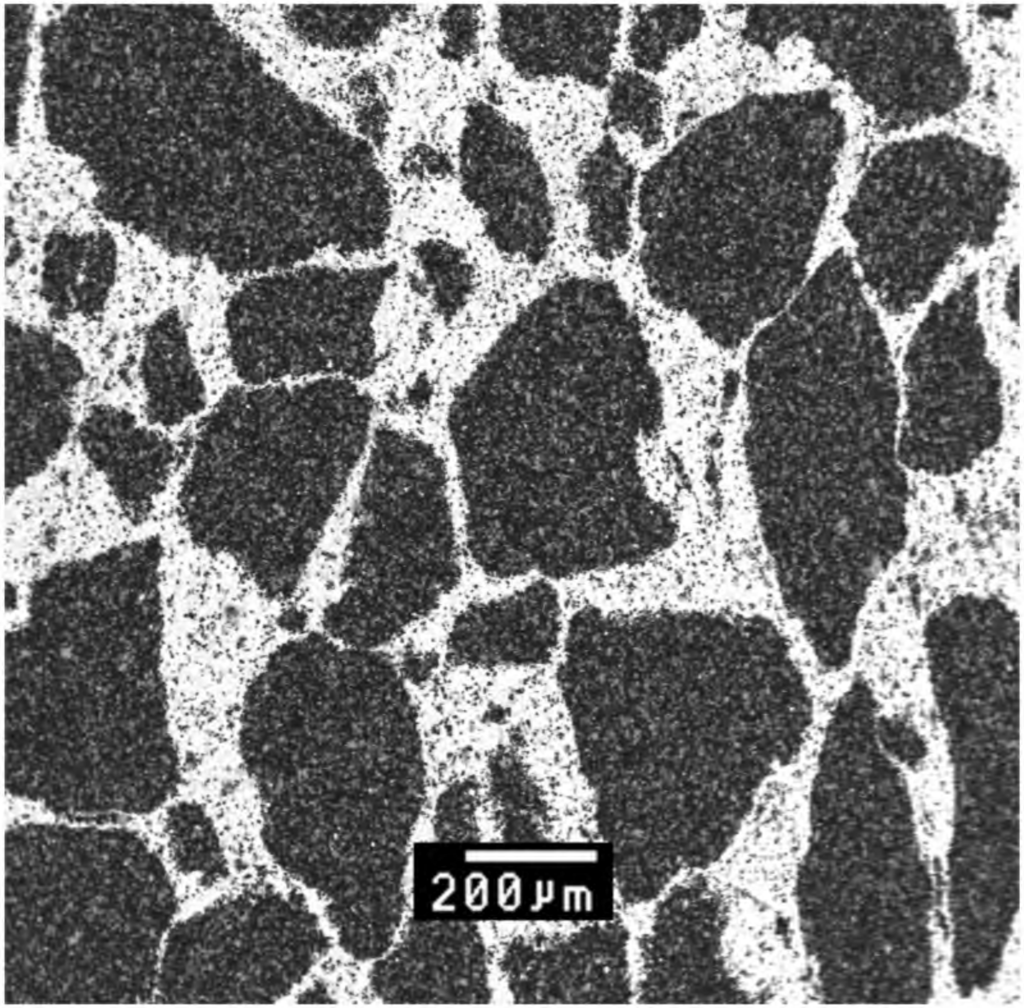

Figure 6.29. Micrograph of a 70v% GDC. The edges of the granules are smoother than the finite model representation.

mesh with satisfactory results. It was found that meshing the voxelated images directly produced better results than the results from the smoothed mesostructures. A data smoothing method was used on the FEA results.

The simulated mesostructure is visible for other diamond volume fractions in later figures showing the results of the stress modeling.

Modeling 3-D Residual and Applied Stresses

The simulated mesostructures were subjected to the same now-familiar modeling procedure as has been used previously in this study. The applied stresses and the residual stresses were evaluated separately, and then were combined to determine the strength of the composite. The HyperWorks FEA software suite by Altair was used to evaluate the simulated mesostructures. The model uses hexahedral elements to model each voxel. The nodes on all of the faces are constrained to displace uniformly together to eliminate any macro shear in the model. Material properties were assigned from Table 5.2.

The three-point bend loading was modeled, with a single axial force being applied to a face that is normal to the X axis. The load was selected to be 2000 N, which produced an average stress of 2000 MPa, which is roughly the magnitude of the critical stresses of the modeled materials. The thermal residual stresses were modeled with a -973°C thermal load applied to each node. The dilatational residual stresses were modeled with a pressure change of -5500 MPa applied to all external nodes. The models were solved for conditions of: Load Only, Thermal Residual Stresses, Dilatational Residual Stresses, Total Residual Stresses, and Total Residual Stresses with Load. Figure

6.30 is an image of a 28v% simulated mesostructure with some of the boundary conditions and applied load.

Results

Residual stress maps of all of the simulated mesostructures were produced. The residual stress maps for 58v% and 74v% are shown in Figures 6.31 and 6.32, respectively. The color gradients are set by the maximum or minimum stress value and are centered about zero. Green indicates near neutral stresses moving into the blues for compression and toward red for tension.

In all residual stress instances, the diamond granules are put into compression and the carbide matrix is in tension, but the amount of stress is not uniform throughout the mesostructure. Stresses are concentrated where narrow necks of material bridge between phases. In composites with more carbide, the magnitude of the stresses in the diamond phase are higher. In composites with less carbide, the stresses in the carbide are greater. All of these phenomena have been seen in previous models.

Stress maps were produced of the residual stresses with applied load models. Stress maps for 58v% and 74v% are shown in Figures 6.33 and 6.34, respectively. The color gradients are still centered about zero, but the colors in the maps are all reddish because the applied load has placed all of the material into tension.

Even though the diamond phase is stiffer than the carbide phase, all of the stress maps show that the matrix is in greater tension than the granules. This is due to the residual stresses which placed the matrix into tension to begin with and moved the

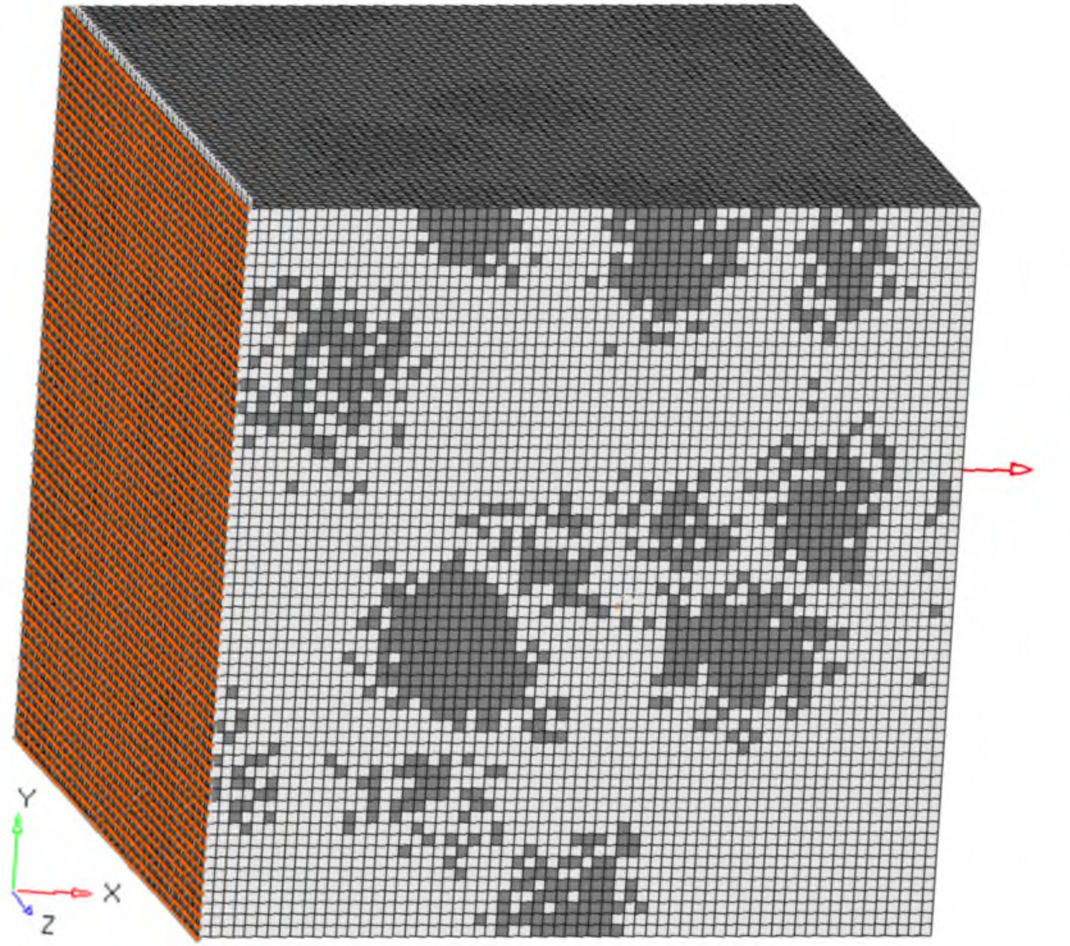

Figure 6.30. Image of the simulated 28v% model. Some of the boundary constraints are visible. The red arrow represents the applied load. The orange anchors represent displacement constraints on individual nodes.

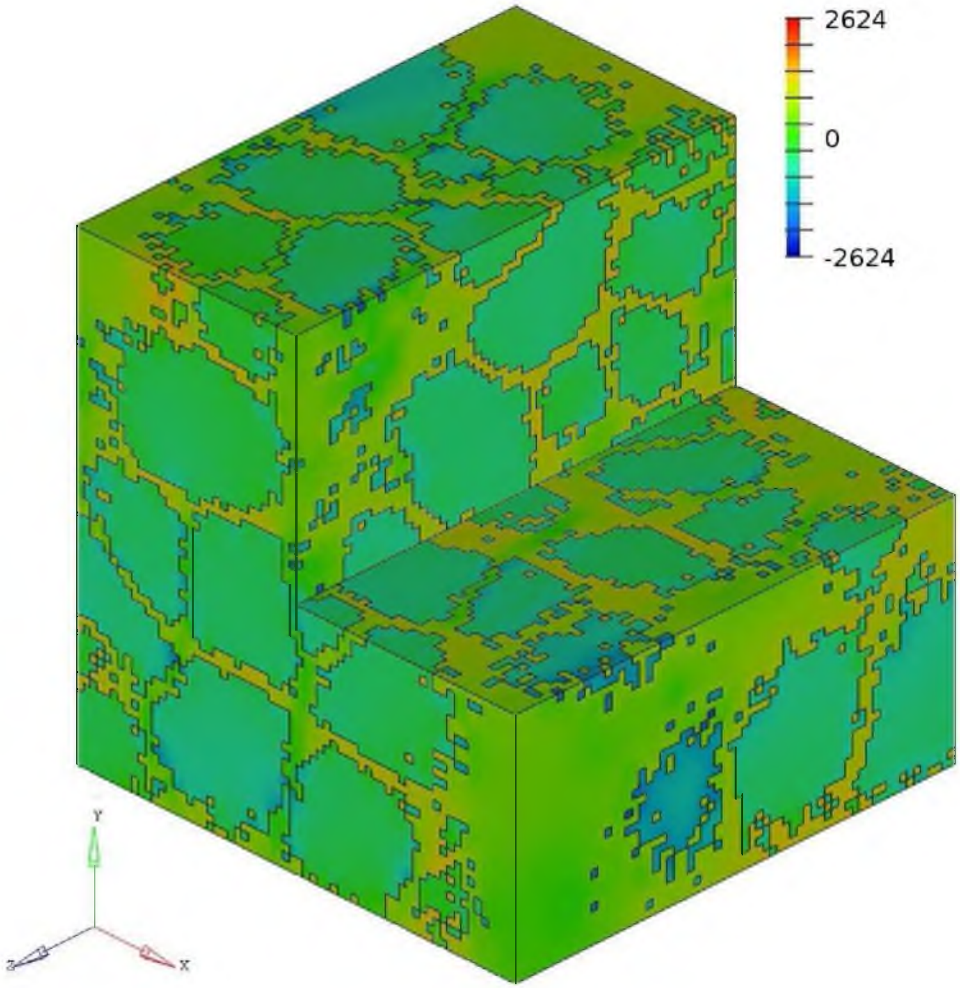

Figure 6.31. Stress map showing the residual stresses in a 58v% simulated mesostructure. With a relatively large amount of carbide phase, the diamond phase accumulates higher stresses.

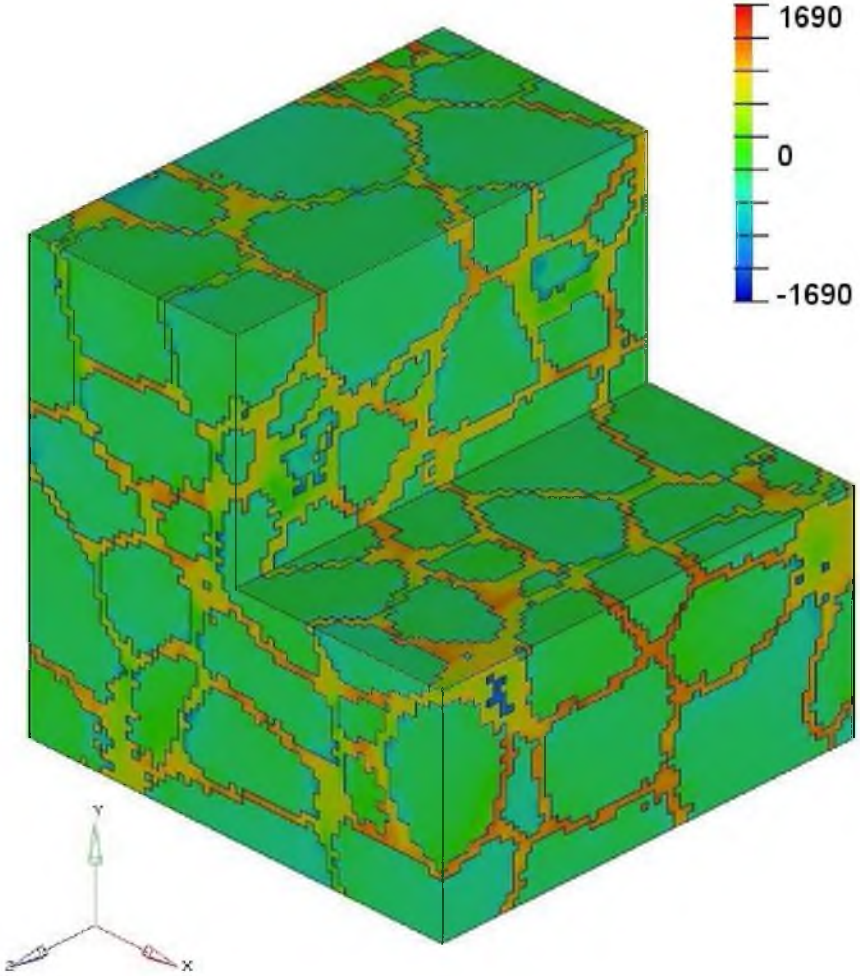

Figure 6.32. Stress map showing the residual stresses in a 58v% simulated mesostructure. With a majority of diamond phase, the carbide phase accumulates higher stresses.

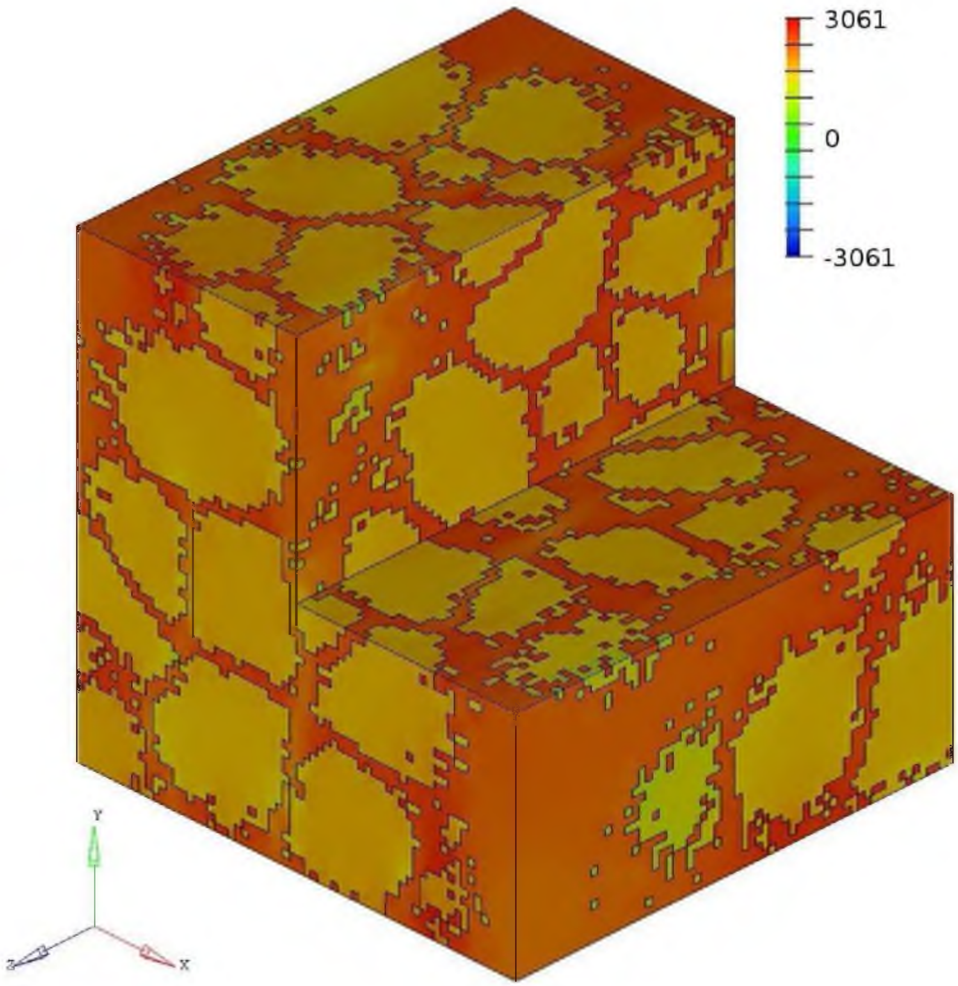

Figure 6.33. Stress map showing the total stresses in a 58v% simulated mesostructure. The stresses are relative to the sintering pressure. The stresses are 5500 MPa lower relative to atmospheric pressure.

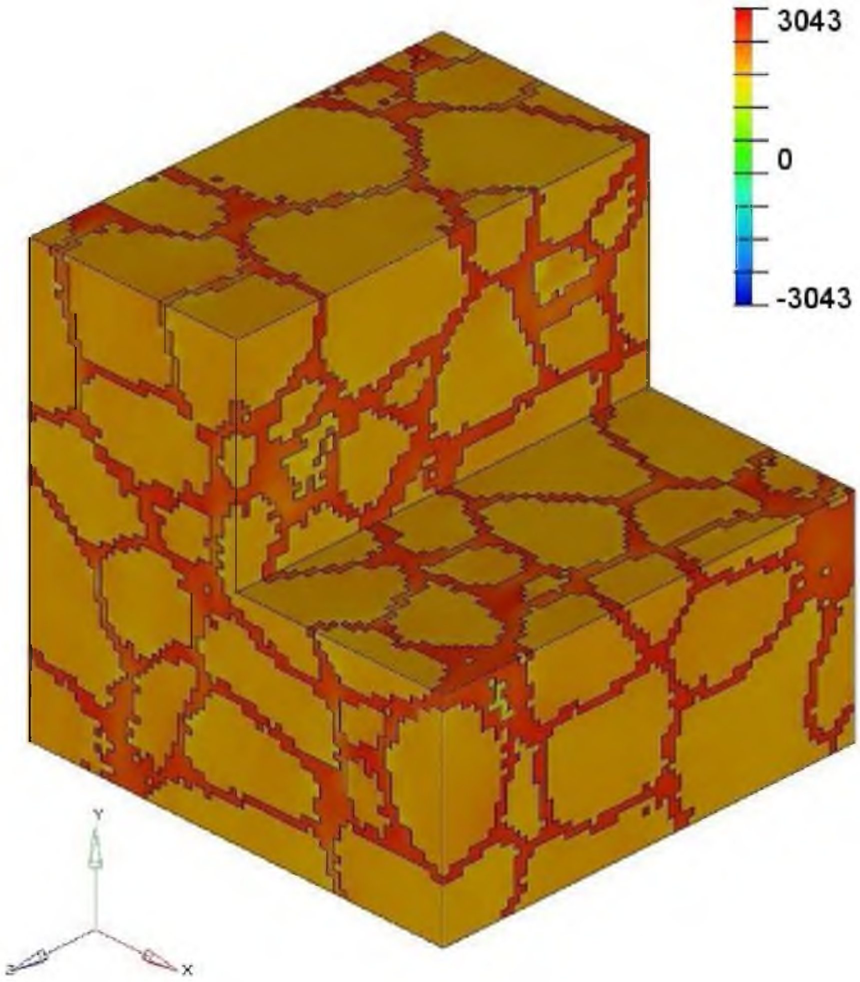

Figure 6.34. Stress map showing the total stresses in a 74v% simulated mesostructure.

granules into compression. Likewise the areas of stress concentration in the diamond are not experiencing significantly more tension due to the concentration of the compressive residual stresses.

The flexural strengths of the simulated mesostructures were estimated using a technique similar to the one used in the 2-D OOF modeling. The TRS was estimated from the distribution of strengths calculated along many lines perpendicular to the external applied stress. The strength along the line was determined by evaluating the flexural strength at each voxel along the line.

The flexural strength of an individual voxel was estimated by using the total residual stress and the voxel's stress intensification factor to determine the external applied stress that would cause the voxel to reach the critical stress for its material (see equation 6.3).

The strength along a single line perpendicular to the applied load is an approximation of a single three-point bend test result. It was estimated by evaluating the external applied stress that would cause the stress in a voxel along the line to exceed the material's strength. When evaluating the results of many simulations from different mesostructures and different procedures, it was found that the blocky models which used no smoothing often had three or four voxels per line which had much lower strength than the other 60 voxels. The smoothed models did not exhibit this phenomenon. Therefore, these outliers were ignored and the strength of each line was determined by the voxel with the fifth lowest strength.

The flexural strength of every third row was calculated, avoiding the exterior of the model by six voxels, for a total of 648 lines, half in the transverse direction, and half in the thickness direction. The flexural strength of the simulated composite was taken to be the mean of the strengths of the 648 line measurements. The Weibull distributions of these measurements were also calculated.

The 3-D flexural strength results are reasonably close to the experimentally obtained values, as seen in Figure 6.35. In general, the 3-D simulation values are lower than the experimental values. This discrepancy could be due to any combination of assumptions or inaccurate material properties or process parameters. The general trend seems to agree quite well. The composite with 95v% diamond is unique in that it has a modeled strength higher than the experimental data. It also has the trend defying increase in strength that is seen in the experimental data. In the 3-D model, this feature is exaggerated due to the voxelated nature of the model. The micrograph of the 95v% composites, Figure 6.36, shows thin bands of matrix mostly separating the granules. In the 3-D model, shown in Figure 6.37, the voxel size limited the coverage of the matrix at 95v% and the granules were mostly contiguous.

Similar to the other models, the 3-D model predicts that the failures will initiate in the carbide phase. The model agrees with the others that the stronger and less stiff component fails first due to the residual stresses which accumulate after sintering. The thermal residual stresses would cause the carbide material to fail at an even lower applied stress were it not for the dilatational residual stresses which mitigate the effect of the thermal residual stresses.

Comparing the Weibull results of the 3-D model, Figure 6.38, with the

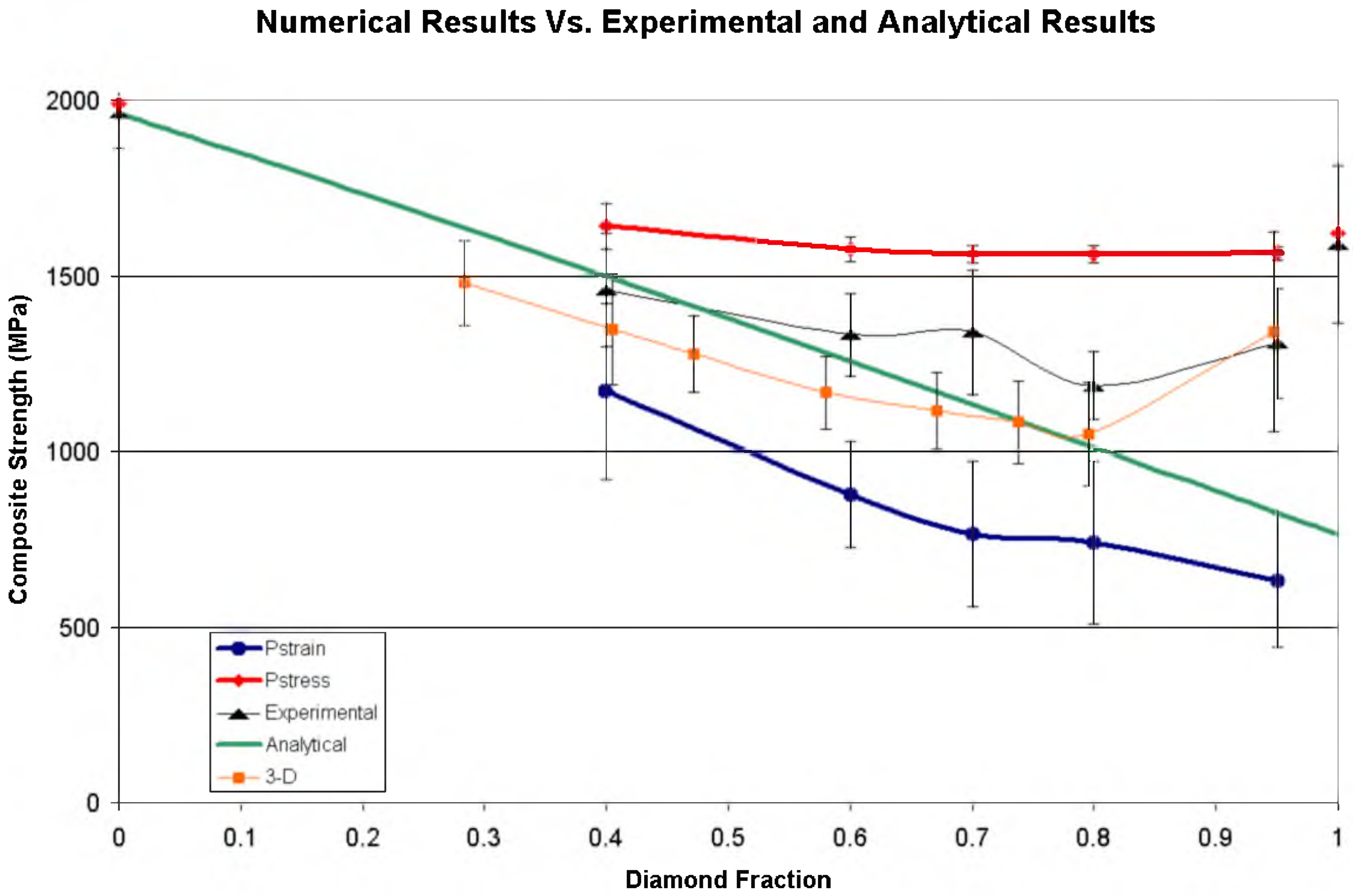

Figure 6.35. Graph comparing the 3-D simulation results with 2-D, analytical, and experimental results.

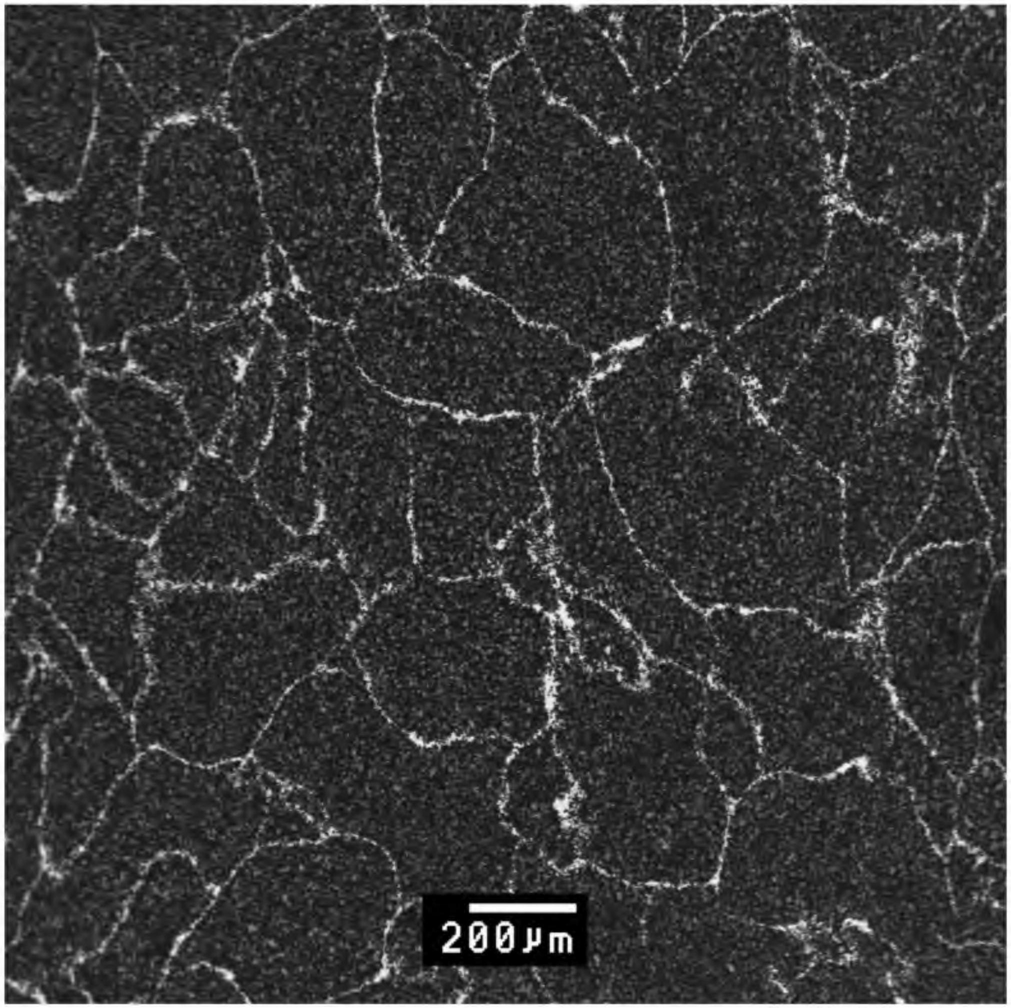

Figure 6.36. Micrograph of a 95v% diamond composite. The tungsten carbide matrix phase forms a thin skin between the diamond granules.

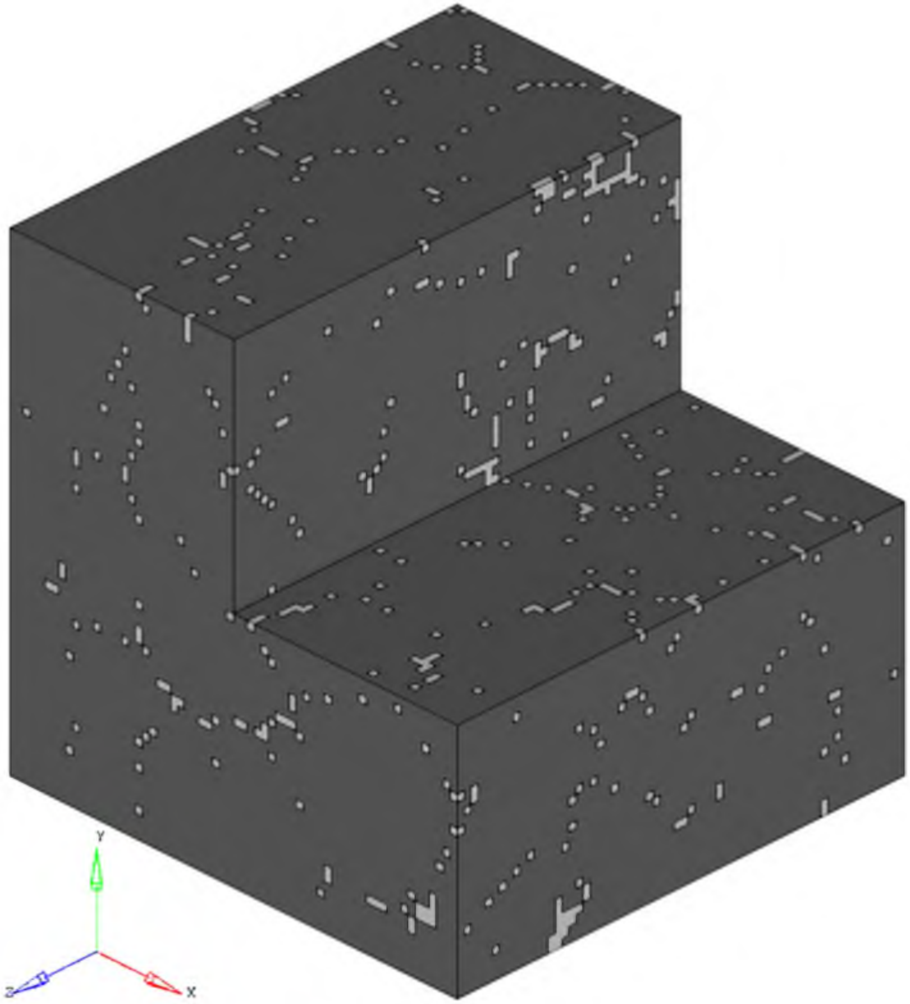

Figure 6.37. Image of the simulated 95v% mesostructure. Due to the blocky nature of the model, the matrix phase does not surround the individual granules.

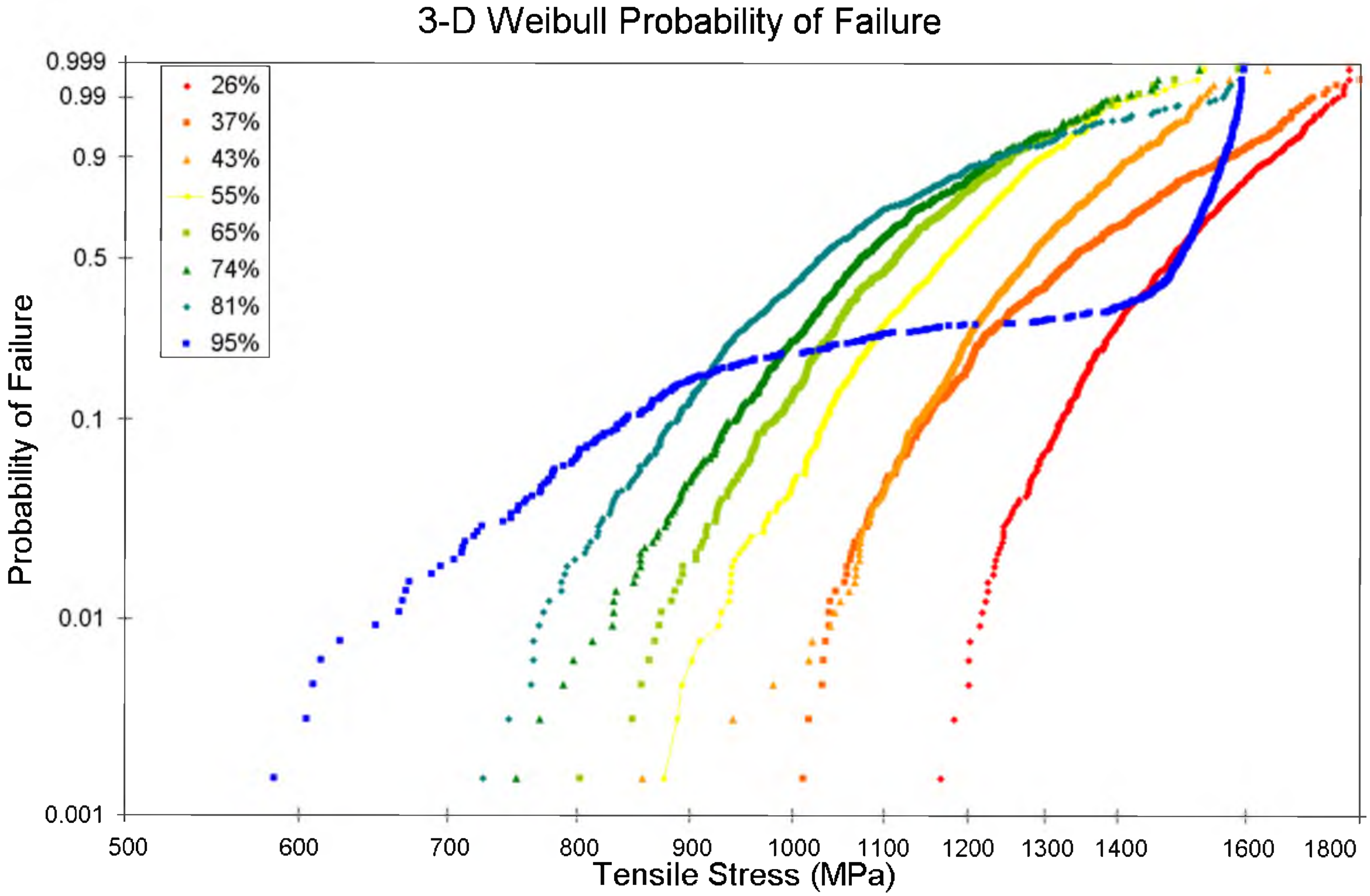

Figure 6.38. Weibull plot of the simulated mesostructures. The carbide matrix was always the phase that failed first in all of the composites, except for 95v%.

experimental Weibull results, Figure 4.4, the model results are much smoother owning to the large number of data points. The data mimics the decreasing slope in higher values. When considering the modeled data only, the results for the 95v% composite stands out from the rest, because it has a very different form. 95v% is the only composite where the diamond granules failed in some of the simulated three-point bend testing. This is because there were some test lines which did not contain any matrix. Figure 6.39 shows the Weibull curves for 95v% if the failures in the matrix and the failures in the granules are treated separately. The Weibull curve for 95v% matrix only follows the trend set by the other composites (which also failed only in the matrix). The lines in the 95v% composite which only ran through the diamond fail in a fairly tight range and at a relatively high value.

Effect of Dilatational Residual Stresses

The effect of neglecting dilatational residual stresses will be considered one last time. The thermal-only residual stress map is shown in Figure 6.40. Compared to the total residual stress map in Figure 6.31, the color is nearly identical, but that is due to the sliding color scale. Note that the maximum tensile stress, which is found in the matrix phase, is 3000 MPa in the thermal residual stress case and is reduced to 1722 MPa once dilatational residual stresses are accounted. It was shown in the last section that this composite is predicted to fail by tension in the matrix. If the dilatational residual stresses are neglected then the composite would be predicted to have a lower strength. This can be seen in Table 6.8. Almost a quarter of the strength estimations for the case neglecting

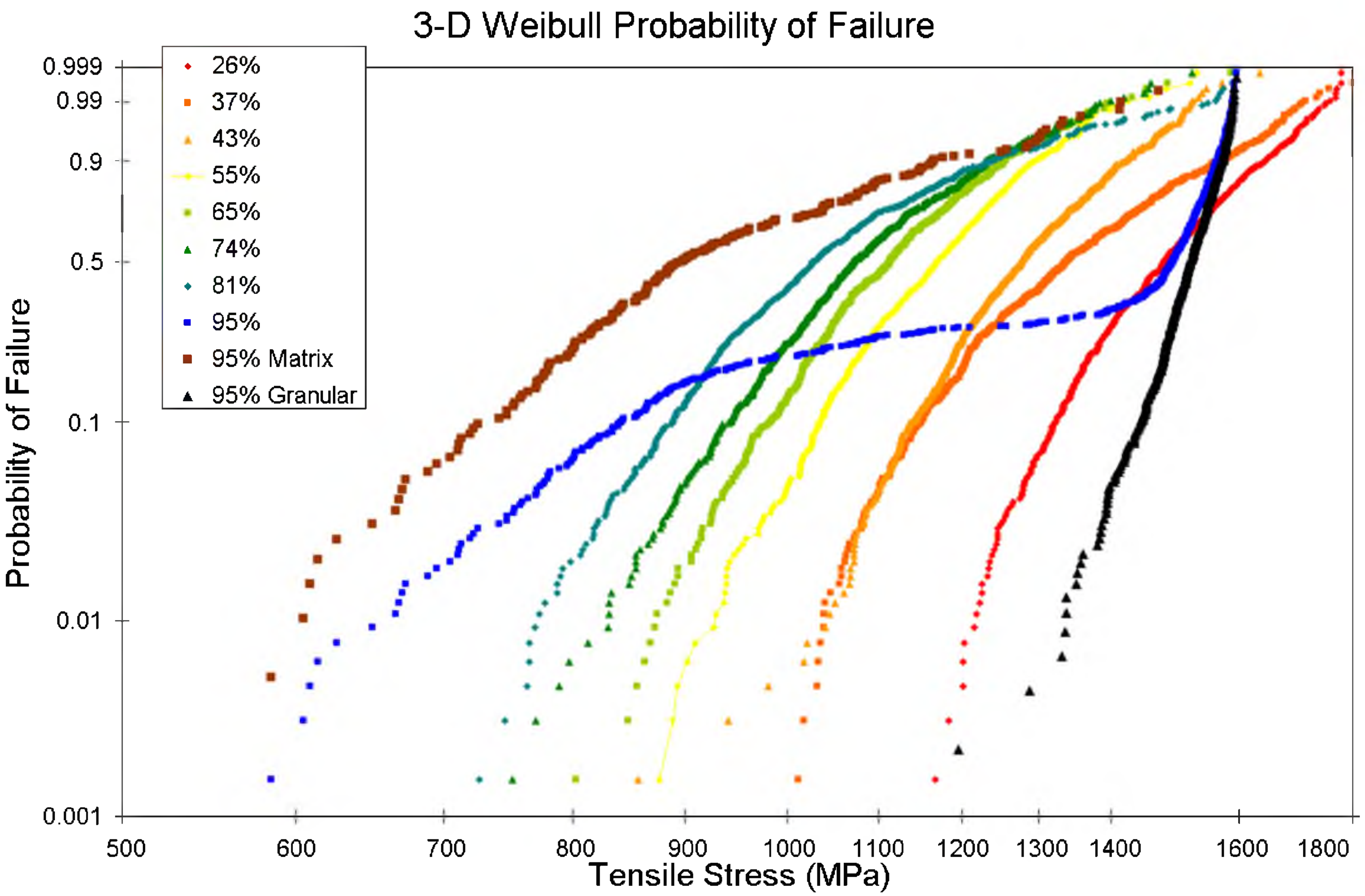

Figure 6.39. Weibull plot of the simulated mesostructures with the 95v% data split into two groups. The brown group plots the failures in the matrix while the black group plots the failures in the granules.

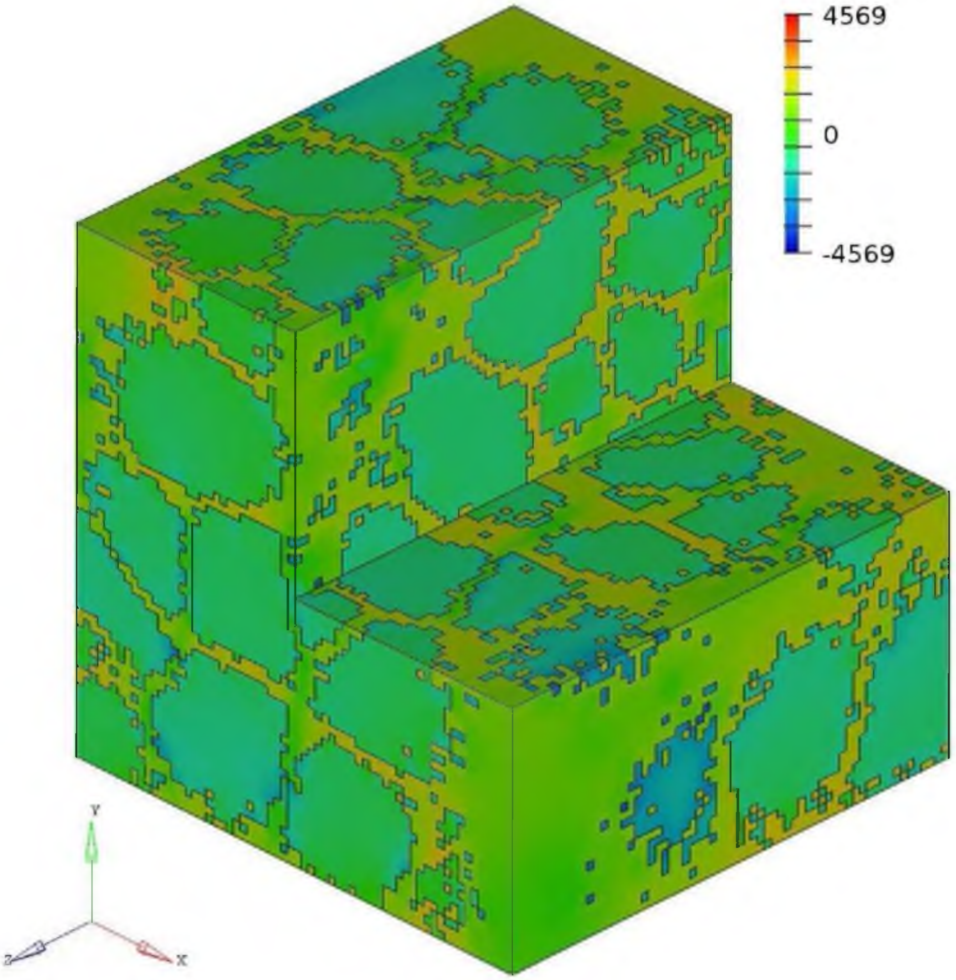

Figure 6.40. Residual stress map of a 58v% diamond simulated mesostructure when neglecting dilatational residual stresses. Compared to the total residual stress map in Figure 6.31, the thermal-only residual stresses are much higher.

Table 6.8

Effect of Dilatational Residual Stresses on Strength

	Average Strength	Standard Deviation
Including Dilatational Residual Stresses	1166	104
Neglecting Dilatational Residual Stresses	189	251

dilatational residual stresses were negative, meaning that the specimen is predicted to fail without any applied load due to the excessive residual stresses. This illustrates the beneficial role of dilatational residual stresses in tempering the thermal residual stresses.

Optimization of Mesostructure

The 3-D model was used to estimate the impact of different mesostructure characteristics upon the flexural strength of the composite. Producing and testing granular diamond composites is costly in terms of time, effort, and resources. The requirements were vastly reduced with a working 3-D model and the ability to generate theoretical mesostructures, thus making it feasible to explore the design space. It was found that smoother, more uniformly distributed, and fully separated mesostructures increased the strength of the composite material.

The flexural strength of the synthetic mesostructures was calculated in the same manner as described in the last section.

Procedure

In this study the results of two mesostructural modifications were compared to data collected in the last section. The first variant was produced by passing the generated mesostructures through a smoothing filter which removes stray voxels. The filter checks each voxel for the number and proximity of neighbor voxels of the same material. Voxels without sufficient neighbor support are switched to the opposite phase. Figure 6.41 illustrates a smoothed mesostructure. It contains 58.5% diamond by volume, comparable

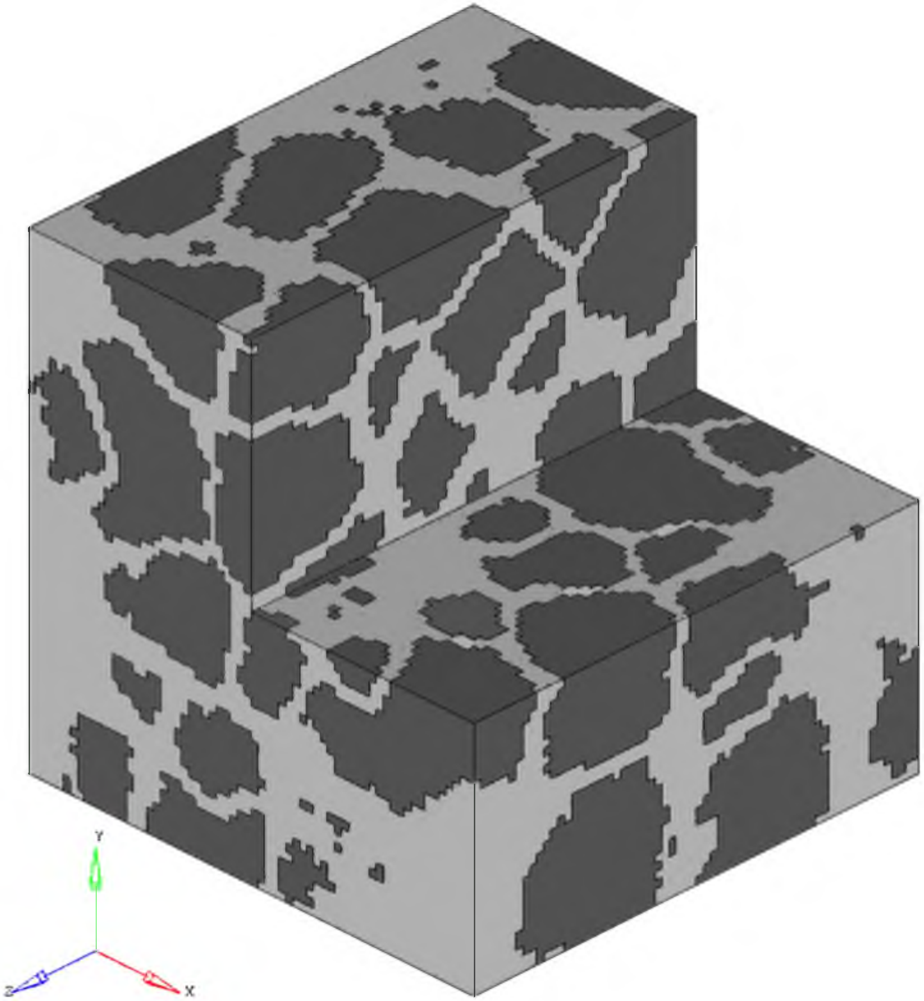

Figure 6.41. GDC with a smoothed mesostructure with 58.5v% diamond. The granules have smoother surfaces and there are fewer stray voxels compared to Figure 6.40, an unsmoothed mesostructure of similar volume fraction.

to the synthetic mesostructure shown in Figure 6.40. The mesostructure in Figure 6.40 more closely matches the mesostructure that was observed in Series A micrographs which also had loose diamond grains in the matrix. The second variation was a fully separated mesostructure. Each granule was fully separated from every other granule by modifying the mesostructure by hand to eliminate any intergranular faces, edges, or nodes. The manually separated mesostructure is shown in Figure 6.42. It has a post-processed diamond concentration of 72.3v%, comparable to the unfiltered mesostruture represented in Figure 6.43.

Results

Figures 6.44 to 6.46 present the total stress maps for a smoothed, smoothed and separated, and an unfiltered mesostructure, respectively. Stress changes in the matrix will have the greatest effect on composite strength because the material is almost always predicted to fail in the matrix first. The smoothed mesostructures do not have as many voxels of matrix surrounded by majority of diamond voxels. Such voxels often have the highest stresses in the unfiltered mesostructure.

The strengths and estimated strength increases of the enhanced mesostructures are tabulated in Table 6.9 and plotted in Figure 6.47. The composites with smoothed mesostructures are predicted to have higher strength than the composites with unfiltered mesostructures. The composite with the smoothed and separated mesostructure has an even higher strength than composite of similar composition with only a smoothed mesostructure. It appears that the strengthening effect of smoothing is greater at lower

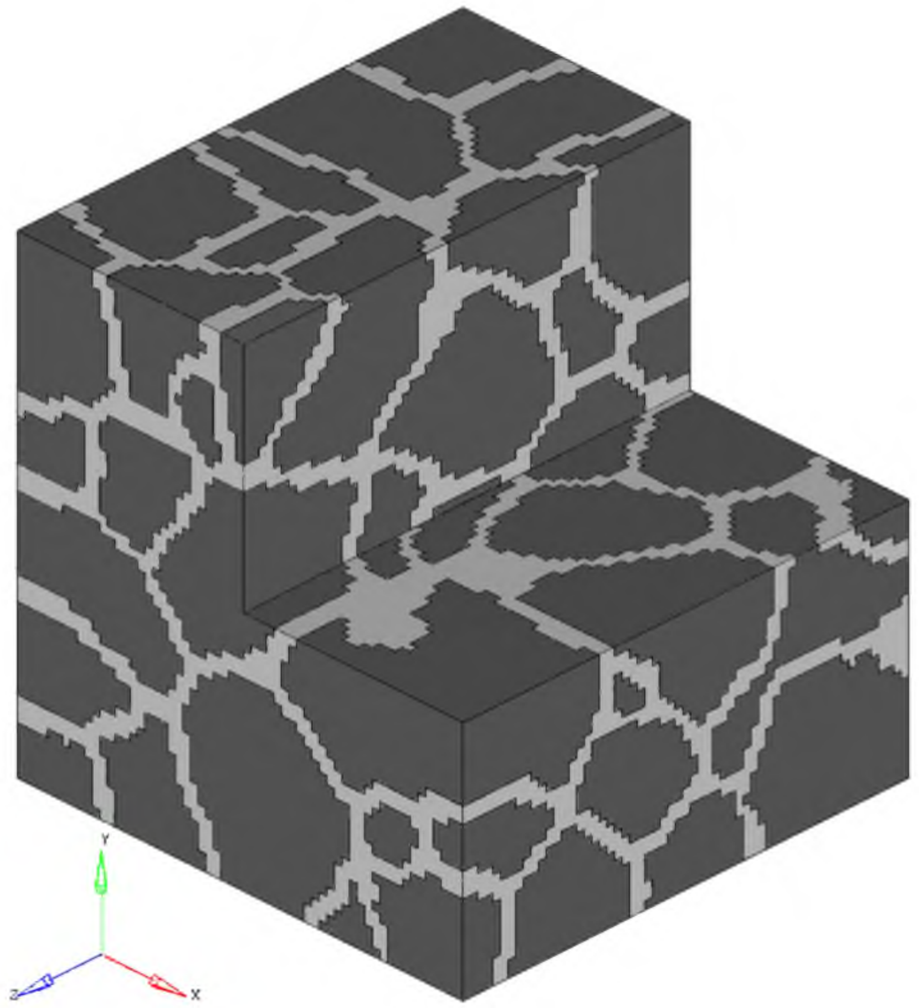

Figure 6.42. GDC with a smoothed and separated mesostructure and a 72.3v% diamond fraction. After the mesostructure was passed through a smoothing filter, any connections between granules were eliminated.

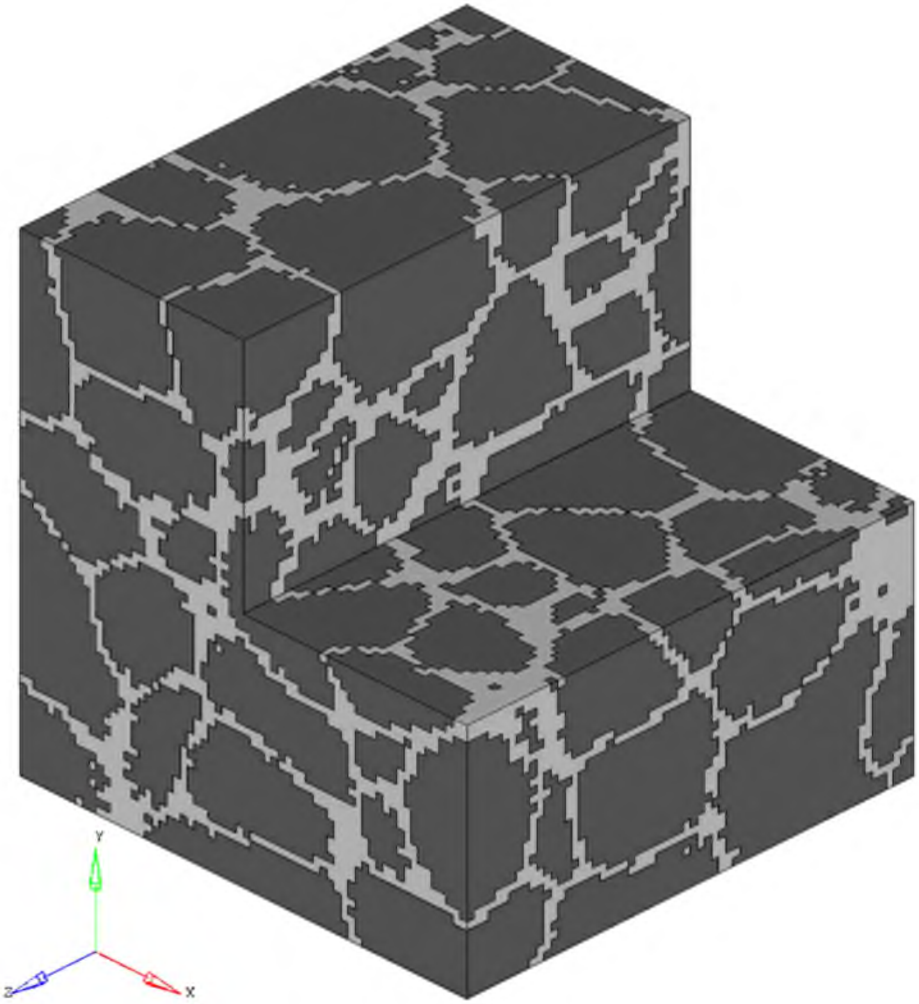

Figure 6.43. An unfiltered GDC mesostructure with 73.8v% diamond fraction. Almost all of the granules are interconnected by shared faces, edges, or points between various granules.

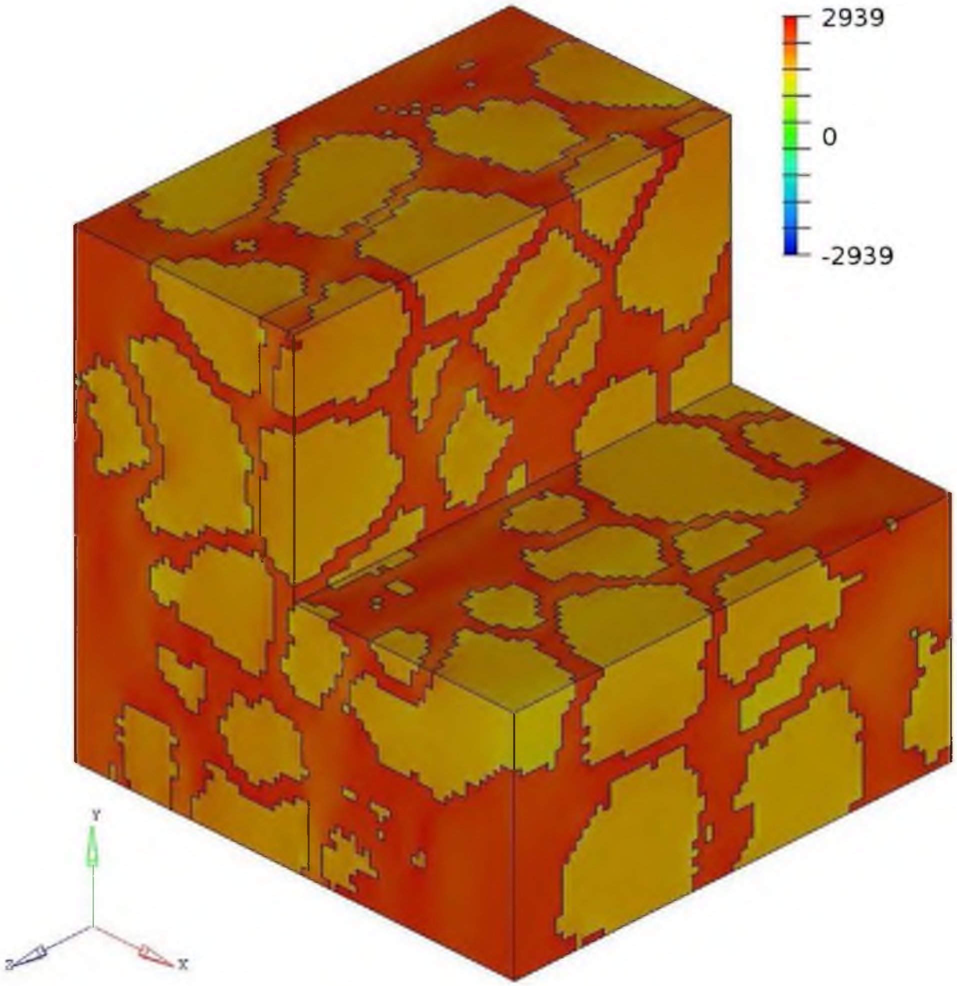

Figure 6.44. Total stress map of a smoothed mesostructure with 58.5v% diamond. The smoothing filter has eliminated many of the voxels with the greatest stress concentration.

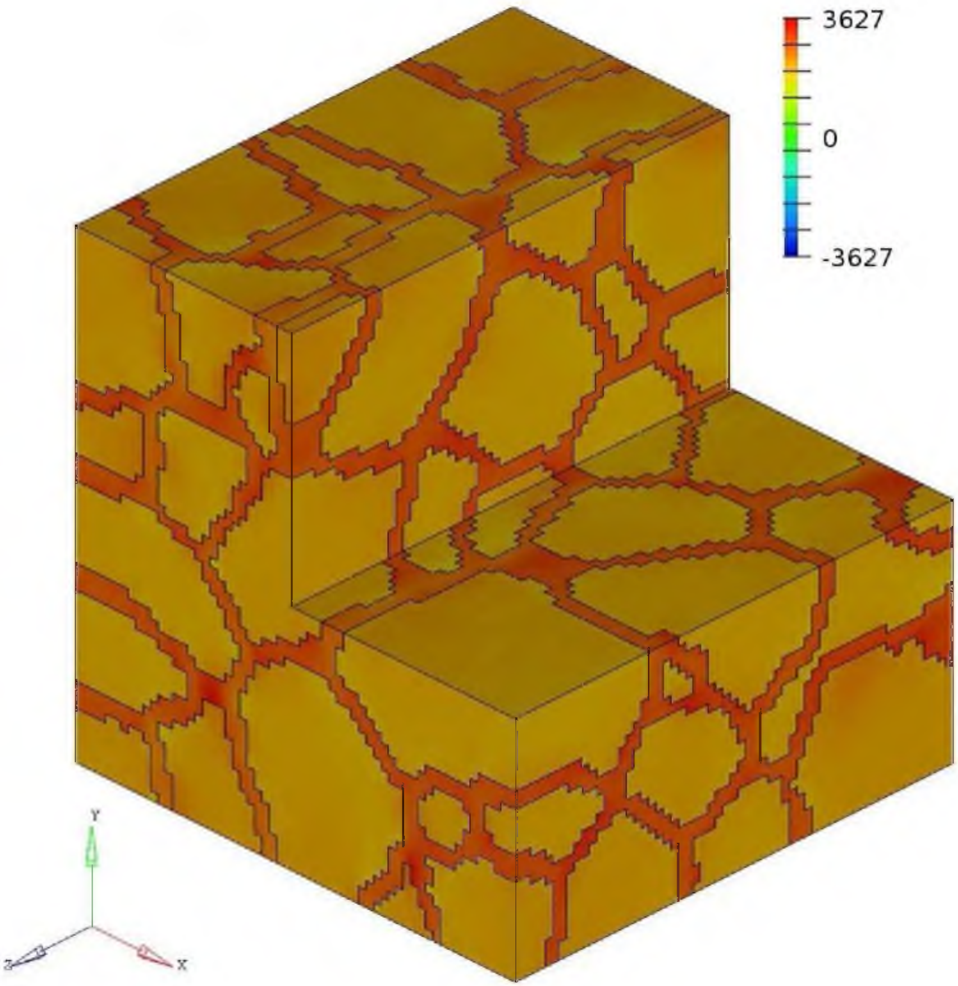

Figure 6.45. Total stress map of a smoothed and separated mesostructure with 72.3v% diamond. Compared to an unfiltered mesostructure of similar diamond fraction (Figure 6.46), This mesostructure has fewer areas of high stress concentration.

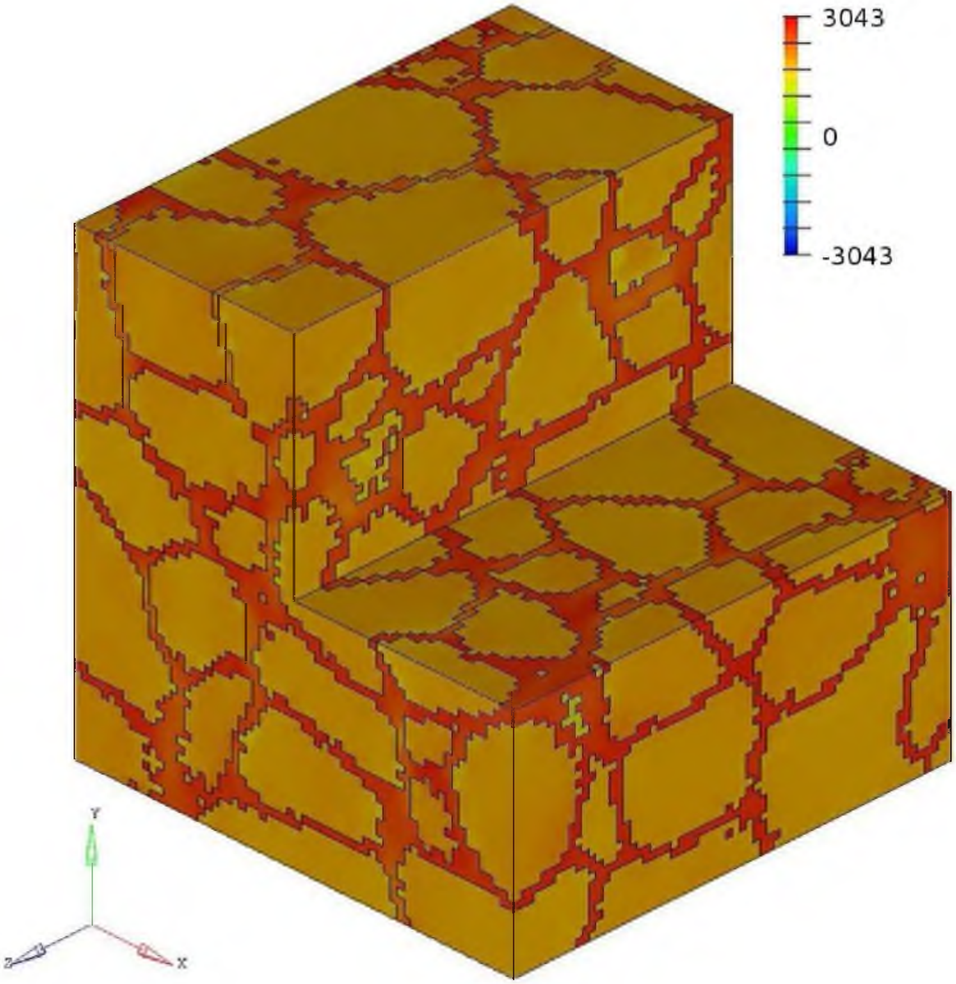

Figure 6.46. Total stress map of an unfiltered mesostructure with 73.8v% diamond.

Table 6.9

Impact of Filtering Synthetic Mesostructures on Flexural Strength

	Diamond Volume Percent	Average Strength (MPa)	Standard Deviation (MPa)	Unfiltered Interpolated Strength (MPa)	Percent Change
Smoothed	58.5	1241	109	1163	6.63%
Smoothed	72.3	1118	120	1080	2.58%
Separated	72.3	1152	146	1080	5.63%

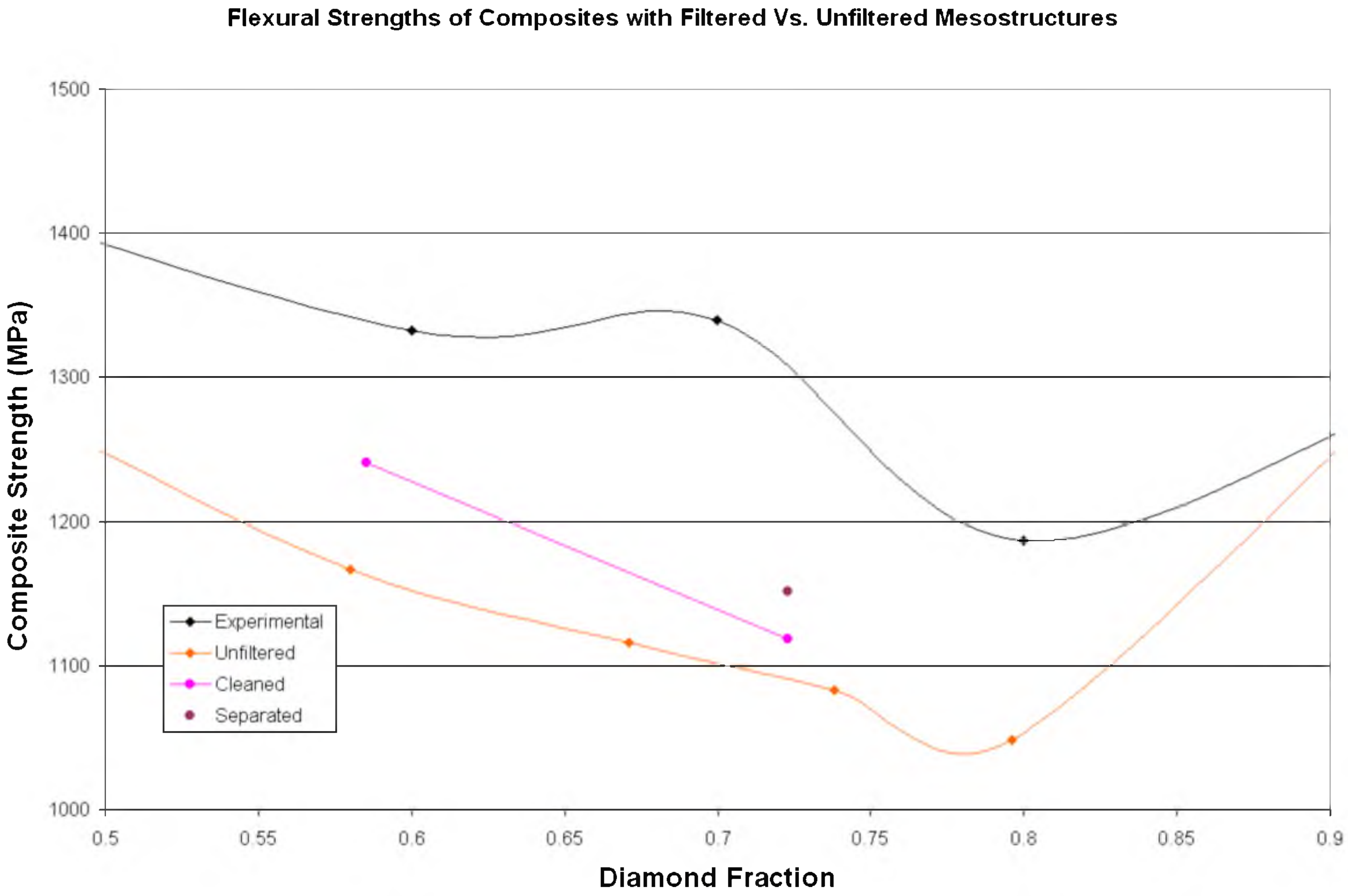

Figure 6.47. Calculated flexural strength of composites with smoothed and separated mesostructures compared to previously calculated strengths of composites with unfiltered mesostructures.

diamond fractions. The 72.3v% smoothed composite has the strength of a 67v% unfiltered composite. The 58.5v% composite has the strength of a 51v% unfiltered composite. The 72.3v% separated composite has the strength of a 60v% unfiltered composite. A Weibull plot is presented in Figure 6.48 for composites of around 73v% diamond with unfiltered, smoothed, and smoothed and separated mesostructures. Increased filtering causes greater curvature on the Weibull plot.

The modeling of smoothed and separated mesostructures have shown that reduction of stress risers in the matrix phase will increase the strength of the composite material. Production methods which increase the smoothness of the granules, decrease the amount diamond grains floating in the matrix, and increase the mutual separation of the diamond granules will increase the flexural strength of the composites.

Chapter Summary

The slab model is a simple enough model to allow for an analytical solution. It was used in the last chapter to explore the interactions between diamond and carbide. In this chapter, the results from the derived analytical equations were compared to the results from a numerical model using a modern finite element analysis package. The only discrepancy between the two was due to the neglect of Poisson strain differences in the transverse direction in the analytical model. The error was found to be well below 1%.

A shear cutter has a material configuration very similar to the slab model. It is a drill bit insert made of a PCD layer and a WC-Co layer. Residual stresses in shear cutters have been studied in the past with both empirical measurements as well as modeling

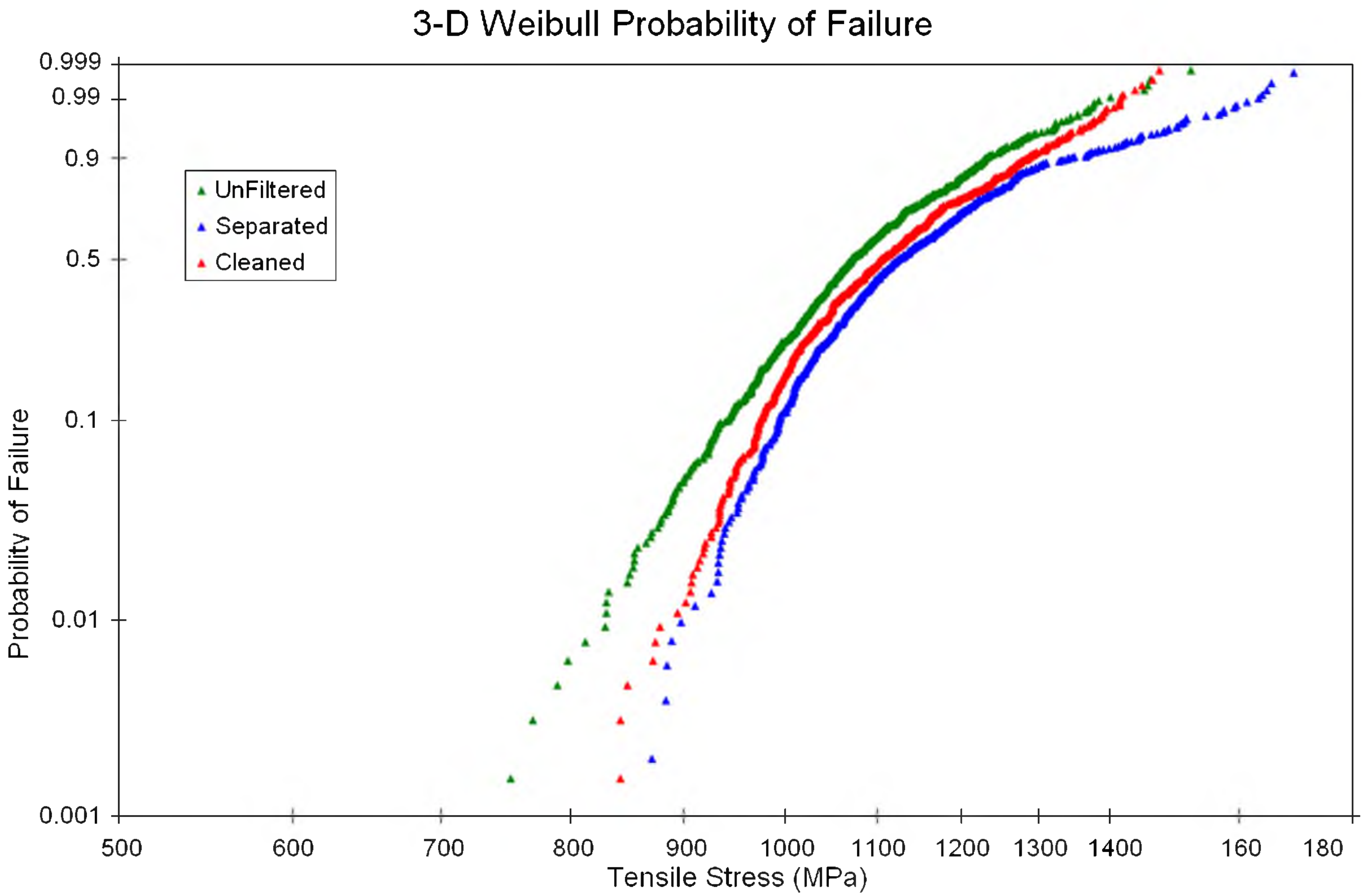

Figure 6.48. Weibull plot of three differently constructed mesostructures with diamond fraction near 0.73. The mesostructures with more filtering have higher strengths and more curvature in the Weibull plot.

estimates. The current modeling procedure and parameters were applied to a previously studied shear cutter configuration and the results were compared. The current model results were a better fit to the empirical data, but the former model results were closer than expected for a model that did not consider dilatational residual stresses. This is because of differences in the material properties that were used.

Numerical modeling was used to estimate the residual stresses and strengths in diamond/carbide composites with granular mesostructures. The 2-D model used either plane stress or plane strain assumptions. The 3-D model used computer generated mesostructures that simulated the actual mesostructures. Both models generated results that followed the trend seen in the experimental data. All of the models predict that the WC-Co will fail first. There are areas of stress concentration in the diamond phase where it might be expected to fail first, but the model showed that these same areas are where the compressive residual stresses also concentrate. The areas of stress concentration in the carbide phase, on the other hand, get both the tensile residual stresses and the applied stresses concentrated there, and are predicted to be the strength determination areas.

An optimization study showed that mesostructures with smoother, more spherical granules that are fully isolated by matrix would be stronger than the material that was actually produced for this research.

References

1. Paggett, J. W.; Drake, E. F.; Krawitz, A. D.; Winholtz, R. A.; Griffin, N. D., Residual stress and stress gradients in polycrystalline diamond compacts. *International Journal of Refractory Metals and Hard Materials* **2002,** *20* (3), 187-194.

2. Lin, T. P.; Hood, M.; Cooper, G. A.; Smith, R. H., Residual stresses in polycrystalline diamond compacts. *Journal of the American Ceramic Society* **1994,** *77* (6), 1562-1568.

3. Hull, D.; Clyne, T. W., *An introduction to composite materials*. Cambridge university press: 1996.

4. Glowka, D. A.; Stone, C. M., Thermal Response of Polycrystalline Diamond Compact Cutters Under Simulated Downhole Conditions. *SPE Journal* **1985,** *Volume 25* (2), 143-156.

5. Carter, W. C.; Langer, S. A.; Fuller, E. R., The OOF Manual. National Institute of Standards and Technology (NIST): 2003. http://www.ctcms.nist.gov/oof/oof1/

CHAPTER 7

SUMMARY AND CONCLUSIONS

This dissertation reports on research into the effect of mesostructure on the functional properties of granular diamond composite (GDC) materials. In order to conduct the research, a method to produce GDC materials was developed, the GDC materials were characterized by measuring intrinsic and functional properties, and several models of mesostructure and flexural strength were developed. Residual stresses, produced as the material exits the sintering conditions, play a significant role in the flexural strength of the resulting GDC materials and a strong argument is made for the inclusion of dilatational residual stress computations in strength modeling.

Granular Diamond Composite Production

A method for producing GDC materials needed to be developed, as this material had not been produced before. The objective of the method was to produce properly sintered GDC materials with uniformly distributed spherical granules of sintered polycrystalline diamond in a tougher matrix. Producing GDC materials proved harder than expected. Much time and effort was invested in developing a satisfactory method, and was never fully accomplished. The diamond granules were not as spherical and the distribution was not as uniform as desired. Also troubling was the amount of diamond grains which mixed into the matrix. Figure 7.1 compares a conceptual image of the target mesostructure (a), along side an actual microimage of a 70v% mesostructure (b).

Material Characterization

Much of the effort to characterize the mechanical properties of the GDC materials produced focused on flexural strength, because it is a good indication of the potential performance of the material. Problems with processing will often be first detected in flexural strength testing. It was telling, therefore, that the measured flexural strength of the A100 sample, which consists of 100v% PCD 1 and produced using the developed method, was roughly 10% lower in flexural strength as measured by Smith Megadiamond, than the PCD 1 material internally processed using their standard methods. Another interesting phenomenon was that the flexural strength of the composites was lower than the flexural strength of its components, see Figure 6.35.

An insufficient quantity of the GDC composites was produced to get a clear understanding of how the material system would behave in the field, but because the flexural strength was measured below the flexural strength of the carbide-only matrix composites, it is not promising.

The wear results of Series A was also disappointing. The A100 performance was roughly 60% below the value of standard PCD 1. Figure 4.8 shows that the measured wear rates did not decrease significantly until the PCD phase dropped below 60v%, but this may not be all that meaningful because the wear performance of the 100v% samples

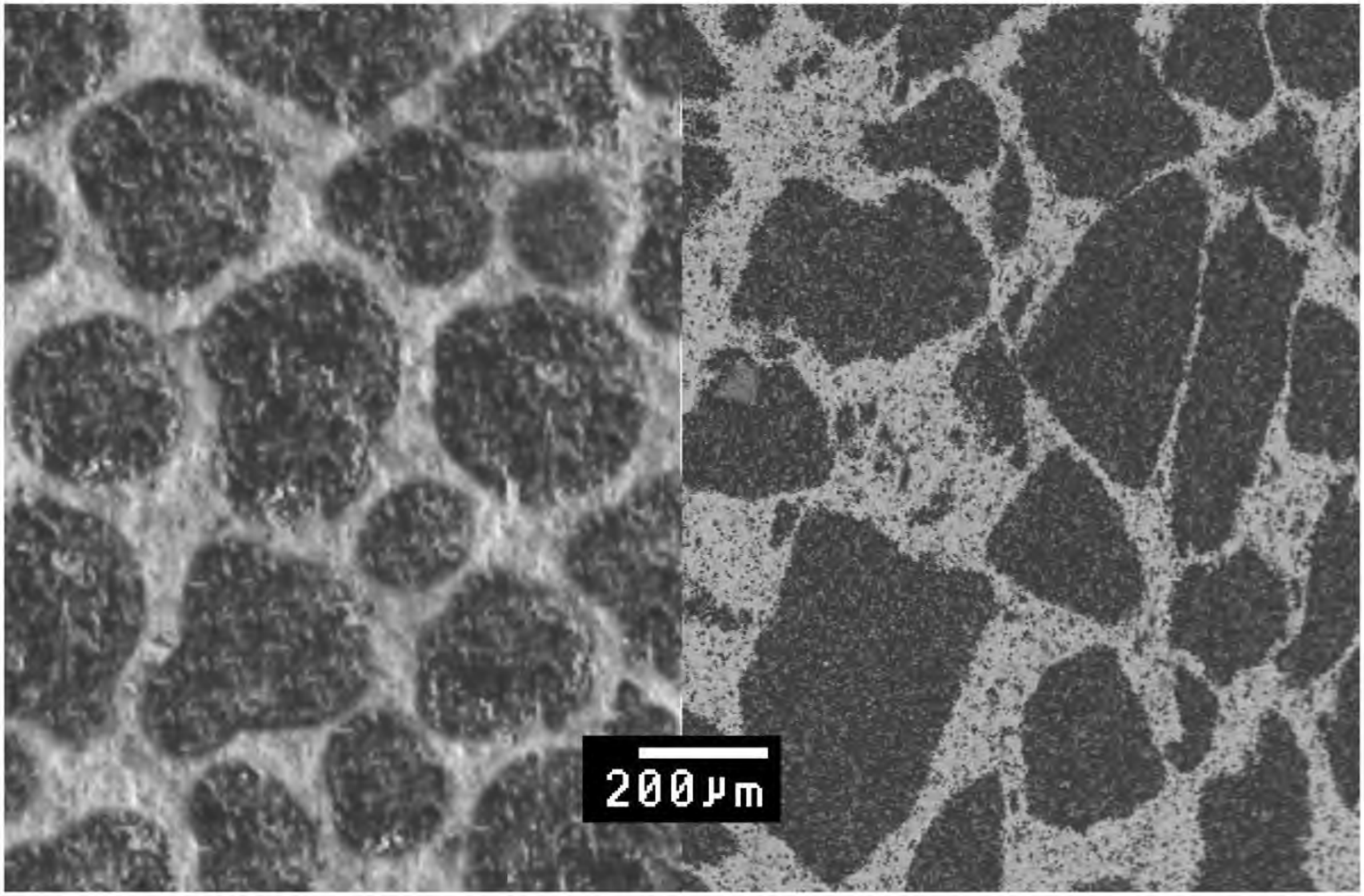

Figure 7.1. (a) A computer generated microimage of an idealized mesostructure compared to (b) an actual microimage showing a typical mesostructure produced in the Series A 70v% grade.

was so poor.

The impact resistance results were also unexpected. The average drop height for failure trended downward as more of the carbide was added. Again, 95v% was the outlier. See Figure 4.11.

One of the GDC grades with diamond in the matrix, G30, was field tested head-to-head with a conventional grade of PCD in the heal row of a roller cone drill bit. Despite the disappointing and unexpected mechanical properties of GDC materials, the field test proved quite promising as the GDC inserts had a markedly improved service life when compared to the conventional PCD inserts, showing less wear coupled with less catastrophic failure.

Analytic Model

An analytical model was developed based on the slab model to predict the residual stresses and flexural strength of the Series A composites. There are several simplifications used in the slab model, and the geometry of the model does not closely match the granular nature of GDC materials, but the model was simple enough to obtain an exact solution. Residual stresses were calculated from both the temperature change and the pressure change when returning to ambient from sintering conditions. The analytical model predicted that the composite strengths should be less than the component strengths and clearly illustrated the affect of the stiffer material being the lower strength component. The analytical model also shows the effects of the thermal and dilatation residual stresses on both the flexural strength and on the material expansion.

The role of dilatational residual stresses was shown to be too important to neglect. Despite the many simplifications and uncertainty in the input variables, the final model reasonably matched the empirical data, see Figure 6.35. A 3-D numeric slab model was used to verify the derived equations and had identical results to the residual stresses and was off less than 1% on the flexural strength predictions. The difference was created by a simplification used in the analytical model to neglect the effect of the difference in the Poisson's ratios in the transverse direction.

2-D Numeric Model

A 2-D numerical model was used to predict the flexural strength based on actual SEM micrographs of the mesostructure. Due to the 2-D nature of the model, it was necessary to use either plain stress or plain strain assumptions. Both were sequentially used. Residual stresses were accounted for, both thermal and dilatational. The experimentally measured flexural strengths fell between the plain stress and plain strain strength measurements, see Figure 6.35. Multiple measurements were taken from each micrograph. A Weibull analysis was conducted to evaluate the variation in strength due only to mesostructure inhomogeneity, without the distribution of microflaws.

3-D Numeric Model

Finally, a 3-D model was created to estimate the residual stresses and flexural strength of GDC materials with a minimum of assumptions and simplifications. The difficulty in recording the actual mesostructure in three dimensions necessitated the creation of a 3-D mesostructure that approximated the mesostructure of the tested material. Hundreds of measurements were taken from each mimicked specimen, resulting in high resolution Weibull plots. The estimated flexural strengths well matched the empirical data, especially the trends including the 95v% outlier, see Figure 6.35. Again, the importance of accounting for the dilatational residual stresses was shown. The 3-D model was used to explore probable outcomes if changes were made to the mesostructure. Mesostructures with cleaner interfaces and more regularly shaped granules were modeled, but mesostructural changes only resulted in slightly better flexural strength predictions.

Composite Behavior

Granular diamond composites are different than most composites, because the phase with the lower strength is stiffer. This causes the stresses to concentrate in the weaker material. In the diamond-carbide system this phenomenon is counter-acted by the residual stresses. The matrix contracts more than the diamond as the composite cools after sintering, putting the diamond phase into compression. Because of this compression the carbide matrix will actually reach is critical stress before the diamond granules, even with the stresses concentrating in the diamond. In fact, if the thermal residual stresses were not mitigated by the dilatational residual stresses, where the matrix expands more than the diamond due to the pressure release after sintering, composites with a higher fraction of diamond would fail without any applied load.

Conclusions

Diamond granular composites hold the potential of increasing the toughness resistance of PDC inserts while reducing the loss of wear resistance that typically results from increases in toughness. In order to achieve this goal, the material production methods need to be improved to allow the individual composite components to have properties closer to those of the component materials after traditional processing. This is particularly true for the tungsten carbide matrix material, because all of the models predict that the strength of the composite is limited by the carbide.

The mesostructure of GDC materials has a strong influence on the functional properties of the material. The parameters with the most significant impact are the component material selection and the volume ratio of the granules to matrix. The sphericity and uniform separation of the granules also improve the material performance.

Residual stresses have a large impact on the performance of GDC and all PDC. Not only do residual stresses arise from dissimilar material CTE and the temperature drop after sintering, but they also arise in bound material with dissimilar bulk moduli and the pressure drop after sintering. This research has shown that the dilatational residual stresses need to be considered, and should be addressed using quantitative and robust modeling methods.

APPENDIX

JAVA CODE FOR GENERATING MESOSTRUCTURE

```
import java.io.*;
import java.util.Random;
import java.lang.Math;


class MesoGen {

  static int side = 70;
  static int nGrains = 70;
  static double vFraction = 0.49;
  static int oBuffer = 4;
  static int gBuffer = 2;

  public static void main(String[] args) throws IOException {
    MesoVolume.fill();
    MesoVolume.nuk(nGrains); //nucleate at the same time
    MesoVolume.grow(vFraction);
//  MesoVolume.writeRaw(1);
    MesoVolume.clean();
    MesoVolume.writeRaw(0);
  }
}

class MesoVolume {
  static int iGrain = 1;
  static int[][][] myCanvas = new int[MesoGen.side][MesoGen.side][MesoGen.side];
  static int[][][] tempCanvas = new int[MesoGen.side][MesoGen.side][MesoGen.side];

  public static void fill() {
    for (int i = 0; i < MesoGen.side; i++)
      for (int j = 0; j < MesoGen.side; j++)
        for (int k = 0; k < MesoGen.side; k++){
          myCanvas[i][j][k] = 0;
        }
//System.err.println("Done Filling");
  }
  public static void nuk(int numGrans) {
    int i,j,k;
    Random chance = new Random();
    for (int l = 0; l < numGrans; l++) {
```

```
    i = chance.nextInt(MesoGen.side-MesoGen.gBuffer*2)+MesoGen.gBuffer;
    j = chance.nextInt(MesoGen.side-MesoGen.gBuffer*2)+MesoGen.gBuffer;
    k = chance.nextInt(MesoGen.side-MesoGen.gBuffer*2)+MesoGen.gBuffer;
    if (check(i,j,k,MesoGen.gBuffer)) myCanvas[i][j][k] = ++iGrain;
    System.out.println("Nuked grain " + iGrain + " at " + i + ", " + j + ", " + k);
  }
}
public static boolean check(int x, int y, int z, int gBuffer) {
  boolean clear = true;
  for (int i = -gBuffer; i <= gBuffer; i++)
    for (int j = -gBuffer; j <= gBuffer; j++)
      for (int k = -gBuffer; k <= gBuffer; k++)
        if (myCanvas[i+x][j+y][k+z] > 0) clear = false;
  if (!clear) System.err.println("bad nuk");
  return clear;
}
public static void grow(double vFraction) throws IOException{
  double vFrac = 0.0;
  int count = 0;
  int step = 0;
  double[] grains = new double[MesoGen.nGrains +2];
  double sum = 0.0;
  double max = 0.0;
  int maxGrain = 0;
  Random chance = new Random();
  for (int i = 0; i < MesoGen.side; i++)
    for (int j = 0; j < MesoGen.side; j++)
      for (int k = 0; k < MesoGen.side; k++)
        tempCanvas[i][j][k] = 0;
  while (vFrac < vFraction) {
    for (int i = MesoGen.gBuffer; i < MesoGen.side-MesoGen.gBuffer; i++)
      for (int j = MesoGen.gBuffer; j < MesoGen.side-MesoGen.gBuffer; j++)
        for (int k = MesoGen.gBuffer; k < MesoGen.side-MesoGen.gBuffer; k++) {
          if (myCanvas[i][j][k] == 0) {
            for (int x = -MesoGen.gBuffer; x <= MesoGen.gBuffer; x++)
              for (int y = -MesoGen.gBuffer; y <= MesoGen.gBuffer; y++)
                for (int z = -MesoGen.gBuffer; z <= MesoGen.gBuffer; z++)
                  if (x != 0 || y != 0 || z != 0) grains[myCanvas[i+x][j+y][k+z]] += 1/(1.0*x*x+y*y+z*z);
            for (int h = 2; h < MesoGen.nGrains+2; h++) {
              if (grains[h] > max) {
                max = grains[h];
                maxGrain = h;
              }
              sum += grains[h];
              grains[h] = 0.0;
            }
            //if (max > 0) System.err.println(max + ", " + (sum-max));
            if (max-2.0*(sum-max) >= 30.0*chance.nextDouble()) {
                tempCanvas[i][j][k] = maxGrain;
            }
            max = 0.0;
            sum = 0.0;
            maxGrain = 0;
          }
        }
    for (int i = 0; i < MesoGen.side; i++)
```

```
        for (int j = 0; j < MesoGen.side; j++)
          for (int k = 0; k < MesoGen.side; k++) {
            if (tempCanvas[i][j][k] > 0) {
              myCanvas[i][j][k] = tempCanvas[i][j][k];
              tempCanvas[i][j][k] = 0;
            }
            if (myCanvas[i][j][k] > 0) count++;
          }
      vFrac = count*1.0/(MesoGen.side-2*MesoGen.gBuffer)/(MesoGen.side-
2*MesoGen.gBuffer)/(MesoGen.side-2*MesoGen.gBuffer);
      count = 0;
      System.err.println("vFrac = " + vFrac);
      step++;
//    writeRaw(step);
//    System.err.println("step " + step);
    }
  }
  public static void writeRaw() throws IOException{
    writeRaw(0);
  }
  public static void writeRaw(int ident) throws IOException{
    System.setOut(new PrintStream(new FileOutputStream("Output" + ident + ".bin")));
    int border = 0;
    for (int i = 0; i < MesoGen.side; i++)
      for (int j = 0; j < MesoGen.side; j++)
        for (int k = 0; k < MesoGen.side; k++)
          tempCanvas[i][j][k] = myCanvas[i][j][k];
    for (int i = MesoGen.oBuffer-1; i < MesoGen.side-MesoGen.oBuffer+1; i++) {
      for (int j = MesoGen.oBuffer-1; j < MesoGen.side-MesoGen.oBuffer+1; j++) {
        for (int k = MesoGen.oBuffer-1; k < MesoGen.side-MesoGen.oBuffer+1; k++) {
          if (tempCanvas[i][j][k] > 0) System.out.print((char)0);
          else System.out.print((char)127);
        }
      }
    }
    System.setOut(new PrintStream(new FileOutputStream("Output" + (ident + 1) + ".bin")));
    for (int i = 0; i < MesoGen.side; i++)
      for (int j = 0; j < MesoGen.side; j++) {
        tempCanvas[i][j][MesoGen.oBuffer-1] = 0;
        tempCanvas[i][j][MesoGen.side-MesoGen.oBuffer] = 0;
        tempCanvas[i][MesoGen.oBuffer-1][j] = 0;
        tempCanvas[i][MesoGen.side-MesoGen.oBuffer][j] = 0;
        tempCanvas[MesoGen.oBuffer-1][i][j] = 0;
        tempCanvas[MesoGen.side-MesoGen.oBuffer][i][j] = 0;
      }
    for (int i = MesoGen.oBuffer-1; i < MesoGen.side-MesoGen.oBuffer+1; i++) {
      for (int j = MesoGen.oBuffer-1; j < MesoGen.side-MesoGen.oBuffer+1; j++) {
        for (int k = MesoGen.oBuffer-1; k < MesoGen.side-MesoGen.oBuffer+1; k++) {
          if (tempCanvas[i][j][k] > 0) System.out.print((char)0);
          else System.out.print((char)127);
        }
      }
    }
    for (int i = 0; i < MesoGen.side; i++)
      for (int j = 0; j < MesoGen.side; j++)
        for (int k = 0; k < MesoGen.side; k++)
```

```
          tempCanvas[i][j][k] = 1;
    for (int i = 0; i < MesoGen.side; i++)
      for (int j = 0; j < MesoGen.side; j++) {
        tempCanvas[i][j][MesoGen.oBuffer-1] = myCanvas[i][j][MesoGen.oBuffer-1];
        tempCanvas[i][j][MesoGen.side-MesoGen.oBuffer] = myCanvas[i][j][MesoGen.side-
MesoGen.oBuffer];
        tempCanvas[i][MesoGen.oBuffer-1][j] = myCanvas[i][MesoGen.oBuffer-1][j];
        tempCanvas[i][MesoGen.side-MesoGen.oBuffer][j] = myCanvas[i][MesoGen.side-
MesoGen.oBuffer][j];
        tempCanvas[MesoGen.oBuffer-1][i][j] = myCanvas[MesoGen.oBuffer-1][i][j];
        tempCanvas[MesoGen.side-MesoGen.oBuffer][i][j] = myCanvas[MesoGen.side-
MesoGen.oBuffer][i][j];
      }
    System.setOut(new PrintStream(new FileOutputStream("Output" + (ident + 2) + ".bin")));
    for (int i = MesoGen.oBuffer-1; i < MesoGen.side-MesoGen.oBuffer+1; i++) {
      for (int j = MesoGen.oBuffer-1; j < MesoGen.side-MesoGen.oBuffer+1; j++) {
        for (int k = MesoGen.oBuffer-1; k < MesoGen.side-MesoGen.oBuffer+1; k++) {
          if (tempCanvas[i][j][k] > 0) System.out.print((char)0);
          else System.out.print((char)127);
        }
      }
    }
  }
  public static void clean() {
    int nNeighbors;
    int nType;
    int count = 0;
    //if this is already part of a granule, remove if it is adjacent to another granule
/*  for (int i = MesoGen.gBuffer; i < MesoGen.side-MesoGen.gBuffer; i++)
      for (int j = MesoGen.gBuffer; j < MesoGen.side-MesoGen.gBufprovo redevelopment
agencyfer; j++)
        for (int k = MesoGen.gBuffer; k < MesoGen.side-MesoGen.gBuffer; k++)
          for (int x = -1; x < 2; x++)
            for (int y = -1; y < 2; y++)
              for (int z = -1; z < 2; z++)
                if(false && myCanvas[i+x][j+y][k+z] > 0 && myCanvas[i+x][j+y][k+z] !=
myCanvas[i][j][k]) myCanvas[i][j][k] = 0;*/
    for (int i = 0; i < MesoGen.side; i++)
      for (int j = 0; j < MesoGen.side; j++)
        for (int k = 0; k < MesoGen.side; k++)
          tempCanvas[i][j][k] = myCanvas[i][j][k];
    for (int i = 1; i < MesoGen.side-1; i++)
      for (int j = 1; j < MesoGen.side-1; j++)
        for (int k = 1; k < MesoGen.side-1; k++) {
          if (myCanvas[i][j][k] > 0) {
            nNeighbors = 0;
            for (int x = -1; x < 2; x++)
              for (int y = -1; y < 2; y++)
                for (int z = -1; z < 2; z++) {
                  if (myCanvas[i+x][j+y][k+z] == myCanvas[i][j][k] ) nNeighbors++;
                  if (myCanvas[i+x][j+y][k+z] != myCanvas[i][j][k] && myCanvas[i+x][j+y][k+z] > 0)
nNeighbors = nNeighbors - 3;
                }
            if (nNeighbors < 13) tempCanvas[i][j][k] = 0;
          }
        }
```

```
    for (int i = MesoGen.gBuffer; i < MesoGen.side-MesoGen.gBuffer; i++)
      for (int j = MesoGen.gBuffer; j < MesoGen.side-MesoGen.gBuffer; j++)
        for (int k = MesoGen.gBuffer; k < MesoGen.side-MesoGen.gBuffer; k++) {
          myCanvas[i][j][k] = tempCanvas[i][j][k];
    }
    for (int i = 1; i < MesoGen.side-1; i++)
      for (int j = 1; j < MesoGen.side-1; j++)
        for (int k = 1; k < MesoGen.side-1; k++) {
          if (myCanvas[i][j][k] == 0) {
            nNeighbors = 0;
            for (int x = -1; x < 2; x++)
              for (int y = -1; y < 2; y++)
                for (int z = -1; z < 2; z++) {
                  if (myCanvas[i+x][j+y][k+z] > 0) tempCanvas[i][j][k] = myCanvas[i+x][j+y][k+z];
                }
            if (tempCanvas[i][j][k] > 0)
              for (int x = -1; x < 2; x++)
                for (int y = -1; y < 2; y++)
                  for (int z = -1; z < 2; z++) {
                    if (myCanvas[i+x][j+y][k+z] == tempCanvas[i][j][k] ) nNeighbors++;
                    if (myCanvas[i+x][j+y][k+z] != tempCanvas[i][j][k] && myCanvas[i+x][j+y][k+z] > 0)
nNeighbors = nNeighbors - 3;
                  }
            if (nNeighbors < 13) tempCanvas[i][j][k] = 0;
          }
        }
    for (int i = MesoGen.gBuffer; i < MesoGen.side-MesoGen.gBuffer; i++)
      for (int j = MesoGen.gBuffer; j < MesoGen.side-MesoGen.gBuffer; j++)
        for (int k = MesoGen.gBuffer; k < MesoGen.side-MesoGen.gBuffer; k++) {
          myCanvas[i][j][k] = tempCanvas[i][j][k];
          if (myCanvas[i][j][k] > 0) count++;
    }
    System.err.println("vf= " + 1.0*count/(MesoGen.side-MesoGen.gBuffer)/(MesoGen.side-
MesoGen.gBuffer)/(MesoGen.side-MesoGen.gBuffer));

  }
}
```